ULTRAFAST COOPERATIVE PHENOMENA IN COHERENTLY PREPARED MEDIA: FROM SUPERFLUORESCENCE TO COHERENT RAMAN SCATTERING AND APPLICATIONS

A Dissertation

by

ARIUNBOLD GOMBOJAV

Submitted to the Office of Graduate Studies of
Texas A&M University
in partial fulfillment of the requirements for the degree of

DOCTOR OF PHILOSOPHY

May 2011

Major Subject: Physics

ULTRAFAST COOPERATIVE PHENOMENA IN COHERENTLY PREPARED MEDIA: FROM SUPERFLUORESCENCE TO COHERENT RAMAN SCATTERING AND APPLICATIONS

A Dissertation

by

ARIUNBOLD GOMBOJAV

Submitted to the Office of Graduate Studies of
Texas A&M University
in partial fulfillment of the requirements for the degree of

DOCTOR OF PHILOSOPHY

Approved by:

Chair of Committee,	Marlan O. Scully
Committee Members,	Vladimir A. Sautenkov
	Jaan Laane
	George R. Welch
	Alexei V. Sokolov
Head of Department,	Edward Fry

May 2011

Major Subject: Physics

ABSTRACT

Ultrafast Cooperative Phenomena in Coherently Prepared Media: From Superfluorescence to Coherent Raman Scattering and Applications. (May 2011)

Ariunbold Gombojav, B.S.; M.Sc., National University of Mongolia;

Ph.D., Palacky University in Olomouc

Chair of Advisory Committee: Dr. Marlan Scully

Technological progress in commercializing ultrafast lasers and detectors has allowed realization of cooperative processes on an ultrashort time scale, which demand a re-evaluation of the conventional cooperative phenomena with a new insight. Ultrafast cooperative phenomena in coherently prepared media and various applications of superfluorescence and coherent Raman scattering are studied in this dissertation. In particular, a simple theoretical testimony on analogy between a cooperative emission and coherent Raman scattering is presented by offering an opportunity to perform parallel research on these two processes from a unified point of view.

On one hand, the superfluorescent pulse with a time duration of a few tens of picoseconds (ps) from alkali metal vapor is observed for the first time, even though cooperative phenomena in atomic vapor have been extensively studied for more than five decades. A dense rubidium vapor pumped by ultrashort (100 femtosecond, fs) pulses allows a realization of the ultrafast superfluorescence while a time-resolved study of superfluorescence is accomplished by using a streak camera with 2 ps time resolution. Experimental research on quantum nature of cooperative emissions has been "frozen" over the years (three decades) possibly because of the technical difficulties. Quantum fluctuations of superfluorescence development are explored experimentally by taking advantage of the ultrafast streak camera. Presumable applications of the superfluorescent pulse in e.g., a remote sensing, and an ultraviolet upconversion of the input

infrared laser pulse are presented. The quantum interference due to different excitation pathways is revealed by the temporal coherent control technique while observing interferometric signals from alkali metal vapors.

On the other hand, a new spectroscopic technique based on ultrafast coherent Raman scattering is developed. The key advantage of the presented technique is to suppress the non-resonant background noise which usually obscures possible applications of the other conventional coherent Raman techniques in practice. A reduction of the background noise is achieved by shaping and delaying the third pulse which probes the coherence of the medium (i.e., an enhancement of specific vibrations of the target molecules in unison) firstly prepared by two broadband pulses. We demonstrate a robustness and superiority of signal-to-noise ratio of the developed technique by identifying as few as 10000 bacterial spores at a single laser shot level.

Finally, several comparative studies between cooperative and uncooperative processes are presented. A picosecond cooperative phenomenon in a three-photon resonant medium induced by a single as well as two-color ultrashort pulses is investigated. A time-resolved study shows that a picosecond cooperative effect is crucial in the well-established fields of resonant-enhanced multiphoton ionizations and harmonic generations. We also present a quantitative analysis for spontaneous versus broadband coherent Raman scattering on pyridine molecules. The spontaneous Raman signal is enhanced by 5 orders as a result of cooperative phenomena.

To my mother Khandaijav Baasanjav

ACKNOWLEDGMENTS

I am lucky to have an advisor who is one of the world leaders in quantum optics. I would like to thank my advisor, Prof. Dr. Marlan O. Scully, for giving me a unique opportunity to pursue my new career as an experimentalist in applied ultrafast laser physics. His enthusiasm and constant support over the years made my research progress possible.

I am greatly indebted to Dr. Vladimir Sautenkov (Texas A&M University and Lebedev Institute of Physics) for his guidance and help in my research.

I would like to express my appreciation to all colleagues: Dr. Dmitry Pestov (Michigan State University), Dr. Yuri Rostovtsev (University of North Texas), Dr. Michael Kash (Lake Forest College), Dr. Hebin Li (University of Colorado), Dr. Alexei Sokolov (Texas A&M University), Dr. George Welch (Texas A&M University), Dr. Anil Patnaik (Wright State University), Xi Wang (Texas A&M University), Dr. Miaochan Zhi (Texas A&M University), Luqi Yuan (Texas A&M University), Dr. Robert Murawski (Drew University), Benjamin Strycker (Texas A&M University) and many others for their research collaborations; Dr. Dudley Herschbach, Dr. Girish Agarwal, Dr. Olga Kocharovskaya, Dr. Vitaly Kocharovsky, Dr. Leonid Keldysh, Dr. Suhail Zubairy, Dr. Robert Lucht, Dr. Jaan Laane, Dr. Kevin Lehmann, Dr. Alexander Lvovsky, and Dr. Robert Nevels for their stimulating discussions and valuable advice and Kimberly Chapin and all other members of the Institute of Quantum Studies, Texas A&M University, for their kind help and friendship throughout the years.

Finally, I thank my loving wife Nara, son Gonchi, and daughter Yanichka, for their support, encouragement and patience.

TABLE OF CONTENTS

CHAPTER Page

CHAPTER Page

LIST OF FIGURES

FIGURE Page

FIGURE Page

FIGURE Page

FIGURE Page

FIGURE Page

FIGURE Page

FIGURE Page

FIGURE Page

FIGURE Page

FIGURE Page

FIGURE Page

FIGURE Page

CHAPTER I

INTRODUCTION

A. Research Objective

Recent technological advances in lasers and detectors have facilitated realizations of ultrafast cooperative processes and demanded for a re-evaluation of the conventional cooperative phenomena with a new insight.

The goal of my research is to study cooperative process such as superfluorescence and its coherent control for new (atomic or molecular) systems on a picosecond time scale for possible implementation in remote sensing; to investigate a resemblance between the ultrafast adaptive spectroscopic technique associated with coherent Raman scattering and the ultrafast cooperative process for future development of comparative quantum formalism, establishing new perspective for both of them; to accomplish a potential improvement of the ultrafast coherent Raman spectroscopic technique for implementation in a rapid detection of biohazards/bacterial spores.

B. Contemporary State of Research

1. Cooperative Emission

Superfluorescence in Two-level System

A burst of radiation is resulted from a collection of excited two-level atomic or molecular system. The peak intensity of this radiation is proportional to the square of the number of excited atoms in the system. Dicke performed the first calculation of cooperative process in 1954 [1]. He described this cooperative process as a "radia-

---

The journal model is *IEEE Transactions on Automatic Control.*

tion bomb". In light of this monumental work, this phenomenon is now referred to as Dicke superradiance. Such radiation, however, can also occur when an optically thick medium is prepared with a sufficiently large population inversion so that, eventually, the medium develops a macroscopic dipole moment resulting in superradiant emission [2, 3]. In general, this is called superfluorescence (SF). Many researchers, sometimes, may be careless to distinguish between SF and Dicke superradiance. The Dicke's simple solution accurately describes the temporal shape of an instantaneous emission from a coherently excited collective system, but, it cannot, however, correctly determine the temporal shape of the delayed emission from a fully excited (inverted) system. Therefore, throughout the dissertation we will adopt the term superradiance for the former and superfluorescence for the latter case.

An experimental realization of SF was pioneered by Skribanowitz et al. [4] using optically pumped hydrogen fluoride gas. The first observation of SF in Rb vapor was reported by Marek [5].

Quantum and semiclassical theories of SF were initiated by Arecchi and Courtens [6], Rehler and Eberly [2], Bonifacio and Lugiato [3], and MacGillivray and Feld [7]. In the framework of the semiclassical approach, the Maxwell-Bloch equations for the atomic system can be properly derived using quantum mechanics and only two parameters: an initial tipping angle θ_0 and superradiant lifetime τ_R are adequate to determine the whole superradiant process [7]. The superradiant lifetime τ_R is approximately the average time for the first photon to be emitted along the input beam axis within the sample [8]. In a collinear laser excitation configuration, the cylindrical or "pencil-shaped" samples, for which the Fresnel number close to 1, provides the SF emissions mostly in the forward and backward directions. The coupling between the backward and forward SF has been studied in [9, 10, 11, 12]. For the cylindrical

sample, the superradiant lifetime τ_R is defined as [13]

$$\tau_R = \frac{AT_1}{\mu N \lambda^2}. \tag{1.1}$$

Here T_1, λ, N, A and $\mu = 3/8\pi$ are the population decay time, the SF center wavelength, the number of excited atoms, the sample area and a geometrical factor [2], respectively. According to Polder et al. [14] the peak of the SF pulse is proportional to N^2 and the SF delay time τ_D is given by

$$\tau_D = \frac{\tau_R}{4}\left(\ln(2\pi N)^{1/2}\right)^2. \tag{1.2}$$

The bottom line is that for an ideal SF (i.e., a pure SF [3]) the peak intensity and delay time are proportional to N^2 and $1/N$, respectively.

However if the number of the excited atoms, N, is increased for a cylindrical atomic sample, then the various regimes of large sample superfluorescence must be taken into account [15]. It was first mentioned by Arecchi and Courtens in 1971 [6] that there is a restriction to the number of cooperative atoms due to the fact that the photons travel with finite speed. For instance, if the sample length is longer than the product of SF delay time and the speed of light, then the remote atoms cannot be considered as cooperative. This restriction is critical in the case of the SF pulse delay and width which are scaled in tens of picoseconds. In particular, the whole system is divided into independent cooperative regions (slices) and each part of the system emits before having interacted with the rest of the sample leading to a "broken" superfluorescent emission [15], also called as oscillatory SF [16, 17]. In this regime the peak intensity and delay time are proportional to N and $1/\sqrt{N}$, respectively [6, 15, 16, 17]. In this case, therefore, the scaling laws for the peak intensity and delay time are different from that for a pure SF mentioned above.

An interesting aspect of SF is a coherent ringing, first studied by Burnham and

Chiao [18]. The origin of temporal ringing is two-fold. The Maxwell-Bloch theory predicts an intrinsic SF ringing [7]. In this case, the temporal ringing results from the energy exchange between field and atoms while the field is propagating inside a single cooperative region (slice) [16, 17]. On the other hand, the ringing can occur when the field is reabsorbed and reemitted while propagating through multiple cooperation regions [16, 17, 19, 20].

Both the diffraction and transverse effects can cause the reduction of the ringing [15]. In particular, if the Fresnel number is very small, then the SF emission strongly diverges because of diffraction; thus, the ringing can disappear. In the case of the transverse effect, the transversal plane of the input beam leads to a non-uniform excitation of the atoms and the emissions smear out the ringing. The transverse effects for the ringing in SF were experimentally studied by Mattar et al. [21] and Heinzen et al. [22]. Therefore, a clear observation of temporal ringing has been a demanding [19, 20]; and the ultrafast excitation and detection techniques promise to overcome this difficulty.

The superfluorescent exponential growth is initiated from the interaction of an atom with vacuum fluctuations. The origin of the macroscopic fluctuations in superfluorescence delay times, therefore, is explained only by quantum mechanics [23]. Statistical properties of SF have been studied, e.g., in the theoretical works by DeGiorgio [24] and Haake et al., [25, 26, 27, 28, 29]. The normalized quantum fluctuations in the SF delay time can be written as follows [24, 30, 31, 32, 33]

$$\frac{\sqrt{\langle \tau_D^2 \rangle - \langle \tau_D \rangle^2}}{\langle \tau_D \rangle} = \frac{\pi}{\sqrt{6}} \frac{1}{\ln N + E_0}. \tag{1.3}$$

Here $\langle x \rangle$ denotes average of variable x, $\langle \tau_D \rangle$ is average delay time and $E_0 = 0.5772...$ is Euler's constant. To the best of our knowledge, no experiment on quantum fluctua-

tions in SF delay times in atomic vapor has been reported since the first observations in Vrehen and Weduwe's experiment in 1981 [34].

Comprehensive reviews of SF studies for a two-level system are available in works by Gross and Haroche [15], Andreev et al., [35], and Benedict et al., [36].

Superfluorescence in Cascade Three-level System

Superfluorescence involving cascade three-level atoms is called cooperative cascade emission. Both the theory and related experiment were first reported by Okada et al. [37]. They study the cooperative emission on the cascade $3S-2P-2S$ transition in lithium atomic vapor. The time development of cooperative cascade emission was also studied by using a streak camera with about 10 ps resolution [38]. A crucial example of the cooperative emission in three-level system is the so-called yoked-SF which was first observed in cesium vapor by Brownell et al. [39]. They studied the yoked-SF emissions on the cascade $6D-6P-6S$ transition where the emissions on both the upper $(6D-6P)$ and lower $(6P-6S)$ transitions appeared simultaneously in the direction of the pump laser pulses. The observation of the yoked-SF via a non-collinear laser excitation (a large Fresnel number greater than 1) in Rb vapor was accomplished by Lvovsky et al. [40, 41]. Recently, Paradis et al. obtained distinguished results while observing the yoked-SF in laser-cooled Rb atoms [42].

Although SF has been extensively studied for six decades, time-resolved study of ultrashort SF pulses has not yet been reported. Ultrafast SF can be achieved if a dense gas of atoms is excited by laser pulses that are considerably shorter than the SF evolution time.

Superfluorescence can be generated in both forward and backward directions. Particularly, the backward generated superfluorescent light is of great interest, as it can be applied in the stand-off sensing (SOS) with a "super" enhanced signal from,

e.g., the target chemicals in the atmosphere. As for another example, superfluorescence can be applied for highly efficient conversion of light into the ultra-violet (UV) region. The bright sources of short wavelength radiation have a wide range of potential applications, particularly in patterning and imaging with high precision, e.g., for medical purposes. The superfluorescent light in one mode can be triggered by another superfluorescent light in the other mode (with different wavelength), if they were emitted from three-level atoms. Until now, the triggered superfluorescence has not been studied in detail from both theoretical and experimental points of views; although, it bears a promising future, e.g., in quantum information communications, in addition to the above mentioned applications.

2. A Temporal Coherent Control of Atomic and Molecular Wave-Packet Dynamics

Among different coherent manipulations, a temporal coherent control has been proved as a promising technique for studying the wave-packet dynamics in atoms and molecules. In temporal coherent control, typically, a pair of ultrashort pulses with a variable time delay excites atoms and molecules.

Wave-Packet Dynamics in Atoms

Enormous attention has been devoted to the femtosecond laser control of two-photon transitions in atoms and molecules [43, 44, 45, 46, 47, 48, 49, 50]. In [44, 45, 46, 48, 49, 50], Rb atoms and molecules are excited to the $7S$ and/or $5D$ states from the $5S$ ground state via two-photon processes which are enhanced by the $5P$ intermediate state. The population dynamics of the excited state are monitored by measuring either fluorescence or the 420 nm SF on the transition $5D - 6P$. For example, in [44, 45, 46] the authors observed a quantum beating at 18.3 THz (55 fs) due to the simultaneous excitations of the $5D$ and $7S$ states. Felinto et al. [48] reported an

observation of a beating at 2.1 THz (473 fs). In addition to this beat note on the femtosecond time scale (473 fs), they also observed the ringing on the picosecond time scale which is typical in SF [1]. Barros et al. [49, 50] demonstrated a control of two-photon transitions in Rb atoms by optimizing the relative phase of the input pulses. Felinto et al. [48] explained the 2.1 THz beating in terms of quantum interference [47]. The frequency 2.1 THz is the difference between sequential transitions. This process involves excitation of the $5P_{3/2}$ intermediate state by the broadband pulses [48, 49, 50].

The conventional method to measure atomic interference is usually based on incoherent processes. Since SF is an extremely fast process compared to the corresponding incoherent processes, SF-based fast inspection of atomic interference can be implemented for example, in fast information communication.

Wave-Packet Dynamics in Molecules

Femtosecond dynamics of vibrational and rotational wave packets of dissociating molecular fragments in chemical reactions was initiated in [51]. Since then, the wave packet generation and evolution have been demonstrated and thoroughly studied for a number of diatomic molecules, including I_2 [52, 53], Na_2 [54, 55], Li_2 [56, 57], and many others [58, 59].

In the case of cesium dimers, Eden and co-workers have studied [60, 61, 62] the population dynamics of the excited electronic states when the cesium molecules are pumped by ultrashort pulses from their ground electronic states. The molecule is probed by another time-delayed pulse. Historically, it is referred to as a pump-probe technique. Conventionally, the probe pulse ionizes the molecules via multi-photon processes and the photoelectron signal is recorded as a function of time-delay of the probe pulse. The time trace of the signal provides adequate information with the interpretation of wave-packet dynamics generated in cesium dimers. In particular in

their experiments [62], $\sim$ 100 fs pulses have been used to investigate the dynamics of vibrational wave packets in $C\ ^1\Pi_u$, $B\ ^1\Pi_u$, and $D\ ^1\Pi_u^+$ electronic excited states in cesium dimers. To study the wave packet dynamics in $B\ ^1\Pi_u$ state, the wave packets have been produced by exciting the Cs_2 dimer with a pump pulse from $X\ ^1\Sigma_g^+$ ground state to the target state, and then photoionizing them into $Cs_2^+\ (X)$ state with a time-delayed probe pulse. It has been also shown in [63, 64, 65, 66] that one can control the wave packet dynamics using a sequence of pump, control and probe fields. In experiments with co-propagating pump and control pulses, wave packets were shown to interfere coherently throughout an extended sample [67, 68].

Wave packet dynamics has also been explored theoretically [69]. Density matrix formalism [23] has been adopted to describe the observables in the femtosecond pump-probe experiments [70, 71, 72, 73].

3. Coherent Raman Spectroscopy

Coherent Raman Anti-Stokes Scattering

Physicist, chemists, and biologists have been using lasers to measure Raman spectra of chemical and biological substances. In the spontaneous Raman process, when light irradiates molecules, the lower frequency (Stokes) light is emitted. This frequency shift (i.e., Raman vibrational spectrum) is unique for each molecule to provide a "fingerprint" for species identification. Generally, the spontaneous Raman signal is relatively weak [74, 75, 76, 77, 78, 79]. One way to improve spontaneous Raman signal is to increase input electric field by many orders by using surface-enhancement mechanism. This technique is called surface-enhanced Raman spectroscopy (SERS) [80]. On the other hand, the so-called coherent Raman spectroscopy based on coherent anti-Stokes Raman scattering (CARS) or coherent Stokes Raman scattering (CSRS)

process ([74, 81, 82] and references therein) is one of the powerful techniques for molecular detection. The Raman signal can be enhanced drastically due to the coherently prepared medium (molecules). Three pulses (historically they are called as pump, Stokes and probe) involved in CARS process. Pump and Stokes pulses coherently excite the molecular vibrational states. Probe pulse scatters off of these coherent oscillations generating a strong anti-Stokes (larger frequency than that of probe) or Stokes (lower frequency than that of probe) signal. However, CARS/CSRS signature is vastly obscured by non-resonant (NR) four-wave mixing (FWM) background contributions from other molecules present in the sample. This unwanted NR FWM is often much stronger than the resonant signal because there are usually many more background molecules than target molecules. Fluctuations of the NR background can, and frequently do, completely wash out the CARS signature [83]. The researchers have tried a variety of methods including polarization-sensitive techniques [84], and heterodyne [85, 86] and interferometric [87, 88, 89, 90] schemes, to counteract these background vibrations, unfortunately, with only limited success. For this reason, CARS spectroscopic technique is deemed being not much practical in, e.g., a rapid and reliable identification of bacterial spores.

Coherent Raman Spectroscopy for Anthrax Detection

The 2001 anthrax (in the mail) incidence in the US killed five people and injured 17 others. Anthrax is an acute disease resulted from Bacillus anthracis. It can form dormant spores. When bacterial spores are inhaled, ingested, or come into contact with a skin lesion on a host they may reactivate and multiply rapidly [91]. The current anthrax test involves time-consuming process in which suspicious substances must be cultured in the lab. A number of optical techniques have been considered as alternatives to well established but cumbersome and time-consuming biological

methods (for a review, see [92]). In recent years, local as well as remote real-time detection and identification of warfare agents has become vital. Whereas the detection of warfare chemical compounds, such as nerve gases [93] and explosives [94], has been developed, there is still an apparent need for satisfactory detection technology targeting biohazards, like Bacillus anthracis.

The use of CARS for spore detection was suggested several years ago [95]. A set of femtosecond adaptive spectroscopic techniques for CARS (FAST CARS), including electronic-resonance- enhanced coherent Raman scattering [96, 97], laser pulse shaping [98], and timing, was proposed and analyzed.

C. Organization of the Dissertation

The dissertation consists of 10 chapters and is organized as follows:

A simple theoretical treatment on analogy between cooperative and coherent Raman processes is established in the following chapter.

The laser system, measurement method and materials are introduced in Chapter III. We utilized in our experiments the commercial Ti:Sapphire laser system as a femtosecond pulse source. Two optical parametric amplifiers were used to tune the input laser wavelength. As working materials, we used two different alkali metal vapors and several different chemical and biological substances. The measurement methods and optical layouts were different from each other and specifically described in the corresponding sectors. An ultrafast streak camera, a couple of spectrometers, and fast and slow photodetectors were used to record generated signal (SF, spontaneous Raman, CARS, CSRS etc.) in the experiments.

A detailed study of ultrafast SF is presented in Chapter IV. It demonstrated a production of SF which had a time duration of tens of picoseconds in a dense Rb vapor

pumped by femtosecond laser. Rb atoms were excited to the $5D$ state from the $5S$ ground state, where two-photon transitions were enhanced by the intermediate level $5P$. The pump laser pulses were broadband ($\Delta\lambda \sim 20$ nm), ultrashort ($\Delta t \sim$100 fs) and thus the excitation were essentially instantaneous. The excited atoms eventually emitted SF on the $6D - 6P - 5S$ cascade transition. The SF emission at 420 nm on the $6P - 5S$ transition was recorded by the ultrafast streak camera and spectrometer. Statistical distributions and fluctuations of the measured SF delay times are studied as functions of the pump laser energy. The especial care was taken to ensure that the measured fluctuations were due to quantum initiation of the SF development.

Chapter V is devoted to a coherent temporal control of radiation from a coherent atomic or molecular system. The chapter begins with a study of the dynamics of wave packets in cesium dimers using a femtosecond controlled pump-probe technique. We implemented configurations with one pulse (pump) or two pulses (pump and control) to produce vibrational wave packets on the electronic excited state. The transmission of an additional, variable delay probe pulse was measured to monitor the time evolution of the wave packets. A theory based on the Liouville equation for the density matrix associated with the Franck-Condon factors is developed to elucidate the observed experimental data. Further, a coherent temporal control in two-photon transitions is demonstrated in this chapter; a pair of collinear ultrashort pulses with variable time delay were used to excite Rb atoms. As an additional control, we fine-tuned the wavelength of the input laser field to study transitions among different two-photon processes. Chapter V reveals also how to inspect quantum interference using the temporal shape of the SF pulse produced in Rb atomic vapor.

Chapter VI discusses implementation of a new coherent Raman spectroscopic technique which is now called as a hybrid CARS. This hybrid technique combines the robustness of frequency-resolved CARS with the advantages of time-resolved CARS

spectroscopy. We used this technique for coherent Raman spectroscopy of sodium dipicolinate powder, which is similar to calcium dipicolinate (a marker molecule for bacterial spores, such as Bacillus subtilis and Bacillus anthracis).

A comparative experimental study between cooperative and uncooperative processes is given in Chapter VII. The chapter starts with a study of a picosecond cooperative phenomenon in three-photon resonant medium. The Rb atoms were pumped by 100 fs laser pulses which were tuned to three-photon resonance to the $6P - 5S$ transition. The emitted 420 nm light on this transition was recorded by the streak camera. A time-resolved study of the 420 nm pulses presented as a function of the input laser field power. At the next stage, the chapter examines a slightly different excitation configuration. Rb atoms were first excited by a 100 fs pulse at 778 nm from the $5S$ ground state to the $5D$ state via two-photon transitions, then subsequently pumped by another 100 fs pulse at 1485 nm, which was resonant to the transition $5D - 12P$. The presence of the 1485 nm pulse triggered an emission of a light pulse centered at 308 nm which was measured by the ultrafast streak camera. The temporal characteristics of the 308 nm pulse are also studied. In the above mentioned cases, a time-resolved comparison between cooperative and spontaneous emissions is studied. At the end, this chapter presents a comparative analysis of spontaneous and broadband coherent Raman scattering on pyridine molecules. The instantaneous multi-mode excitation of the molecular vibrations was done by a pair of ultrashort preparation pulses. The hybrid technique which was described in Chapter VI, allowed for single-shot acquisition of background-free coherent Raman spectrum within the excitation band and its straightforward comparison with the spontaneous Raman measurements, performed within the same setup.

Some applications of the presented techniques based on ultrafast cooperative phenomena are listed in Chapter VIII. The first part of the chapter tests a possi-

bility of SOS with SF. Two aspects (catch-up and distributed gain) of the earlier proposed SOS technique [99] were demonstrated using a femtosecond laser system and an organic dye solution. The last part of the chapter explores practical implementation of the hybrid CARS technique in a rapid identification of bacterial spores at a single-laser-shot level.

Chapter IX summarizes our results which are presented in the dissertation.

The dissertation concentrates on the experiments performed by the authors during his PhD study (2006-2010). The other projects accomplished by the author that are not included in the body of the dissertation are listed in Appendices.

CHAPTER II

ANALOGY BETWEEN COOPERATIVE EMISSION AND COHERENT RAMAN SCATTERING

An analogy between the well-known processes: cooperative emission and coherent Raman scattering; is discussed in this chapter. Under a special condition of the initial states of the medium, one can justify equivalence between these two processes. In the next part, cooperative emission for a two-level system is considered.

A. Cooperative Emission in Atomic Product State

To obtain the desired result for the cooperative emission we follow an approach presented in the text book by L. Mandel and E. Wolf [100]. A Hamiltonian for a two-level atom in the interaction picture is expressed as

$$V(t) = \sum_{j,\mathbf{k}} \hbar g_{\mathbf{k}} a_{\mathbf{k}} \sigma_j^{\dagger} \mathrm{e}^{-i(\nu_{\mathbf{k}} - \omega_{ab})t} + h.c. \tag{2.1}$$

A coupling constant is expressed in terms of dipole matrix elements, $\wp_{ab}$, as [23]

$$g_{\mathbf{k}}^2 = \frac{\nu_{\mathbf{k}}}{2\hbar\epsilon_0 V} \wp_{ab}^2 \cos^2\theta. \tag{2.2}$$

The Liouville or Von Neumann equation for the density operator [23] is given by

$$\frac{d\rho}{dt} = \frac{1}{i\hbar}\left[V, \rho\right]. \tag{2.3}$$

An exact solution for $\rho(t)$ is given explicitly by

$$\begin{aligned} \rho(t) &= \rho_0(t_0) + \sum_{l=1}^{\infty} \frac{1}{(i\hbar)^l} \int_{t_0}^{t} dt_1 \int_{t_0}^{t_1} dt_2 \\ &\times \ \ldots \int_{t=0}^{t} dt_l \left[V(t_1), [V(t_1), \ldots, [V(t_l), \rho(t_0)]] \ldots\right]. \end{aligned} \tag{2.4}$$

Let us define atomic product state as [100]

$$|\Phi\rangle = \prod_{j=1}^{N} \left(\alpha|a\rangle + \beta|b\rangle\right)_j , \tag{2.5}$$

where α and β satisfy $|\alpha|^2 + |\beta|^2 = 1$. This relation is the same for every atom. We assume that the system is prepared at time t_0 as

$$\rho(t_0) = |\Phi\rangle\langle\Phi| \otimes |0\rangle\langle 0|. \tag{2.6}$$

We are interested in the probability, $P(t)$, that the system emits one photon in a short time interval, Δt. The probability at time $t = t_0 + \Delta t$ is given by

$$P(t) = \sum_{\mathbf{k}'} \mathrm{Tr_A}\left(\langle 1_{\mathbf{k}'}|\rho(t)|1_{\mathbf{k}'}\rangle\right), \tag{2.7}$$

where $\mathrm{Tr_A}(...) = \sum_{\mathrm{All}}\langle\Psi_\mathrm{A}|...|\Psi_\mathrm{A}\rangle$ denotes the trace over all atomic variables and $|1_{\mathbf{k}'}\rangle$ is a one-photon state with wave vector $\mathbf{k}'$. Since the one-photon state is orthogonal with the vacuum state the lowest non-vanishing term is written from Eq.(2.4) as

$$P(t) = \frac{\Delta t}{\hbar^2}\mathrm{Tr_A}\left(\sum_{\mathbf{k}'}\int_{t_0}^{t} dt'\langle 1_{\mathbf{k}'}|V(t)\rho(t_0)V(t') + V(t')\rho(t_0)V(t)|1_{\mathbf{k}'}\rangle\right). \tag{2.8}$$

Substituting an explicit expression for $V(t)$, it becomes

$$\begin{aligned} P(t) &= \frac{\Delta t}{\hbar^2}\sum_{\mathrm{All}}\sum_{\mathbf{k}'}\int_{t_0}^{t} dt'(\langle 1_{\mathbf{k}'}|\langle\Psi_A|\sum_{j,\mathbf{k}}\hbar g_{\mathbf{k}} a^\dagger_{\mathbf{k}}\sigma_j \mathrm{e}^{i(\nu_{\mathbf{k}}-\omega_{ab})t}|\Phi\rangle|0\rangle \\ &\times \langle 0|\langle\Psi_A|\sum_{j,\mathbf{k}}\hbar g_{\mathbf{k}} a_{\mathbf{k}}\sigma^\dagger_j \mathrm{e}^{-i(\nu_{\mathbf{k}}-\omega_{ab})t'}|\Phi\rangle|1_{\mathbf{k}'}\rangle + h.c.). \end{aligned}$$

Using the identity $\sum_{\mathrm{All}}|\Psi_A\rangle\langle\Psi_A| \equiv 1$, we obtain

$$P(t) = 2\Delta t\sum_{i,j}\langle\Phi|\sigma^\dagger_i\sigma_j|\Phi\rangle\int_{t_0}^{t} dt' \times \sum_{\mathbf{k}} g^2_{\mathbf{k}}\cos\{(\nu_{\mathbf{k}} - \omega_{ab})(t-t')\}.$$

A summation can be changed by the integral as [23]

$$\sum_{\mathbf{k}} \to 2\frac{V}{(2\pi)^2}\int_0^{2\pi} d\phi\int_0^{\pi} d\theta\sin\theta\int_0^{\infty} dk k^2. \tag{2.9}$$

The Einstein A coefficient is defined as [23]

$$A = \frac{1}{4\pi\epsilon_0}\frac{4\omega_{ab}^3\wp_{ab}^2}{3\hbar c^3}. \tag{2.10}$$

The probability that a photon emitted in time Δt is, thus, found to be

$$P(t) = A\Delta t\left(N|\alpha|^2 + N(N-1)|\alpha|^2|\beta|^2\right). \tag{2.11}$$

If $|\beta|^2 = 0$ and $|\alpha|^2 = 1$, then radiation is proportional to N which corresponds to spontaneous emission. However, for $\alpha \neq 0$, and $\beta \neq 0$ (non-zero atomic dipole moment), cooperative emission is proportional to N^2, where $N \geq 2$. The maximum emission can be achieved when atoms are prepared in a maximal coherent state, $|\alpha|^2 = |\beta|^2$.

B. Spontaneous Raman Scattering and The Einstein-Raman A and B Coefficients

The Hamiltonian for Raman system in the interaction picture is given by

$$\begin{aligned} V(t) &= \sum_{j,\mathbf{k_1}} \hbar G_{\mathbf{k_1}} a_p a_{\mathbf{k_1}}^\dagger \sigma_j^\dagger \mathrm{e}^{-i(\nu_{\mathbf{k_1}} - \nu_p - \omega_{bc})t} \\ &+ \sum_{j,\mathbf{k_2}} \hbar G_{\mathbf{k_2}} a_S^\dagger a_{\mathbf{k_2}} \sigma_j^\dagger \mathrm{e}^{-i(\nu_{\mathbf{k_2}} - \nu_S - \omega_{bc})t} + h.c., \end{aligned} \tag{2.12}$$

where the frequencies ν_p and ν_S, the bosonic operators a_p and a_S correspond to the input pump and Stokes field modes, respectively; the wave vectors $\mathbf{k_1}$ and $\mathbf{k_2}$ and bosonic operators $a_{\mathbf{k_1}}$ and $a_{\mathbf{k_2}}$ are, respectively, for Stokes and anti-Stokes emitted photons. A lowering operator from the excited $|b\rangle$ to the ground $|c\rangle$ states for the jth atom is $\sigma = |c\rangle\langle b|$. A coupling constant is explicitly written as

$$\begin{aligned} G_{\mathbf{k_{1,2}}} &= \frac{1}{\hbar^2}\sqrt{\frac{\hbar\nu_{1,2}}{\epsilon_0 V}}\sqrt{\frac{\hbar\nu_{p,S}}{\epsilon_0 V}} \\ &\times \sum_i \left\{ \frac{(\wp_{bi}\cdot\mathbf{e_{k_i}})(\wp_{ic}\cdot\mathbf{e_{k_{p,S}}})}{\nu_{p,S} - (\varepsilon_i - \varepsilon_{c,b})/\hbar} - \frac{(\wp_{bi}\cdot\mathbf{e_{k_{p,S}}})(\wp_{ic}\cdot\mathbf{e_{k_i}})}{\nu_{1,2} + (\varepsilon_i - \varepsilon_{c,b})/\hbar} \right\}, \end{aligned} \tag{2.13}$$

where ϵ_0 is the free space permittivity, $\mathbf{e_{k_j}}$ is a unit polarization vector of the field with wave vector $\mathbf{k_j}$, $\sqrt{\hbar\nu_j/(\epsilon_0 V)}$ has the dimensions of an electric field, V is a volume, and and ε_j is atomic (or molecular vibrational) energy for the jth level. Frequencies (and wave vectors) for anti-Stokes and Stokes fields are $\nu_{1,2} = \nu_{p,S} \pm \omega_{bc}$ (and $\mathbf{k_{p,S}}$), see Fig. 1. From Eq.(2.3), the equation with up to the second order perturbation

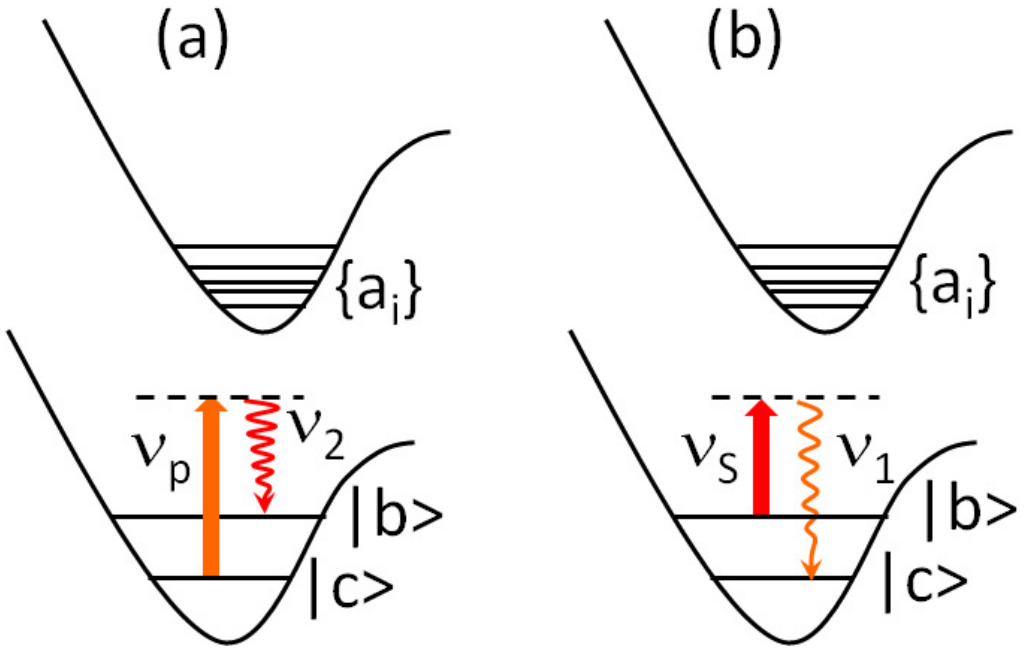

Fig. 1. Schematics of spontaneous Raman process. (a) Stokes and (b) anti-Stokes emissions.

terms is given by

$$\dot{\rho}_A = -\frac{1}{\hbar^2}\int_{t_0}^{t} dt' \mathrm{Tr}_F\{[V(t),[V(t'),\rho_A(t')\otimes\rho_F(t_0)]]\}, \tag{2.14}$$

where ρ_A and ρ_F are atomic and field density operators, and the trace is taken over all possible field states, $\mathrm{Tr}_F\{\ldots\} = \sum_{n_p,n_S,n_{\mathbf{k_1}},n_{\mathbf{k_2}}} \langle n_{\mathbf{k_1}}, n_{\mathbf{k_2}}, n_p, n_S| \ldots |n_{\mathbf{k_1}}, n_{\mathbf{k_2}}, n_p, n_S\rangle$. We first use the identity $\mathrm{Tr}_F\{ABC\} = \mathrm{Tr}_F\{CAB\} = \mathrm{Tr}_F\{BCA\}$ for arbitrary A,

B and C operators, then, employ the relations for mean value of photon numbers, $\mathrm{Tr}_F\{a_1 a_1^\dagger a_{\mathbf{k_1}}^\dagger a_{\mathbf{k_1}} \rho_F(t_0)\} = (\bar{n}_p + 1)\bar{n}_{\mathbf{k_1}}$ and $\mathrm{Tr}_F\{a_1^\dagger a_1 a_{\mathbf{k_1}} a_{\mathbf{k_1}}^\dagger \rho_F(t_0)\} = \bar{n}_S(\bar{n}_{\mathbf{k_1}} + 1)$. According to the Weisskopf-Wigner approximations we obtain

$$\begin{aligned}\sum_{\mathbf{k_{1,2}}} G_{\mathbf{k_{1,2}}}^2 \mathrm{e}^{-i(\nu_{p,S} - \nu_{\mathbf{k_{1,2}}} \mp \omega_{bc})(t-t')} &= \int_0^\infty d\nu_{\mathbf{k_{1,2}}} \mathcal{D}_{\mathbf{k_{1,2}}} G_{\mathbf{k_{1,2}}}^2 \mathrm{e}^{-i(\nu_{p,S} - \nu_{\mathbf{k_{1,2}}} \mp \omega_{bc})(t-t')} \\ &\approx \pi \mathcal{D}_{1,2} G_{1,2}^2 \delta(t-t'), \end{aligned} \tag{2.15}$$

where the mode densities are $\mathcal{D}_{1,2} = V\nu_{1,2}^2/(\pi^2 c^3)$. The probability of the atoms excited in $|\alpha\rangle$ state is $\rho_{\alpha,\alpha} = \langle\alpha|\rho_A|\alpha\rangle$ and number of the atoms in this state is $N_\alpha = N\rho_{\alpha,\alpha}$, where N is the total number of atoms. The equations for N_α are as follows

$$\begin{aligned}\dot{N}_b &= A_{R_1}\bar{n}_p N_c - B_{R_1}(\bar{n}_p + 1)N_b + B_{R_1}\bar{n}_p N_c \\ &- (A_{R_2}\bar{n}_S N_b - B_{R_2}(\bar{n}_S + 1)N_c + B_{R_2}\bar{n}_S N_b), \end{aligned} \tag{2.16}$$

where $N_c + N_b = N$. The Einstein-Raman A and B coefficients are defined as

$$\begin{aligned} A_{R_{1,2}} &= 2\pi \mathcal{D}_{1,2} G_{1,2}^2 \\ B_{R_{1,2}} &= 2\pi \mathcal{D}_{1,2} \bar{n}_{1,2} G_{1,2}^2, \end{aligned} \tag{2.17}$$

where $\bar{n}_{1,2}$ are mean photon numbers of the Stokes and anti-Stokes field modes. An exact solution of Eq.(2.16) reads

$$N_b = \frac{\Gamma_2 N}{\Gamma_1 + \Gamma_2}\left(1 - \mathrm{e}^{-(\Gamma_1+\Gamma_2)t}\right), \tag{2.18}$$

where $N_c = N - N_b$ and $\Gamma_{1,2} = B_{R_{1,2}}(\bar{n}_{p,S} + 1) + \bar{n}_{S,p}(A_{R_{2,1}} + B_{R_{2,1}}) > 0$. Let us compare the growth rates of the number of the excited atoms N_b with and without the input Stokes field. The growth rate of N_b without the input Stokes field for $\bar{n}_S = 0$

is given by

$$\Gamma_1 + \Gamma_2 = B_{R_1}(\bar{n}_p + 1) + \bar{n}_p(A_{R_1} + B_{R_1}) + B_{R_2}, \tag{2.19}$$

whereas in the presence of the input Stokes field the total rate is given by

$$\begin{aligned} \Gamma_1 + \Gamma_2 &= B_{R_1}(\bar{n}_p + 1) + \bar{n}_S(A_{R_2} + B_{R_2}) \\ &+ B_{R_2}(\bar{n}_S + 1) + \bar{n}_p(A_{R_1} + B_{R_1}). \end{aligned} \tag{2.20}$$

The latter is greater than the former. This means that the presence of the input Stokes field in addition to the input pump field, therefore, yields more efficient "preparation" of the coherence before it could be suppressed by relaxation of the molecular vibrational coherence.

C. Raman Scattering from Coherently Prepared Medium

In the previous part, we showed how efficiently the molecules are prepared in the coherent state by using the input pump and Stokes fields. In this part, we assume that the molecules are initially prepared in a special coherent state similar to the previously mentioned product state as

$$\rho_A(t_0) = \prod_{j=1}^{N} (\rho_{bb}|b\rangle\langle b| + \rho_{bc}|b\rangle\langle c| + \rho_{cb}|c\rangle\langle b| + \rho_{cc}|c\rangle\langle c|)_j, \tag{2.21}$$

where $|b\rangle$ and $|c\rangle$ are, e.g., vibrational states of the molecule. The relation, $\rho_{aa} + \rho_{bb} = 1$, is the same for every molecule. The Hamiltonian for Raman system (see, Fig. 2) in the interaction picture is given by

$$V(t) = \sum_{j,\mathbf{k}} \hbar G_{\mathbf{k}} a_{pr}^{\dagger} a_{\mathbf{k}} \sigma_j^{\dagger} \mathrm{e}^{-i(\nu_{\mathbf{k}} - \nu_{pr} - \omega_{bc})t} + h.c., \tag{2.22}$$

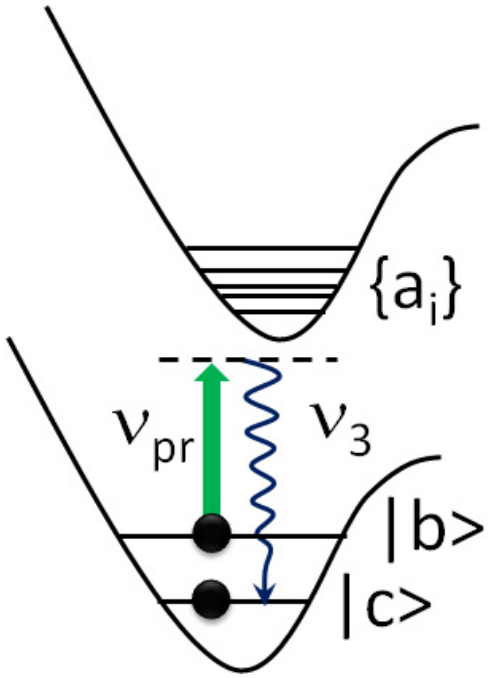

Fig. 2. Coherent Raman process. The input probe field is scattered off from coherently prepared medium.

where a_{pr} and ν_{pr} are annihilation operator for and frequency of the input probe field. The initial state at time t_0 is given by

$$\rho(t_0) = \rho_A(t_0) \otimes |n, 0\rangle\langle n, 0|, \tag{2.23}$$

where n photons are present in the probe beam. Similarly, we are interested in the probability, $P(t)$, that the system absorbs one photon from the probe beam and emits one photon at time $t = t_0 + \Delta t$ as given by

$$P(t) = \Delta t \sum_{\mathbf{k}'} \mathrm{Tr_A} \left(\langle n-1, 1_{\mathbf{k}'} | \rho(t) | n-1, 1_{\mathbf{k}'} \rangle \right). \tag{2.24}$$

Using the same procedure as above, we obtain

$$P(t) = 2n\Delta t \mathrm{Tr_A}\left\{\sigma_j \rho_A(t_0)\sigma_i^\dagger\right\}\int_{t_0}^{t} dt' \times \sum_{\mathbf{k}} G_{\mathbf{k}}^2 \cos\{(\nu_{\mathbf{k}} - \nu_{pr} - \omega_{ab})(t-t')\}.$$

Finally the probability $P(t)$ that a photon emitted in time Δt is obtained to be

$$P(t) = nA_{R_3}\Delta t\left(N\rho_{bb} + N(N-1)|\rho_{bc}|^2\right), \tag{2.25}$$

where A_{R_3} is the Einstein-Raman A coefficient. The first term stands for spontaneous Raman while the second term corresponds to coherent Raman contribution. The ratio between spontaneous and coherent Raman emissions, thus, given by

$$\frac{I_{CARS}}{I_{Spon.Raman}} = \frac{(N-1)|\rho_{bc}|^2}{\rho_{cc}}. \tag{2.26}$$

We will discuss this ratio later in Chapter VII in relation to the comparative experiment between spontaneous and broadband coherent Raman processes.

CHAPTER III

EXPERIMENTAL TECHNIQUE AND MATERIALS

The purpose of this chapter is to give a brief overview of the laser systems, and detection methods that we used to obtain the results discussed in the rest of the dissertation. The measured signal (light) was produced in different working materials which are also introduced in this chapter.

A. Femtosecond Laser System

In all experiments presented in the dissertation, a Ti:Sapphire-based regenerative amplifier system with either one or two optical parametric amplifiers (OPAs) was utilized as a source for 50-100 fs pulses, see Fig. 3. The ultrafast laser system is provided by Coherent Inc. and its main components include two pump lasers (Verdi and Evolution), a femtosecond oscillator-seed (Mira), and a regenerative amplifier (Legend). A pump laser, Verdi, produces a single mode, continuous wave (CW) laser light. A set of fiber-coupled diode lasers operating at 804 nm enters a cavity with a gain medium (Nd:YVO4 crystal) which has a peak emission at 1064 nm. The output green light (532.1 nm) of Verdi is a result of the second harmonic of the laser emission (1064 nm) in the LBO frequency doubling nonlinear crystal.

The 532.1 nm laser light seeds the Mira oscillator. The Mira produces a stable train of 20-50 fs pulses at 76 MHz repetition rate at center wavelength $\sim$ 800 nm. A ultrashort pulse formation consists of five essential steps. First, the starter glass-plate, which can disturb the Mira's cavity length lets a set of modes in the cavity to laze in Ti-Sapphire crystal. The third order nonlinear effect, which is often called as Kerr effect, dominates while the peak intensity of the modes increases. Due to Kerr effect the refractive index of the medium changes, thus the phase of the modes alter

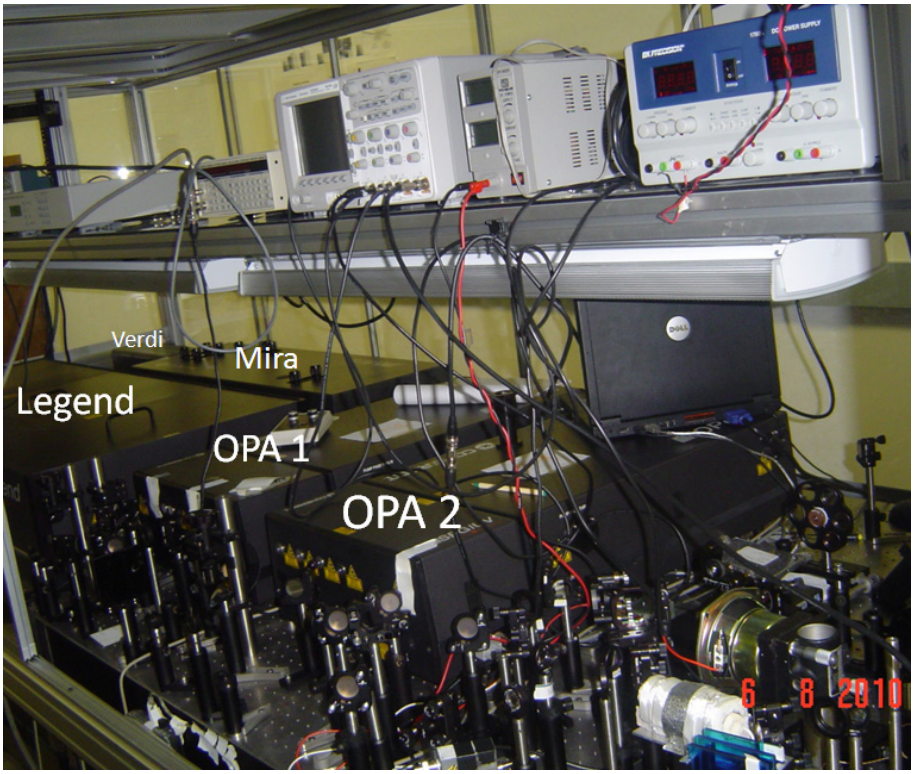

Fig. 3. A photo of the femtosecond laser system.

(the effect is called self-phase modulation). A self-phase modulation (the third step) ensures that a set of frequencies can be trapped (phase-locked) in the cavity forming a short pulse, i.e., broadens the bandwidth. A mode-locked beam (pulses) is focused because of the Kerr effect, thus, as the fourth step, femtosecond pulses are spatially filtered out by a mechanical slit from a CW divergent beam. The pulse temporal shape is chirped, i.e., the modes propagate with a different speed. If no adjustment of the group velocity dispersion is performed which completes all steps for the ultrashort pulse formation. The Ti:Sapphire rod is cooled by water at a constant temperature to avoid a possible damage and the thermal effect which can cause instability of the laser output.

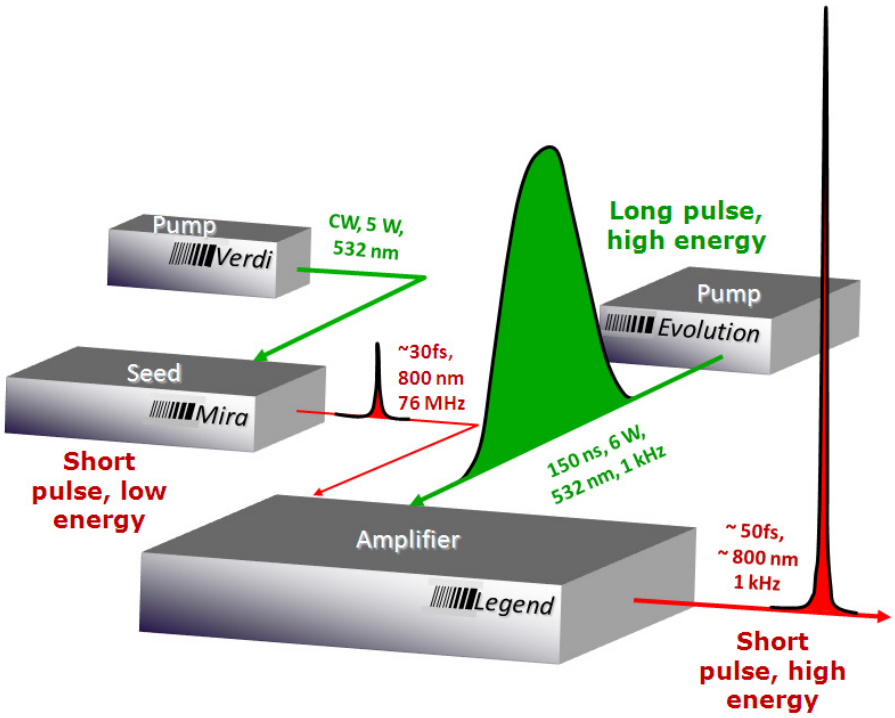

Fig. 4. A schematic diagram of the ultrashort pulse amplification (adapted from Coherent Laser System Tutorial: Training Presentation), see text for detail.

The amplification of the oscillator pulse is accomplished by seeding into an amplifier Legend. The Legend is pumped by the Evolution. The pump laser produces $\sim$ 150 ns pulses at 1 kHz with center wavelength of 1064 nm, where the mode locking is based on Q-switching. The gain medium for the Evolution is Nd:YLF rod which makes this laser being the most reliable, high power laser. In our system, the Evolution produces 532.1 nm (second harmonic of the 1064 nm laser beam) at 6 W power. The amplification of the seed (oscillator) beam occurs in the Ti:Sapphire rod in the Legend. In particular, the pump at 532.1 nm is absorbed exciting the intermediate state from the ground state. Due to a non-radiative transfer, the (down-shifted) upper state is excited as it fulfils a lasing condition at center wavelength 800 nm. However,

a special procedure is necessary for the ultrashort pulse amplification. The damage threshold of the optical materials is much lower than the peak power of the femtosecond pulse. Thus, to amplify the ultrashort pulse, it is unavoidable that the pulse is first stretched before amplification. The stretched (long) pulse is amplified, then, compressed without depletion of its energy. In the Legend, once in a millisecond, a seed pulse first enters a stretcher unit, then, is injected into a cavity to be amplified. At the end of making 10-13 round-trips, the amplified pulse is ejected from the cavity. The fast injection and ejection of the pulse are controlled by a polarization sensitive cell (the Pockel's cell). Finally, after a proper compression, the pulse has a duration of $\sim$ 50 fs and energy of 1 mJ/pulse at 1 kHz repetition rate, see Fig. 4. Next, the amplified output beam evenly split feeding two OPAs (OPA 1 and OPA 2). The main unit of the OPA is based on production of the signal and idler beams of the input pump (fundamental) beam, which consists of a pre-amplifier seeded by white light and power amplifier of signal and idler beams. The add-on units consist of several different nonlinear crystals which are capable to produce a fourth-harmonic of idler and signal, and a second harmonic of the sum-frequency. On the whole, two OPAs can produce pulses as short as 50-100 fs in duration at available center wavelength from 240 nm to 2600 nm with various efficiencies.

B. Ultrafast Streak Camera

A streak camera is a superb detector of light emission phenomena with a high temporal resolution. In addition to capture light emission in ultrashort time, it can simultaneously measure the spatial distribution of input light pulses. Thus, a streak camera is one of the ideal devices to measure the temporal characteristics of ultrafast cooperative emissions. An operating principle of streak camera can be understood as

follows (adapted from a data sheet of the Hamamatsu c5680 streak camera). Let us suppose that we measure four input pulses which are temporally as well as spatially separated, see Fig. 5 (a). By a spatial separation, we mean along the horizontal di-

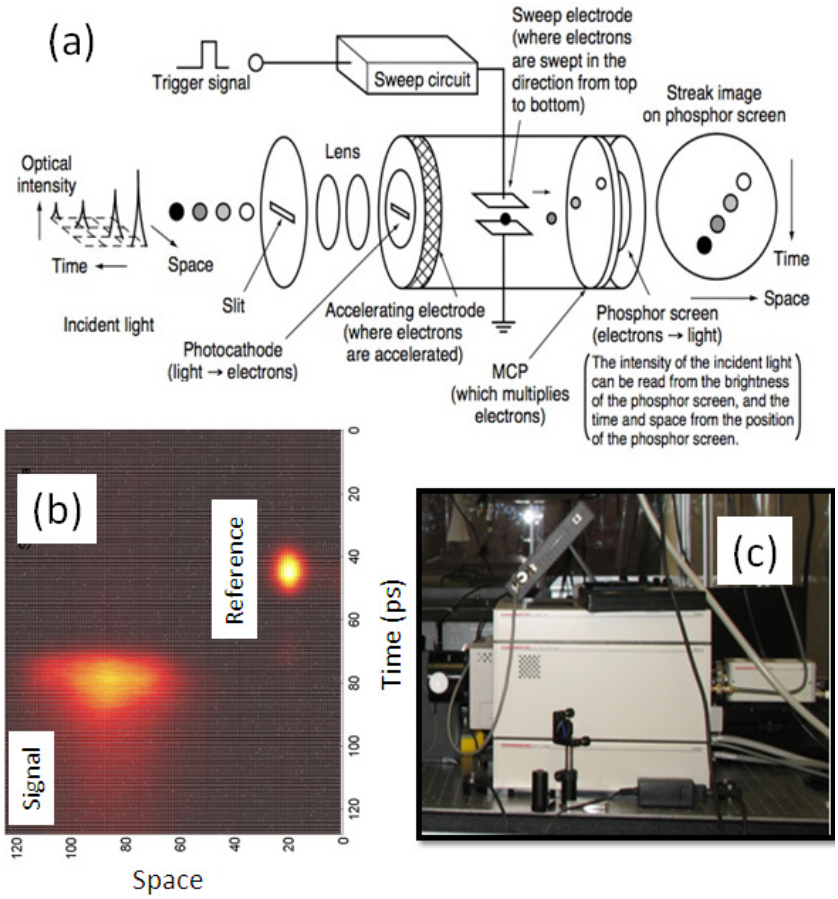

Fig. 5. (a) Operating principle of streak camera (adapted from a data sheet of the Hamamatsu c5680 streak camera). (b) An example of the data image taken by the streak camera. The two beams (reference and signal), which are separated in time and space, are measured as an example. (c) A photo of the Hamamatsu c5680 streak camera.

rection parallel to a narrow mechanical slit of the streak camera. After passing the slit, photons hit the photocathode to produce electrons. The number of photons are

converted to the number of electrons which are accelerated between the electrodes then pass through a high-speed sweep electrode. As a result of the sweep voltage the electrons are deflected in the perpendicular direction and form a streak of electrons depending on their arrival times at the electrode. Next, the electrons are multiplied and converted back into photons. An image of the photon-beam is, then, taken by a camera. The temporal characteristics (intensity variations, relative delay, time duration, etc.) can be inferred from the resulting image. In Fig. 5 (b), an example of a real data image which was taken for the 420 nm superfluorescence pulse together with an input 100 fs pulse centered at 778 nm. Fig. 5 (c) is a photo of the Hamamatsu c5680 streak camera.

C. Materials

The alkali metal vapor cells were used in most of our experiments. A partial energy level diagram for Rb atom is plotted in Fig. 6. In the experiments with Rb which presented in Chapter IV and V, we excite the atoms into $5D$ state from the ground $5S$ state and detect the forward (in the direction of the pump beam) 420 nm light on the transition $6P - 5S$. In each experiment, we repeatedly present the details including the energy diagram with the corresponding excitation configuration.

The Rb cell was fabricated from a sapphire body and YAG garnet windows, and had a cylindrical shape with a length of 7 cm and a diameter of 1 cm. A narrow tube was attached to the bottom of the cell, which is called the cold-spot. The cell permitted high temperature operation and, except for the windows, was heated uniformly. To avoid atomic condensation, the windows were kept a bit hotter than the body of the cell. The most of the data displayed in this research were taken at the cold-spot temperature of 204 C, as measured by a thermocouple, giving a rubidium

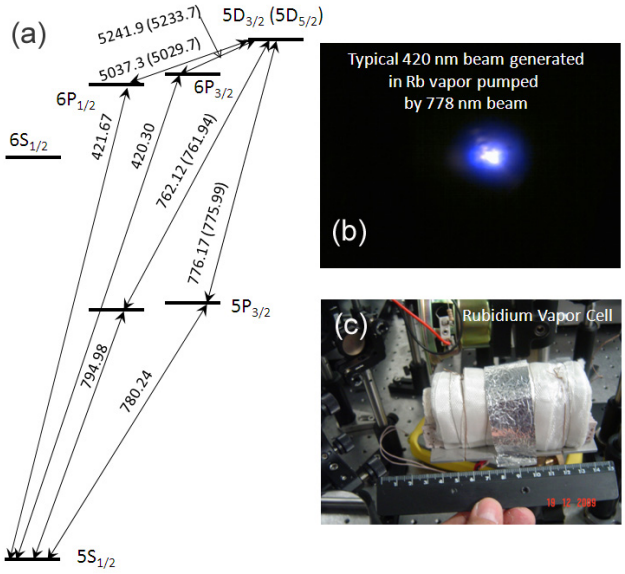

Fig. 6. (a) Energy level scheme for rubidium atoms. The energy level difference is in units of nanometer. (b) A photo of the reflected (from a screen) typical 420 nm beam which is generated in a Rb vapor pumped by 778 nm beam. (c) A photo of a Rb cell.

density of $\sim 9 \times 10^{14}$ cm^{-3}.

In Chapter V, we used a cesium vapor cell with a length of 3 inches. The cell was heated up to 240-250°C with the temperature variation below 1°C. These temperatures correspond to 1.2-1.9 mTorr pressure of Cs dimers or their density of (2.3-3.6)$\times 10^{13}$ cm^{-3}. The input pulses induce Cs_2 vibrations (wave packets) in the excited $B\ ^1\Pi_u$ state, and probe pulses read out the wave-packet evolution by promoting excited molecules back into the ground $X\ ^1\Sigma_g^+$ state. We also used several chemicals including a powder of sodium dipicolinic acid (NaDPA), pyridine and rhodamine B (rhodamine 610), see Fig. 7 for their molecular structure. More than sixteen percent of the dry weight of bacterial spores is occupied by calcium dipicolinate (CaDPA). In this reason, CaDPA is often considered as a marker molecule of bacterial spores.

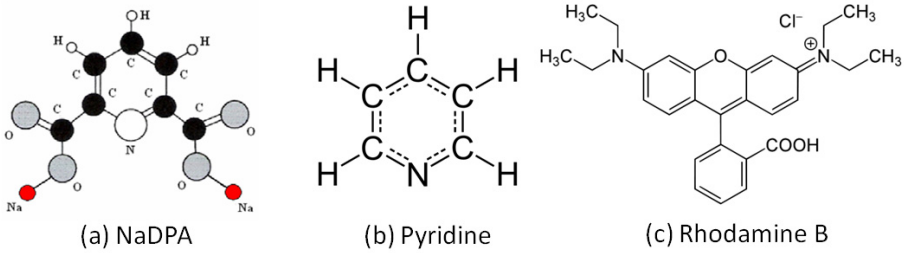

Fig. 7. Molecular structures of (a) sodium dipicolinic acid, (b) pyridine, and (c) rhodamine B.

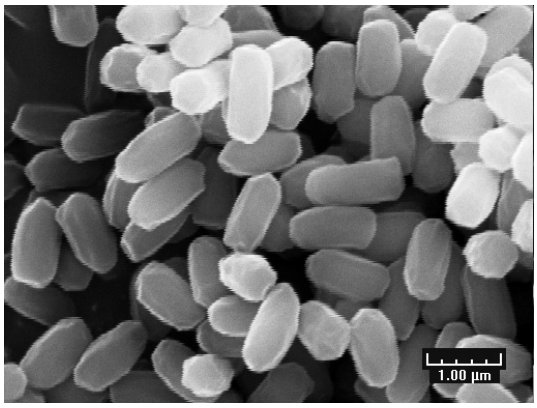

Fig. 8. An image of Bacillus subtilis spores taken by scanning electron microscopy (Courtesy of the Microscopy and Imaging Center, Texas A&M University).

A similarity of Raman spectra between CaDPA and NaDPA suggests that an easy-to-prepare NaDPA can be studied, instead. In Chapter VI, we measure CARS on NaDPA and compare with that for Bacillus subtilis spores (Fig. 8). Pyridine and rhodamine B were used in a comparative experiment in Chapter VII and stand-off sensing experiment in Chapter VIII, respectively.

CHAPTER IV

PICOSECOND SUPERFLUORESCENCE*

In this chapter, we study SF generated in a gas of Rb atoms. The time duration of the generated SF is tens of picoseconds, which is much shorter than the time scale of the usual relaxation processes. The dependence of the average time delay between the reference input pulse and SF is measured by the streak camera as a function of laser power. The experimental data are described quantitatively by a simulation based on the semiclassical atom-field interaction theory. The observed change in scaling laws for the peak intensity and delay time can be elucidated by a SF theory in which the sample length is larger than the cooperation length. At the next stage, a study of the statistics of SF delay times is presented. Delay times of the SF pulses are recorded by the streak camera for laser shot-to-shot. Statistical distributions and fluctuations of the measured delay times are also investigated as functions of the pump laser energy.

A. Observation of Picosecond Superfluorescent Pulses

1. Introduction

Both the theory and related experiment for the SF involving cascade three-level atoms were first reported in [37]. The time development of the cascade SF emission was studied by using a streak camera with about 10 ps. An important special case of cascade SF is the yoked-SF which has been observed in a cesium vapor [39], in a Rb

*Part of the data reported in this chapter is reprinted with permission from "Observation of Picosecond Superfluorescent Pulses in Rubidium Atomic Vapor Pumped by 100-fs Laser Pulses", 2010. G.O. Ariunbold, M.M. Kash, V.A. Sautenkov, H. Li, Yu.V. Rostovtsev, George R. Welch, and M.O. Scully, *Phys. Rev.* A 82, 043421. Copyright [2010] The American Physical Society

vapor [40, 41], and in laser-cooled Rb atoms [42].

Even though, SF has been extensively studied since 1954, an observation of the SF with a few tens of picoseconds time duration has not yet been reported.

In this part, we present experimental results in which the Rb atoms are excited into the $5D$ state from the $5S$ state by a two-photon process driven by laser pulses of 100 fs duration at 778 nm. Many of the excited atoms decay into the $6P$ state by emitting infrared light at 5 μm. Superfluorescent emission occurs on the $6P - 5S$ transition at 420 nm, which is recorded by the streak camera. The observed SF pulse duration is tens of picoseconds.

The same atomic configuration and associated radiation processes were recently considered by Lvovsky et al. [40, 41] and Paradis et al. [42]. The delay between the input pulse and SF as a function of the number density of the atoms was presented by Lvovsky [41] by varying input pulse energy or the temperature of the vapor, and by Paradis [42] by loading different numbers of atoms into the magneto-optical trap.

In the present work, we follow the former approach. The initial population of the upper level (the $5D$ state) is varied by adjusting the laser input power. For relatively high laser powers, one can observe saturation and Rabi oscillations in both the 5 μm and 420 nm emissions [41]. However, for low powers, far below the onset of saturation and/or oscillation, a simple correspondence between the input power and number of the excited atoms can be established. In this regime, we study the dependence of the time delay between the reference pulse and SF as the input beam power is varied, effectively changing the number of participating atoms.

2. Experimental Details

The atoms are initially prepared into a coherent superposition of the excited level, $5D$, and ground level, $5S$. Eventually, atoms decay to the ground state through the

intermediate state $6P$. The wavelengths of the generated fields in the upper, $5D-6P$, and lower, $6P-5S$, transitions are at 5 μm and 420 nm, respectively (see Fig. 9).

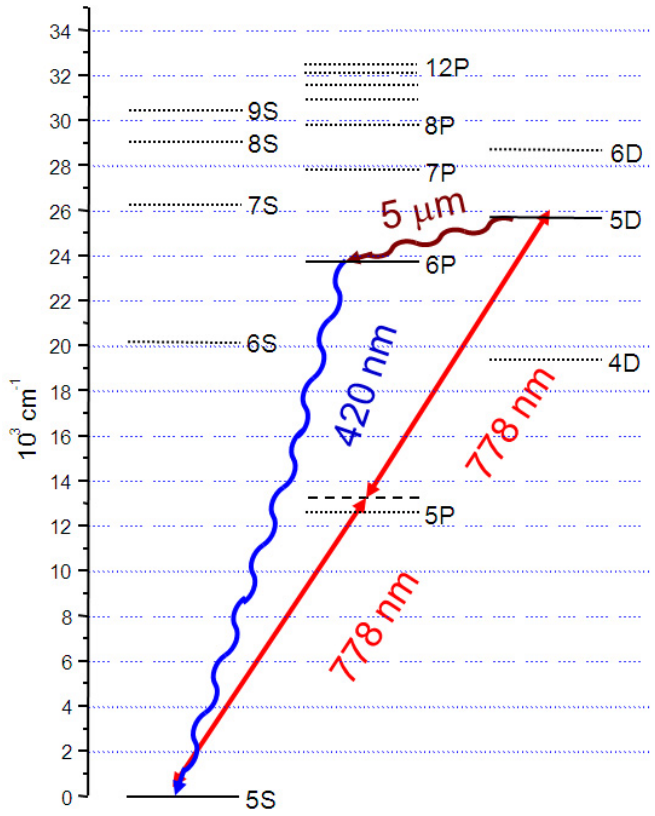

Fig. 9. The Rb atomic level scheme. After essentially instantaneous two-photon excitation of the input 778 nm pulse from the ground state ($5S$) to the upper level ($5D$), the atoms emit SF light at 5 μm which triggers SF at 420 nm.

A schematic of our experiment is shown in Fig. 10. The input light was furnished by the commercial femtosecond laser system. The pulses entered the Rb vapor cell. The generated pulses were analyzed by the spectrometer and the streak camera after passing through a colored absorption filter which is transparent for the 420 nm beam and blocks the 778 nm beam. Details of the experiment appear below.

The 778 nm (center wavelength) laser pulses were generated by an optical para-

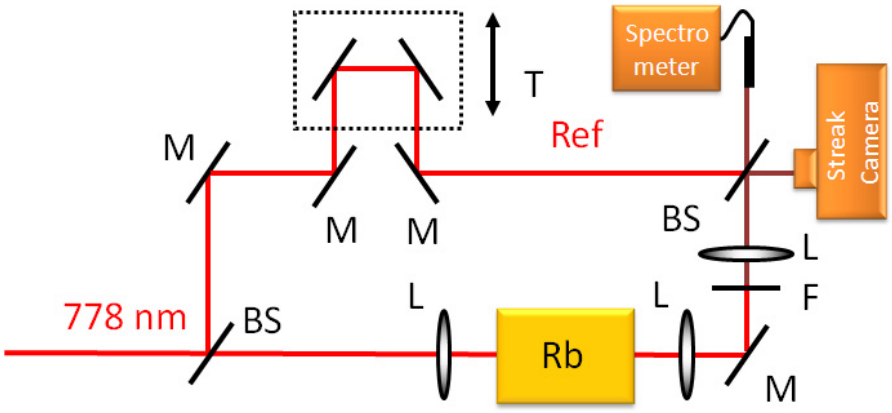

Fig. 10. Diagram of experimental setup. 778 nm: input laser beam, BS: beam splitter, T: translation stage, M: mirror, L: lens, F: filter which is transparent for the 420 nm beam and blocks the 778 nm beam, SC: streak camera, S: spectrometer, Ref: timing reference beam, Rb: rubidium vapor cell.

metric amplifier (OPA) driven by the commercial femtosecond laser system. The resulting 778 nm pulses were vertically polarized with respect to the laser table and had a duration of ∼100 fs as measured by a commercial autocorrelator. The beam was focused by a 20 cm plano-convex BK7 glass lens. The beam spatial profile at the focus was somewhat elliptical: FWHM was 50 μm (vertical) by 55 μm (horizontal) as measured by the knife-edge method. Next the laser beam entered a Rb vapor cell. The data displayed in this work were taken at temperature of 204 C, as measured by a thermocouple, giving a Rb density of $\sim 9 \times 10^{14}$ cm^{-3}. The beam at 778 nm passed through a beam splitter and provided a time reference pulse for a streak camera. The reference beam passed through a corner-cube retroreflector mounted on a translation stage that provided an adjustable time delay. A second beam splitter combined the light from the cell with the time reference beam before both entered the streak camera. The violet light at 420 nm generated in Rb vapor was emitted primarily in a narrow beam, parallel to the laser beams. The 420 nm beam had a divergence of

about 8 mrad. Upon exiting the cell, the beam was collimated and made parallel by a lens with a 10 cm focal length. The 778 nm beam was isolated by a filter. This filter was transparent to the 420 nm beam. The 420 nm light was focused by another lens (focal 15 cm) into the streak camera's entrance slit. The beam splitter reflected some 420 nm light toward the input fiber of the spectrometer. The power of the input and reference beams were adjusted by two variable neutral density filters, which are not shown in Fig. 10.

3. Experimental Results

We first recorded the spectra of the 420 nm light for different input powers. In Fig. 11 the magnitude at 420 nm light from the measured spectra is plotted as a function of input power, and shows a monotonic dependence. However, for sufficiently high power the dependence becomes much more complex [41].

Next, to detect the temporal characteristics of the generated signal, we used the streak camera. We concentrated on the measurement of the average time delay. The main results are shown in Fig. 12. The 420 nm light and reference beam were recorded by the streak camera. The set of measurements was done for several input powers ranging from 0.3 to 2.1 mW (note that 1 mW average power corresponds to $\sim$1 μJ/pulse). Because the signal was not stable, mostly due to laser jitter, up to 100 shots were averaged after jitter correction. This correction procedure results in an additional systematic error in time resolution. The time duration of the reference pulse was about 100 fs, which should ideally be displayed by streak camera as a $\sim$ 2 ps pulse, the limit of its resolution. In our case, the FWHM of the reference signal was approximately $\sim$ 6 ps (>2 ps).

One of the intriguing temporal properties of SF is ringing. The result for $\sim$ 0.3 mW input power clearly exhibited this feature. In Fig. 12, the 420 nm signal was

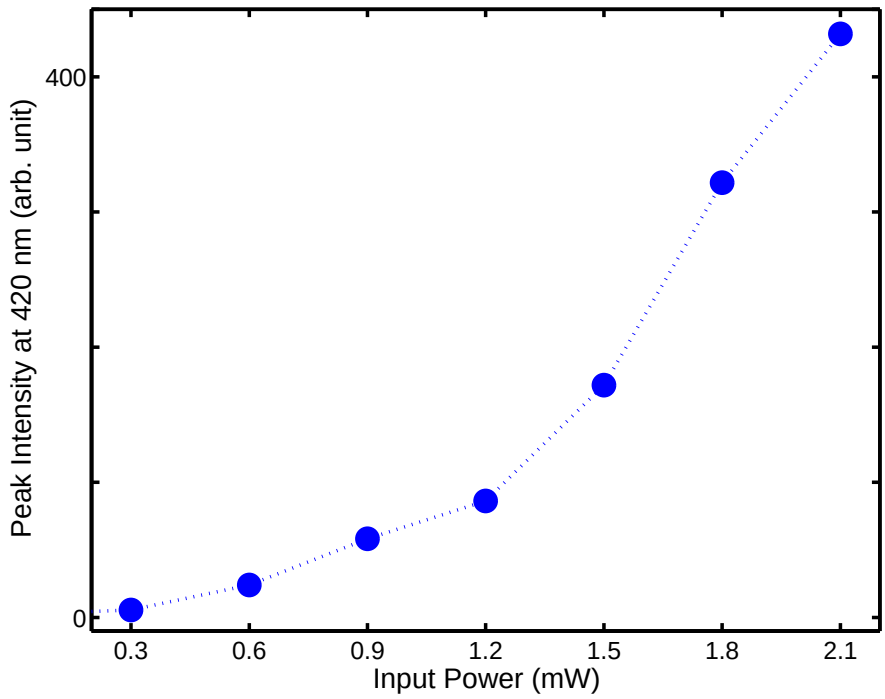

Fig. 11. The power dependence of the magnitude at 420 nm from the recorded spectra.

normalized: each measurement was taken with different gain settings of the camera and attenuation of the neutral density filters in order to improve the signal to noise ratio. As a result, in Fig. 12, the peaks of the reference beam have different heights. The peaks of the reference beams are adjusted to coincide with each other in time, thus enabling us to distinguish relative delays for each pulse. Generally, the temporal behavior of the 420 nm signal had a steep rising edge with moderately long tail. The delay is defined as a time-interval between the reference and 420 nm pulses, as shown in Fig. 12. The delay was calculated at the half-maximum of the rising edge of the reference and 420 nm pulses and summarized as a function of input power in Fig. 13. The error bars are estimated to be $\sim$3 ps for the average delay and $\sim$ 0.05 mW for the average power measurements. It is obvious from the observed data that SF appears

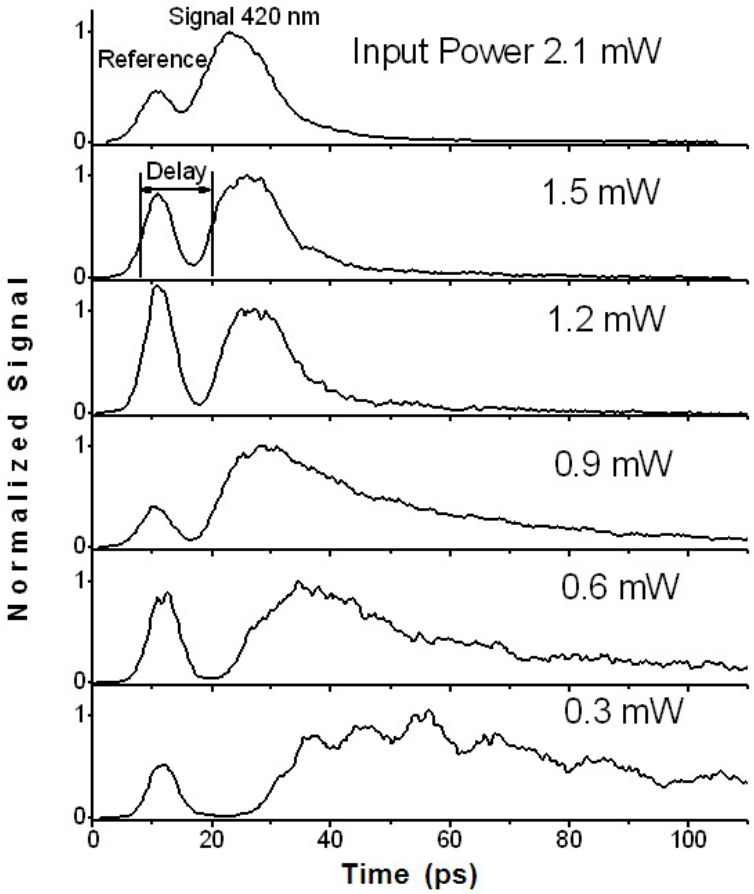

Fig. 12. The streak camera data for the reference and 420 nm pulses. The input beam power was varied from 0.3 to 2.1 mW.

sooner as input pulse energy increases.

4. Numerical Results

The semiclassical theory is presented in this part. In order to include the pulse excitation explicitly, we consider a five-level atomic system. Figure 14 defines $|c\rangle$ as a ground level ($5S$ state), $|a\rangle$ as an upper level ($5D$ state), $|b_1\rangle$ and $|b_2\rangle$ as the intermediate levels (two D-lines, $5P_{1/2}$ and $5P_{3/2}$ states, respectively) for two-photon excitation, and $|b\rangle$ as another intermediate level ($6P$ state) for yoked-SF emissions.

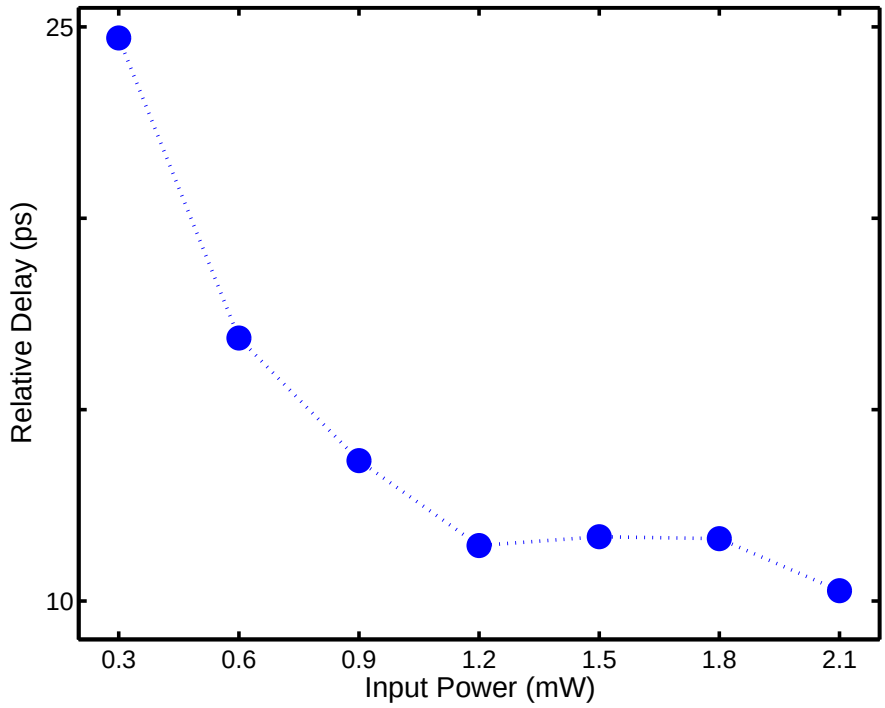

Fig. 13. The relation between the relative time delay with respect to the arrival time of the reference pulse and input power.

The frequency $\nu_{\alpha\beta}$ and the Rabi frequency $\Omega_{\alpha\beta}$ stand for the field mode coupled to the transition $|\alpha\rangle \leftrightarrow |\beta\rangle$. Note that the initial value of the Rabi frequency $\Omega_{\alpha\beta}$ is a very small phenomenological parameter, in order to start the temporal development of the system [39]. The two-photon detuning is $\Delta_2 = (\omega_a - \omega_c) - 2\nu_{in}$, where ω_i is the frequency of the ith level and ν_{in} is the frequency of the input field. In contrast, the single-photon detuning is $\Delta_1 = \nu_{in} - (\omega_{b_1} - \omega_c)$. The splitting between D-lines is $\Delta_0 = \omega_{b_2} - \omega_{b_1}$. One of the important parameters is the input field's Rabi frequency Ω_{in}. In the semiclassical treatment, the interaction of the atom with the classical field is governed by the Maxwell-Bloch equations in a retarded time frame. The semiclassical Hamiltonian in the interaction picture for this system can be written as

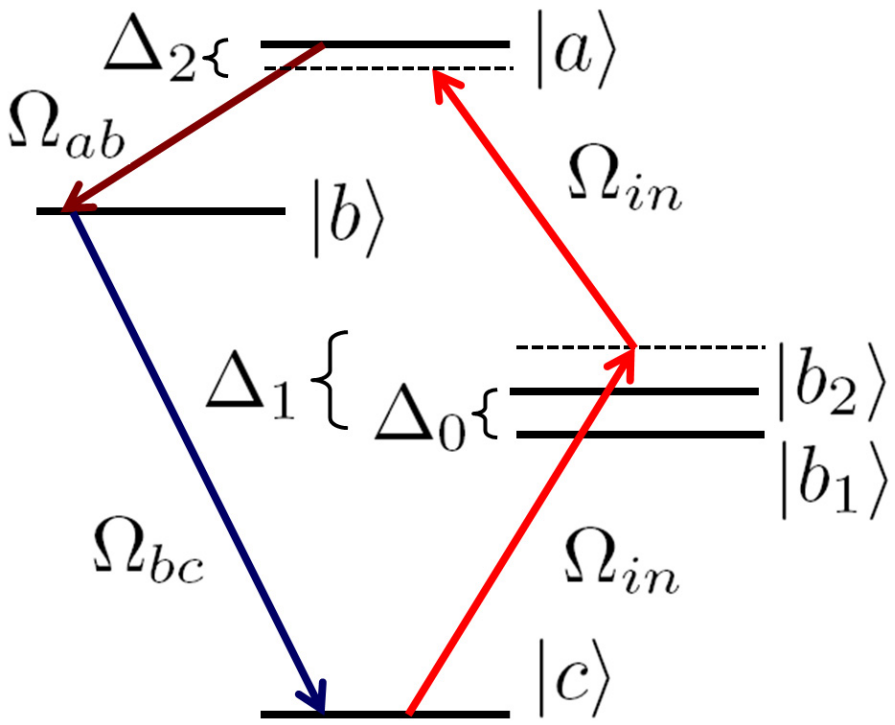

Fig. 14. A model of a five-level atomic system, see text for detail.

($\hbar \equiv 1$)

$$\begin{aligned}\hat{V}(t) &= -\Omega_{in}(e^{-i\phi_1 t}|a\rangle\langle b_1| + e^{-i\phi_2 t}|a\rangle\langle b_2| + e^{-i\Delta_1 t}|b_1\rangle\langle c| \\ &+ e^{-i(\Delta_1-\Delta_0)t}|b_2\rangle\langle c|) - \Omega_{ab}|a\rangle\langle b| - \Omega_{bc}|b\rangle\langle c| + h.c.,\end{aligned}$$

where $\phi_1 = 2\nu_{in} - (\nu_{ab} + \nu_{bc}) \equiv -\Delta_2$ and $\phi_2 = \phi_1 + \Delta_0 - \Delta_1$. The equation of motion for the atomic density operator $\hat{\rho}$ is given by

$$\frac{\partial \hat{\rho}}{\partial t} = -i[\hat{V}(t), \hat{\rho}]. \tag{4.1}$$

Note that no population decay or atomic coherence dephasing is included here.

Yoked-Superfluorescence

We consider the field generated in the axial direction, that is, along the z axis. Assuming that the backward 5 μm SF is uncoupled from the forward 5 μm and forward 420 nm SF, the Maxwell equations for two co-propagating modes in the retarded time frame $t \to t - z/c$, are given by [37, 39, 101]

$$\begin{aligned} \frac{\partial \Omega_{ab}}{\partial z} &= i\eta_{ab}\rho_{ab} \\ \frac{\partial \Omega_{bc}}{\partial z} &= i\eta_{bc}\rho_{bc}. \end{aligned} \tag{4.2}$$

Here the Rabi frequency can be expressed in terms of the field amplitude $E_{\alpha\beta}$ and transition dipole moment $\wp_{\alpha\beta}$ as $\Omega_{\alpha\beta} = \wp_{\alpha\beta}E_{\alpha\beta}$. The relevant coupling constant $\eta_{\alpha\beta}$ is given by $2\pi\mathcal{N}|\wp_{\alpha\beta}|^2\omega_{\alpha\beta}/c$, where $\mathcal{N}$ is the atomic number density, $\omega_{\alpha\beta} = \omega_\alpha - \omega_\beta$ is the transition frequency between the αth and βth levels, and c is the speed of light.

It is useful to simplify the present model and find analytical solutions, because it furnishes a qualitative understanding of the observed experimental results. The input pulse duration used in the experiment is 100 fs, which is an instantaneous excitation compared to the delay and duration of the yoked-SF pulse. Thus the three-level atomic configuration should be a good approximation. In this case, the initial populations of the upper and lower states are the control parameters rather than input pump power. This model of co-propagating modes for cascade three-level atoms has been studied in [37, 101] where the backward propagating mode is assumed to be generated independently. The reduced equation of motion for three-level atoms can be obtained from the five-level case by eliminating levels $|b_1\rangle$ and $|b_2\rangle$. For the sake of simplicity, assume that the populations of the levels are time independent and expressed by their initial values, i.e., $\rho_{cc}(t) \simeq \rho_{cc}(0)$, $\rho_{aa}(t) \simeq \rho_{aa}(0)$ and $\rho_{bb}(t) \simeq 0$. In the linear approximation [101], nonlinear terms $\Omega_{bc}\rho_{ab}$ and $\Omega_{ab}\rho_{bc}$ are neglected;

thus, $\rho_{ac}(t) \simeq \rho_{ac}(0)$. Similarly, as found in [37, 39, 101], the Rabi frequencies are given by

$$\begin{aligned} \Omega_{ab}(z,t) &\propto -\eta_{ab}\rho_{ac}(0) I_0(2\sqrt{\xi z t}) \\ \Omega^*_{bc}(z,t) &\propto \eta_{bc}\rho_{cc}(0) I_0(2\sqrt{\xi z t}), \end{aligned} \tag{4.3}$$

where $\xi = \eta_{ab}\rho_{aa}(0) - \eta_{bc}\rho_{cc}(0)$ and $|\rho_{ac}(0)|^2 = \rho_{aa}(0)\rho_{cc}(0)$. From the approximate solutions in Eq.(4.3), we infer the characteristic exponential growth [101] of the emissions on both the upper (ab) and lower (bc) transitions, i.e., both the 5 μm and 420 nm pulses are superfluorescent emissions [39]. The growth rate does depend solely on the main parameter ξ leading to yoked-SF [39]. In other words, there is no delay between the 5 μm and 420 nm pulses. Eq.(4.3) also shows that the passage time at which the field intensity reaches a specified value [25], depends on the initial population $\rho_{aa}(0)$, since $\eta_{ab} > \eta_{bc}$. The increase of the population leads to a faster growth, i.e., a shorter delay. At the next stage, we numerically solve Eq.(4.1) together with Eq.(4.2). The normalized 5 μm and 420 nm SF pulse shapes are shown in Fig. 15. The excitation input pulse is assumed to be a Gaussian with amplitude $\Omega_0 = 3$. The coupling parameters used here are $\eta_{ab} = 4$ and $\eta_{bc} = 0.08$, and the sample length is $L = 160$. In addition, we assume that all initial populations are zero except for $\rho_{cc}(0) = 1$. The other parameters are taken to be $\Delta_0 = C(1/780 - 1/795)$ (splitting between rubidium D lines), $\Delta_1 = C(1/778 - 1/795)$ (detuning between rubidium D_1 line and the wavelength of the input pulse), where $C = 7/(1/780 - 1/795)$ and $\Delta_2 = 0$ (two-photon detuning). Here Δ_0, Δ_1, Δ_2, $(\eta_{ab}L)$ and $(\eta_{bc}L)$ have units of THz; time t has units of ps. The SF delay can be calculated at the half-maximum of the pulse of the rising edge (see Fig. 15). The delay varies when input pulse amplitude Ω_0 is changed from 2.5 to 4.5. The delay dependence on amplitude of the input Gaussian

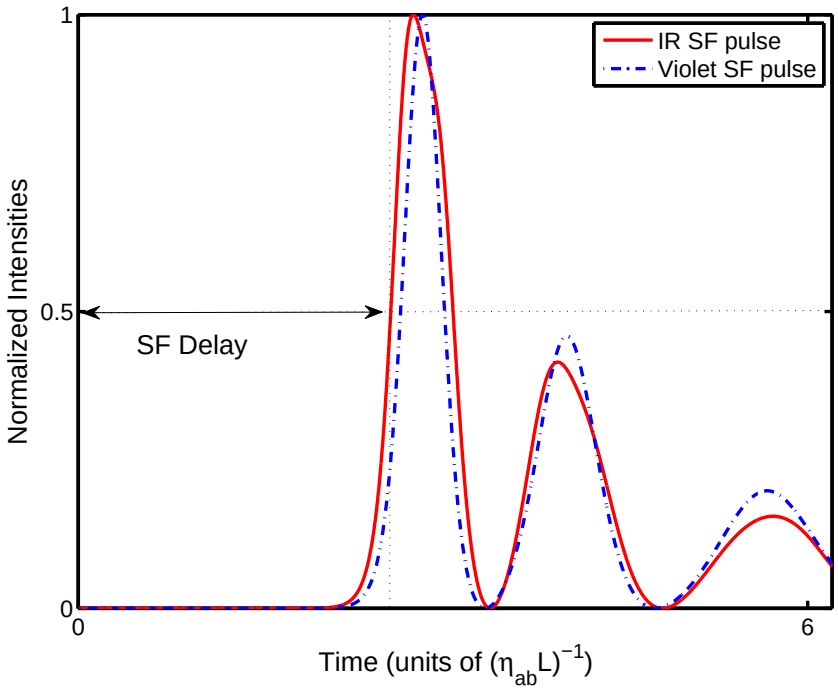

Fig. 15. The time evolution of the normalized intensities $|\Omega_{ab}|^2$ (the 5 μm pulse) and $|\Omega_{bc}|^2$ (the 420 nm pulse) for an input Gaussian pulse with amplitude $\Omega_0 = 3$.

pulse is plotted in Fig. 16. As is seen from Fig. 16, the forward 5 μm and 420 nm SF pulses are developed simultaneously. While these numerical results provide qualitative agreement with experimental data, they do not, however, provide quantitative agreement. This is because we assume that the forward and backward SF pulses are developed independently. Next, we simulate the backward propagating SF pulse.

Phenomenological Theory and Its Connection to Experiment

The coupling between the backward and forward SF for two-level atoms has been studied in [9]. Recently, Brownell et al., [39] have observed a cascade SF in the backward direction. Inclusion of all SF pulses simultaneously in the general Maxwell

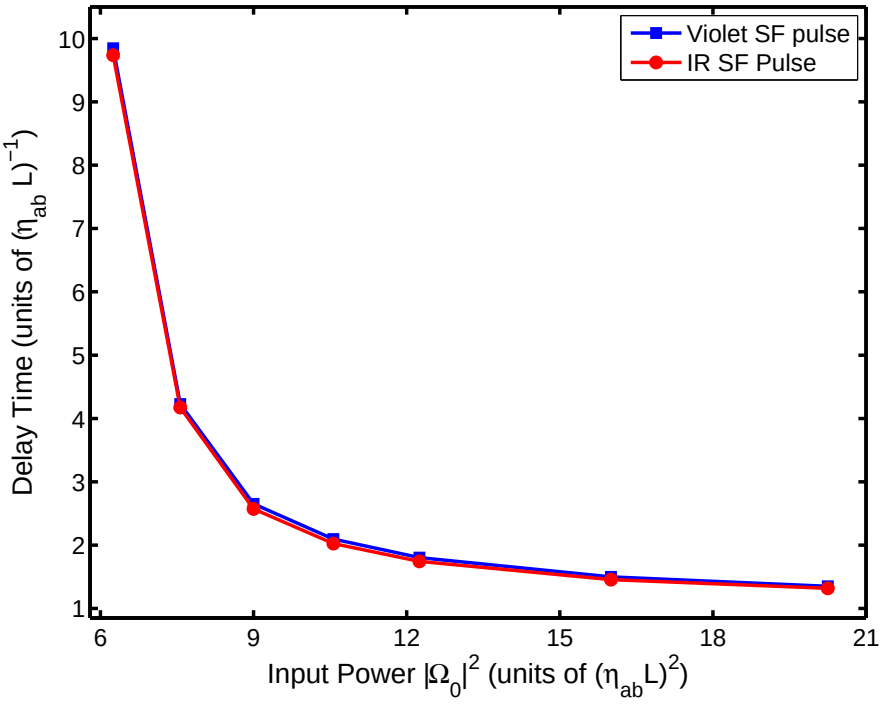

Fig. 16. The simulations for delay times of the 5 μm and 420 nm pulses as functions of the amplitude of the input Gaussian pulse. The parameters are the same as used in Fig. 15, but $\Omega_0 = 2.5$, 2.75, 3, 3.25, 3.5, 4 and 4.5.

equations is cumbersome. In the previous part it is assumed that the SF emissions in the forward and backward directions are independent [39, 101], i.e., the backward 5 μm SF is uncoupled from the forward 5 μm SF and forward 420 nm SF. In contrast, let us assume here that the backward 5 μm SF and forward 420 nm SF are coupled, and the forward 5 μm SF is independent. Further, we make the following assumption. The propagation equation for the backward 5 μm SF is written in time frame $t - z/c$, while the equation for the forward 420 nm SF is written in time frame $t + z/c$. Thus, the phenomenological propagation equations for two modes travelling in opposite

directions are given by

$$\begin{aligned} \frac{\partial \Omega_{ab}}{\partial z} &= i\eta_{ab}\rho_{ab} \\ -\frac{\partial \Omega_{bc}}{\partial z} &= i\eta_{bc}\rho_{bc}. \end{aligned} \tag{4.4}$$

Here, the z axis is taken to be along the backward 5 μm light propagation direction. The 420 nm SF pulse shapes are shown in Fig. 17 for several different input amplitudes. All other parameters are the same as used in Fig. 15. The curves in Fig. 17

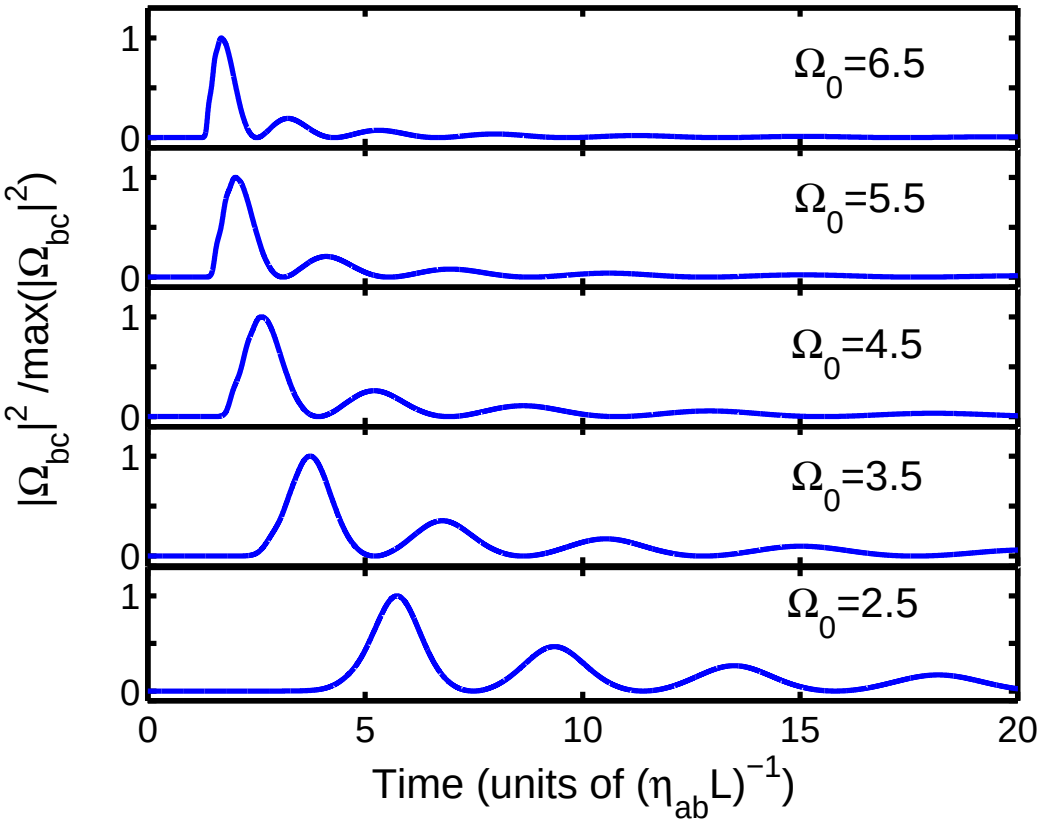

Fig. 17. The time evolution of the normalized intensity $|\Omega_{bc}|^2$ for different input pulse amplitudes. The input Gaussian pulse amplitudes are $\Omega_0 = 2.5,\ 3.5,\ 4.5,\ 5.5$ and 6.5.

are similar to ones in Fig. 12. In Fig. 17, if the square of the Rabi frequency $|\Omega_0|^2$ was scaled by some factor α, then time should be scaled by $\sqrt{1/\alpha}$. Comparing the pulse temporal shapes for $|\Omega_0|^2 = 6.25$ and 25 with the experimental results for input powers 0.3 mW and 1.2 mW, we choose $\alpha = 0.0480$. We are now able to quantitatively match the simulation to the experimental data. Note that, in the experiment, the delay between the input reference (but not the pump) and 420 nm pulse was measured. Because of the additional optical pathlengths resulting from the lens, beamsplitter and filters used in the detection configuration, an accurate time delay with respect to the pump cannot be measured directly. However, in a special case, there is a certain technique to measure this delay accurately using the higher order harmonics of the input laser pulses in Chapter VII. It is important to know the delay accurately as this knowledge helps us to understand the details of the experiment, such as the number of atoms participating in the cooperative emission. This particular example will be discussed in Part 5.

Keeping in mind the fact that the simulated delay time is relative to the pump, we find the offset to be ~ 3.2 ps. The simulated (solid curve) and experimental (full circles) results for delay times of the 420 nm pulse are shown in Fig. 18. An excellent agreement between the experiment and simulation is obtained. It must be borne in mind that there is no free fitting parameter used in the simulations. We simply start with the semiclassical Hamiltonian and numerically solve Eq.(4.1) and Eq.(4.4). The streak camera, lens and filters we used in the experiment are not appropriate for detection of the 5 μm pulse. Lvovsky et al. [41], have obtained partial information for the 5 μm light using a germanium detector. In this work, the results obtained for the 420 nm pulse reasonably predict the delay time dependence for the 5 μm pulse. The dotted curve in Fig. 18 stands for the 5 μm pulse delay dependence on input power; it increases as power decreases. A non-zero delay occurs between the generations of

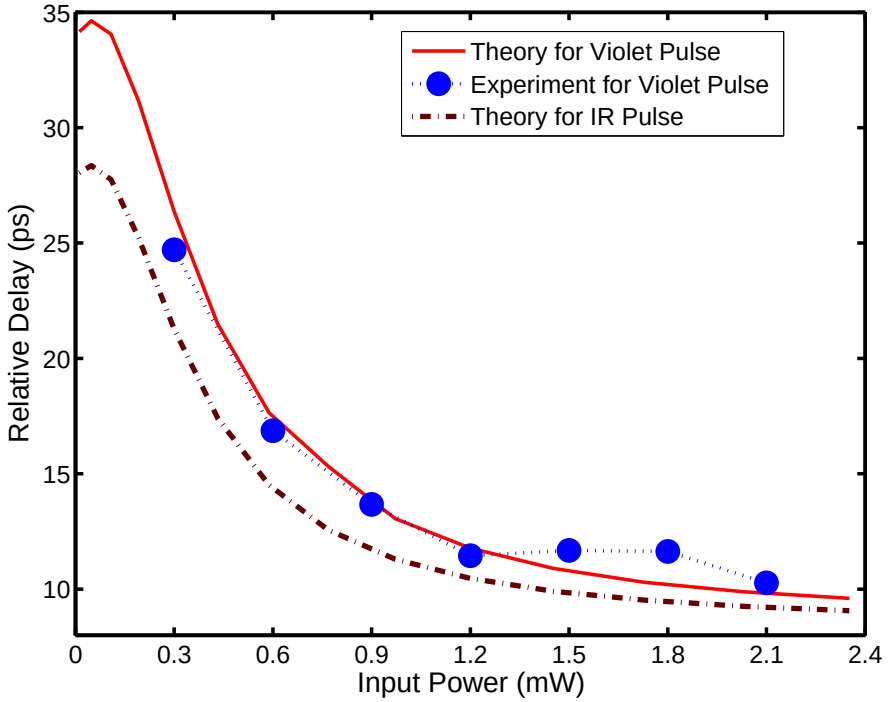

Fig. 18. The measured relative delay time for the 420 nm pulse as a function of input power (full circles) and simulations for both the 5 μm (dotted curve) and 420 nm (solid curve) pulses with scaling factor $\alpha = 0.0480$.

the 5 μm SF and 420 nm SF. Brownell et al. [39] found that the backward SF pulse in the upper transition arrived first in time, followed by the yoked-SF emissions in both the upper and lower transitions in the forward direction. In this sense, one should anticipate some delay between the backward 5 μm SF and forward 420 nm SF for both the cascade and yoked SF in the forward direction; unfortunately, we could not give a reasonable physical explanation for this phenomenon. To do that one needs a rigorous analytical treatment of the cascade three-level atomic system, which would be beyond the framework of this work.

Since the experiment and simulation are in agreement for the 420 nm violet pulses, we can find the delay relative to the pump. For instance, at 1.2 mW and 0.3

mW input power, the relative delay is found to be 8.6 ps and 23.2 ps, respectively. Similarly, for the 5 μm pulses at 1.2 mW and 0.3 mW input power, these are 7.3 ps and 18.1 ps, respectively. So far, the delay times have been determined at the rising edge of the pulse. The 5 μm pulse delay defined at its maximum is given by 19.6 ps at 0.3 mW (7.6 ps at 1.2 mW). Note that in Chapter VII, we probe the excitation of the 5D state using an extra IR input pulses. The delayed IR pulse probes the population of the 5D state to show that it decays in $\sim$ 16 ps which is consistent with the results obtained here.

The population of the excited state is calculated numerically as the amplitude of the input pulse varies. In Fig. 19, the population of the excited state $|a\rangle$ (full circles) is plotted as a function of the input Gaussian pulse intensity. A fit (solid curve) is given by the formula $|\Omega_0|^{2x}/10^{7.6}$ with $x = 1.8$. The population is expected to be proportional to the square of input energy, as is typical for the two-photon transient excitation. Using the scaling factor $\alpha = 0.0480$, we can estimate the population of the excited state ρ_{aa} as a function of input power. In Fig. 19, it is shown that for particular input values $|\Omega_0|^2$ =6.25 and 25, the populations are $\sim$ 0.02 and $\sim$ 0.19, respectively. This means that at 0.3 mW and 1.2 mW input powers only 2 and 19 percent of the atoms are excited, respectively. 50 percent of the atoms can be excited at 2.1 mW. A simple relation between population and input intensity supports the assumptions for the three-level atomic model.

5. Discussions Based on Existing Theories

In this part, we discuss the main results in terms of existing theories. Let us estimate the number of atoms in the focal region. The diameter of the focused beam at the focus of the lens is $d = 4\lambda_{778nm} f/(\pi D) \sim 80$ μm, where the unfocused beam diameter is $D = 2.5$ mm, and lens focal length is $f = 20$ cm. This is consistent with the

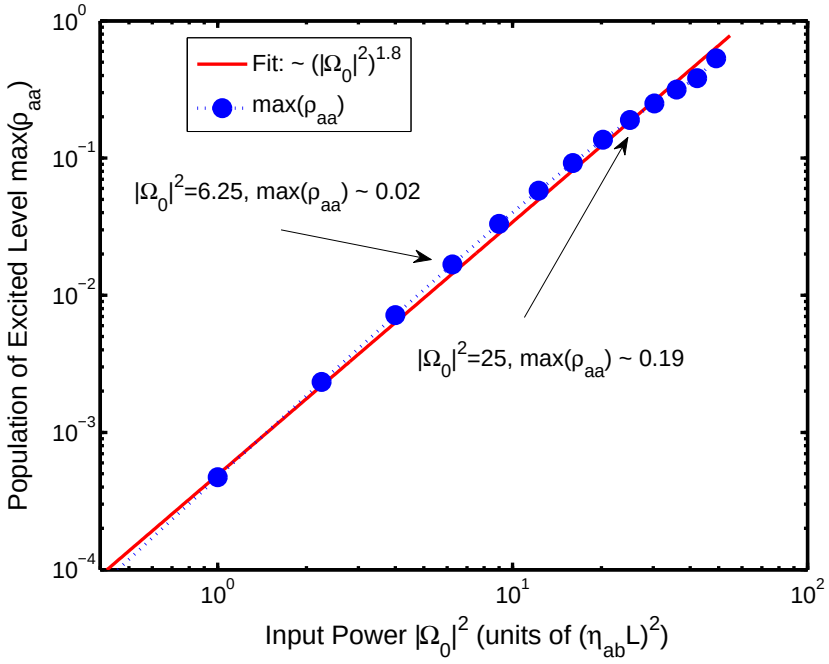

Fig. 19. The log-log scaled relations of the population of the excited state $max(\rho_{aa})$ (full circles) and its fit with function $|\Omega_0|^{3.6}$ (solid curve) and input intensity.

measured beam sizes at the focal plane, which are 50 μm and 55 μm. The depth of focus $DOF = 8\lambda_{778nm}f^2/(\pi D^2) \sim 1$ cm. Thus, at a temperature of 204 C, the total number of atoms in this volume is $N_{total} = \pi d^2/4 \cdot DOF \cdot \mathcal{N} \sim 4.5 \cdot 10^{10}$ where the number density $\mathcal{N}$ is $9 \cdot 10^{14}\text{cm}^{-3}$, and the area is $\pi d^2/4$.

It was first mentioned by Arecchi and Courtens in 1971 [6] that there is a restriction to the number of cooperative atoms due to the fact that the photons travel with finite speed. For instance, if the sample length is longer than the product of SF delay and the speed of light, then the remote atoms cannot be considered as cooperative. This restriction is critical in our case, since the SF pulse delay and width are measured in tens of picoseconds.

Let us first compare the delays at the specific powers, 0.3 mW and 1.2 mW.

Earlier, we found that at 0.3 mW and 1.2 mW the 5 μm SF pulse has 19.6 ps and 7.6 ps delays (defined at the maximum of the pulse), respectively. The corresponding cooperation lengths are $l_{0.3mW} \sim 5.9$ mm and $l_{1.2mW} \sim 2.3$ mm. At this stage, we can estimate the Fresnel number $F_{5\mu m} = 2(\pi d^2/4)/(L\lambda_{5\mu m})$, which was used by MacGillivray and Feld [7], as $1 \leq F_{5\mu m} \leq 3$. The maximum cooperation number is given by $N = Al\mathcal{N}$. Taking into account the percentage of the excitation for two powers, the number of excited atoms are estimated to be

$$\begin{aligned} N_{0.3mW} &= 0.02 \cdot A \cdot l_{0.3mW}\mathcal{N} = 5 \cdot 10^8 \\ N_{1.2mW} &= 0.19 \cdot A \cdot l_{1.2mW}\mathcal{N} = 2 \cdot 10^9. \end{aligned} \tag{4.5}$$

The ratio of these values is $N_{1.2mW}/N_{0.3mW} \sim 4$, whereas the ratio for delay times is 19.6 ps/7.6 ps ~ 3. Therefore, based on the above estimation, the emission on the upper transition (5 μm pulse) is SF in which the inverse of the delay is approximately proportional to the number of the excited cooperative atoms.

According to Polder et al. [14], the ratio between delay time τ_D and the superradiant lifetime τ_R is:

$$\frac{\tau_D}{\tau_R} = \frac{1}{4}\left(\ln(2\pi N)^{1/2}\right)^2. \tag{4.6}$$

In particular, for $N_{1.2mW} = 2 \cdot 10^9$, this ratio is given by $\tau_D/\tau_R \sim 5.8$. From Eq.(1.1) the superradiant lifetime is $\tau_R \sim 0.6$ ps for $T_1 = 0.69$ μs and $\lambda = 5$ μm. Therefore, delay time becomes $\tau_D \sim 3.3$ ps. For $N_{0.3mW} = 5 \cdot 10^8$ the ratio is $\tau_D/\tau_R \sim 5.4$. The delay time is $\tau_D \sim 12.5$ ps for $\tau_R \sim 2.3$ ps. The experiment suggests that delay times for 1.2 mW and 0.3 mW are 7.6 ps and 19.6 ps, respectively. According to the above estimation, we found 3.3 ps and 12.5 ps. The ratio between delays in theory and experiment are 12.5 ps/3.3 ps ~ 4 and 19.6 ps/7.6 ps ~ 3, respectively, yielding a consistent result.

Next we study the changes in scaling laws for the peak intensity and delay time in more detail. In order to be more precise, let us consider the experimental data for powers from 0.3 mW to 1.2 mW. In Fig. 20 we plot the experimental data for the

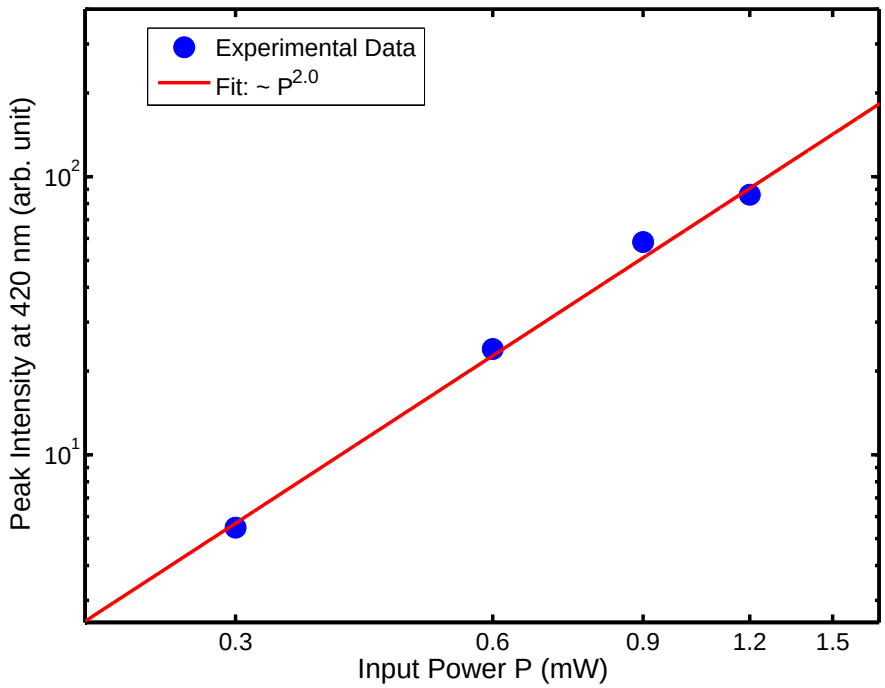

Fig. 20. The power dependence of the magnitude at 420 nm from the recorded spectra for the 420 nm SF light (full circles) and its fit with function $P^{2.0}$ (solid curve) in a log-log scale.

relationship between peak intensity and input power. A fit (solid curve) of the data (full circles) demonstrates that the peak intensity of the 420 nm light is approximately proportional to the square of input power as $I_{max} \propto P^x$, where $x = 2.0 + \Delta x$. Taking into account the experimental errors in power measurement we find $-0.2 < \Delta x < 0.2$. For the case of the two-photon pumping, the number of participating atoms is proportional to the square of input power as $N \propto P^2$ (see Fig. 19). This means that the peak intensity is proportional to N, but not N^2. In Fig. 21, we show the

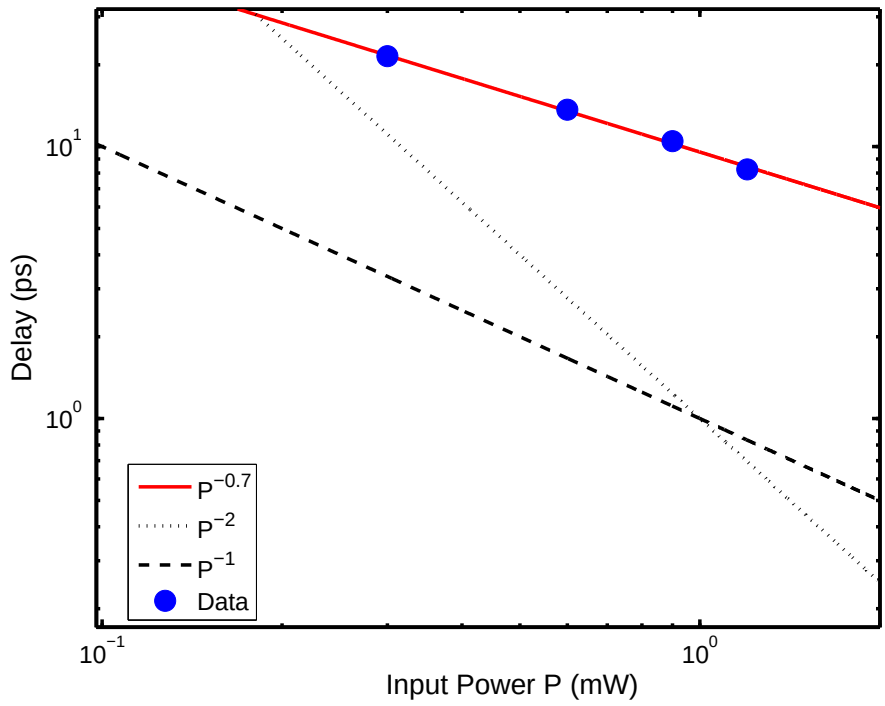

Fig. 21. A log-log plot that shows the 420 nm SF delay time relative to the reference pulse as a function of input power (full circles). A fit is given by $\propto P^{-0.7}$ (solid curve). The data is also compared to functions P^{-2} (dots) and P^{-1} (dashed curve).

experimental data (full circles) for the relative delay versus input power in a log-log scale. In this figure, the dashed curve and dots correspond to the power-laws P^{-1} and P^{-2}, respectively. We fit the delay data to the form $a/P^x + b$, where a fitting parameter x provides information about the power-law. In Part 4, we estimated the temporal offset to be b=3.2 ps. Using this offset, from the fit (solid curve) we obtain $x = 0.7 + \Delta x$. In view of the error bars in delay and power measurements, Δx is found to be $-0.2 < \Delta x < 0.3$. For pure SF [3], the peak intensity and time delay scale as N^2 and N^{-1}, respectively. For the oscillatory SF [15, 16], they are scaled by N and $N^{-1/2}$. Therefore, our observed data can be explained best by the oscillatory SF

theory. A little discrepancy between the fit $N^{-x/2}$ and prediction for the oscillatory SF, $N^{-1/2}$, can be explained by the following. (i) The data for delay was measured at the rising edge but not at the peak of the SF pulse. (ii) The data was taken for the SF at 420 nm rather than the SF at 5 μm. A delay between the 5 μm SF and 420 nm SF is non-zero. Considering these points one would obtain more precise agreement. Nevertheless, even without the above mentioned points, we can clearly recognize the consistency of the data with $N^{-1/2}$ dependence.

Finally we discuss the temporal ringing in more detail. The SF temporal ringing in two-level atoms has been widely studied [7, 18, 19, 21, 22, 16, 102]. However, the ringing has not been investigated in a cascade three-level system. The detailed theory for temporal ringing in this case would be much more complicated because of the cascade emissions. It can be simplified under the yoked-SF condition where the SF emissions on the upper and lower transitions occur simultaneously. In this case, one can consider the yoked-SF on the lower transition as the same as that on the upper transition, i.e., the SF for two-level atoms.

The origin of temporal ringing is two-fold. The Maxwell-Bloch theory predicts an intrinsic SF ringing [7]. In this case, the temporal ringing results from the energy exchange between field and atoms while the field is propagating inside a single zone (slice) [16]. On the other hand, the ringing occurs when the field is reabsorbed and reemitted while propagating through multiple cooperation zones [16, 19]. We did not perform a specific experiment to distinguish the two types of ringing, and in the present situation it could possibly be a mixture of the two. However, in Fig. 12, the temporal ringing is caused by the energy exchange between field and atoms within a single cooperative zone. From Fig. 12, one can estimate that the width is less than 5 ps (the width of the SF pulse at 0.3 mW), and the delay is longer than 15 ps (a time interval between arrival times of the SF pulses for low and high power). Their

ratio is greater than 3. According to [16], if the ratio is much greater than unity then an intrinsic SF ringing is important. It is also interesting to note that the observed temporal ringing was reproducible. The temporal ringing demonstrated a quasi-periodic dependence on the square root of time variable. Therefore the ringing was not due to a succession of SF pulses from multiple cooperation zones with diminishing intensity [19].

Both the diffraction and transverse effects can cause the reduction of the ringing [15]. The diffraction effect is negligible in this case because the Fresnel number is greater than one for a single zone even if it is close to one for the entire sample. The transverse effect is expected to be dominant since the input light was focused into the sample. The transversal plane of the input beam leads to a non-uniform excitation of the atoms and the emissions smear out the ringing. In particular, when input power increases, the length of the cooperative zone decreases, i.e., the emissions from the atoms on the transversal plane would be more noticeable.

According to simulations based on the semiclassical atom-field interaction, the ringing for the SF at 420 nm is different than that for the SF at 5 μm. Neither diffraction nor transverse effects are included in the simulations. Therefore, the ringing in Fig. 17 cannot represent the observed ringing in Fig. 12. However the origins of the simulated ringing in Fig. 17 and observed ringing in Fig. 12 are consistent.

6. Conclusion

The Rb atomic vapor was excited to the $5D$ from the $5S$ state via a two-photon process with 100 fs laser pulses. The experiment was designed to measure the SF emission on the $6P - 5S$ transition at 420 nm. The spectrum of the 420 nm light was measured as a function of pulse energy. A simple correspondence between the 420 nm light intensity and input power was obtained. The temporal characteristics

of the 420 nm SF was studied using an ultrafast streak camera.

Our system furnished a first-ever observation of a SF pulse lasting a few tens of picoseconds from the dense Rb atomic vapor. On this time scale, relaxation processes such as spontaneous emission of the individual atoms, the Doppler effect and atomic coherence/collisional dephasing are negligible. The SF pulse shape changed considerably for different input pulse energies. For low power, significant temporal ringing was recorded. For high power, however, the ringing was not observed.

A numerical simulation, based on a semiclassical theory for five-level atoms with no free fitting parameters, yielded excellent agreement with our experimental data. Furthermore, the experimental results were compared with several existing SF theories. The distinct change in the scaling laws for the peak intensity and delay time versus input power is noticeable. The oscillatory SF theory, in which the sample length is larger than the cooperation length, explains the observed data most successfully.

We believe this study will be useful in various applications directly related to SF processes. For instance, the possibility of rapid inspection of quantum interference using the temporal characteristics of the coherent emissions of multiple atoms could be of great interest, see Chapter V.

B. Quantum Fluctuations in Superfluorescence Delay Times

Most of the SF pulse characteristics can be explained by the semiclassical theory; however, understanding fluctuations in delay time of the SF pulse requires a full quantum theory [24, 26]. To the best of our knowledge, no experiment on quantum fluctuations in SF delay times in atomic vapor has been reported since the first observation in Vrehen and Weduwe's experiment in 1981 [34]. Recent technological

advances, for example, in lasers and streak cameras have offered an opportunity to explore the quantum nature of SF in atomic vapor on a picosecond time scale.

In this work we present an observation of fluctuations in delay times of the generated SF pulses in atomic Rb. A statistical distribution and fluctuations of delay times were studied as the pump laser energy varied, effectively changing the number of participating atoms.

The Rb atomic level scheme is shown in Fig. 9. The atoms were excited to the 5D state from the ground $5S$ state via two-photon transitions. Eventually, the excited atoms radiated SF pulses at 5 μm and 420 nm resonant to the $5D-6P$ and $6P-5S$ transitions, respectively. The input 778 nm pulses, which were off-resonant to any of the $5D-6P$ and $6P-5S$ transitions, could not populate the $6P$ state. Thus a macroscopic dipole polarization for the $5D-6P$ transition required some build-up time, i.e., emission of the 5 μm SF pulses was delayed. In this sense, the 5 μm SF was the same as the conventional SF for two-level atoms. The SF delay varied according to the number of excited atoms, which in turn depended on the input power. In particular the 5 μm SF appeared sooner as input pulse energy increased. The atomic coherence between the $5D$ and $5S$ states was created by the input 778 nm pulses which allowed the yoked SF emission in which the 420 nm SF pulses could be emitted simultaneously with the 5 μm SF emission [39]. Therefore, in the case of coherent excitation, the power dependence of the 420 nm SF time delay could represent that for the 5 μm SF pulses. Average delay times of the 420 nm SF pulses as functions of the input pulse energy were measured in previous part. However, in general, measurement of fluctuations in delay times of the 420 nm SF pulses is not straightforward. That is because fluctuations in delay time consist of the extrinsic and intrinsic parts [34]. The extrinsic fluctuations are mainly due to non-reproducibility of the laser pulses while the intrinsic fluctuations are due to the quantum initiation of SF. In order to

suppress the extrinsic fluctuations, Vrehen and Weduwe used a beamdivider, preparing two separate samples in their experiment. The samples emitted two statistically independent SF pulses; the difference of the delay times of those pulses on the same laser shot was attributed to the intrinsic fluctuations [34]. A similar technique was used in our experiment. Fig. 22 illustrates the experimental setup. The input light

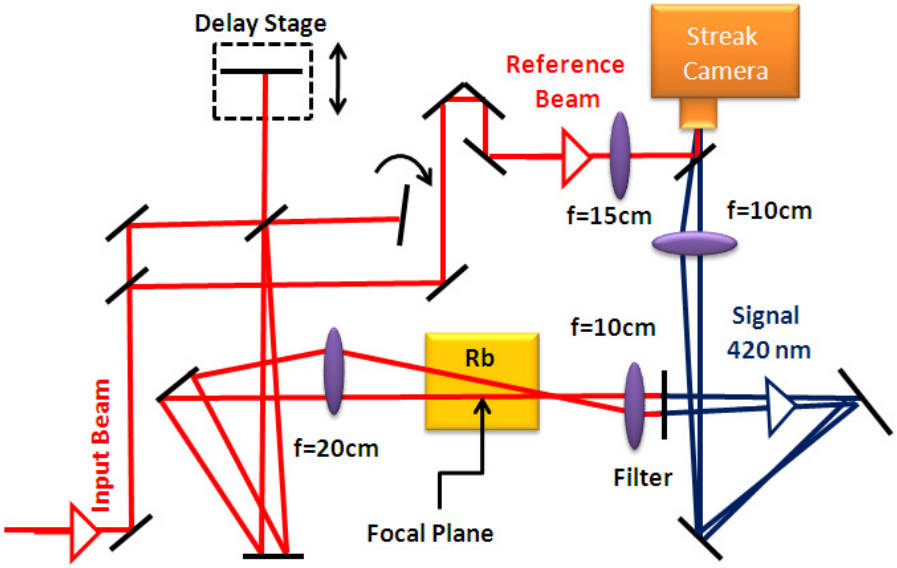

Fig. 22. Diagram of the experimental setup. Two beams were focused into Rb vapor to prepare two spatially separated, identical samples near the focal plane. A reference beam was used for timing the pulses that were measured by a streak camera. The delay stage was used to separate input pulses in time. The Rb atomic density was approximately 4.6×10^{14} cm^{-3}.

(100 fs pulses) was furnished by the commercial femtosecond laser system. The 778 nm beam was divided by the first beamsplitter (a thin glass plate which reflected a very small fraction of the input beam) to provide a reference beam which was used for timing the arrivals of the pulses recorded in the streak camera. A second 50/50 beamsplitter divided the input beam into two, each of which was further focused by a

20 cm lens. Using a commercial beamprofiler we checked beam intensities at different positions. The beams were separated about 6 mm apart at the focal plane and had Gaussian transversal profiles with similar peak heights. The beam intensities became much small at the beam crossing position, which was 4 cm away from the focal plane. Time delay between input pulses was adjusted by a translation delay stage. The Rb vapor cell mentioned in the previous part, was inserted into the focal region of the beams. The data were taken at a temperature of about 188 C, giving a Rb density of approximately 4.6×10^{14} cm^{-3}. Two samples prepared near the focal region emitted the yoked SF pulses. Since the streak camera was not designed for the 5 μm SF pulses, filters were used to transmit only the 420 nm SF pulses towards the streak camera. A third beamsplitter (another thin glass plate) was used to partially reflect the reference beam into the streak camera. The streak camera recorded the temporal profiles of a pair of the 420 nm SF pulses one from each beam, and a reference pulse in a single laser shot operation mode. In order to obtain enough statistical information, up to 400 pairs of the 420 nm SF pulses were collected at each input power. These collected data and the mean values (thick solid curves) are depicted in Fig. 23 (a) for several different input powers. The preceding pulses were separated from the following pulses by a fixed delay time, although this delay can be chosen to be zero. Note that any relaxation processes, such as spontaneous emission, the Doppler effect and dephasing were extremely slow (in nano/microsecond time scale) compared to the picosecond SF and, thus, discarded here. Therefore the two 420 nm SF pulses were statistically independent. In Fig. 23 (a) the temporal shape of the 420 nm pulses has a steep rising edge followed by a long tail. It was more accurate to define delay time (relative to a reference pulse) at the half-maximum on the rising edge. The difference of the delay times for the preceding and following pulses was obtained for each trace. The experimental histograms of the statistical distributions of the difference of delay

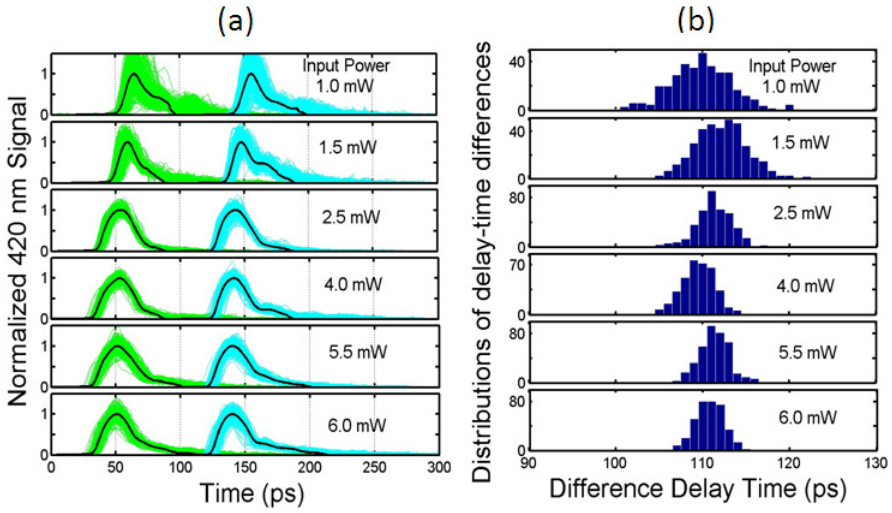

Fig. 23. (a) Picosecond time-resolved temporal characteristics of the 420 nm SF pulses. A successive pair of input pulses excited the atoms at the two different regions near the focal plane. Both 420 nm SF pulses generated from those regions were recorded by a streak camera. At each input power the measurement was repeated shot-to-shot, collecting up to 400 data samples. The corresponding traces, averaged over data samples, are plotted by thick solid curves demonstrating the preceding and following 420 nm SF pulses. (b) Experimental histograms for the statistical distributions of the delay time differences. The histograms were constructed by counting those pairs of pulses for which differences of the delay times fell within certain time-intervals.

times for several input powers are shown in Fig. 23 (b). In Figs. 24 (a) and (b) the average delay times for the preceding and following pulses demonstrated a typical power dependence as in the previous part. After subtracting the minimum values, the power dependencies of the average delay times for the preceding and following pulses were accurately matched. In general, a standard deviation for the number of τ_i variables n with mean value $\langle\tau\rangle = \sum_{i=0}^{n} \tau_i/n$ is defined by $[\sum_{i=1}^{n}(\tau_i - \langle\tau\rangle)^2/(n-1)]^{0.5}$. The standard deviations, as defined above, were obtained for delay times and the

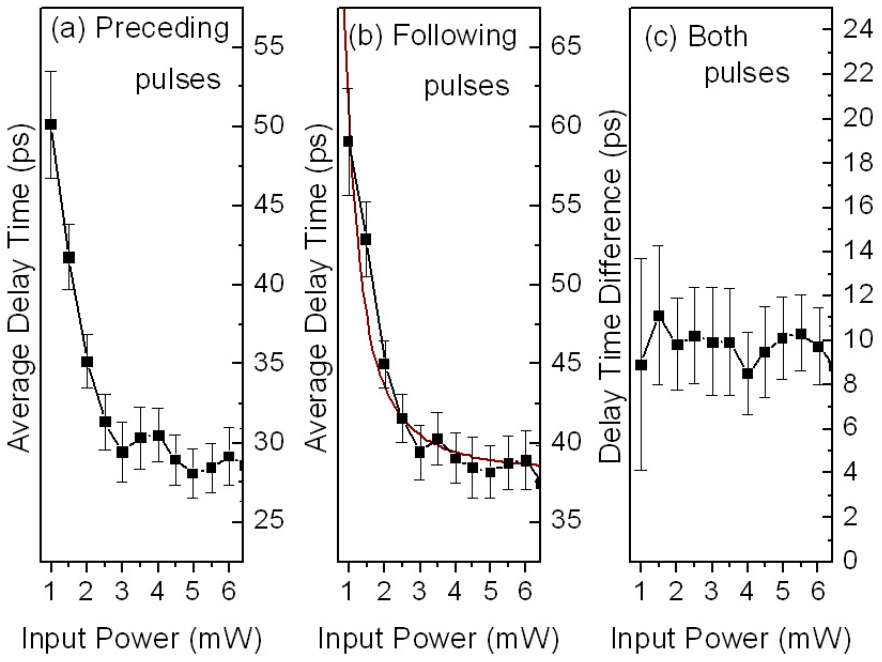

Fig. 24. The average delay times with respect to the arrival times of the reference pulses for (a) the preceding and (b) following 420 nm SF pulses as well as (c) the average difference of delay times of the preceding and following pulses plotted as functions of input power. The corresponding standard deviations (error bars) for each measured data point are added.

differences, see error bars in Fig. 24 (a) and (b). In Fig. 24 (c), the mean value of the difference of the delay times were not changed while the input power varied. In contrast, the corresponding standard deviations were altered. The power dependencies for the standard deviations are summarized in Fig. 25. The fluctuations for the delay time differences (triangles) increased as input power decreased. It was also true for fluctuations for the preceding (squares) and following (circles) pulses. In particular, in the power region from 1 mW to 3.5 mW in Fig. 25, fluctuations for delay times (circles) and delay time differences (triangles) were almost indistinguishable. Hence it was inferred that the extrinsic fluctuations were not crucial in our experiment and

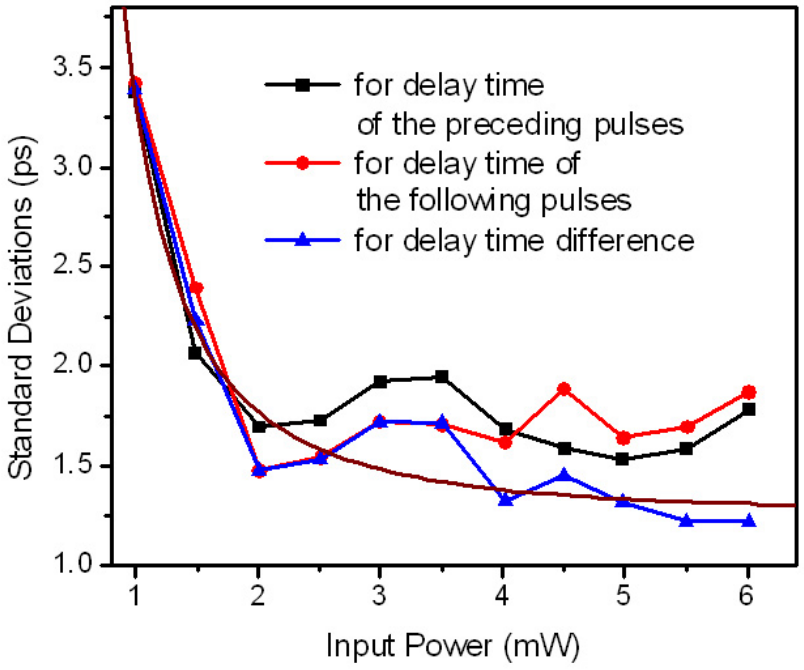

Fig. 25. Fluctuations in SF delay times. The standard deviations for the delay times of the preceding (curve with squares) and following (curve with circles) 420 nm SF pulses as well as the difference of the delay times (curve with triangles) are plotted as functions of input power. The standard deviations for the difference is divided by $\sqrt{2}$, taking into account the statistical independence of the two samples.

the data obtained in this work revealed quantum fluctuations. In the range of 1 mW to 6 mW input power, the delay times (see Fig. 24 (a) and (b)) and fluctuations of the delay time differences (see Fig. 25) for the 420 nm SF pulses were varied within 20 ps and 2.5 ps, respectively. A quantum theory predicts a ratio between fluctuations and average delay times to be $R_{Theory} = 1.28/\ln N$ [24]. Under the present experimental conditions, the number of participating atoms N is proportional to P^2, where P is an average input power, and estimated to be $2 \times 10^6 \leq N \leq 10^8$, see [103] for more detail. Thus, the ratio is given by $0.07 \leq R_{Theory} \leq 0.09$. In Figs 24(b) and 25 (see,

the solid curves), the data for average delay and fluctuations of the delay time differences were fitted by functions in the forms $A_1/P^2 + B_1$ and $A_2/P^2 + B_2$, respectively. Here $A_{1,2}$ and $B_{1,2}$ are fitting parameters. Let us define a ratio as $R_{Exp.} = A_2/A_1$ to compare with R_{Theory}. Using the fitting parameters, the ratio was estimated to be $0.08 \leq R_{Exp.} \leq 0.11$. Therefore, the present experiment supports the quantum theoretical prediction on the SF delay statistics. The development of the detailed quantum theory for cascade three-level atoms and the delay measurement at a pulse peak rather than at a half-maximum on the rising edge of the SF pulse will certainly improve the present study.

In conclusion, fluctuations in delay time originating from the quantum initiation of the SF were measured in Rb vapor. The power dependencies of the delay time and fluctuations were studied. We believe that the observed results enrich our understanding of SF phenomena and stimulate new theoretical studies for delay time fluctuations for the SF in three-level atoms.

CHAPTER V

COHERENT TEMPORAL CONTROL OF RADIATION IN ALKALI METAL VAPOR*

In this chapter, two examples of coherent temporal control of radiation are considered. First, we demonstrate temporal coherent control in two-photon transitions. A pair of broadband ($\Delta\lambda \approx 20$ nm), ultrashort ($\Delta t \approx 100$ fs), collinear pulses with variable time delay excite rubidium atoms into the $5D$ state from the $5S$ ground state where two-photon transitions are enhanced by the intermediate level $5P$. The excited atoms radiate 5 μm ($5D$-$6P$) and 420 nm ($6P$-$5S$) light. As a result of tuning the wavelength of the input laser, a superfluorescence at 420 nm exhibits different temporal behaviors. A switching from a beating at the frequency given by the difference between the sequential atomic transitions which involve the $5P_{3/2}$ intermediate level, to a quantum beating due to two different two-photon excitation-paths, $5S$-$5P_{1/2}$-$5D$ and $5S$-$5P_{3/2}$-$5D$ is observed. Based on a simple atom-field interaction theory, an analytic solution, which qualitatively elucidates experimental results, is obtained. Next, we study the dynamics of wave packets in cesium dimers using a femtosecond-controlled pump-probe technique. We implement configurations with one pulse (pump) or two pulses (pump and control) to produce vibrational wave packets on the electronic excited state. The transmission of an additional, variable delay probe pulse is measured to monitor the time evolution of the wave packets. In

*Part of the data reported in this chapter is reprinted with permission from "Femtosecond Wave-Packet Dynamics in Cesium Dimers Studied through Controlled Stimulated Emission", 2010. L. Yuan, G.O. Ariunbold, R.K. Murawski, D. Pestov, X. Wang, A.K. Patnaik, V.A. Sautenkov, A.V. Sokolov, Yu.V. Rostovtsev, and M.O. Scully, *Phys. Rev.* A 81, 053405. Copyright [2010] The American Physical Society

the case of the pump-control-probe configuration, a superposition of two independent wave packets is observed. In order to elucidate the observed experimental data, we develop a theory based on the Liouville equation for the density matrix associated with the Franck-Condon factors. Both the numerical and analytical calculations are in good agreement with our experimental results.

A. A Switching from a Sequential Transition to Quantum Beating in Atomic Rubidium Pumped by a Femtosecond Laser

1. Introduction

In temporal coherent control, a pair of ultrashort pulses with variable time delay excites atoms and molecules. In [44] the authors observed a quantum beating at 18.3 THz (55 fs) due to the simultaneous excitations of the $5D$ and $7S$ states. Felinto et al. [48] reported an observation of a beating at 2.1 THz (473 fs). In addition to this beat note on the femtosecond time scale (473 fs), they also observed the ringing on the picosecond time scale which is typical in SF [1] and explained the 2.1 THz beating in terms of quantum interference [47]. The frequency 2.1 THz is the difference between sequential transitions. This process involves excitation of the $5P_{3/2}$ intermediate state by the broadband pulses [44, 48, 49]. On the other hand, however, a splitting of the Rb doublet line ($5P_{3/2}$ and $5P_{1/2}$) is 7.12 THz (140 fs). In the case of broadband input pulses, the $5P_{1/2}$ state can also be excited, and one should not oversimplify by neglecting the effect caused by this state on a femtosecond time scale less than 140 fs.

In this work, we experimentally explore the two-photon transitions which are unambiguously influenced by both the $5P_{3/2}$ and $5P_{1/2}$ intermediate states in Rb atoms. As considered in [44, 48, 49], the Rb atoms are excited to the $5D$ state

from the $5S$ ground state by a pair of collinear ultrashort pulses with variable time delay. The population dynamics of the $5D$ state is superimposed onto the intensity of the signal at 420 nm on the transition $6P - 5S$. Similarly as in [44, 48], we measure the forward propagating SF at 420 nm [42, 103], see also Chapter IV. In our experiment, the center wavelength of the input laser is tuned to control the population dynamics of the Rb atom, and the beating at different frequencies, presumably due to various types of two-photon excitations, is observed. A simple atom-field interaction theory is developed to provide an analytical solution which qualitatively explains the experimental results.

2. Experiment

A schematic diagram of the experiment is presented in Fig. 26(a). Laser pulses with

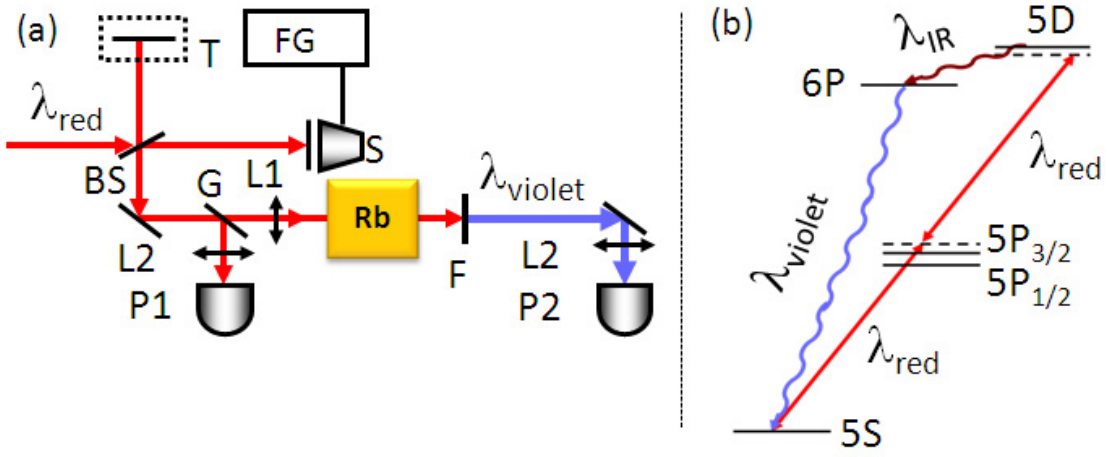

Fig. 26. (a) Schematic diagram. BS: beamsplitter, T: translation stage, S: scanning mirror, FG: function generator, G: glass plate, L1 (20 cm) and L2 (5 cm) lenses, F: short wavelength pass filter, P1 and P2: photodiodes. (b) A Rb energy level scheme.

a center wavelength λ_{in} were produced by the OPA. The center wavelength of the input laser, λ_{in}, was tuned from 770 nm to 795 nm. The FWHM (full width at half maximum) of the spectrum of the input beam was approximately 20 nm. The beam size of the input light (λ_{in}) was 2.5 mm, while at the focal plane it was about 50 μm. The Michelson interferometer allowed us to control the time delay between two input collinear pulses. The position of a mirror (attached to a loud-speaker) was controlled by a function generator. This mirror travels about 54 μm per Volt. The amplitudes of the function generator were 10 V (long range) and 1 V (short range). The frequency of the function generator, and hence the scanning rate, was either 0.02 or 0.5 Hz. The Rb cell had approximately 10^{15} Rb atoms per cm^3 at a temperature of about 200 C. The response time of the commercially available photodiodes (OPT101,Thorlabs) was increased to 0.5 ms; this time-integrated detection scheme provides a much better signal to noise ratio. A digital storage oscilloscope (Tektronix) displayed and recorded the signals. A Rb atomic energy level scheme is shown in Fig. 26(b). A two-photon pumping promotes the atoms into the $5D$ state from the $5S$ ground state. The excited atoms emit SF in both the upper ($5D$ – $6P$) and lower ($6P$–$5S$) transitions. The SF at 5 μm in the upper transition was measured by using a special dichroic mirror and IR detector (Vigo) which are not shown in Fig. 26(a). Under the present experimental conditions, the measured results for both the SF at 420 nm and 5 μm were alike and in agreement with expected temporal behavior. However, the signal to noise ratio for the SF at 420 nm was much better compared to that for the SF at 5 μm. Therefore, the present experiment was designed for the SF at 420 nm. The beam power, 1 mW, was measured after the beamsplitter. The recorded data measured by photodiode P1 were processed to represent a signal as a function of time delay between two input pulses. A loud-speaker scan within short range with a scan period of 50 s (0.02 Hz) provided visible interference fringes. For example, for $\lambda_{in} = 785$ nm, the FFT (fast

Fourier transform) of the data exhibits a sharp peak at 380 THz that correspond to an oscillation period of 2.6 fs (see an inset of Fig. 27(a)). This is consistent with $\lambda_{in}/c = 2.6$ fs, where c is the speed of light. In a long range scan with a scan period of 2 s (0.5 Hz), the FWHM of an envelope of interference fringes, i.e., a region where two pulses overlap in time (see Fig. 27(a)), was about 138 fs. Assuming a transform-limited Gaussian pulse shape, this corresponds to the pulse width of about 100 fs. The pulse width was also measured by a commercial autocorrelator (PulseCheck) to be less than 130 fs. The data for the 420 nm light were recorded by photodiode P2.

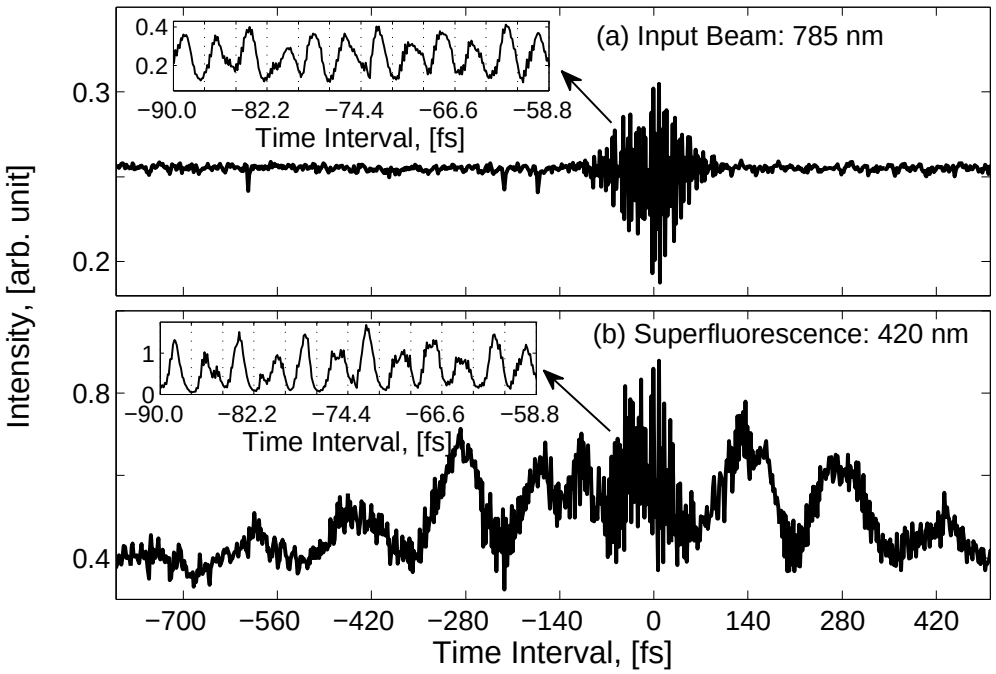

Fig. 27. The data scanned on a large time interval for the input 785 nm (a) and generated 420 nm (b) light as functions of delay time between input pulses. The data scanned on a small time interval are shown in insets.

In an inset of Fig. 27(b), the data were scanned in a short range. The FFT resulted

in the same peak at 380 THz which corresponds to optical interference fringes with a period of 2.6 fs. We observed a partial indication of a fast oscillation with a period approximately 1 fs in a certain region of the recorded data. It is worth to note that the lack of clear observations of the quantum interference [47] with a period 1.3 fs was due to a scan period limiting a higher resolution in the measurement. In a long range scan, the data clearly exhibited a beating. The detailed experimental study of this beating will be discussed in Part 4.

3. Theoretical Model

In this part, we adopt a simplified theoretical model to fit the present experiment. Let us denote atomic states as $|a\rangle$ (the $5D$ excited state), $|b_1\rangle$ (the Rb D_2 line, $5P_{3/2}$), $|b_2\rangle$ (the Rb D_1 line, $5P_{1/2}$) and $|c\rangle$ (the $5S$ ground state). In the interaction picture, the Hamiltonian for this system is written as [23]

$$\begin{aligned} V(t) &= -\hbar\Omega\{\mathrm{e}^{i(\omega_{ac}-\nu_{in}-\omega_{b_1c})t}|a\rangle\langle b_1| + \mathrm{e}^{i(\omega_{ac}-\nu_{in}-\omega_{b_2c})t}|a\rangle\langle b_2| \\ &+ \mathrm{e}^{i(\omega_{b_1c}-\nu_{in})t}|b_1\rangle\langle c| + \mathrm{e}^{i(\omega_{b_2c}-\nu_{in})t}|b_2\rangle\langle c|\} + \mathrm{h.c.},, \end{aligned} \tag{5.1}$$

where ω_{ij} is the transition frequency between the ith and jth atomic states; ν_{in} is the center frequency of the input beam. The Schrödinger equation is given by

$$\frac{\partial}{\partial t}|\Psi_I(t)\rangle = -\frac{i}{\hbar}V(t)|\Psi_I(t)\rangle, \tag{5.2}$$

where $|\Psi_I(t)\rangle$ is a superposition of atomic states $|\Psi_I(t)\rangle = a|a\rangle + b_1|b_1\rangle + b_2|b_2\rangle + c|c\rangle$ with probability amplitudes a, b_1, b_2 and c. Note that the SF emission is much faster than spontaneous emissions and dephasing of atomic coherence. Thus incoherent processes are discarded in this case. In order to find an analytical solution for $|a|^2$ as a function of τ, which is an interval between arrival times of two input pulses, we consider the following assumptions. (i) The atoms are instantaneously excited by the

input pulses. Thus, the input pulses are written in terms of δ-functions as $\Omega(t) = \delta(t) + \delta(t+\tau)\exp(-i\nu_{in}\tau)$. (ii) We assume that $|a|,\ |b_1|,\ |b_2| \ll |c| \sim 1$. (iii) The input pulse spectrum is given by a Gaussian function $A(\lambda) = \exp[-(\lambda_c - \lambda)^2/\Delta\lambda^2]$, where λ_c and $\Delta\lambda$ are the center wavelength of the input beam and its spectral width, respectively. We denote the spectral Gaussian weights for D-lines as $A_1 = A(\lambda = 780)$ and $A_2 = A(\lambda = 795)$. (iv) The population $|a|^2$ eventually decays with a rate defined by the duration of the SF pulse. This is included in the solution as $|a|^2 \rightarrow [\exp(-\tau^2/\tau_{SF}^2) + C]|a|^2$, where τ_{SF} is the temporal duration of the SF pulse and C is a constant associated with non-zero background due to fluorescence. At this stage, we also neglect the SF ringing. The 420 nm SF ringing was observed and discussed in Chapter IV. (v) The fast oscillating terms are neglected. Under these assumptions, an analytic solution is obtained to be

$$\begin{aligned} |a|^2 &\approx \mathcal{N}(\mathrm{e}^{-\tau^2/\tau_{SF}^2} + C)[2A_1^2 + 2A_2^2 + 2A_1A_2 \\ &+ A_1^2\cos\Delta_1\tau + A_2^2\cos\Delta_2\tau + 2A_1A_2(\cos\Delta_0\tau + \cos\Delta_3\tau)], \end{aligned} \tag{5.3}$$

where $\mathcal{N}$ is a normalization coefficient. A Rb 5P state splitting is denoted by $\Delta_0 = \omega_{b_1c} - \omega_{b_2c}$, and the parameters related to sequential transitions are defined as $\Delta_1 = \omega_{ab_1} - \omega_{b_1c}$, $\Delta_2 = \omega_{ab_2} - \omega_{b_2c} \equiv \Delta_1 + 2\Delta_0$ and $\Delta_3 = \omega_{ab_1} - \omega_{b_2c} \equiv \omega_{ab_2} - \omega_{b_1c} \equiv \Delta_1 + \Delta_0$. The two-photon transitions associated with Δ_i $(i = 0, 1, 2, 3)$ are sketched in Fig. 28. In particular, a process depicted in Fig. 28(i) was observed by Felinto et al. in [48]. The similar sequential transition, however, for the lower intermediate level $|b_2\rangle$ as in Fig. 28(ii), has not yet been observed experimentally. It is interesting to note that there is a new process that can be realized if the broadband input pulses are used (see Fig. 28(iii) and (iv)). Fig. 28(v) demonstrates a quantum beating.

The FFT of $|a|^2$ (without a slow time-varying amplitude) displays four peaks at

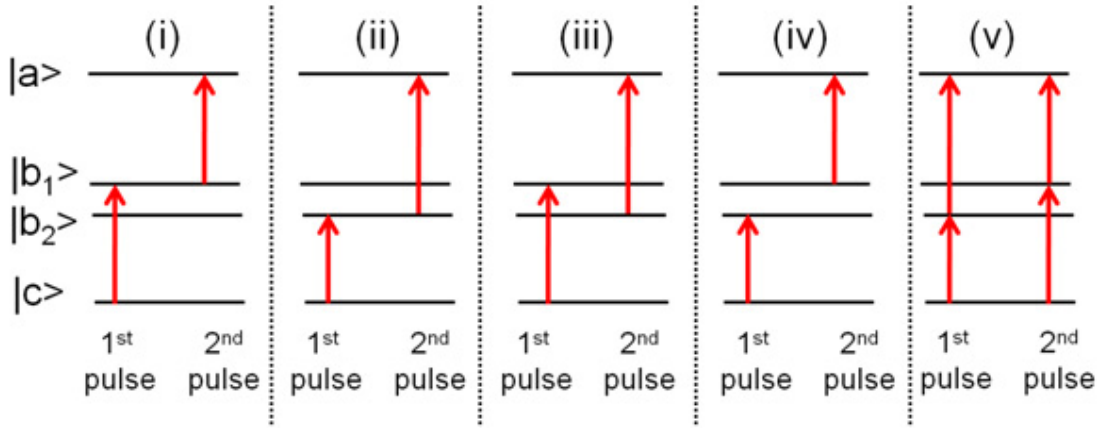

Fig. 28. Diagrams for Two-Photon Transitions. Two-photon transitions are associated with parameters such as (i) $\Delta_1 = \omega_{ab_1} - \omega_{b_1c}$; (ii) $\Delta_2 = \omega_{ab_2} - \omega_{b_2c}$; (iii) and (iv) $\Delta_3 = \omega_{ab_2} - \omega_{b_1c} = \omega_{ab_1} - \omega_{b_2c}$; and (v) $\Delta_0 = \omega_{b_1c} - \omega_{b_2c}$.

Δ_i. The magnitude of each peak depends on the weights A_1 and A_2. Therefore one can control a beating by tuning the wavelength of the input laser, λ_{in}.

4. Discussions

The main results are shown in Fig. 29. In the left column of Fig. 29, the 420 nm signal is displayed (solid curves) for three different input laser center-wavelengths which are (a) 770 nm, (b) 785 nm and (c) 795 nm. In the insets, input spectra are compared with the Rb D_1 (795 nm) and D_2 (780 nm) lines. In the right column of Fig. 29, the normalized population of the excited state $|a|^2$ in Eq.(5.3) is revealed as a function of time delay τ. The parameters used here are $\Delta_0 = 1$, $\Delta_1 = 0.27$, $\Delta\lambda = 12$, $\tau_{SF} = 20$ and $C = 0.1$. Before taking the FFT from the observed data, we subtract the slow varying envelope. This can be done with the help of adjacent averaging smoothing up to 100 points. The obtained FFTs are shown in the left column of Fig. 30. The Fourier analysis shows a broad peak about 2 THz in Fig. 30(a). This

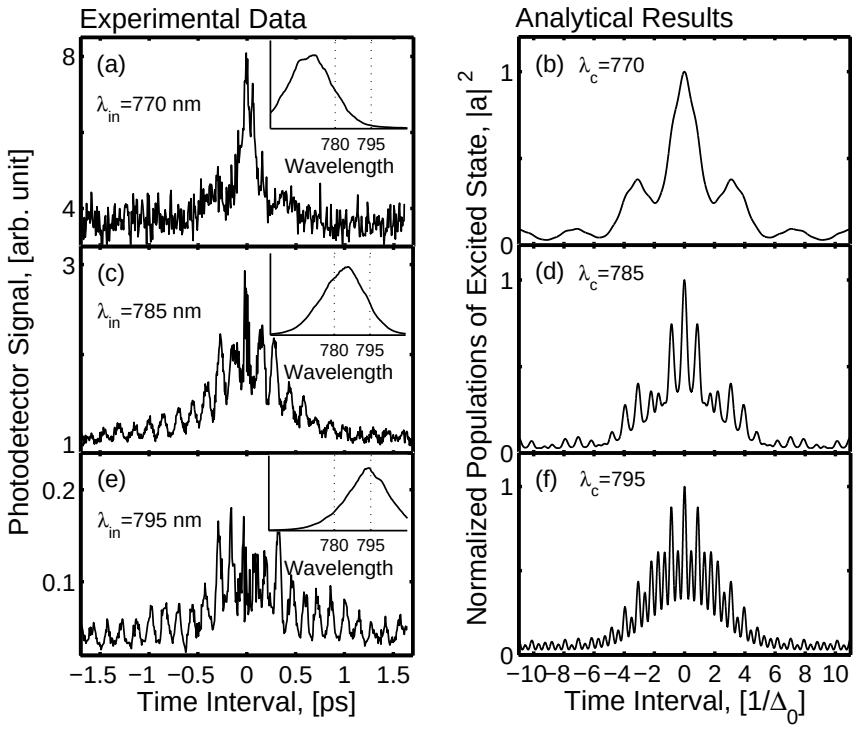

Fig. 29. (Left column): The SF at 420 nm was recorded for three different input laser center-wavelengths, λ_{in} = 770 nm (a), 785 nm (c) and 795 nm (e). Each data-curve is averaged over 8 samples. The scan period was 50 s. The actual spectra of the input lasers are shown in the insets. (Right column): The analytical results are presented for three different input parameters, $\lambda_c = 770$ (b), 785 (d) and 795 (e).

is consistent with an observation of a quantum beat at 2.1 THz (473 fs) in [48]. We did not clearly distinguish a beat frequency of 18.3 THz (55 fs) as reported in [44], although the fast "noisy" oscillations in Fig. 29(a) may be indicative of this signal. A slower scan may be able to resolve this signal. Furthermore, at this center wavelength the $7S$ state can also be excited along with the $5D$ state resulting in an additional contribution to the magnitude of the 420 nm signal compared to the rest of the data. In Fig. 30(c,e) a peak at 7.12 THz confirms that the time period is 140 fs, which is due

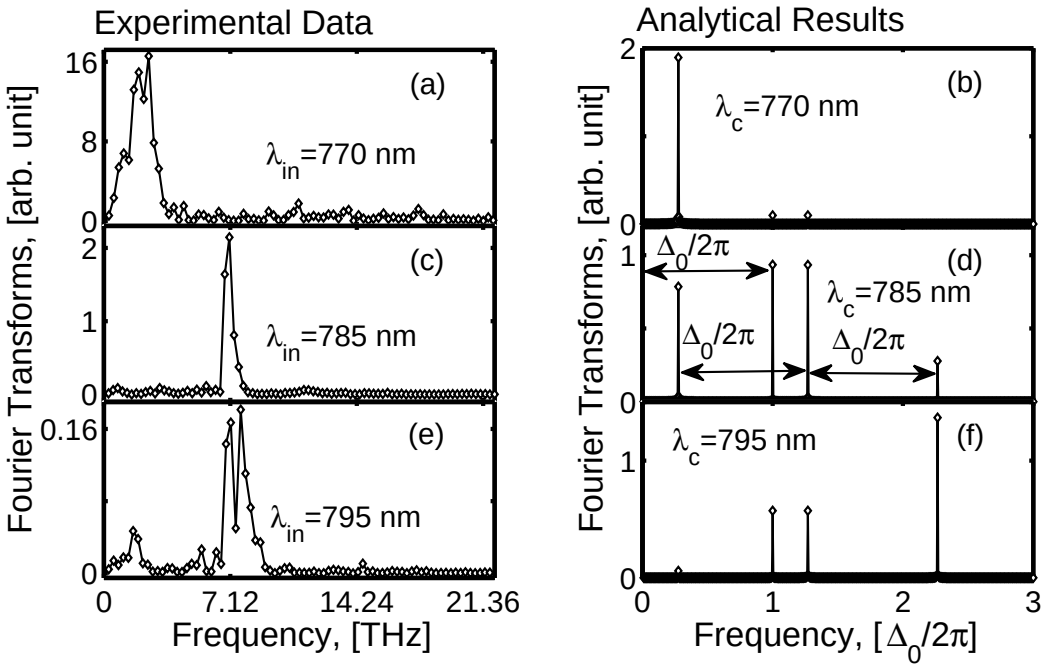

Fig. 30. The FFTs of the corresponding experimental and theoretical results from Fig. 29.

to two excitation channels, $5S \rightarrow 5P_{3/2} \rightarrow 5D$ and $5S \rightarrow 5P_{1/2} \rightarrow 5D$. The quantum beating at this frequency was measured in an atomic pump-probe experiment [104]. In Fig. 30(e), we observed another peak next to 7.12 THz. This peak was qualitatively predicted by the analytical results as one of four peaks suggested by the analytical solution, see Fig. 30(b,d,f). As mentioned earlier, the positions (frequencies) of these peaks are independent of input laser wavelength while the magnitude of the peaks depends on the wavelength of the input laser. The peak at frequency Δ_1 dominates for $\lambda_c = 770$ (see Fig. 30(b)). All four peaks comparable in Fig. 30(d). However, the corresponding experimental data shows only one peak at 7.12 THz. In this case, a

quantum beating due to two different excitations dominates. Fig. 30(f) demonstrates that the second and third peaks at frequencies Δ_0 and Δ_3 are much more visible than others. In our experiment we did not observe the high frequency component (the fourth peak); the signal may have been washed out as a result of scan period used. Finally in Fig. 31, the experimental and analytical results for $\lambda_{in} = 790$ nm

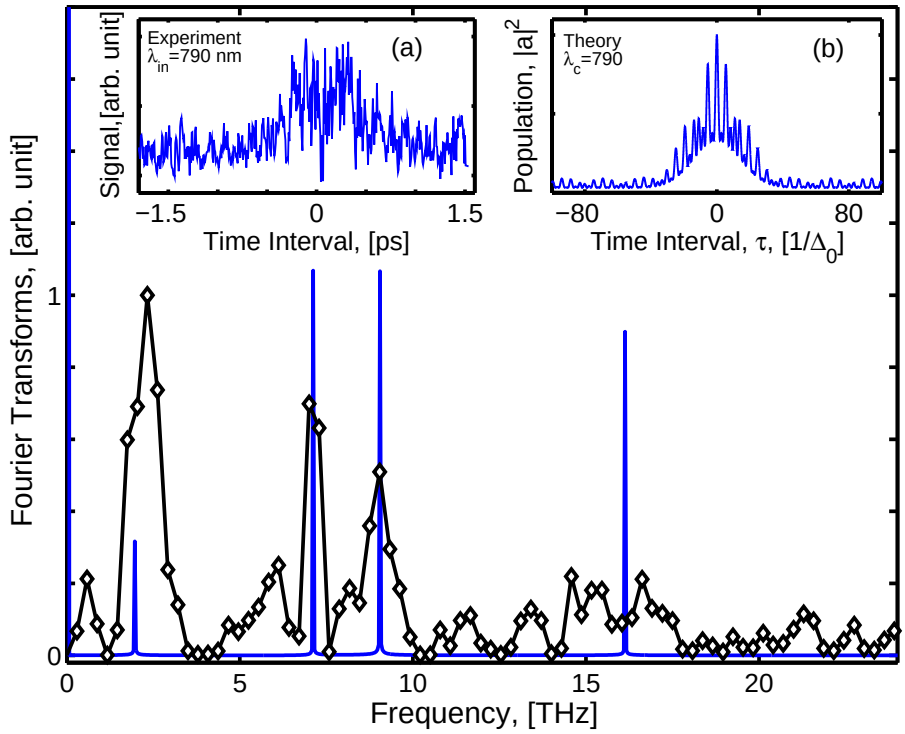

Fig. 31. The FFTs of the recorded SF at 420 nm (curve with diamonds) and an analytical result (solid curve). The 420 nm data without averaging and the corresponding analytical result are shown in insets (a) and (b), respectively. The input center-wavelength of the laser λ_{in} is 790 nm and input parameter λ_c is 790. For the analytical FFT result, the x-axis is scaled by 7.12 THz.

and $\lambda_c = 790$ are compared. In this particular case, the experiment and theory are in better quantitative agreement.

5. Conclusion

We demonstrated a temporal coherent control in two-photon transitions by tuning the input laser wavelength. A pair of broadband, collinear pulses with variable time delay was used to excite rubidium atoms to the $5D$ state from the $5S$ ground state where two-photon transitions were influenced by the intermediate levels $5P_{1/2}$ and $5P_{3/2}$. After the laser excitation the atoms emit 5 μm and 420 nm light on the transitions $5D-6P$ and $6P-5S$, respectively. The SF at 420 nm was monitored rather than the SF at 5 μm because of its better signal-to-noise ratio. The time-integrated 420 nm signal exhibited a beating when the time delay of the input pulses was varied. It was observed that a beating at the frequency given by the difference between the sequential transitions via the $5P_{1/2}$ state switches to a beating at the frequency given by the difference between the Rb D-lines depending on the input laser wavelength. The appropriate theoretical model was developed. The beat frequencies predicted by the analytical solution were in qualitative agreement with the Fourier transforms taken from the experimental data.

We believe the present study can be applied in fast information communications. For instance, the possibility of rapid inspection of quantum interference using the temporal characteristics of the coherent emissions of multiple atoms [105] could be of great interest.

B. Femtosecond Wave-Packet Dynamics in Cesium Dimers Studied through Controlled Stimulated Emission

1. Introduction

In this work, we present an all-optical alternative to the conventional photoionizing detection scheme [60, 61, 62] to monitor the fs wave packet dynamics. Namely the

Λ-type configuration for energy levels is considered. That is, after the pump pulse creates the wave packet in the excited electronic state, the probe pulse stimulates this excitation down to some vibrational levels in the ground state. We use this method to visualize wave packet time evolution in $B\ ^1\Pi_u$ state in Cs_2, as is reported briefly in [106]. Furthermore, we extend it to the pump-control-probe case by adding a control pulse. Instead of collinear setup as in [67, 68], we use non-collinear beam geometry in both the femtosecond pump-probe and pump-control-probe experiments. It does not require sub-femtosecond stabilization of the time delay between the pump and control pulses and allows for straightforward spatial filtering of the probe beam. To explain the observed results, we develop a detailed theoretical model based on the time dependent density matrix equations with the Franck-Condon factors. Both numerical simulations and analytical calculations for transmission of the probe pulse are presented. These results are compared with experimental data.

The organization of the present part of this chapter is as follows. The pump-probe and pump-control-probe experimental setup is discussed in Part 2. In Part 3, a theoretical model based on Λ-type system is presented and an analytical solution is obtained for the absorption of the fs probe pulse assuming the pump and control excitations are independent of each other. The experimental and corresponding theoretical results on the wave packet dynamics are discussed in detail in Part 4. The results are summarized in Part 5.

2. Experimental Setup

The experiments are performed using the femtosecond laser system and the OPA. The beam geometry at the sample and the signal acquisition arm are outlined schematically in Fig. 32. Briefly, the output of the regenerative amplifier is split into two uneven parts. The smaller fraction is used as a probe. The other part pumps the

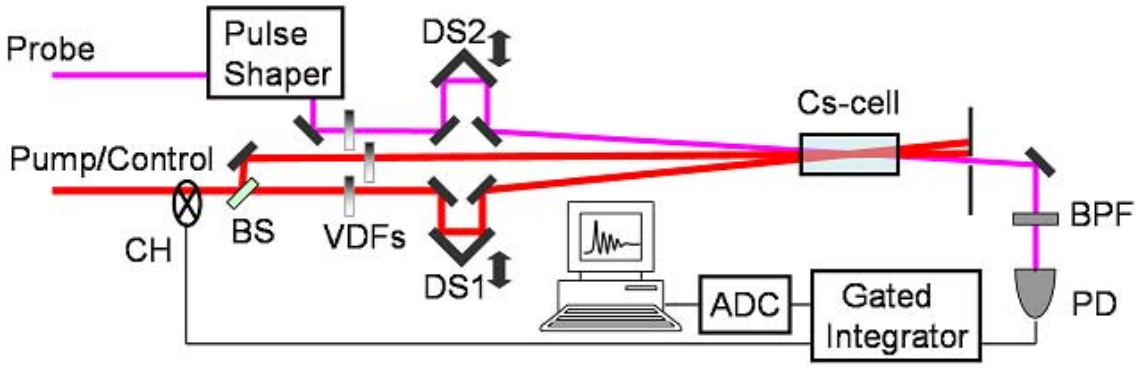

Fig. 32. Experimental setup layout. CH: chopper; BS: beam splitter; VDF: variable neutral density filter; DS1,2: delay stages; BPF: variable bandpass filter such as a spectrometer with an adjustable exit slit; PD: photodiode; ADC: analog–to-digital converter.

OPA, which produces pulses at 760 nm with the spectral full-width-at-half-maximum (FWHM) of $\sim$ 12 nm. The 760 nm beam is further split into two even fractions for the pump and control delay lines. The probe pulse spectrum is centered at 805 nm and has FWHM of 31 nm. To ensure delivery of the transform-limited probe pulses at the sample, the probe beam passes through a pulse shaper, aided with the multiphoton intrapulse interference phase scan (MIIPS) algorithm that corrects for pulse phase distortions [107]. The pump and control pulse energies are $\sim$ 1 μJ (1 mW average power in each beam). The probe pulse energy is at least 10-fold lower but is varied from one experiment to another to provide similar photon flux at the photodetector in the acquisition arm. The three collimated but non-collinear beams are overlapped in a 3-inch-long cesium cell, crossing under small angles ($\sim 1^\circ$) to each other. Their $1/e^2$-diameters, estimated by the knife edge method, are about 3 mm and 2.5 mm for the pump/control and probe beams, respectively. The pump (and control) pulses induce Cs_2 vibrations (wave packets) in the excited $B\ ^1\Pi_u$ state, and

the probe pulses read out the wave-packet evolution by promoting excited molecules back into the ground $X\ ^1\Sigma_g^+$ state. After the Cs-cell, the probe beam is spatially and spectrally filtered and focused at a photodiode (DET-210, Thorlabs). For most of the experiments, only a small part of the full probe bandwidth reaches the detector. The signal from the photodiode is averaged by Gated Integrator (SR250, Stanford Research Systems). To retrieve the contribution due to the pump and/or control fields, we chop the pump/control beam at the half of the laser repetition rate (i.e., $\sim$ 500 Hz) and subtract every other acquired shot. The resulting signal is digitized and recorded as a function of the probe pulse delay. It reflects the change in the transmitted energy of the probe pulse due to the motion of molecular wave packets. The cell is heated up to 240-250 °C with the temperature variation below 1 °C for each particular measurement. These temperatures correspond to 1.2-1.9 mTorr pressure of Cs dimers or their density of (2.3-3.6)$\times 10^{13}$ cm^{-3} [108]. We estimate the interaction volume of the order of 0.1 cm^3, i.e., $\sim 10^{12}$ of contributing Cs_2 molecules.

3. Theoretical Model

First, we present the theoretical model of the pump-probe measurements. To calculate the absorption of the probe pulse in the pump-probe measurements, we choose a four-level system in which levels $|b\rangle$ and $|c\rangle$ are two vibrational levels in the ground state, $X\ ^1\Sigma_g^+$, and levels $|a\rangle$ and $|a'\rangle$ are two vibrational levels in the excited state, $B\ ^1\Pi_u$ (Fig. 33). The Hamiltonian of this system is

$$H = H_0 + H_I, \tag{5.4}$$

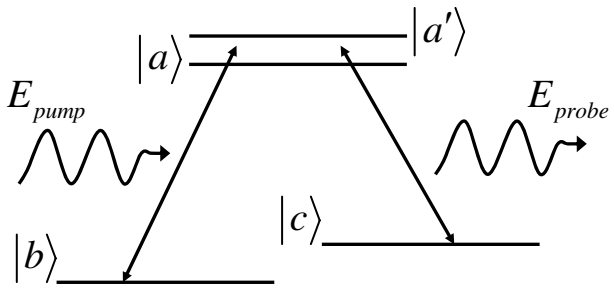

Fig. 33. Energy level diagram of a four-level system.

where the unperturbed part of the Hamiltonian, H_0, and the interaction part of the Hamiltonian, H_I, are given by

$$H_0 = \hbar\omega_a |a\rangle \langle a| + \hbar\omega_{a'} |a'\rangle \langle a'| + \hbar\omega_b |b\rangle \langle b| + \hbar\omega_c |c\rangle \langle c| , \tag{5.5}$$

$$H_I = -\left(\wp_{ab} |a\rangle \langle b| + \wp_{ac} |a\rangle \langle c| + \wp_{a'b} |a'\rangle \langle b| + \wp_{a'c} |a'\rangle \langle c| + c.c.\right) E(t) . \tag{5.6}$$

Here the vibrational level ν is displaced from the bottom of the potential well by $\hbar\omega$, which is defined as [109]

$$\hbar\omega = \hbar\omega_e(\nu + \frac{1}{2}) - \hbar\omega_e\chi_e(\nu + \frac{1}{2})^2, \tag{5.7}$$

where ω_e is the vibrational frequency and $\omega_e\chi_e$ is the vibrational anharmonicity. The electric dipole transition moment between vibrational level ν' and vibrational level ν'', $\wp_{\nu'\nu''}$, is [110]

$$\wp_{\nu'\nu''} = \mu S(\nu', \nu'') , \tag{5.8}$$

where μ is the electronic transition moment. It is assumed to be constant, since the displacement of the nuclei from their equilibrium is relatively small (even at temperatures of 240-250 °C); the (smooth) R-dependence of the electronic matrix elements

would provide higher-order corrections to our results. $S(\nu', \nu'') = \int \psi^*_{\nu'}(R)\, \psi_{\nu''}(R)\, d\tau_N$ is the overlap integral between the two vibrational states $\psi_{\nu'}$ and $\psi_{\nu''}$ in their respective electronic states. Here, R is the internuclear distance and $d\tau_N$ is the element of volume of the space of the nuclear coordinates [111]. So $|S(\nu', \nu'')|^2$ is the Franck-Condon factor. The electronic transition between levels $|a\rangle$ and $|b\rangle$ and that between levels $|a'\rangle$ and $|b\rangle$ are near resonant with the frequency of the pump pulse. Also the electronic transition between levels $|a\rangle$ and $|c\rangle$ and that between levels $|a'\rangle$ and $|c\rangle$ are near resonant with the frequency of the probe pulse. After calculating the absorption of the probe pulse in this four-level system, vibrational levels in the ground and excited states are re-chosen and the calculations are repeated for another set of vibrational levels. The total absorption of the probe pulse is defined as a sum over all possible absorption (emission) paths for such four-level configurations. Because of the large relaxation time of cesium dimer ($\sim$ 1 ns), the equation of motion for the density matrix is [23]

$$\dot{\rho} = -\frac{i}{\hbar}[H, \rho]. \tag{5.9}$$

Since the durations of the pump pulse and the probe pulse ($<$ 100 fs) are much smaller than the time delay of the probe pulse ($>$ 1 ps), we can calculate the corresponding molecular polarizations induced by them separately. Let us consider individual radiation field modes, $E_i(t) = E_i^0 \cos(\nu_i t + \varphi_i)$, where $i = p$ for the pump and $i = pr$ for the probe, and do the Rotation-Wave-Approximation (RWA)

$$\rho_{ab} = \tilde{\rho}_{ab} e^{-i\nu_i t - i\varphi_i}, \tag{5.10}$$

$$\rho_{ac} = \tilde{\rho}_{ac} e^{-i\nu_i t - i\varphi_i}, \tag{5.11}$$

$$\rho_{a'b} = \tilde{\rho}_{a'b} e^{-i\nu_i t - i\varphi_i}, \tag{5.12}$$

$$\rho_{a'c} = \tilde{\rho}_{a'c} e^{-i\nu_i t - i\varphi_i}. \tag{5.13}$$

We can write down the density matrix elements explicitly as

$$\dot{\tilde{\rho}}_{ab} = -i\left(\omega_{ab} - \nu_i\right)\tilde{\rho}_{ab} - \frac{i}{\hbar}\frac{\wp_{ab}E_i^0}{2}\left(\rho_{aa} - \rho_{bb}\right) + \frac{i}{\hbar}\frac{\wp_{ac}E_i^0}{2}\rho_{cb} - \frac{i}{\hbar}\frac{\wp_{a'b}E_i^0}{2}\rho_{aa'}, \tag{5.14}$$

$$\dot{\tilde{\rho}}_{ac} = -i\left(\omega_{ac} - \nu_i\right)\tilde{\rho}_{ac} - \frac{i}{\hbar}\frac{\wp_{ac}E_i^0}{2}\left(\rho_{aa} - \rho_{cc}\right) + \frac{i}{\hbar}\frac{\wp_{ab}E_i^0}{2}\rho_{bc} - \frac{i}{\hbar}\frac{\wp_{a'c}E_i^0}{2}\rho_{aa'}, \tag{5.15}$$

$$\dot{\tilde{\rho}}_{a'b} = -i\left(\omega_{a'b} - \nu_i\right)\tilde{\rho}_{a'b} - \frac{i}{\hbar}\frac{\wp_{a'b}E_i^0}{2}\left(\rho_{a'a'} - \rho_{bb}\right) + \frac{i}{\hbar}\frac{\wp_{a'c}E_i^0}{2}\rho_{cb} - \frac{i}{\hbar}\frac{\wp_{ab}E_i^0}{2}\rho_{a'a}, \tag{5.16}$$

$$\dot{\tilde{\rho}}_{a'c} = -i\left(\omega_{a'c} - \nu_i\right)\tilde{\rho}_{a'c} - \frac{i}{\hbar}\frac{\wp_{a'c}E_i^0}{2}\left(\rho_{a'a'} - \rho_{cc}\right) + \frac{i}{\hbar}\frac{\wp_{a'b}E_i^0}{2}\rho_{bc} - \frac{i}{\hbar}\frac{\wp_{ac}E_i^0}{2}\rho_{a'a}, \tag{5.17}$$

$$\dot{\rho}_{bc} = i\omega_{cb}\rho_{bc} + \frac{i}{\hbar}\frac{\wp_{ba}E_i^0}{2}\tilde{\rho}_{ac} + \frac{i}{\hbar}\frac{\wp_{ba'}E_i^0}{2}\tilde{\rho}_{a'c} - \frac{i}{\hbar}\frac{\wp_{ac}E_i^0}{2}\tilde{\rho}_{ba} - \frac{i}{\hbar}\frac{\wp_{a'c}E_i^0}{2}\tilde{\rho}_{ba'}, \tag{5.18}$$

$$\dot{\rho}_{aa'} = i\omega_{a'a}\rho_{aa'} + \frac{i}{\hbar}\frac{\wp_{ab}E_i^0}{2}\tilde{\rho}_{ba'} + \frac{i}{\hbar}\frac{\wp_{ac}E_i^0}{2}\tilde{\rho}_{ca'} - \frac{i}{\hbar}\frac{\wp_{ba'}E_i^0}{2}\tilde{\rho}_{ab} - \frac{i}{\hbar}\frac{\wp_{ca'}E_i^0}{2}\tilde{\rho}_{ac}, \tag{5.19}$$

$$\dot{\rho}_{aa} = \frac{i}{\hbar}\left(\frac{\wp_{ab}E_i^0}{2}\tilde{\rho}_{ba} + \frac{\wp_{ac}E_i^0}{2}\tilde{\rho}_{ca} - \frac{\wp_{ba}E_i^0}{2}\tilde{\rho}_{ab} - \frac{\wp_{ca}E_i^0}{2}\tilde{\rho}_{ac}\right), \tag{5.20}$$

$$\dot{\rho}_{bb} = \frac{i}{\hbar}\left(\frac{\wp_{ba}E_i^0}{2}\tilde{\rho}_{ab} + \frac{\wp_{ba'}E_i^0}{2}\tilde{\rho}_{a'b} - \frac{\wp_{ab}E_i^0}{2}\tilde{\rho}_{ba} - \frac{\wp_{a'b}E_i^0}{2}\tilde{\rho}_{ba'}\right), \tag{5.21}$$

$$\dot{\rho}_{cc} = \frac{i}{\hbar}\left(\frac{\wp_{ca}E_i^0}{2}\tilde{\rho}_{ac} + \frac{\wp_{ca'}E_i^0}{2}\tilde{\rho}_{a'c} - \frac{\wp_{ac}E_i^0}{2}\tilde{\rho}_{ca} - \frac{\wp_{a'c}E_i^0}{2}\tilde{\rho}_{ca'}\right), \tag{5.22}$$

$$\dot{\rho}_{a'a'} = \frac{i}{\hbar}\left(\frac{\wp_{a'b}E_i^0}{2}\tilde{\rho}_{ba'} + \frac{\wp_{a'c}E_i^0}{2}\tilde{\rho}_{ca'} - \frac{\wp_{ba'}E_i^0}{2}\tilde{\rho}_{a'b} - \frac{\wp_{ca'}E_i^0}{2}\tilde{\rho}_{a'c}\right). \tag{5.23}$$

The general equation for the absorption of this field is [73]

$$Q = \int \dot{\mathcal{P}} E dt = \int (\wp_{ab}\dot{\rho}_{ba} + \wp_{ac}\dot{\rho}_{ca} + \wp_{a'b}\dot{\rho}_{ba'} + \wp_{a'c}\dot{\rho}_{ca'} + c.c.) E_i(t)\, dt. \quad (5.24)$$

After RWA and using the approximation $\dot{\tilde{\rho}} << \nu_{pr}\tilde{\rho}$, this absorption equation will turn to

$$Q = 2\mathrm{Im} \int \nu_{pr} \left(\frac{\wp_{ba}E^0_{pr}}{2}\tilde{\rho}_{ab} + \frac{\wp_{ca}E^0_{pr}}{2}\tilde{\rho}_{ac} + \frac{\wp_{ba'}E^0_{pr}}{2}\tilde{\rho}_{a'b} + \frac{\wp_{ca'}E^0_{pr}}{2}\tilde{\rho}_{a'c} \right) dt. \quad (5.25)$$

Therefore, the density matrix elements can be found when the pump pulse with frequency ν_p and phase φ_p comes in first if we use the Eqs. (5.14) to (5.23). Then these results can be the initial conditions for the calculation when the probe pulse with frequency ν_{pr} and phase φ_{pr} comes in with the time delay Δt. Validity of this assumption rests on the fact that the decay time scale of Cs_2 is too long ($\sim$ 1 ns) compared to the probe delay time Δt. Matrix elements can be found with the Eqs. (5.14) to (5.23). The absorption can also be found by the Eq. (5.25) with the time delay. We have to average over all possible phases because of the non-collinear beam geometry. Pulses do not co-propagate in our experiments. Even if the phase of each pulse is stable, it is still different in different parts of the sample. Therefore, we should average our results of absorption with different phases in each pairs of pulses to obtain our final numerical result.

Let us consider how to find the analytical solution. First, we consider one pump pulse coming at time $t = 0$ with the Gaussian pulse shape, $E_p(t) = E^0_p \cos(\nu_p t + \varphi_p)$, where $E^0_p = \varepsilon_p e^{-1/2(t/\Delta\tau_p)^2}$. Since $\rho_{bb} \approx \rho^0_{bb} \gg \rho_{aa}$, ρ_{cb}, and $\rho_{aa'}$ where ρ^0_{bb} is the initial condition, Eq. (5.14) can be approximated with

$$\dot{\tilde{\rho}}_{ab} \approx -i(\omega_{ab} - \nu_p)\tilde{\rho}_{ab} + \frac{i}{\hbar}\frac{\wp_{ab}E^0_p}{2}\rho^0_{bb}. \quad (5.26)$$

This equation with the first-order approximation can be solved easily and giving the

result as

$$\tilde{\rho}_{ab}(t) = i\sqrt{2\pi}\Delta\tau_p \rho^0_{bb} \frac{\wp_{ab}\mathcal{E}_p}{2\hbar} e^{-\frac{1}{2}\Delta\tau_p^2(\omega_{ab}-\nu_p)^2} e^{-i(\omega_{ab}-\nu_p)t}. \tag{5.27}$$

Similarly, solutions for matrix elements $\tilde{\rho}_{ac}(t)$, $\tilde{\rho}_{a'b}(t)$, and $\tilde{\rho}_{a'c}(t)$ can be found. If we plug these results into Eq. (5.18) and take into account that the transitions between vibrational levels are near-resonant to the carrier frequencies of the corresponding pulses, this differential equation in the second-order approximation will give

$$\begin{aligned} \rho_{bc}(t) &\propto -\rho^0_{bb}\left[\frac{\wp_{ac}\mathcal{E}_p}{\hbar}\frac{\wp_{ba}\mathcal{E}_p}{\hbar} e^{-\frac{1}{2}\Delta\tau_p^2(\omega_{ab}-\nu_p)^2} + \frac{\wp_{a'c}\mathcal{E}_p}{\hbar}\frac{\wp_{ba'}\mathcal{E}_p}{\hbar} e^{-\frac{1}{2}\Delta\tau_p^2(\omega_{a'b}-\nu_p)^2}\right] \\ &\times e^{-\frac{1}{2}\Delta\tau_p^2\omega_{cb}^2} e^{i\omega_{cb}t}. \end{aligned} \tag{5.28}$$

Similarly, the coherent element $\rho_{aa'}$ is

$$\begin{aligned} \rho_{aa'}(t) &\propto \rho^0_{bb}\left[\frac{\wp_{ab}\mathcal{E}_p}{\hbar}\frac{\wp_{ba'}\mathcal{E}_p}{\hbar} e^{-\frac{1}{2}\Delta\tau_p^2(\omega_{a'b}-\nu_p)^2} + \frac{\wp_{ba'}\mathcal{E}_p}{\hbar}\frac{\wp_{ab}\mathcal{E}_p}{\hbar} e^{-\frac{1}{2}\Delta\tau_p^2(\omega_{ab}-\nu_p)^2}\right] \\ &\times e^{-\frac{1}{2}\Delta\tau_p^2\omega_{a'a}^2} e^{i\omega_{a'a}t}. \end{aligned} \tag{5.29}$$

Next, let us consider that the probe pulse, $E_{pr}(t) = E^0_{pr}\cos(\nu_{pr}t + \varphi_{pr})$, comes at $t = \Delta t$. Here, $E^0_{pr} = \varepsilon_{pr} e^{-\frac{1}{2}\left(\frac{t-\Delta t}{\Delta\tau_{pr}}\right)^2}$. With the results for the density matrix elements ρ_{bc} and $\rho_{aa'}$ (Eqs. (5.28) and (5.29)), the differential equation for $\tilde{\rho}_{ab}$ (Eq. (5.14)) can be solved as

$$\begin{aligned} \tilde{\rho}_{ab}(t) = i\sqrt{2\pi}\Delta\tau_{pr}\left[\frac{\wp_{ab}\mathcal{E}_{pr}}{2\hbar}\rho^0_{bb} + \frac{\wp_{ac}\mathcal{E}_{pr}}{2\hbar}\rho_{cb}(\Delta t) - \frac{\wp_{a'b}\mathcal{E}_{pr}}{2\hbar}\rho_{aa'}(\Delta t)\right] \\ \times e^{-\frac{1}{2}\Delta\tau_{pr}^2(\omega_{ab}-\nu_{pr})^2} e^{-i(\omega_{ab}-\nu_{pr})(t-\Delta t)}. \end{aligned} \tag{5.30}$$

Similar results can also be found for $\tilde{\rho}_{ac}(t)$, $\tilde{\rho}_{a'b}(t)$, and $\tilde{\rho}_{a'c}(t)$. We plug these results into Eq. (5.25) and neglect the constant terms. Thus, the analytical expression for the absorption of the probe pulse at delay Δt can be written as

$$Q(\Delta t) \propto \sum_{a,a',b,c}\Big[\Big(\wp_{ca}\wp_{ab}e^{-\Delta\tau_{pr}^2(\omega_{ac}-\nu_{pr})^2} + \wp_{ca'}\wp_{a'b}e^{-\Delta\tau_{pr}^2(\omega_{a'c}-\nu_{pr})^2}\Big)$$

$$\times \quad \left(\wp_{ac}\wp_{ba}e^{-\frac{1}{2}\Delta\tau_p^2(\omega_{ab}-\nu_p)^2} + \wp_{a'c}\wp_{ba'}e^{-\frac{1}{2}\Delta\tau_p^2(\omega_{a'b}-\nu_p)^2}\right) e^{-\frac{1}{2}\Delta\tau_p^2\omega_{cb}^2}\sin\left(\omega_{cb}\Delta t\right)$$

$$- \quad \left(\wp_{ca}\wp_{a'c}e^{-\Delta\tau_{pr}^2(\omega_{ac}-\nu_{pr})^2} + \wp_{ca'}\wp_{ac}e^{-\Delta\tau_{pr}^2(\omega_{a'c}-\nu_{pr})^2}\right) \tag{5.31}$$

$$\times \quad \left(\wp_{ba'}\wp_{ab}e^{-\frac{1}{2}\Delta\tau_p^2(\omega_{ab}-\nu_p)^2} + \wp_{ab}\wp_{ba'}e^{-\frac{1}{2}\Delta\tau_p^2(\omega_{a'b}-\nu_p)^2}\right) e^{-\frac{1}{2}\Delta\tau_p^2\omega_{a'a}^2}\sin\left(\omega_{a'a}\Delta t\right)\Big].$$

For study of the pump-control-probe measurements, we assume that two wave packets generated by the pump and control pulses are independent because the population is still mostly located in the ground levels and the coherent elements are relatively small when the control pulse comes in after the pump pulse. Therefore, we can calculate these two wave packets separately by using the the above mentioned pump-probe model.

4. Results and Discussions

The Franck-Condon factors, $|S(\nu', \nu'')|^2$, can be found by using the exact eigen wave-function for the Morse Potential [112]. Figure 34 shows the calculated absolute value of the overlap integral between one vibrational state in the ground state $X\ ^1\Sigma_g^+$ and that in the excited state $B\ ^1\Pi_u$ in cesium dimer, $|S(\nu', \nu'')|$. The (ν', ν'') transitions for which $\nu' \sim \nu'' + 3$ are coupled by the pump field and have the largest Franck-Condon factors. While the (ν', ν'') transitions for which $\nu'' \sim \nu' + 15$ are coupled by the probe field and still have the large Franck-Condon factors. The parameters used in the theoretical calculations are chosen from those in the experiments. The initial conditions for the density matrix elements are all $\rho_{ij}^0 = 0$ except that $\rho_{bb}^0 = \hbar\omega_b/k_BT$ and $\rho_{cc}^0 = \hbar\omega_b/k_BT$ with $k_BT \sim 356\ \text{cm}^{-1}$. Fig. 35 shows the experimental result for the pump-probe measurements. The probe pulse transmission is plotted as a function of its time delay relative to the pump pulse. The corresponding FFT spectra are given on the right panel. The same signal is recorded for spectral acquisition windows of variable width and exhibits different dephasing rates. In particular, the dephasing

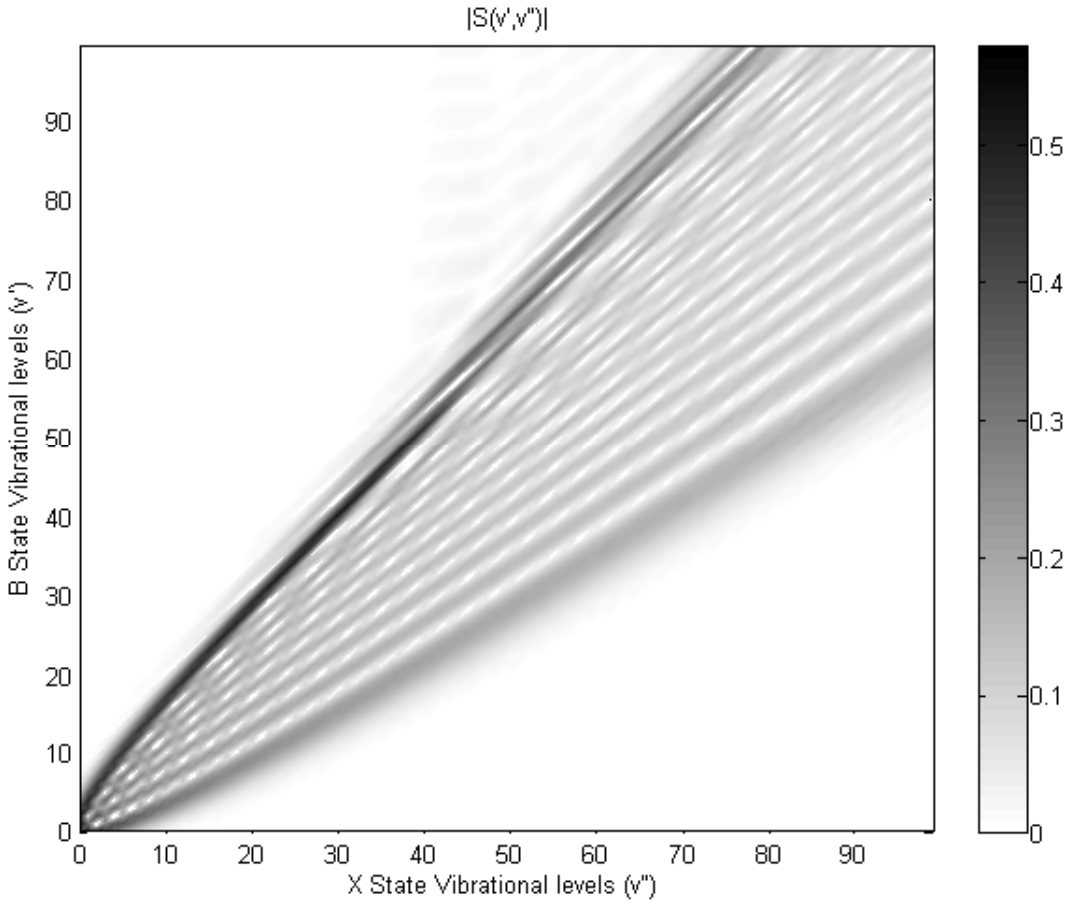

Fig. 34. $|S(\nu', \nu'')|$ where ν'' is the vibrational level in the X ground state and ν' is the vibrational level in the B excited state in Cs_2.

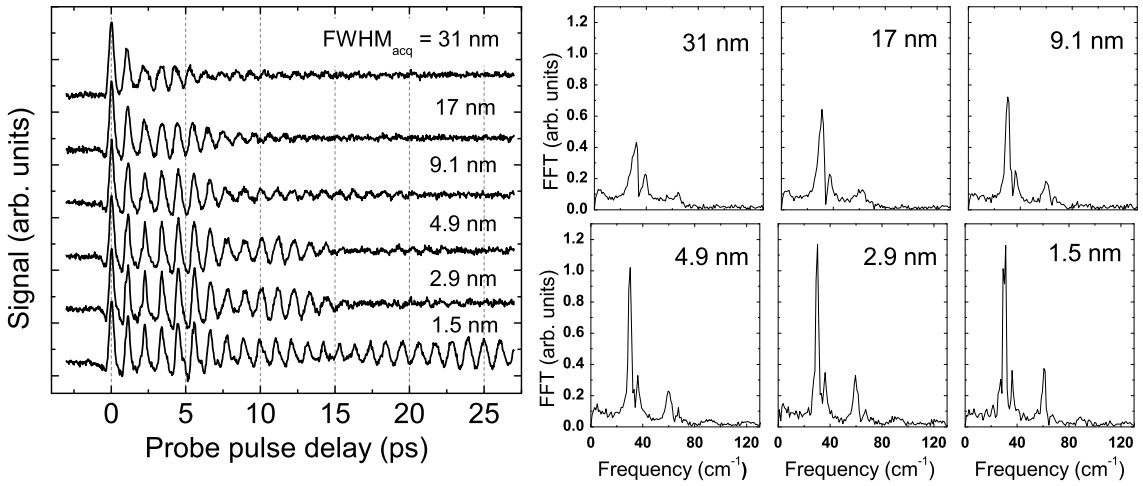

Fig. 35. The time dependence of the signal observed with one pump beam is shown on the left. The spectral width of the probe beam is varied from 31 nm to 1.5 nm by using a spectrometer with an adjustable exit slit. The observed temporal behavior of the spectrally selected wavepacket is changed from a simple decay (probe 31 nm) to decay and revival (probe 1.5 nm). The FFT spectra of the the recorded time-domain profiles are shown on the right.

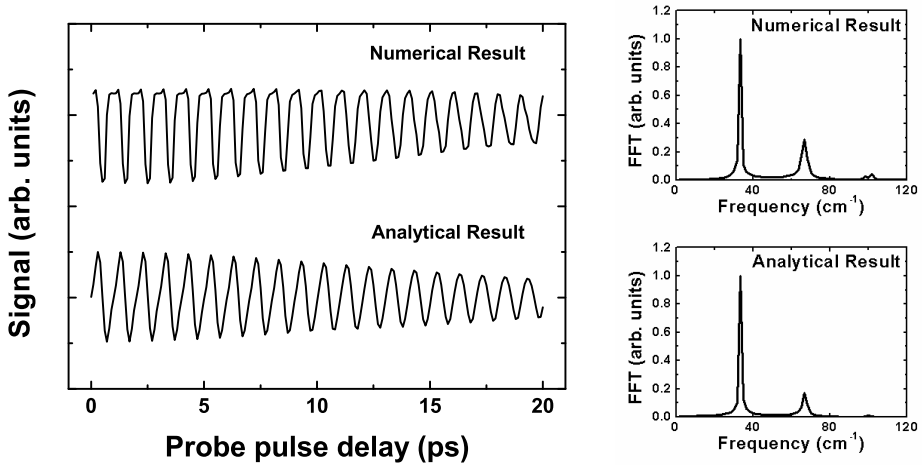

Fig. 36. The dependence of the absorptions of the probe pulse with width 31 nm, obtained from both the numerical simulation and analytical solution, on the probe pulse delay in the pump-probe measurements. The corresponding FFT spectra are shown on the right.

rate is maximal when the whole probe spectrum reaches the detector. It is significantly reduced, on the other hand, when the accepted FWHM bandwidth is narrow down to 1.5 nm. Note that the probe pulse duration at the sample stays the same. All modifications are made in the acquisition arm, after the sample. The acquisition bandwidth, however, provides a straightforward means to adjust the number (subset) of contributing vibrational levels. Numerical and analytical results for the small acquisition width limit are summarized in Fig. 36. They exhibit similar oscillations dominated by those at about 34 cm^{-1} and 68 cm^{-1}, i.e., at the vibrational frequency ω_e in the excited B state and its overtone. This can be understood from the analytical result in (5.31). Because the near resonance of the pump pulse and the electronic transitions between vibration states $|a\rangle$, $|a'\rangle$, and $|b\rangle$ and that of the probe pulse and the transitions between states $|a\rangle$, $|a'\rangle$, and $|c\rangle$, the $\sin(\omega_{a'a}\Delta t)$ term becomes much larger than the $\sin(\omega_{cb}\Delta t)$ term. Furthermore, due to the exponential functions in

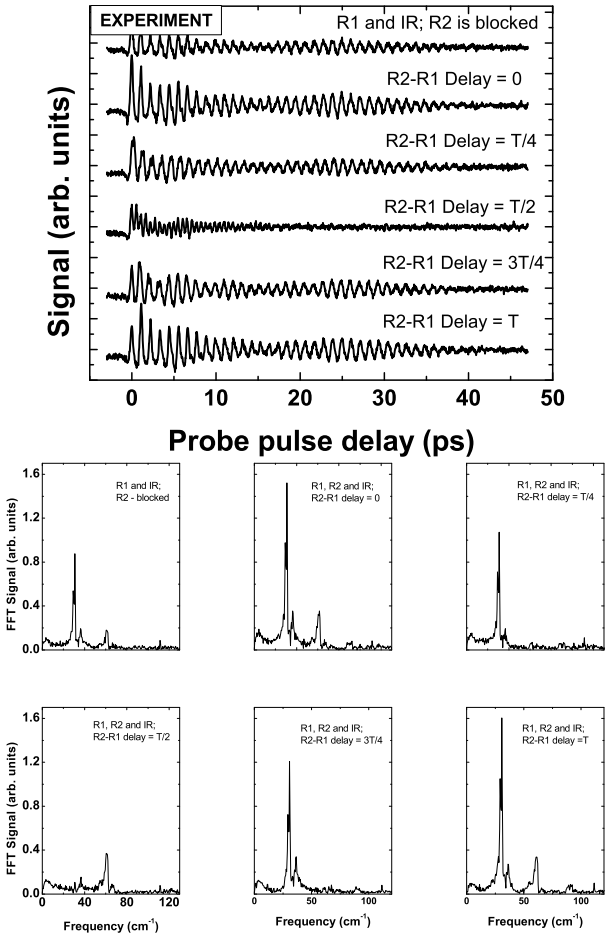

Fig. 37. The dependence of experimental signal on the probe (IR) delay, with different time delay between the pump (R1) and control (R2) in the pump-control-probe measurements. FFT spectra are on the bottom.

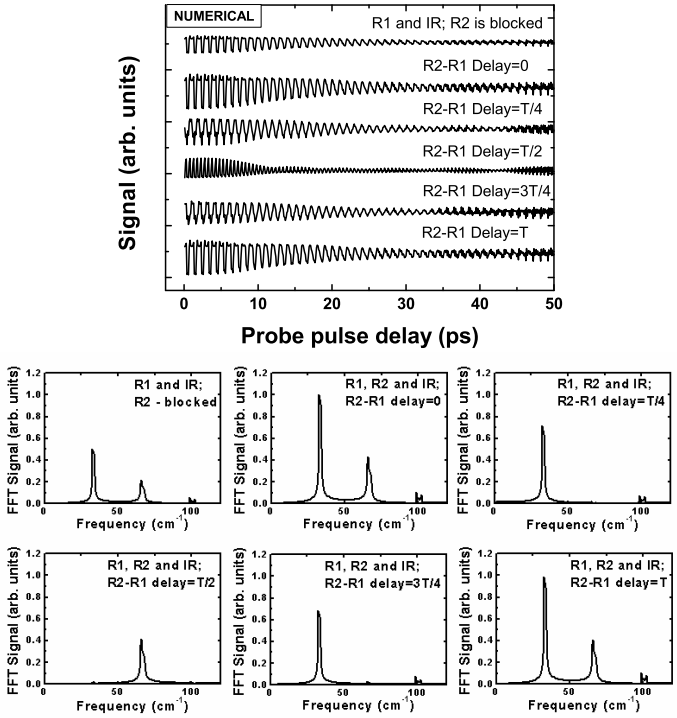

Fig. 38. The numerical results of the pump-control-probe measurements with different time delay between the pump and control pulses. FFT spectra of the absorption signal are on the bottom.

the equation, the term with frequency, $\omega_{a'a}$, around the vibrational frequency of the B excited state, 34 cm^{-1}, contributes most to the signal while terms with higher-order harmonic frequency contribute less to the signal. Therefore, both experimental and theoretical results show a high peak at 34 cm^{-1} but a much lower peak at 68 cm^{-1}. The dephasing of the oscillation amplitude is also shown in theory. It is the result of the vibrational anharmonicity term, $\omega_e\chi_e$. However, the dephasing rate from experiment and that from theory does not match quite well. The possible reason is that we do not include rotational levels in our model. Besides the anharmonicity of the molecular internuclear potential, the ro-vibrational coupling also effects on the dephasing of the wave packet motion [113]. Next, we evaluate the results of our pump-control-probe measurements and simulate the observed dynamics by extending the above model. We assume that two wave packets, generated by the pump and control pulses, are independent. The recorded signal for different time delays between the pump and control pulses is shown in Fig. 37. The time delay between the pump and control pulses is changing from 0 to T, where T is the period of the signal oscillation in the pump-probe measurements, which is about 1 ps. The acquisition bandwidth used for observing the signal is 1.5 nm. The superposition pattern between two wave packets in the cesium dimer can be seen. When the time delays between the pump and control pulses are 0 and T, two FFT peaks are found in the FFT spectra. One is at the frequency 34 cm^{-1} and the other one is at 68 cm^{-1}, which are the same with the results in the pump-probe measurements. However, when the time delays between the pump and control pulses are $T/4$ and $3T/4$, only the peak at 34 cm^{-1} is surviving. This means that the oscillations of the two wave packets are well synchronized and in phase. When the delay time become half of the period, say $T/2$, the first peak at 34 cm^{-1} disappears but the peak at the second-harmonic frequency 68 cm^{-1} appears again. This means that the oscillations of the two wave packets are

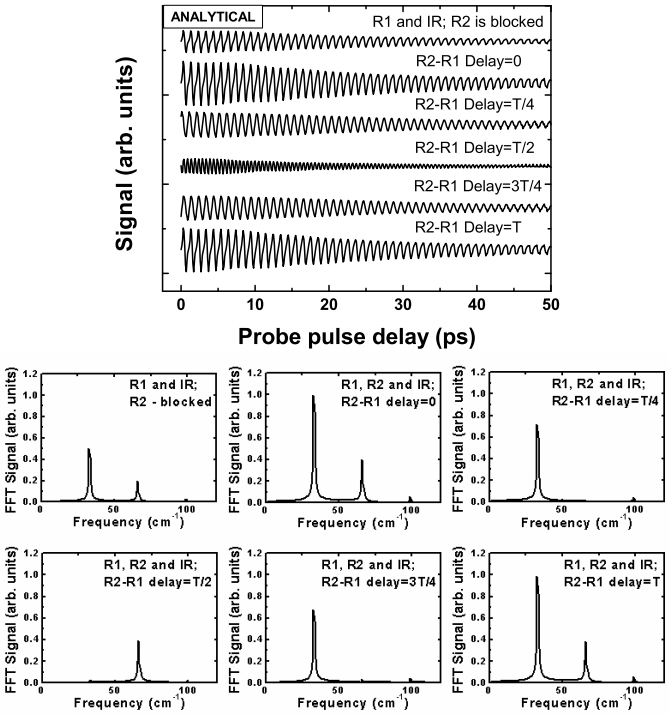

Fig. 39. The analytical results of the pump-control-probe measurements with different time delay between the pump and control pulses. FFT spectra of the absorption signal are on the bottom.

well synchronized, however, they are out of phase. Therefore, one should expect the two-times-faster oscillation. In this case, we believe that the two macroscopic states (two wave packets) are maximally entangled. Both numerical simulation (Fig. 38) and analytical calculation (Fig. 39) show the similar results with the experiment. Therefore, we are convinced that two wave packets generated by the pump and control pulses are independent and they produce the superposition pattern as shown above. Such superposition pattern can also be read using the analytical result for the pump-probe measurement (Eq. (5.31)). Since two wave packets generated by the pump and control pulses are independent, this superposition pattern shown above is the result of the superposition of the sine functions listed in this equation. When

the time delays between the pump and control pulses are $T/4$ and $3T/4$, the second-harmonic frequency terms, with frequency 68 cm^{-1} and period $T/2$, are destructive. On the other hand, when this time delay becomes $T/2$, the frequency terms, with frequency 34 cm^{-1} and period T, generate a destructive superposition. Therefore, with different time delays between the pump and control pulses, FFT peaks appear or disappear accordingly.

Interestingly, we can see the oscillation in the experiment shows some kind of "revival" at the large probe time delay (Fig. 37, on the left). Also, such "revival" is found in the numerical simulation results (Fig. 38), though at different delay time. However, it is not seen in the analytical solutions (Fig. 39). The reason may be that we neglect the weak wave packets in the ground state in theory for easy calculation and also we use a number of approximations in finding the analytical solutions.

5. Conclusion

We study the wave packet dynamics by using the pump-probe and pump-control-probe techniques associated with Λ-type configuration. The transmission of the probe pulse is measured to monitor the wave packet dynamics created either by one (pump) or two (pump and control) pulses into excited electronic state , $B\,^1\Pi_u$, from the ground state, $X\,^1\Sigma_g^+$, in cesium dimers. The FFT spectra extracted from the time-dependent transmission traces for the probe pulse exhibit peaks at frequencies 34 cm^{-1} and 68 cm^{-1} that correspond to vibrational level splitting (and its overtone) in the excited state. It is also shown that a proper choice of time delay between the pump and control pulses does alter the temporal characteristics of superposition of wave packets. In particularly, at the delay equal to half-period of 34 cm^{-1} modulation, the main peak in the FFT spectrum is eliminated and the oscillations feature only the double-frequency component at 68 cm^{-1}. For the pump-control delay matching the full

time period of 34 cm^{-1} frequency splitting, however, the initial emission/absorption dynamics is restored.

The experimental observations are supported by a theoretical model based on the density matrix formalism with the Franck-Condon factors. The theoretical results illustrate quite good agreement with the experimental data. In addition to numerical simulations, the simplified analytical treatment that elucidates the origin of the probe pulse transmission modulation is also presented.

The present theoretical method can be presumably applied to other similar experiments on ultrafast processes in diatomic molecules. This includes the study of coherent anti-Stokes Raman scattering (CARS) in cesium dimers. We have plans for detailed simulation for such experiments.

CHAPTER VI

HYBRID COHERENT RAMAN SPECTROSCOPIC TECHNIQUE*

A. Optimizing the Laser-Pulse Configuration for Coherent Raman Spectroscopy

We introduce a hybrid technique that combines the robustness of frequency-resolved coherent anti-Stokes Raman scattering (CARS) with the advantages of time-resolved CARS spectroscopy. Instantaneous coherent broadband excitation of several characteristic molecular vibrations and the subsequent probing of these vibrations by an optimally shaped time-delayed narrow-band laser pulse help to suppress the nonresonant background and to retrieve the species-specific signal. We used this technique for coherent Raman spectroscopy of sodium dipicolinate powder, which is similar to calcium dipicolinate (a marker molecule for bacterial spores, such as Bacillus subtilis and Bacillus anthracis), and we demonstrated a rapid and highly specific detection scheme that works even in the presence of multiple scattering.

1. Introduction

The Raman vibrational spectrum of molecules provides an excellent fingerprint for species identification. Because of the Raman effect, lower-frequency (Stokes) radiation is emitted when light irradiates a molecule, see Fig. 40A. The Raman signal is weak,

---

*Reprinted with permission from "Optimizing the laser-pulse configuration for coherent Raman spectroscopy" by D. Pestov, R. K. Murawski, G. O. Ariunbold, X. Wang, M. Zhi, A. V. Sokolov, V. A. Sautenkov, Y. V. Rostovtsev, A. Dogariu, Y. Huang, and M. O. Scully, 2007. *Science*, 316, 265-268, Copyright [2007] by the American Association for the Advancement of Science

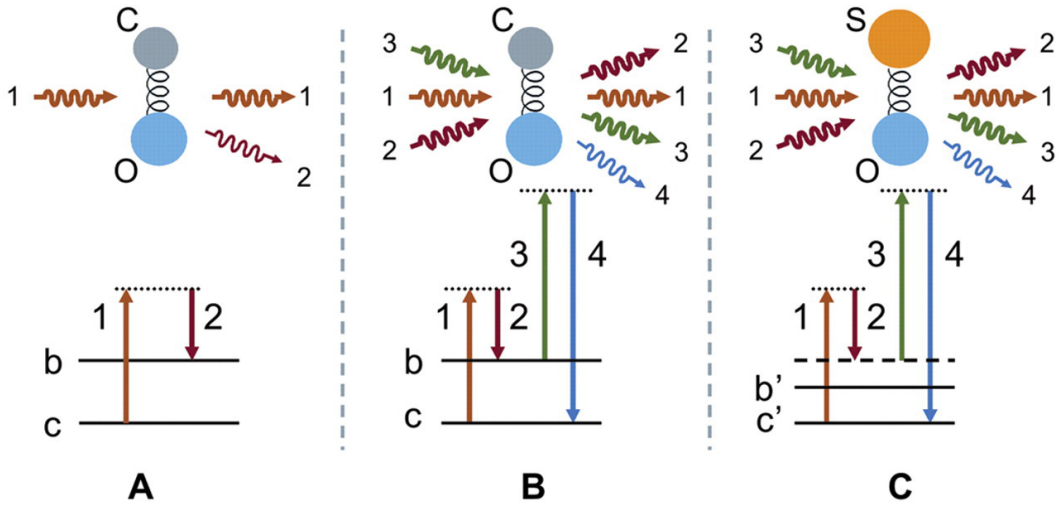

Fig. 40. Level diagram and schematic of different scattering processes on simple molecules. In this example, CO is a target molecule and SO is a background molecule.(A) Incoherent Raman scattering (pulse 2) was derived from laser pulse 1 scattering off of the CO molecule. (B) CARS signal 4 was derived from probe pulse 3 scattering off of the CO molecular vibration, coherently prepared by pulses 1 and 2. (C) One of the possible channels for the NR background generation in SO. c the ground state of the CO molecule; b the target vibrational state of the CO molecule; c', the ground state of the background molecule; b', anoff-resonant vibrational state of the background molecule.

but with the advent of powerful lasers, spontaneous Raman spectroscopy became a useful technique. When the molecules are put into coherent oscillation by a pair of preparation pulses (pulses 1 (pump) and 2 (Stokes) in Fig. 40B) and a third (probe) pulse is scattered off of this coherent molecular vibration, a strong anti-Stokes signal (pulse 4) is generated (Fig. 40C). This process is called coherent anti-Stokes Raman scattering (CARS) ([74, 81, 82] and references therein).

Unfortunately, CARS from the molecules of interest is frequently obscured by the non-resonant (NR) four-wave mixing (FWM) signal from other molecules (Fig. 40C),

or even from the same molecules, because of contributions from multiple off-resonant vibrational modes and the instantaneous electronic response. To overcome this difficulty, a variety of methods, including polarization-sensitive techniques [84] and heterodyne [85, 86] and interferometric [87, 88, 89, 90] schemes, have been developed. However, these methods do not work well in the presence of strong multiple scattering in rough samples because scattering randomizes spectral phases and polarization. For this reason, applications of CARS for rapid detection and recognition of strongly scattering media, such as anthrax spores, have often been deemed impractical.

In the present work, we used ultrashort (50 fs) transform-limited pulses 1 and 2 for uniform broadband Raman excitation and a tailored narrow-band (several hundred femtosecond long) probe. We employed the femtosecond laser system with two OPAs. The output of the first OPA ($\lambda_1 = 712 - 742$ nm, tunable; FWHM 12 nm) and a small fraction of the amplifier output ($\lambda_2 = 803$ nm, FWHM 32 nm) were used as pump and Stokes beams, respectively. The output of the second OPA, the probe beam ($\lambda_3 = 578$ nm), was sent through a home-made pulse shaper with an adjustable slit (see Fig. 41) that cut the bandwidth of the pulse. Next, the Stokes and probe pulses passed through delay stages (DS1,2) and then all the three beams were focused by a convex 2-inch lens (with the focal length f = 200 mm) on the rotated sample. The scattered light was collected with a 2- inch achromatic lens (f = 100 mm) and focused onto the entrance slit of the spectrometer (Chromex Spectrograph 250is) with a liquid nitrogen cooled charge-coupled device (CCD: Spec-10, Princeton Instruments) attached. We used a multichannel detector to simultaneously record the anti-Stokes signal at all optical frequencies within the band of interest. These modifications allowed us to discriminate between the resonant contribution and the NR background, as is explained below, and to extract the CARS signal even at zero probe delay. Furthermore, combining this method with the probe-pulse delay provided a means to

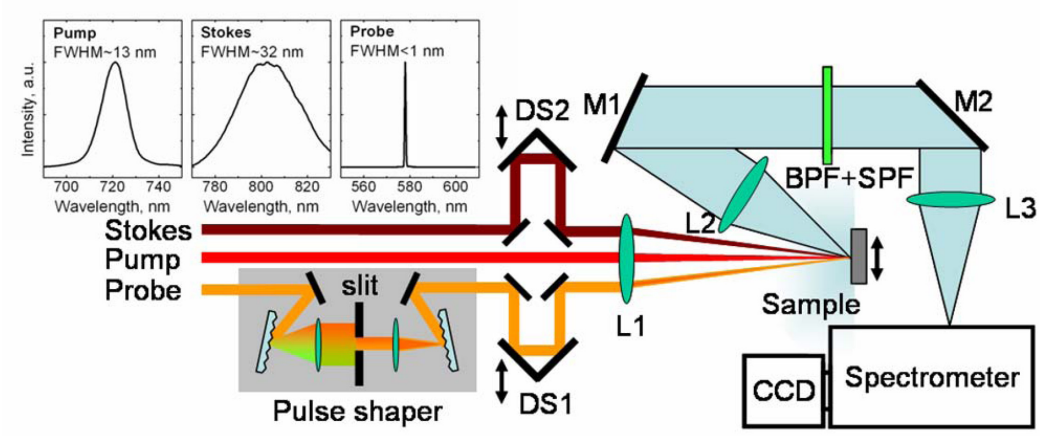

Fig. 41. Schematics for the CARS experiment: DS1,2 are computer controlled delay stages; L1-3 are lenses; BPF+SPF is a set of bandpass and shortpass filters; M1,2 are alignment mirrors; CCD is a charge-coupled device attached to the spectrometer. The insets in the top-left corner show typical spectra of the pump, Stokes, and probe pulses.

suppress the interfering FWM and associated noise. This combination of broadband preparation and frequency-resolved multichannel acquisition [114, 115, 116, 117] with time-delayed narrow-band probing yields a very sensitive and robust technique that allows us to identify bacterial spores, such as anthrax, in real time. We refer to this technique as hybrid CARS for short, and we used it to study the Raman signature of spores, which is dominated by the contribution from the dipicolinic acid (DPA) molecules.

2. A Simple Theoretical Background

In order to provide better insight into the advantages of the proposed scheme, we review here a few important aspects of the theory behind CARS, which has been extensively described elsewhere [74, 81, 82, 87, 90, 115, 118]. In general, the third-order polarization induced by the pump, Stokes, and probe pulses can be split into reso-

nant and NR contributions. If we assume that there are no one-photon resonances involved, the NR part can be attributed to the instantaneous electronic response and a sum over the contributions from far-detuned Raman transitions. The resonant part of the third-order polarization is attributed to the Raman transitions of interest. The NR component, $\chi^{(3)}_{NR}$, of the nonlinear susceptibility is usually frequency-insensitive within the considered spectral band and can be treated as a constant. The resonant component $\chi^{(3)}_{R}$, under the assumption of Lorentz-shape Raman lines, can be presented as

$$\chi^{(3)}_{R}(\omega_1 - \omega_2) = \Sigma_j A_j \Gamma_j / [\Omega_j - (\omega_1 - \omega_2) - i\Gamma_j], \tag{6.1}$$

where ω_1 and ω_2 are the pump and Stokes laser frequencies, j is the summation index over all covered Raman transitions, A_j is a constant related to the spontaneous Raman cross section of the j^{th} Raman transition and molecular density, Γ_j denotes the j^{th} Raman line half-width, Ω_j denotes the jth vibrational frequency [118], and $i = \sqrt{-1}$. The summation is held over all of the Raman transitions involved [118].

In the frequency domain [87], the third-order polarization $P^{(3)}(\omega)$ can be written as

$$P^{(3)}(\omega) = P^{(3)}_{NR}(\omega) + P^{(3)}_{R}(\omega) = \int_0^{+\infty} d\Omega \times [\chi^{(3)}_{NR} + \chi^{(3)}_{R}(\Omega)] E_3(\omega - \Omega) \times S_{12}(\Omega), \tag{6.2}$$

where $P^{(3)}_{NR}$ is the NR component of the polarization, $P^{(3)}_{R}$ is the resonant component, $E_3(\omega)$ is the spectral amplitude of the probe pulse, and $S_{12}(\Omega) = \int_0^{+\infty} d\omega' \times E_1(\omega') E_2^*(\omega' - \Omega)$ is the convolution of the pump and Stokes field amplitudes, $E_1(\omega)$ and $E_2(\omega)$. The signal arising from the nonlinear response of the medium is proportional to $|P^{(3)}(\omega)|^2$, so the spectra generally have complex shapes caused by the interference between both resonant contributions from different vibrational modes and the NR background. A straightforward analogy with the spontaneous Raman spec-

tra can be made only for well-separated lines with no NR background. Otherwise, the direct fit of the recorded CARS spectrum is required for Raman spectrum retrieval [119]. The convolution of the pump and Stokes spectra, $S_{12}(\Omega)$, enters the two parts of the third order polarization on equal grounds. It defines a Raman frequency band covered by the preparation pulses and is maximized for transform-limited ones; i.e., pulses with the constant spectral phase. The difference between the two contributions comes from the susceptibility and can be enhanced by the use of a properly shaped probe. One way to proceed is to modify the spectral phase of the probe pulse, as it was demonstrated by Oron et al. [88]. Another way, which seems to be more robust and straightforward, is to shape its spectral amplitude,$|E_3(\omega)|$, as we did in our experiment. If a narrow-band probe is applied together with the broadband transform-limited preparation pulses, the NR contribution inherits a smooth, featureless profile of $S_{12}(\Omega)$ with some characteristic width $\Delta\omega_{12}$, whereas the resonant part generates a set of narrow peaks (one for each excited vibrational mode) whose width is determined either by the Raman linewidth or the probe spectral width whichever is greater. The amplitude ratio between the resonant signal and the NR background at a Raman-shifted frequency is also affected by the spectral width of the probe pulse. At the zero probe delay, the ratio is inversely proportional to the square of the probe spectral width when the last one is in between the Raman linewidth and the width of the pump-Stokes convolution profile (i.e.,$\Gamma \ll \Delta\omega_3 \ll \Delta\omega_{12}$) and the probe-pulse energy is fixed. This ratio saturates at the limits and leads to a superior but finite signal-to-background ratio for the optimum probe width on the order of the Raman linewidth.

3. Results and Discussions

The present measurement strategy combines the benefits of frequency-resolved CARS signal discrimination against the NR FWM(pointed out above) with the NR background suppression as in time-resolved CARS ([120, 121, 122, 123] and references therein). Indeed, when the probe delay is adjustable, further optimization is possible. In the plane of two parameters (the probe-pulse duration and its delay), the resonant response peaks for both parameters on the order of the inverse Raman linewidth. However, the NR FWM at the Raman-shifted frequency is maximized for zero probe delay, and the probe-pulse duration is matched to the time span of the pump-Stokes convolution profile. As mentioned above, we can eliminate the NR background by just delaying the probe pulse, which gives a theoretically unlimited signal-to-background ratio. Unfortunately, this approach does not properly optimize the resonant contribution, and we can end up with no detectable signal at all. We suggest the simultaneous use of the two parameters (the probe-pulse duration and its delay) to achieve close-to-optimal resonant response with reasonable suppression of the NR background. The actual optimal values of the parameters depend on the Raman linewidth, the sensitivity of the setup used, and the relative strength of the resonant and NR susceptibilities.

Proper tailoring of the probe pulse can help to reduce the contribution of the NR background for probe delays comparable to the pulse length. For example, a rectangular-like spectrum gives a sinc squared temporal profile of the probe-pulse intensity, which goes as

$$[\sin(\Delta\omega_3 t/2)/(\Delta\omega_3 t/2)]^2 \tag{6.3}$$

with the time t. Putting the preparation pulses in one of its nodes would result in the effective suppression of the NR background.

We compromise between the resolution, signal strength, and the extent of the NR background suppression. On a single-shot basis, the spectral resolution is usually determined by the probe bandwidth. However, this is not an intrinsic limit, and much better resolution can be achieved by recording the anti-Stokes spectrum while varying the probe-pulse delay, if the measurements are not overwhelmed by the fluctuations.

As mentioned above, we applied the developed technique in the context of the spore detection problem. A marker molecule for bacterial spores is calcium dipicolinate (CaDPA), which accounts for 10 to 17% of the bacterial spore dry weight [95]. We focus here on NaDPA, which is easier to make and is a good surrogate for CaDPA. The spontaneous Raman spectrum of NaDPA (Fig. 42) exhibits a similar set of strong Raman lines as that of CaDPA. Both differ somewhat from the Raman spectrum of DPA itself [124]. The important point is that although spores are fairly complex in structure, their Raman spectra are dominated by several vibrational modes of CaDPA. The CARS spectra of NaDPA powder as a function of the probe-pulse delay are shown in Fig. 43. The spectrograms were taken at different pump wavelengths to cover the whole spectral-fingerprint region of the molecule (800 to 1700 cm^{-1}). Streaklike horizontal lines are the signature of excited NaDPA Raman transitions. The broadband pedestal is the NR background. As expected, the tuning of the pump wavelength spectrally shifts the NR FWM but leaves the position of the resonant lines untouched. Also, the resonant and NR contributions exhibit different dependencies on the probe delay. The magnitude of the NR background is determined by the overlap of the three laser pulses and follows the probe-pulse profile. However, a relatively long decay time of the Raman transitions under consideration favors their long-lasting presence and makes them stand out when the probe is delayed. The cross sections of the spectrograms at two different probe delays are given in Fig. 44. The integration time for each of those is only 1 s. When the three pulses are overlapped

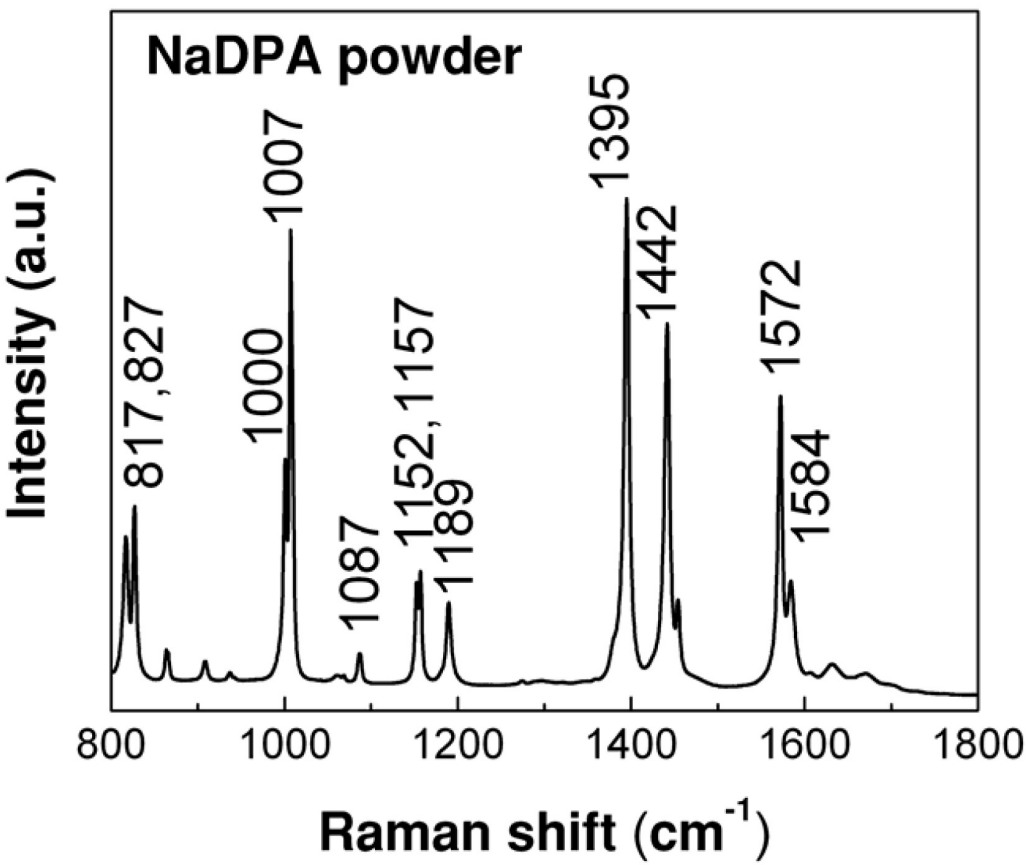

Fig. 42. Spontaneous Raman spectrum of NaDPA excited by 532 nm light.

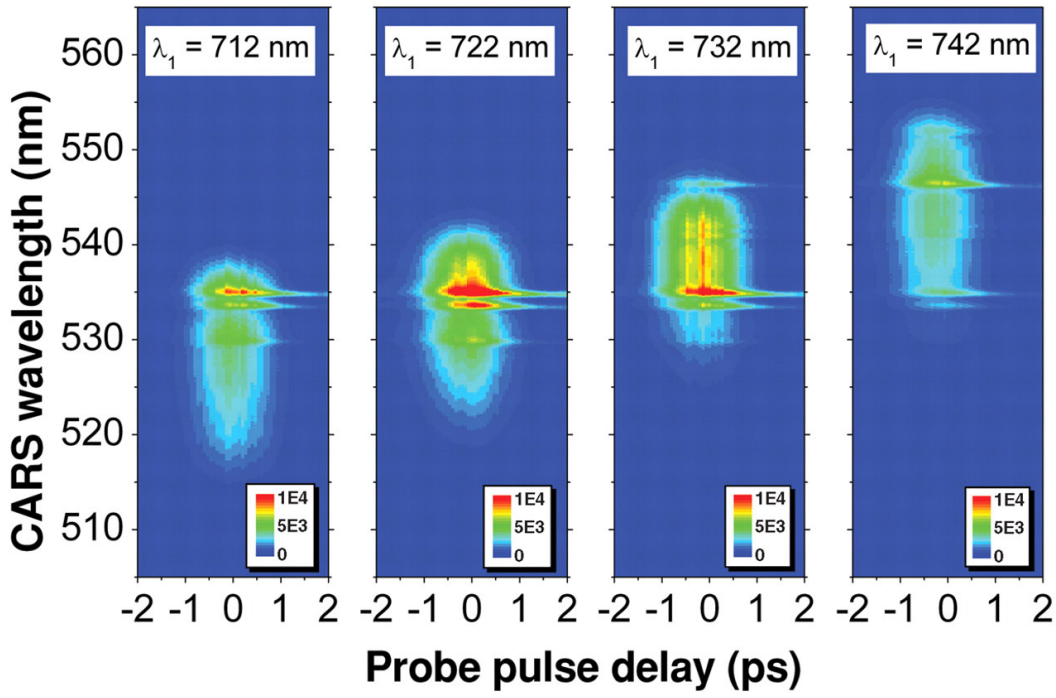

Fig. 43. CARS spectrograms recorded on NaDPA powder at different pump wavelengths. The CARS spectrum is shown as a function of the probe-pulse delay for the pump wavelength λ_1 = 712, 722, 732, and 742 nm, respectively (left to right). The other parameters are: pump, full width at half maximum (FWHM)∼12 nm, 2 μJ per pulse; Stokes, λ_2 = 803 nm, FWHM ∼32 nm, 3.9 μJ per pulse; probe, λ_3 = 577.9 nm, FWHM ∼0.7 nm, 0.5 μJ per pulse. The integration time was 1 s per probe-delay step. $1E4 \equiv 1 \times 10^4$.

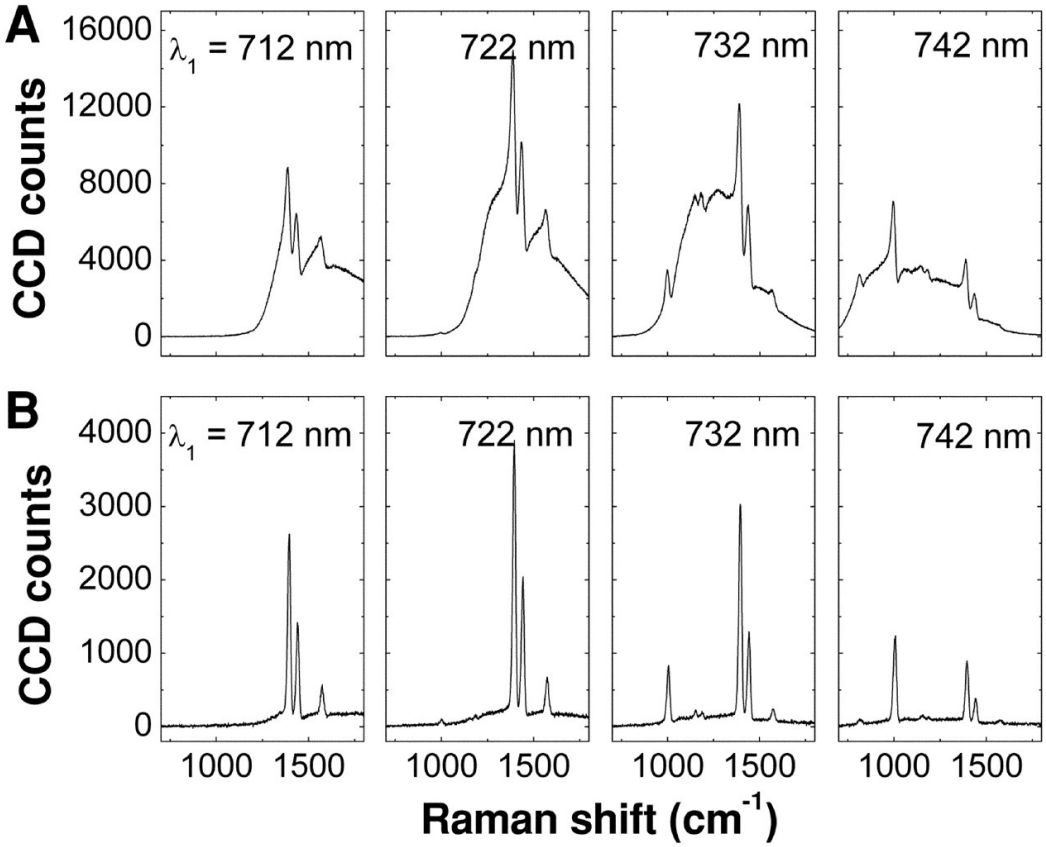

Fig. 44. Cross sections of the CARS spectrograms from Fig. 43 for two probe delays, (*A*) 0 ps and (*B*) 1.5 ps. The wavelengths within the observed range were transferred into the Raman shift, relative to the probe central frequency. The integration time was 1 s: 0.5 s for the signal and 0.5 s for the background acquired for the delayed Stokes pulse. CCD is a charge-coupled device.

(zero delay), the resonant contribution is severely distorted by the interference with the NR FWM. Delaying the probe by 1.5 ps, that is, putting the preparation pulses into the first node of the sinc-shaped probe pulse.improves the signal-to- background ratio by at least one order of magnitude. In this case, the NR background suppression is limited by multiple scattering that scrambles the timing between the preparation and probe photons. Extracted CARS contributions from our first measurements on Bacillus subtilis spores (a surrogate for anthrax), in which we maximized the signal rather than the signal-to-background ratio, are summarized in Fig. 45. The Raman peaks are not normalized on the strength of the excitation and thus have an imprint of the pump-Stokes spectral convolution function, which sweeps through the Raman band from 800 to 1700 cm^{-1} while the pump wavelength is tuned. We assign the Raman transitions in the band and compare the retrieved line positions with the known positions from spontaneous Raman measurements [78, 76]. Within the estimated experimental uncertainty of 15 cm^{-1}, the values are in good agreement. The data shown in Fig. 45 were acquired at zero probe delay over 2 min, although the Raman lines stand out from the background even after a few seconds of integration. Under similar experimental conditions, the signal arising from spontaneous Raman scattering is weaker by a few orders of magnitude and typically requires a longer integration time than the CARS signal.

4. A Comparison to Existing Techniques and Conclusion

To place the present work in context, our approach comes from the superposition of two well-known techniques developed over the past few decades and employed for combustion diagnostics ([81, 122, 123] and references therein) and chemically selective microscopic biological imaging [125, 126]. Multifrequency acquisition has been implemented in so-called broadband or multiplex CARS [115, 116, 117, 118], where

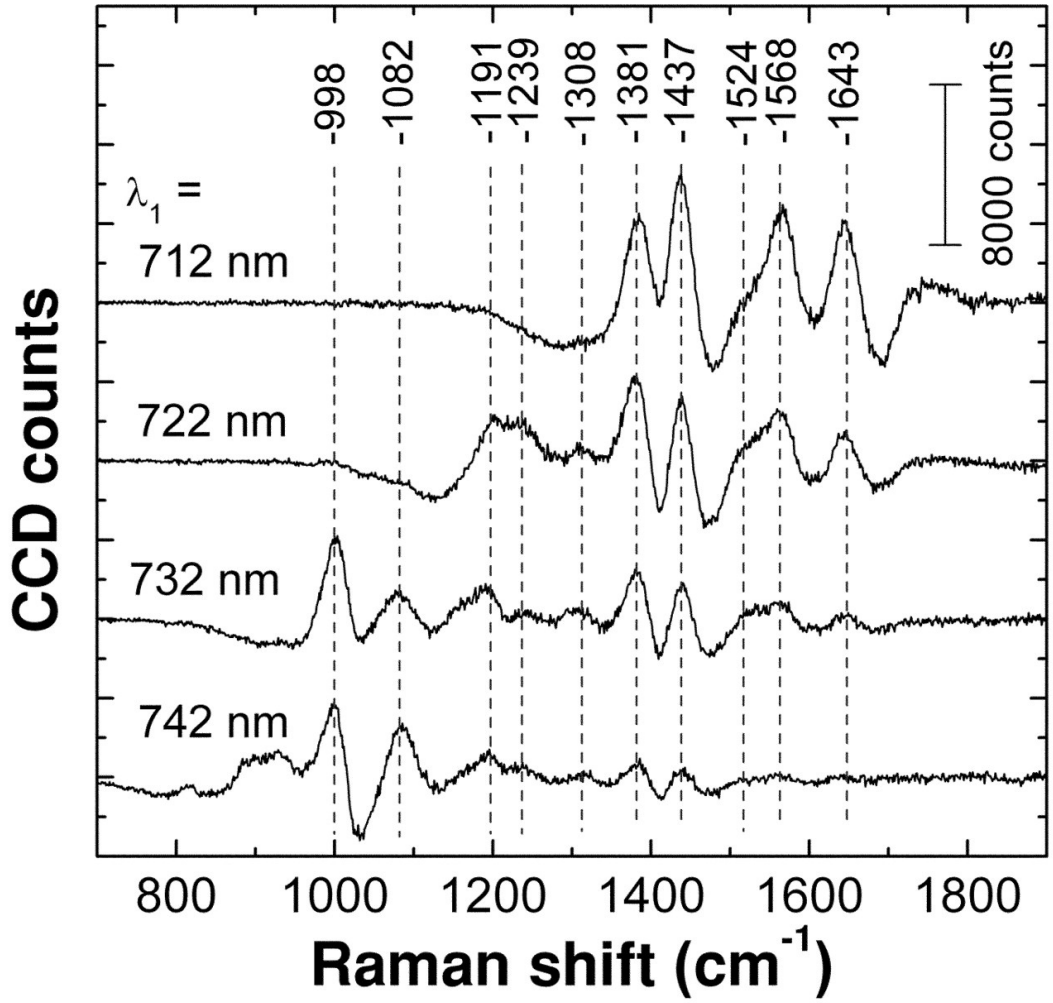

Fig. 45. CARS on Bacillus subtilis spores at zero probe delay. The resonant contribution was retrieved by fitting the NR background with a smooth curve and subtracting it from the total acquired signal. The sample used was a pullet of spores fixed in a rotating sample holder. The pump wavelength, λ_1, was varied from 712 to 742 nm. Other parameters were the same as those for Fig. 43. The integration time was 2 min.

together with the multichannel detection, a combination of narrow-band pump-probe and broadband Stokes pulses is used to address a wide range of vibrational frequencies (Fig. 45). In this degenerate scheme, the NR background has been addressed by means of the polarization-sensitive and interferometric techniques mentioned above. A delayed probe has been used in time-resolved CARS [120, 121, 122, 123]. That technique uses ultrashort pulses for preparation and probing (Fig. 45). Its ultimate source of species-specific information is multimode interference in the probe-delay signal profile, generally referred to as quantum beats [120]. Time-resolved CARS eliminates the NR contribution by delaying the probe pulse, but the technique still remains vulnerable to fluctuations. It has been successfully applied to polycrystalline and opaque solids [127] to observe vibrational dephasing of single excited Raman transitions. However, the use of the multimode interference pattern for species recognition requires the ability to record high-quality quantum-beat profiles over a relatively large probe-delay span and therefore is challenging in the presence of scattering and fluctuations.

In our scheme, a generalized broadband or multiplex CARS technique is combined with background suppression by means of an optimal sequence of coherent excitation and time-delayed probe pulses (Fig. 45).

As in conclusion, we diverge from the conventional broadband CARS arrangement and deal with the probe and the two preparation pulses, pump and Stokes, separately. By adjusting the probe-pulse delay and its spectral width, we suppress the NR background, as in time-resolved CARS, but keep the advantages of the frequency-resolved multiplex CARS spectroscopy, see Fig. 46. The experimental data demonstrate the efficacy of the ultrafast broadband excitation and time-variable narrowband probing, whereas the described implementation supports the versatility of the technique.

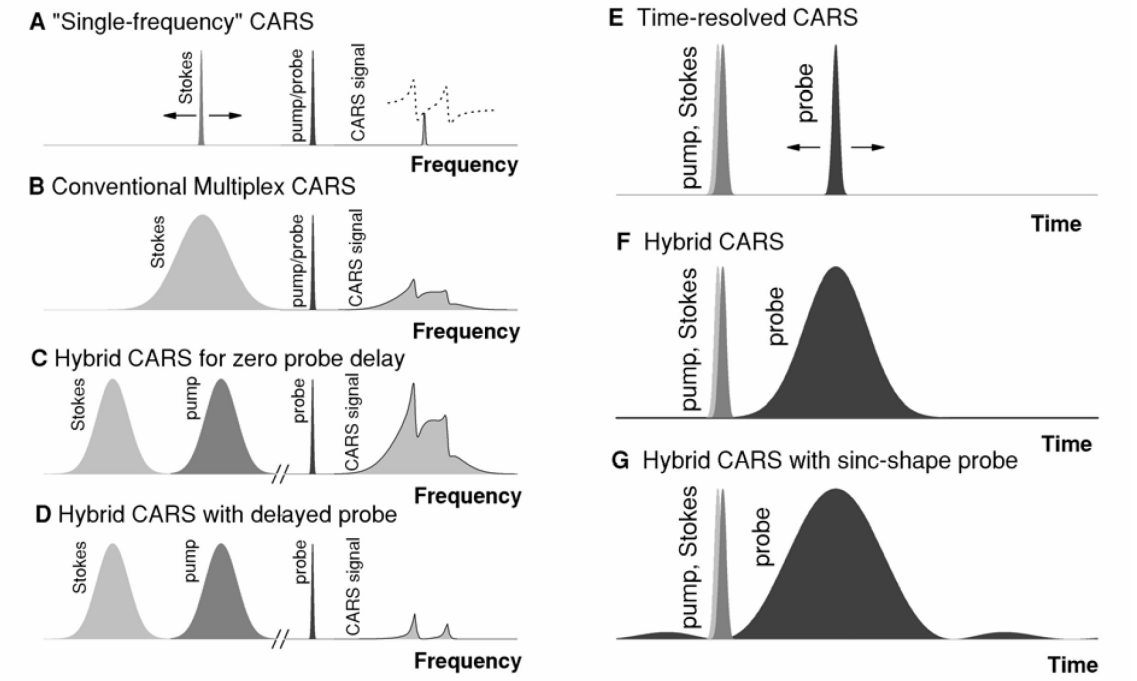

Fig. 46. (A to D) Schematic layout of frequency-resolved techniques for CARS spectroscopy. The presence of two Raman lines within the considered band is implied: (A) Single-frequency CARS with two narrow-band lasers, one of those is tuned; (B) Multiplex CARS with a combination of narrow-band and broadband laser sources; (C) Hybrid CARS at zero probe delay, which is equivalent to non-degenerate multiplex CARS. The use of two ultrashort preparation pulses, rather than a combination of a narrow-band and broadband ones, provide superior time overlap between the two and larger Raman frequency span; (D) Hybrid CARS with the delayed probe for the NR background suppression. (E to G) The NR background suppression by proper timing of the probe pulse: (E) Time-resolved CARS, which implies the use of ultrashort pulses with the variable probe delay; (F) Hybrid CARS with the time-delayed probe, assuming it has Gaussian profile; (G) Hybrid CARS with the tailored time-delayed probe pulse. The time delay is chosen such that the preparation pulses overlap at the node of the sinc-shaped probe to minimize the NR background.

CHAPTER VII

COOPERATIVE VERSUS UNCOOPERATIVE PROCESSES*

Three different examples on comparison between cooperative and uncooperative processes are given in this chapter. In the first part, we show the observation of coherent UV light pulses at 308 nm by the coherent scattering of IR pulses from atomic Rb vapor. Rb atoms were first excited by a 100 fs pulse at 778 nm from the $5S$ ground state to the $5D$ state via a two-photon transition. The atoms were then pumped by another 100 fs pulse at 1485 nm, which was resonant with the $5D - 12P$ transition. The presence of the 1485 nm pulse triggered the instantaneous emission of a UV light pulse centered at 308 nm corresponding to the $12P - 5S$ transition. The pulse had a time duration of tens of picoseconds. The temporal characteristics of the 308 nm pulse were independent of the input power for the range used in this experiment. The robust temporal shape of the generated light is explained by a simplified atom-field interaction theory.

In the second part, we study a picosecond cooperative phenomenon in three-photon resonant medium. The Rb atoms were pumped by 100 fs laser pulses which were tuned to three-photon resonance to the $6P - 5S$ transition. The 420 nm pulses were produced simultaneously with input pulses and both the peak intensity and pulse duration were changed as input power varied.

In the final part of this chapter, we present a comparative analysis of sponta-

---

*Part of the data reported in this chapter is reprinted with permission from "Coherent versus incoherent Raman scattering: molecular coherence excitation and measurement", 2007. D. Pestov, G. O. Ariunbold, X. Wang, R. K. Murawski, V. A. Sautenkov, A. V. Sokolov, and M. O. Scully, *Opt. Lett.* 32, 1725-1727. Copyright [2007] Optical Society of America

neous and coherent Raman scattering on pyridine. The instantaneous excitation of the molecular coherence was done by a pair of ultrashort preparation pulses. Then, a long narrow-band probe pulse was scattered off the molecular vibrations. The described hybrid technique allowed for the single-shot acquisition of a background-free coherent Raman spectrum within the excitation band and its straightforward comparison with the spontaneous Raman measurements, performed in the same setup. We demonstrate a 10^5-fold increase in the efficiency of the Raman scattering process due to the broadband pump Stokes preparation. The coherence magnitude $\sim 0.5 \times 10^{-3}$ is inferred experimentally, without a priori knowledge about the molecular structure.

A. An Observation of Picosecond UV Pulses Produced by Coherent Scattering of IR Femtosecond Pulses in Atomic Rubidium Vapor

1. Introduction

The latest advances in laser technology have made ultraviolet light practical in photolithography, imaging, optical communications or storage, healthcare, industry and astronomy, including countless other applications. A typical method to produce intense UV light is based on nonlinear processes [128]. Considerable attention has been devoted to frequency up-conversion of IR light by utilizing nonlinear processes in metal vapors [129, 130, 131, 132, 133, 134].

In the present work we report the generation of 308 nm light from an atomic vapor of Rb. The specific process can be understood by referring to the energy-level diagram in Fig. 47. The atoms were excited by three photons from ultrashort laser pulses: two photons at 778 nm drove the atoms from $5S$ to $5D$; one photon at 1485 nm promoted the atoms from $5D$ to $12P$. The atoms emitted UV light at 308 nm on a transition from $12P$ to $5S$. We also refer to the pulses centered at 1485 nm, 778

nm and 308 nm as IR, red and UV, respectively. The input IR pulse was subject to

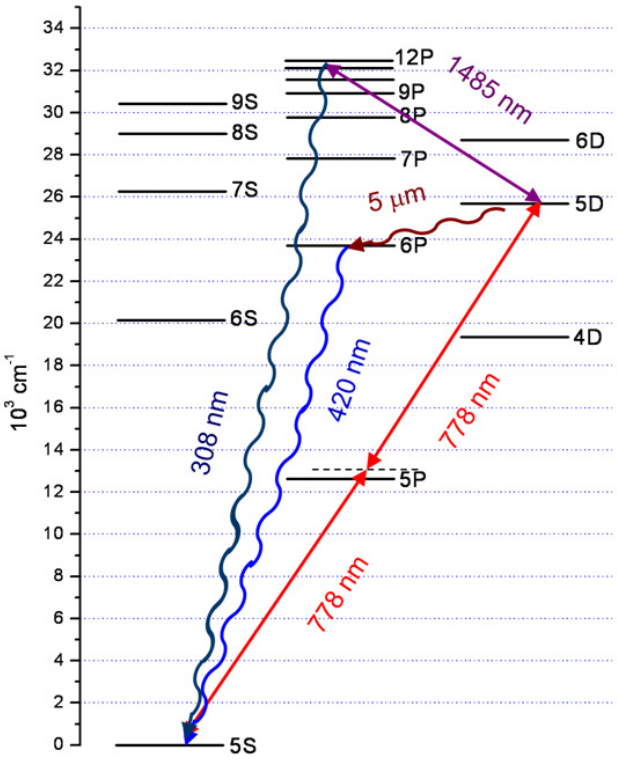

Fig. 47. Energy level diagram and excitation scheme. Two red photons at 778 nm drive the transition from $5S$ to $5D$, and give the yoked superfluorescence consisting of far infrared light ($5D$ to $6P$) at 5 μm and violet light ($6P$ to $5S$) at 420 nm. One IR photon at 1485 nm drives the transition from $5D$ to $12P$, and gives the ultraviolet light at 308 nm ($12P$ to $5S$).

variable delay with respect to the arrival of the red pulses. In the case of relatively large delay, three-level cascade processes [37] are most probable. In this case, Rb atoms emit superfluorescent light [1] from $5D$ to $6P$ at 5 μm. This triggers the superfluorescence from $6P$ to $5S$ at 420 nm [42]. The temporal properties of this violet light were measured in our previous experiments.

In the present case, by varying delay between the IR and red pulses and measuring the spectrum of the 308 nm generated pulse with the spectrometer, we probed the fast (picosecond) decay of the excited $5D$ atomic level. For a fixed time-delay between the IR and red pulses, temporal characteristics of the 308 nm pulses were studied by a streak camera with about 2 ps time resolution. The dependence of the temporal pulse shape on the input power was investigated experimentally. A simple atom-field interaction theory is developed to provide an analytical solution which qualitatively explains the experimental results.

2. Experimental Details

A schematic of our experiment is shown in Fig. 48. In short, the 1485 nm and 778 nm pulses were combined on a beam splitter before entering a Rb vapor cell. After passing through a colored absorption filter, the generated 308 nm pulses were analyzed by a spectrometer and a streak camera. Details of the experiment are enumerated below:

The 778 nm laser pulses were the doubled signal output of a first OPA and vertically polarized with respect to the laser table, whereas the 1485 nm pulses came from the signal output of a second OPA and were horizontally polarized. The polarization of this second beam was rotated by a half-wave plate to be vertical. Both beams had durations of approximately 100 fs. The power emitted by each OPA was attenuated by a variable metallic neutral density filter. The neutral density filters used in the experiment are not shown in Fig. 48. The 1485 nm beam passed through a corner-cube retroreflector (Newport) mounted on a translation stage. This functioned as an adjustable time delay. The beam reached a pellicle beam splitter (Thorlabs). The beam splitter transmitted about 61% of the 1485 nm beam and 63% of the 778 nm beam. After the beam splitter, the beams were focused by a (f=20 cm) lens. The beam spatial intensity profiles at the focus in the air were somewhat elliptical; the

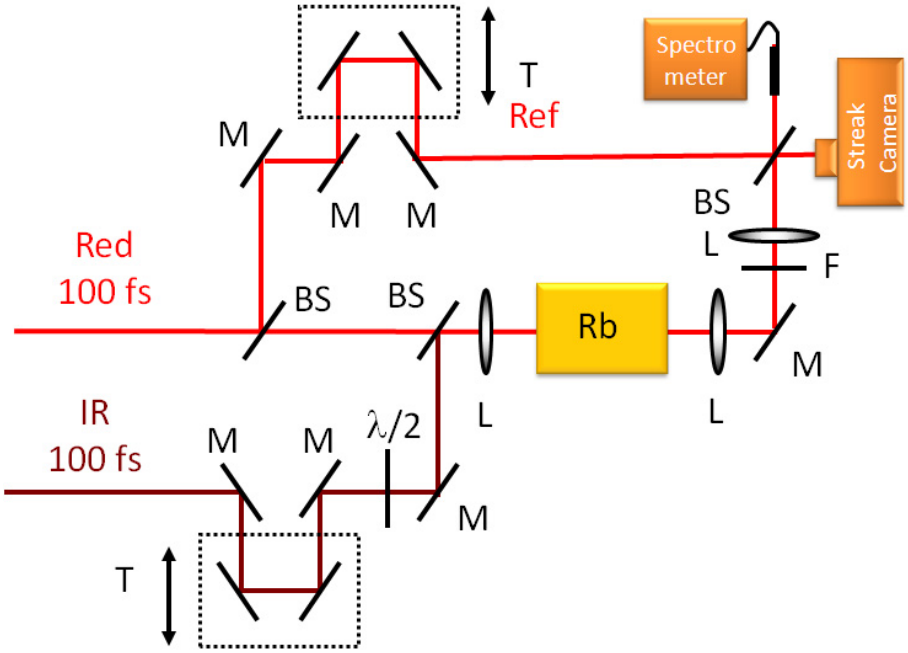

Fig. 48. Experimental schematic. Red: 778 nm input laser beam, IR: 1485 nm input laser beam, Ref: timing reference beam, T: translation stage for delaying IR and Ref pulses, $\lambda/2$: half-wave plate, BS: beam splitter, M: mirror, L: lens, F: colored glass filter, SC: streak camera, S: spectrometer, Rb: rubidium vapor cell.

778 nm beam FWHM was 50 μm (vertical) by 55 μm (horizontal), and the 1485 nm beam was 160 μm (vertical) by 100 μm (horizontal) as measured by the knife-edge method.

A Rb vapor cell was inserted into the focal region of the beams, such that the focal point of the 20 cm lens was at the center of the cell. Most of the data displayed in this part were taken at a temperature of about 200 C, giving a Rb density of approximately 9×10^{14} cm^{-3}.

In addition to producing the UV 308 nm and violet 420 nm light mentioned earlier, the cell provided wavelength and timing references. At the beginning of

an experimental run, we sent in only 1485 nm light at high power and produced significant amounts of the third harmonic at 495 nm, which allowed us to fine-tune the input wavelength (1485 nm) of the infrared laser. We occasionally operated the cell at a temperature of 300 C, giving a density of about 2×10^{16} cm^{-3}, and sent in only 1485 nm light producing significant amounts of the fifth harmonic at 297 nm, which was close to the wavelength of the generated UV 308 nm light. The emission of the fifth harmonic is known to be coincident with the incident laser pulse. The arrival time of the fifth harmonic was compared to a reference pulse of 778 nm, as described in the next paragraph.

Before the pellicle beam splitter, the beam at 778 nm passed through a thin glass slide, which was used as a beam splitter and provided a time reference pulse for the streak camera. A second thin glass slide (beam splitter) combined the light from the cell (see below) with the time reference beam before both entered the streak camera. The reference beam was focused by a lens with a 15 cm focal length which is not shown in Fig. 48.

Both the 308 nm and 420 nm light generated in the Rb vapor were emitted primarily in a narrow beam, parallel to the laser beams. The UV beam had a divergence of approximately 5 mrad. Upon exiting the cell, the beams were collimated and made parallel by a lens with a 10 cm focal length. Later, the beams were focused again into the streak camera by another lens with a 15 cm focal length. The different wavelengths were isolated by colored absorption filters which had different thicknesses and were made from different materials, depending on which wavelength we were studying. The non-isolated beam traversed a thin glass slide (beam splitter), sending most of the light toward the streak camera and reflecting some of the light toward the input fiber of the spectrometer (Ocean Optics). This slide was the same one which also deflected the time reference beam into the streak camera, as mentioned above.

3. Results and Discussions

Experimental Results

The delay between red and IR pulses was controlled by a translation stage T, see Fig. 48. For each value of the time delay between the IR and red pulses the spectrum of the generated UV light was recorded. In Fig. 49, the spectral magnitude at 308

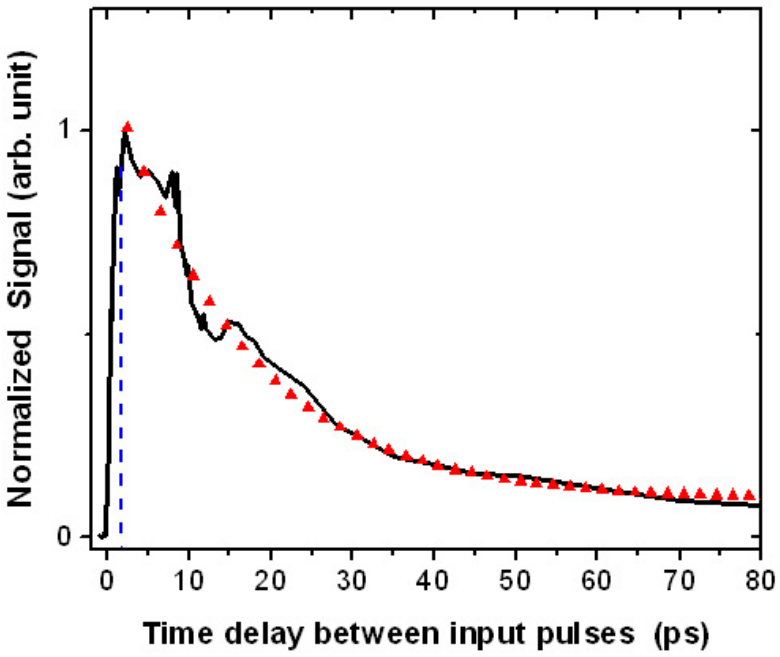

Fig. 49. UV light signal versus time delay. A positive delay means that the IR input laser pulse entered the cell after the red input laser pulse. The triangles show representative points of an exponential fit to the data beyond the maximum of the curve. A strong UV signal, consisting entirely of light at 308 nm, was produced at a time delay of 1.45 ps (dashed vertical line). This particular time delay was used in all of the measurements presented in this part.

nm from the recorded spectra is plotted as a normalized function of time delay. The

delay dependence consists of a steep rising edge followed by a relatively long tail. The tail of the curve can be fitted in the form of $\exp(-\tau/15.8)+0.1$ as a function of time delay τ, where the decay rate is given by approximately 16 ps and the constant 0.1 corresponds to a non-zero background due to fluorescence which is, in this case, on a nanosecond time scale.

The results shown in Fig. 49 can be understood as follows. For the time delay which was comparable with the time duration of the input pulses, the 308 nm emission resulted from a typical four-wave mixing process, $\omega_{UV} = 2\omega_{red} + \omega_{IR}$. Therefore, a steep rising edge of the data curve in Fig. 49 is in quantitative agreement with the temporal overlap of two pulses. For relatively large time delay, the 308 nm emission was suppressed because of the yoked superfluorescence emission [39] via the cascade transition $5D-6P-5S$ which becomes available as the dominant process, see Chapter IV. It is shown below that the 308 nm pulse is emitted simultaneously with the input IR pulse. Therefore, the width of the data curve in Fig. 49 is consistent with the previously observed superfluorescence time delay in Chapter IV. In this spirit, the delayed IR pulse probes the population dynamics of the $5D$ state. As a result of the yoked superfluorescence, the $6P$ state is also populated; thus, not only the $5D$ state but also the $6P$ state can be probed by the delayed IR pulse, inferring from the fact that new lines appeared at 335 nm, 360 nm etc., in addition to the lines at 308 nm and 420 nm in the recorded spectra when the IR delay increased. Although these additional nonlinear processes may be of interest, in this work we considered the small IR delay where only 308 nm signal was dominant. We also avoided the time overlap region between the IR and red pulses because the 308 nm signal was not stable. We chose the IR delay to be 1.45 ps, and the rest of the data was taken at this particular delay, see dashed vertical line at 1.45 ps in Fig. 49. It is obvious that at this delay the generation of the 308 nm pulse was not because of a typical four-wave mixing

process in which all beams are supposed to be present simultaneously.

It is interesting and important to measure the temporal characteristics of the 308 nm light. The 308 nm UV signal was recorded by the streak camera. At the same time, we checked the spectrum to make sure that only 308 nm was present and that the other generated light at different wavelengths, if any, were properly isolated by filters. One of the main results is shown in Fig. 50. The jitter introduced by the laser was carefully corrected shot to shot. After averaging over up to 100 laser shots, the normalized UV signal is plotted by solid curves in Fig. 50. The temporal pulse shape of the UV light had a steep rising edge followed by a slowly decreasing trailing edge. The FWHM of the UV pulse was about 14-16 ps, which is much shorter than the duration of any incoherent processes, including spontaneous emissions, dephasing and Doppler broadening. In the present experiment the variation of the input power was limited because the other unwanted nonlinear processes become dominant for relatively high power (> 2.0 mW), and the signal-to-noise ratio becomes poor for very small power (< 0.3 mW). The power of the input red pulse was changed from 0.3 to 2.0 mW while keeping the IR power constant at 1.2 mW, where 1 mW average power corresponds to 1 μJ/pulse, taking into account the 1 kHz pulse repetition rate provided by the laser system. Peaks of the reference pulses for different input powers were aligned in time, which are not shown in Fig. 50. In this way, the reference beam provided the relative time delay between the reference and 308 nm pulses.

We managed to measure the relative time delay between the IR and 308 nm pulses. The measurement was based on an idea to use the fifth harmonic of the IR pulse. Much denser atomic vapor allowed higher order nonlinear processes to be observable. For instance, at temperature 300 C, where the density was an order greater than that at 200 C, the fifth harmonic 297 nm was generated only when IR beam was present and the red beam was blocked. Conveniently, there was no need to

change the filters, etc., in the setup since 297 nm is close to 308 nm. At temperature 300 C, the fifth harmonic of the IR input beam and reference beam were recorded by the streak camera. After adjusting for the reference pulse timing, the 297 nm signal is plotted by dots in Fig. 50. The 297 nm signal was expected to have the same time duration (100 fs) as the input pulses; instead, however, the FWHM of the 297 nm pulse was about 5 ps. This is because of uncertainty in data processing (jitter corrections) in addition to the limited time resolution of the streak camera. This suggests that the measurement error for data recorded by the streak camera was about ± 2.5 ps.

We can conclude the following from Fig. 50: (i) The rising edge of the UV pulse was approximately determined by the width of the input IR pulse. This means that the 308 nm occurred simultaneously with the input IR pulses (i.e., there was no observable time delay between the 308 nm and IR pulses). (ii) Temporal shape and zero time-delay of the 308 nm pulse were invariant under the variation of the input power of the red pulses used in the current experiment. Note that the situation was completely different when the IR pulse was blocked and only the red pulse was present. In this case, the 420 nm pulse was produced, and the time delay as well as time duration of the 420 nm pulse obviously increased when the input power of the red pulse decreased (see, Chapter IV).

Keeping the red power constant at 1.2 mW and changing the IR power from 0.3 to 2.0 mW, we observed similar temporal behavior as in Fig. 50. In Fig. 51, the curves for the 308 nm pulse did not change with input IR power. There was, again, no time delay observed. In addition, the simultaneous variation of the input powers of both the red and IR pulses also provided the same shape-invariant results. The bottom line is that the 308 nm signal was produced simultaneously with the input IR pulse and that its temporal duration and delay were insensitive to the input powers

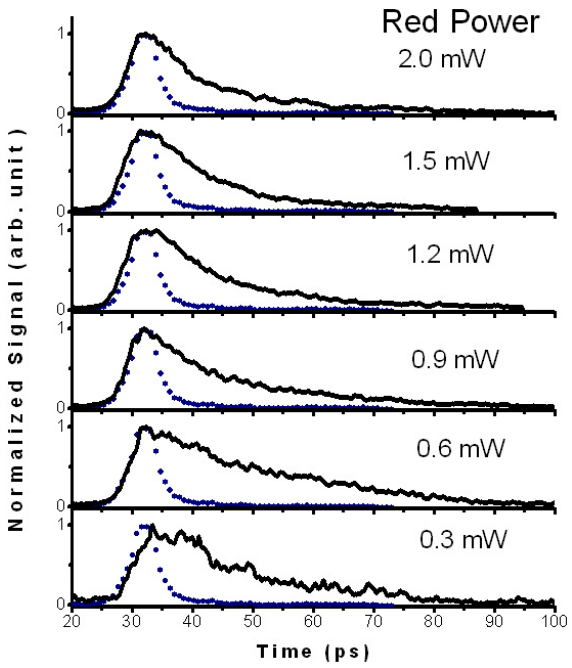

Fig. 50. Temporal behavior of UV light for several red input laser powers. The solid curve shows the UV light signal. The IR input laser power was fixed at 1.2 mW. The dotted curve shows the fifth harmonic of the IR input laser pulse. These signals were aligned using the timing reference pulses, which are not shown in these graphs. Note that the rise and maximum of the UV light signal are coincident with the fifth harmonic signal and are independent of the input red laser power.

in the region from 0.3 to 2.0 mW. In all cases, the trailing edges were well fitted in the form of $8.5 \times \exp(-t/15.8)$ as functions of the time variable t, where the temporal width of the UV pulse was approximately 16 ps. Using a commercial photodetector, we measured the average power for the UV pulse to be 5 nW for an average input power of 1.2 mW for both the IR and red pulses. The conversion efficiency was estimated to be of the order of 0.001%. This efficiency might be improved at least by one order of magnitude over that of the present experiment. For instance, for a fixed input IR power, the red input power can be increased. The spectra of 308 nm signal

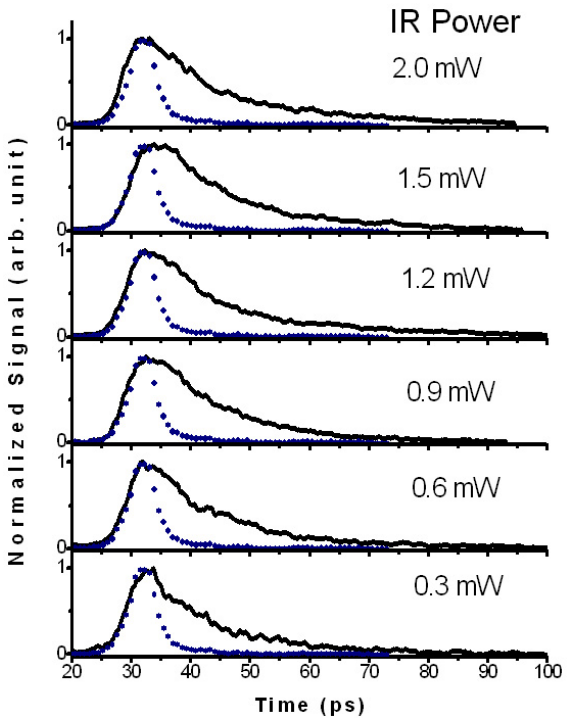

Fig. 51. Temporal behavior of the UV light for several IR input laser powers. The solid curve shows the UV light signal. The red input laser power was fixed at 1.2 mW. The dotted curve shows the fifth harmonic of the IR input laser pulse. These signals were aligned using the timing reference pulses, which are not shown in these graphs. As in Fig. 50, note that the rise and maximum of the UV light signal are coincident with the fifth harmonic signal.

were recorded and the spectral magnitudes at 308 nm are depicted in Fig. 52. By comparing the red power dependencies for two different fixed input IR powers (see, the circles and squares in Fig. 52), the 308 nm signal was improved by 3.5 times. The red power can be further increased before it reaches a saturation region. Note that under the present experimental conditions, the conversion efficiency of the red input light into the 420 nm superfluorescent light was estimated to be 0.06%, an order higher than that for the 308 nm signal. In the recent experiments of Vernier, Akulshin and

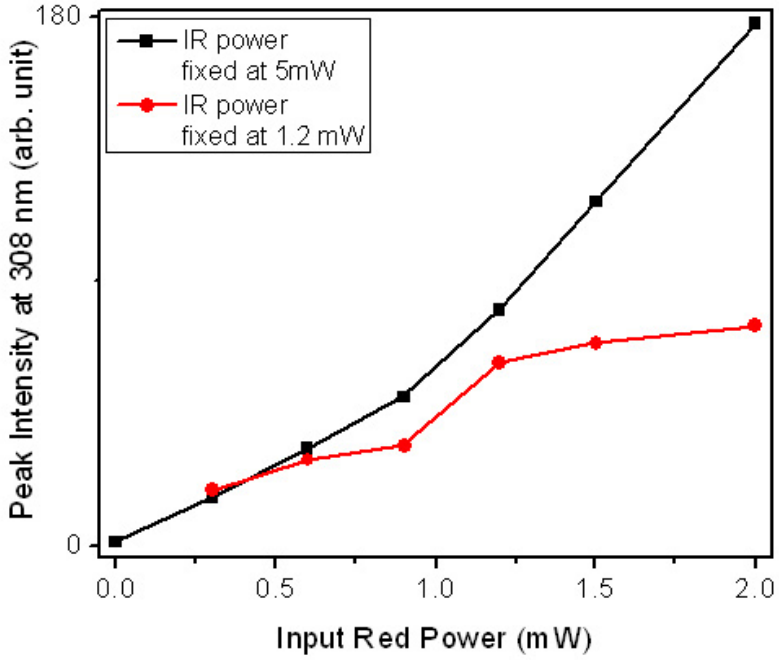

Fig. 52. The spectral magnitude at 308 nm from recorded spectra as a function of input red laser power at IR powers of 5 mW (squares) and 1.2 mW (circles).

Zibrov [131, 133, 134] the conversion efficiency of the red light into the 420 nm light has been improved by several orders of magnitude. In the future, we plan to perform similar experiments to those of Vernier, Akulshin and Zibrov in [131, 133, 134] to improve the conversion efficiencies for both the 308 nm and 420 nm signals.

Approximate Analytical Results

A rigorous mathematical treatment will not be considered in the present part. In this part we only give the simplest, yet promising, explanation to the robustness (or invariance) of the temporal shapes of the UV pulses for variation of the input power.

The input 100 fs pulse excitations can be assumed to be instantaneous. After

instantaneous excitations it is reasonable to consider the three-level atomic configuration. We denote the atomic states $12P$, $5D$ and $5S$ by $|a\rangle$, $|b\rangle$ and $|c\rangle$, respectively. The interaction of the atom with the classical field is governed by the Maxwell-Bloch equations [23] in a retarded time frame. We here adopted the formalism presented in [101, 39]. In the linear approximation we assume that $\rho_{bc} \sim \rho_{bc}(0)$, $\rho_{aa} \ll \rho_{bb}(\rho_{cc})$, $\rho_{bb} \sim \rho_{bb}(0)$ and $\rho_{cc} \sim \rho_{cc}(0)$. The approximate Maxwell-Bloch equations are given by

$$\begin{aligned}
\frac{\partial \Omega_{ac}}{\partial z} &= i\eta_{ac}\rho_{ac} \\
\frac{\partial \Omega_{ab}}{\partial z} &= i\eta_{ab}\rho_{ab} \\
\frac{\partial \rho_{ab}}{\partial t} &\cong i(\Omega_{ab}\rho_{bb}(0) + \Omega_{ac}\rho_{cb}(0)) \\
\frac{\partial \rho_{ac}}{\partial t} &\cong i(\Omega_{ac}\rho_{cc}(0) + \Omega_{ab}\rho_{bc}(0)),
\end{aligned} \tag{7.1}$$

where Ω_{ij} is the Rabi frequency, ρ_{ij} is the atomic density matrix elements and the coupling constant is given by $\eta_{ij} = 2\pi N\mu_{ij}^2\omega_{ij}/c$ with N - atomic number density, μ_{ij} - atomic dipole moment, ω_{ij} - transition frequency between the ith and jth levels, and c - the speed of light. Note that we consider the field to be generated in the axial direction along the z axis. The exact analytical solution of Eq.(7.1) is easily found in terms of the zeroth order Bessel functions $J_0(x)$ as

$$\begin{aligned}
\Omega_{ac}(z,t) &\cong \rho_{bc}(0)\eta_{ac}J_0(2\sqrt{\lambda_1 zt}) - \rho_{bc}(0)\eta_{ab}C \\
\Omega_{ab}(z,t) &\cong \rho_{bb}(0)\eta_{ab}J_0(2\sqrt{\lambda_1 zt}) + \rho_{cc}(0)\eta_{ab}C,
\end{aligned} \tag{7.2}$$

where C is a constant and the eigenvalue λ_1 is given by $\lambda_1 = \eta_{ac}\rho_{cc}(0) + \eta_{ab}\rho_{bb}(0)$. We infer the following important points from Eq.(7.2): (i) There is no exponential growth in the intensity since the solution is not given by the modified Bessel functions. (ii) The obtained solutions predict a zero time delay which is consistent with

the experimental results. However, note that in the case where the solutions are given by the zeroth order modified Bessel functions, a passage-time can be defined to quantify the time delay [25]. (iii) The time dependence of the obtained solution is robust with respect to the variation of atomic populations, where we assume that the atomic populations are proportional to the input laser powers. In the special case of identical coupling constants for the two transitions (i.e., $\eta_{ac} \sim \eta_{ab}$) the eigenvalue becomes independent of atomic populations as $\lambda_1 \sim \eta_{ac}(\rho_{bb}(0) + \rho_{cc}(0)) \sim \eta_{ac}$ where we used $\rho_{aa} \ll \rho_{bb}, \rho_{cc}$. (iv) The zeroth order Bessel function exhibits temporal ringing. Similar temporal ringings for superfluorescence for two-level [18] and three-level cascade atoms have already been studied in Chapter IV. In Figs. 50 and 51, we did not observe the temporal coherent ringing. It is possible that the temporal ringing was washed out by the transverse effect [18] since the input pulses were focused inside the cell. (v) The UV light intensity $|\Omega_{ac}|^2$ is proportional to the coherence term $|\rho_{bc}(0)|^2$. This is a hallmark for coherent Raman processes, which were earlier studied (e.g., in [135]).

Note that all the above points, (i)-(v), predicted from the solution based on the linear approximation, were supported by exact numerical simulations. For instance, for the similar coupling constants the temporal shape was insensitive of input power. The peak intensity was proportional to the square of coherence term $|\rho_{bc}(0)|^2$. Moreover, one can include the yoked superfluorescence process on the transition $5D - 6P - 5S$ and obtain more realistic results. One can even phenomenologically include the population decay to $\rho_{bb}(0)$ as $\rho_{bb}(0) \times \exp(-t/\tau_{Del.SF})$, where $\tau_{Del.SF}$ is the time delay for the yoked superfluorescence. This yields an exact analytical solution similar to Eq.(7.2) but with different eigenvalues. In any case, we believe that the temporal shape would remain relatively unchanged within a certain interval of input power.

4. Conclusion

Rb atomic vapor was excited to the $12P$ state from the $5S$ state on the $5S - 5D$ and $5D - 12P$ transitions by 100 femtosecond laser pulses at 778 nm and 1485 nm, respectively. A bright and directional (coherent) UV light pulse at 308 nm was observed, corresponding to the $12P - 5S$ transition. The arrival of the IR pulse at 1485 nm was delayed with respect to the 778 nm pulse. By varying the delay between the IR and the 778 nm pulses, the fast decay of the $5D$ state was inferred from the observed spectra of the 308 nm light. We observed no delay between the generated 308 nm and input IR pulses, as determined by a streak camera with picosecond resolution. The time duration of the 308 nm pulse was tens of picoseconds. The temporal shape of the 308 nm pulse did not change appreciably when input power varied. This was qualitatively explained by a simple atom-field theory.

We believe the present study will be useful in the production of efficient ultrafast UV pulses in metal vapors with possible applications in ultrafast processes in physics, chemistry, and biology.

B. Picosecond Superradiance in Three-Photon Resonant Medium

1. Introduction

A control of multiphoton ionization of atoms and molecules in gas-phase has been of great interest. In particular, the so-called resonance-enhanced multiphoton ionization (REMPI) is well-established topic. Since the first observation of three-photon resonantly enhanced multiphoton ionization in Xe gas by Miller et al. [136, 137], a suppression (inhibition) in REMPI has been extensively studied [138, 139, 140] (for more recent work, see, e.g., [141]). In their theoretical work [138], Payne, Garret

and Baker first predicted that multiphoton ionization can be affected by cooperative emissions [1] in addition to the third harmonic generation [118]. For 30 years since then, to the best of our knowledge, no experiment on time-resolved study of the interplay between the third harmonic generation [118] and cooperative emission has been reported. Recent technological advances, for example, in ultrafast lasers and streak cameras have made time-resolved study on the above mentioned topic feasible on a picosecond time scale. A picosecond-time resolved study of cooperative emissions in atomic vapor was accomplished in Chapter IV.

2. Experimental Setup

In this part, we investigate ultrafast cooperative emission in Rb atomic vapor. The input laser pulses had about 100 fs time duration. The center wavelength of the input laser from one OPA was tuned to $\lambda_{in} = 1260$ nm which is three-photon resonant to the $6P - 5S$ transition, see Fig. 53. The coherently excited atoms emitted light centered at 420 nm in the direction of the input laser field. A diagram of the experimental setup is illustrated in Fig. 54. The input laser pulse was focused by a lens (f=10 cm) into Rb cell. The cell operated at temperature of about 204 C and provided 9×10^{14} atoms per cm^3. A reference beam at 778 nm (see Fig. 54) furnished by another OPA, was used as a time reference for the recorded pulses by the streak camera. Note that the cell also provided timing in addition to producing 420 nm light. At center wavelength $\lambda_{in} = 1188$ nm, the light at 396 nm, the usual third harmonic of the input field, was dominant in view of recorded spectra. In this off-resonant case, only the third harmonic signal was measurable which was generated simultaneously with the input laser field. The streak camera data exhibited that the generated 396 nm pulse had the same temporal shape as for input laser pulse. Thus, the 396 nm signal was used as a reference pulse for timing the recorded pulses relative to the input pulse.

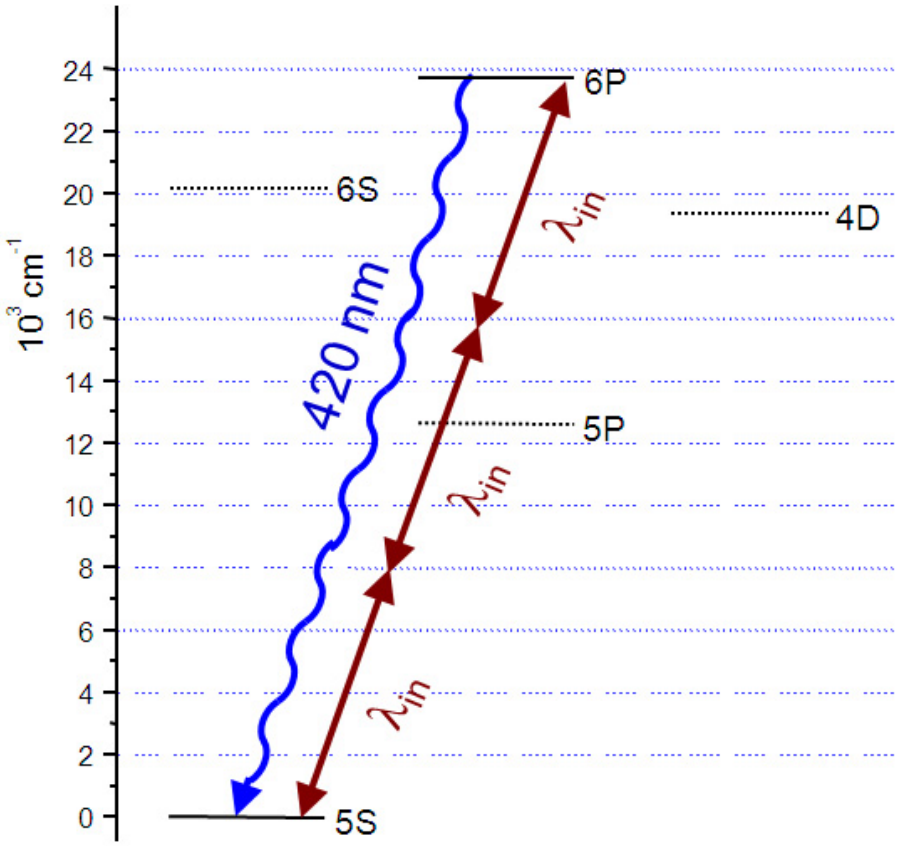

Fig. 53. Rb atomic level scheme. Rb atoms were excited via a three-photon transition to $6P$ from $5S$. The atoms emitted light at 420 nm on the $6P-5S$ transition.

3. Results and Discussions

The main results are summarized in Fig. 55. The 396 nm reference pulses were recorded at input laser power of 4 mW. The 396 nm reference pulses were averaged over up to 100 laser shots. The averaged 396 nm reference pulse is included in the graph (see, sharp peaks filled with dense pattern). The recorded data for the 420 nm pulses were first averaged up to 100 laser shots then, smoothed by adjacent-averaging method using up to 20 data points which are shown in Fig. 55. In Fig. 55, the 420 nm pulse, in general, has a steep rising edge with a moderately long tail. No

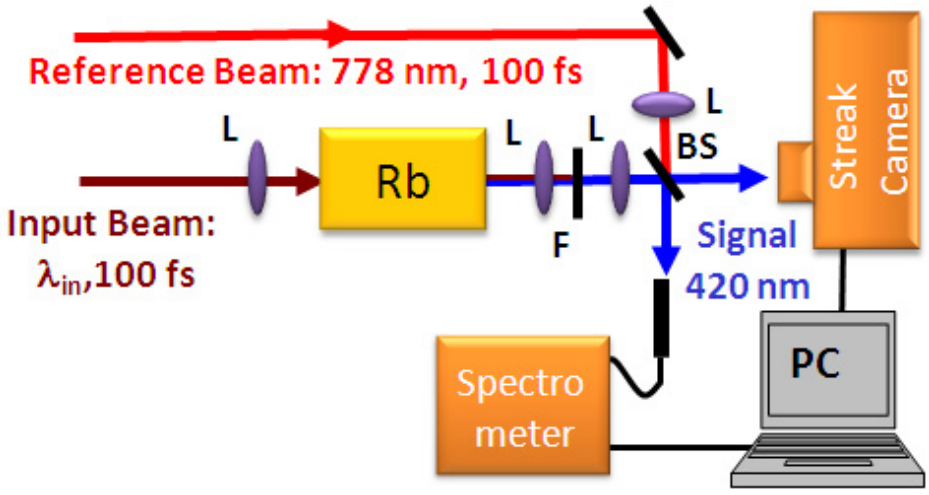

Fig. 54. A diagram of the experimental setup. Rb: rubidium vapor cell, L: lens, F: filter, BS: thin glass plate (beamsplitter), PC: computer. The input light was furnished by the commercial femtosecond laser system. The input laser's center wavelength was tuned to $\lambda_{in} = 1260$ nm. The produced 420 nm light was recorded both by the streak camera and spectrometer. The Rb atomic density was approximately 9×10^{14} cm^{-3}.

measurable delay was observed between the 396 nm reference and 420 nm pulses i.e., the macroscopic dipole of the medium was built-up instantaneously by the 100 fs input laser pulses. The steep rising edge of the 420 nm pulse was determined by time duration of the input laser pulse and independent of input power. In contrast, the pulse tail-part was longer than that of the input pulse. Time duration of the 420 nm pulse was of a few tens of picoseconds and much shorter compared to fluorescence lifetime (0.36 μs on the $6P - 5S$ transition). The atomic coherence dephasing and other incoherent relaxation processes were negligible. The peak of the 420 nm pulse was obtained for each power and reveals a highly nonlinear relation, see Fig. 56(a). A nonlinear dependence was expected because the strength of the macroscopic dipole moment should vary according to input electric field strength. One of the intriguing

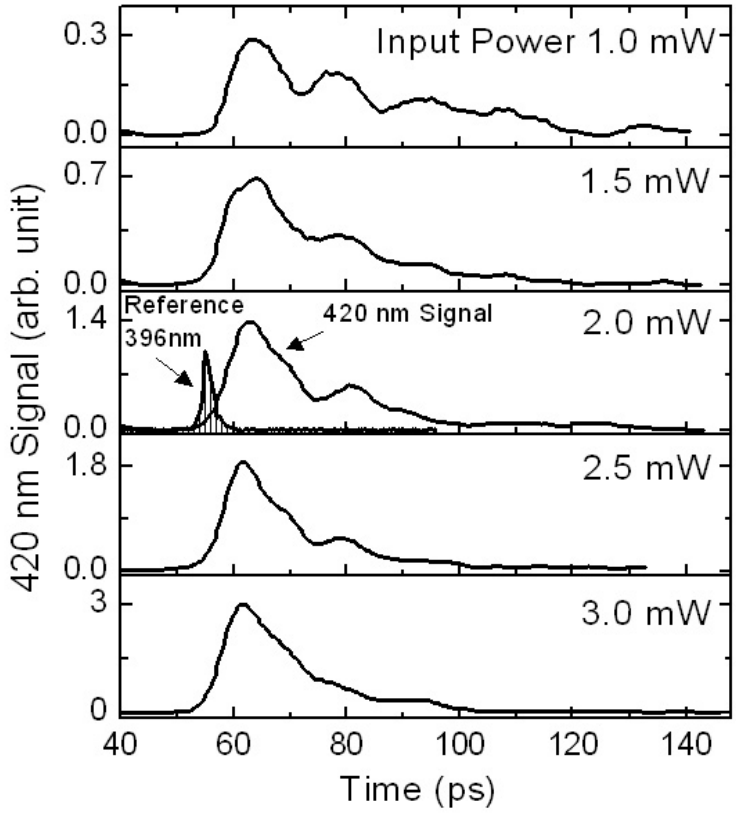

Fig. 55. The streak camera data for the 396 nm reference (curves filled with pattern) and 420 nm pulses. The input beam power was varied from 1 to 3 mW.

feature of SR in the extended medium is the temporal coherent ringing which exhibits no periodic oscillation in time [18]. In our experiment we observed the temporal ringing, see Fig. 55. The input laser beam was focused, thus, emissions of non-uniformly excited atoms in the focal region smeared out the ringing, see, Chapter IV. The pulse temporal shape was fitted by an exponential function in the form of $A\exp(-t/\Delta t) + B$ where t is time variable and a fitting parameter Δt corresponds approximately to the time duration of the 420 nm pulse. The 420 nm pulse duration, Δt is plotted as a function of input power in Fig. 56 (b). In the present work a

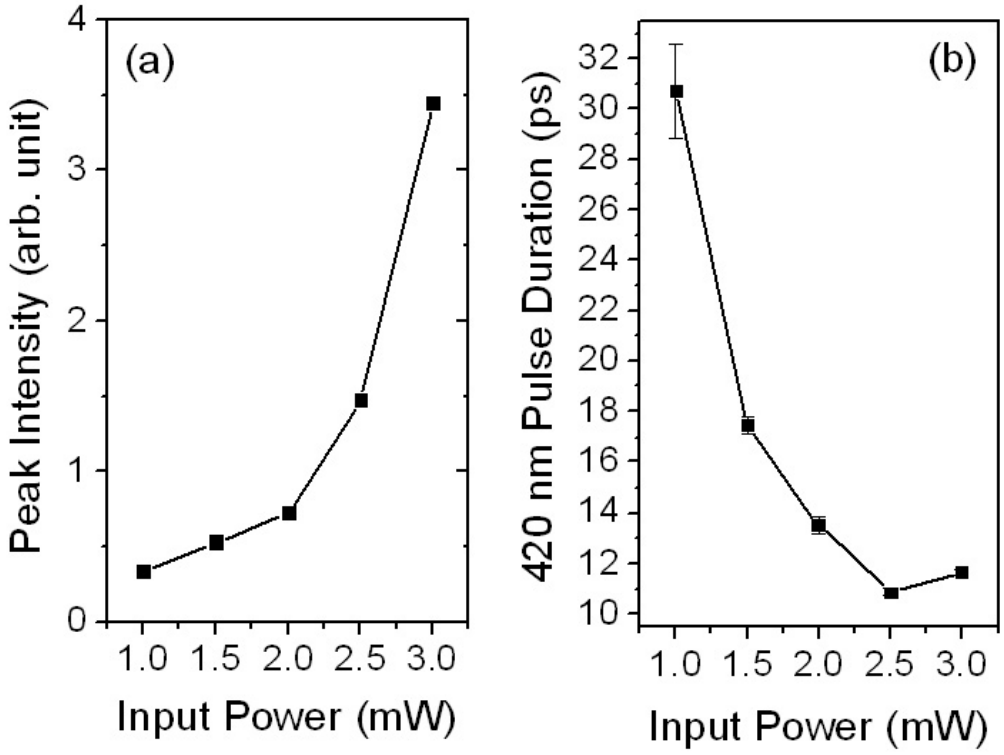

Fig. 56. (a) Time duration of 420 nm pulse as a function of input power, and (b) Power dependence of the peak of the 420 nm pulse.

quantitative analysis was hampered due to limited number of data points and we admit that a rigorous theoretical formalism is needed to clarify our results.

4. Conclusion

As in conclusion, the cooperative emission was observed in the three-photon resonant medium of Rb atomic vapor pumped by 100 fs pulses. We believe that this experimental work demonstrated an importance of cooperative emission e.g., in resonance-enhanced multiphoton ionization. On the other hand, an efficient frequency upconversion has been attracted because of its emerging practical applications, in pho-

tolithography, imaging, optical communications or storage, healthcare, industry and astronomy to name a few. A typical method to produce the frequency upconversion of the input IR light is based on multiphoton nonlinear processes. Considerable interest has been devoted to the frequency upconversion in alkali metal vapors [142] (and see the previous part). In this context, the cooperative emission resulted from the frequency upconversion may be of great interest.

C. Coherent versus Incoherent Raman Scattering: Molecular Coherence Excitation and Measurement

1. Introduction

Raman spectroscopy is a vital and well-established tool that provides insight into molecular structure and its dynamics. It encompasses a variety of techniques, but there are only two distinct underlying processes that form the foundation of Raman spectroscopy. The first process is a spontaneous inelastic scattering of photons of some frequency ω_{pr} on molecular vibrations with a gain or loss of vibrational quanta, ω_v, i.e., $\omega_{SpRaman} = \omega_{pr} \pm \omega_v$. The second one is the coherent anti-Stokes/Stokes Raman scattering (CARS/CSRS) due to the macroscopic oscillations of molecular polarization, induced by pump and Stokes laser fields with the difference frequency, $\omega_p - \omega_s$, tuned close to the vibrational resonance [118]. Conventionally, coherent Raman spectroscopy is considered to be superior to spontaneous Raman measurements because of the enhanced efficiency of the Raman scattering process [82, 143]. The enhancement comes from the presence of the driving fields and the coherent buildup of the generated signal over the sample volume when the phase-matching condition is satisfied. However, the driving-field argument generally implies the use of strong laser pulses with durations, τ, of the order of the decoherence time of molecular vi-

brations or longer. Since the last one usually exceeds the vibration period, T_{vib}, by a few orders of magnitude, the relation $\tau \gg T_{vib}$ is fulfilled. On the other hand, ultrashort pulses, utilized in time-resolved CARS and femtosecond stimulated Raman spectroscopy [120, 121, 123, 144, 145], have a duration of the order of the vibrational period or less. Moreover, the strengths of the driving fields are limited in practice by undesirable processes, such as photodissociation, ionization, self-focusing, and continuum generation. For those reasons, the traditional viewpoint needs to be reevaluated, and a fair comparison between spontaneous Raman and ultrafast coherent Raman spectroscopy should be made.

2. Results and Discussions

We make such a comparison for two strong Raman lines, 992 and 1031 cm^{-1}, in pyridine (C_5H_5N). From the relation [146] (also from Chapter II):

$$\frac{P_{CSRS}}{P_{SpRaman}} \cong \lambda_{pr}^2 \frac{N}{V} \frac{|\rho_{bc}|^2}{\rho_{cc}} \Delta L, \tag{7.3}$$

we also infer the magnitude of the coherence for the excited Raman transitions. Here, P_{CSRS} and $P_{SpRaman}$ are time-averaged total fluxes of the photons generated through CSRS and spontaneous Raman scattering off a particular vibrational mode; λ_{pr} is the wavelength of the probe pulse, ΔL is the length of the medium, and N/V is the concentration of the target molecules; ρ_{cc} is the population of the molecular ground state $|c\rangle$; and ρ_{bc} is the coherence between the state $|c\rangle$ and excited Raman active state $|b\rangle$. It is an off-diagonal element of the density matrix that characterizes the degree to which the molecules in the ensemble oscillate in unison. For straightforward comparative analysis of the two processes, we employ a hybrid technique for CSRS, described in Chapter VI in the context of CARS spectroscopy [147]. This hybrid approach combines broadband pumpStokes excitation with a frequency-resolved probing of molec-

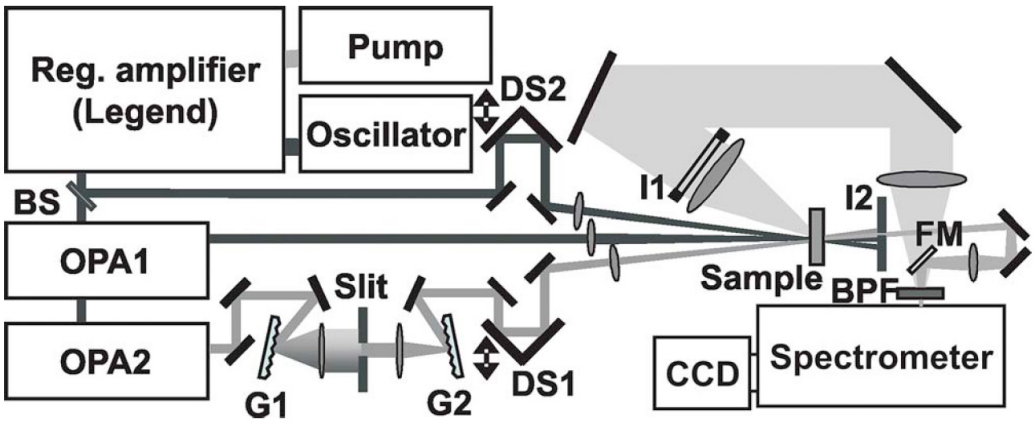

Fig. 57. Schematics of the experimental setup for the spontaneous Raman and CSRS measurements. BS: beam splitter, G1,2: gratings, DS1,2: computer-controlled delay stages, I1,2: irises, BPF: bandpass and neutral density filters, FM: flip mirror, CCD: imaging charge-coupled device.

ular vibrations by an optimally delayed narrow-band laser pulse. Conveniently, in such a scheme the same narrow-band laser pulse can be used for spontaneous Raman measurements. Only the differences in the collection of the generated signal have to be taken into account (see Fig. 57). We utilized the commercial femtosecond system with two OPAs. The output of the first OPA and a small fraction of the regenerative amplifier output were used as pump ($\lambda_p = 738$ nm) and Stokes ($\lambda_s = 802$ nm) beams. The output of the second OPA, the probe beam ($\lambda_{pr} = 577.9$ nm), was sent through a homemade pulse shaper with an adjustable slit in its Fourier plane. The three beams were overlapped in a boxcar geometry (under 5 to each other) and focused on a sample. The FWHMs of beam diameters in the focal plane were about 57, 75, and 47 μm for the pump, Stokes, and probe, respectively. The collection part for CSRS and spontaneous Raman photons differed. While the directional CSRS beam was spatially filtered with a small-aperture iris, the incoherently scattered light was

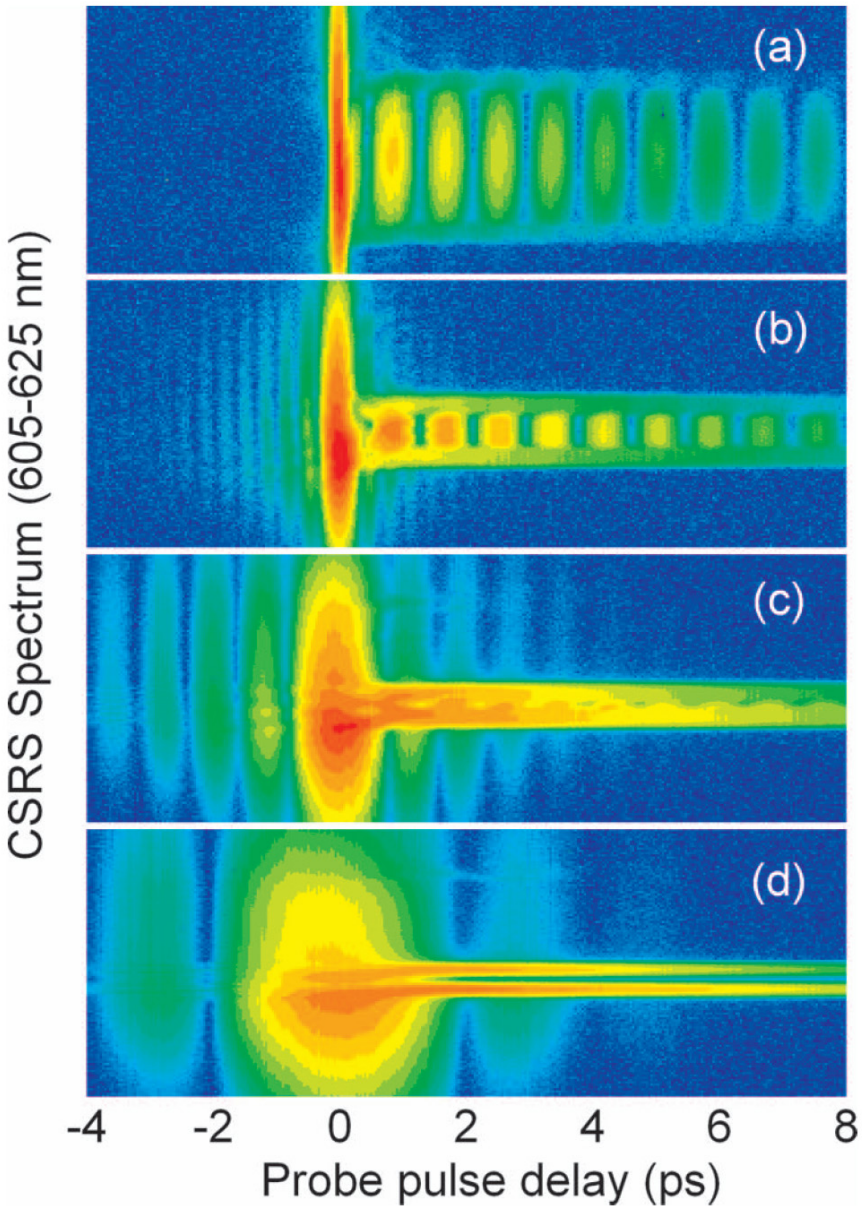

Fig. 58. Transition from time-resolved to hybrid CSRS. CSRS spectrograms for different spectral bandwidths of the probe pulse: (a) 300 cm^{-1}, (b) 100 cm^{-1}, (c) 40 cm^{-1}, (d) 15 cm^{-1}. Two Raman lines of pyridine, 992 and 1031 cm^{-1}, are excited via a pair of ultrashort laser pulses. Pump: λ_p = 737 nm, FWHM $\approx$ 260 cm^{-1}, 0.5 μJ/pulse. Stokes: λ_s = 801 nm, FWHM $\approx$ 480 cm^{-1}, 0.9 μJ/pulse. Probe:λ_{pr} = 577.9 nm, 0.15 μJ/pulse.

collected from the back of the sample (under 30 to the main axis) with a 2 in. short-focal lens (f=10 cm). Each of the two acquired signals was sent through the same set of bandpass filters and refocused onto the entrance slit of a spectrometer with a liquid-nitrogen-cooled CCD. The employed hybrid technique can be best understood through its comparison with time-resolved CARS (CSRS) [120, 121, 123, 144]. Figure 58 illustrates the transition from the traditional time-resolved measurement of free-induction decay in pyridine to the frequency-resolved one while the bandwidth of the probe pulse was reduced from 300 cm^{-1} to 15 cm^{-1}. The beating pattern between two excited Raman modes, 992 and 1031 cm^{-1}, gradually transformed into a couple of spectrally isolated streak lines. The smooth FWM profile was due to multiple off-resonant vibrational modes and the instantaneous electronic response stretched along the time axis (indicating the expected lengthening of the probe pulse) and gained side-fringes due to the rectangular-like spectral amplitude transmission mask. A cross section of the spectrograms for the narrow-band probe at some fixed positive delay gives a CSRS spectrum. It is advantageous to pick up the delay corresponding to the first node of the FWM. For such a delay, one gets strong CSRS signal without the interfering non-resonant background. Spontaneous Raman and CSRS spectra of the excited vibrational modes, acquired with a 200 μm cuvette of pyridine, are shown in Fig. 59. The spontaneous Raman measurements were performed with the pump and Stokes beams blocked. The integration time was 3 min. The CSRS spectrum was acquired for the close-to-limit pump and Stokes pulse energies. They were 0.74 and 1.36 $\mu J/pulse$, respectively. We estimate their peak intensities on the sample to be about $4 \times 10^{11} W/\mathrm{cm}^2$. The integration time was only 1 s even after 10^4-fold attenuation of the CSRS photon flux. The probe delay relative to the preparation pulses ($\sim$ 1.8 ps) was chosen to get rid of the non-resonant background contribution while keeping the CSRS signal amplitude close to the maximal. The numbers clearly indi-

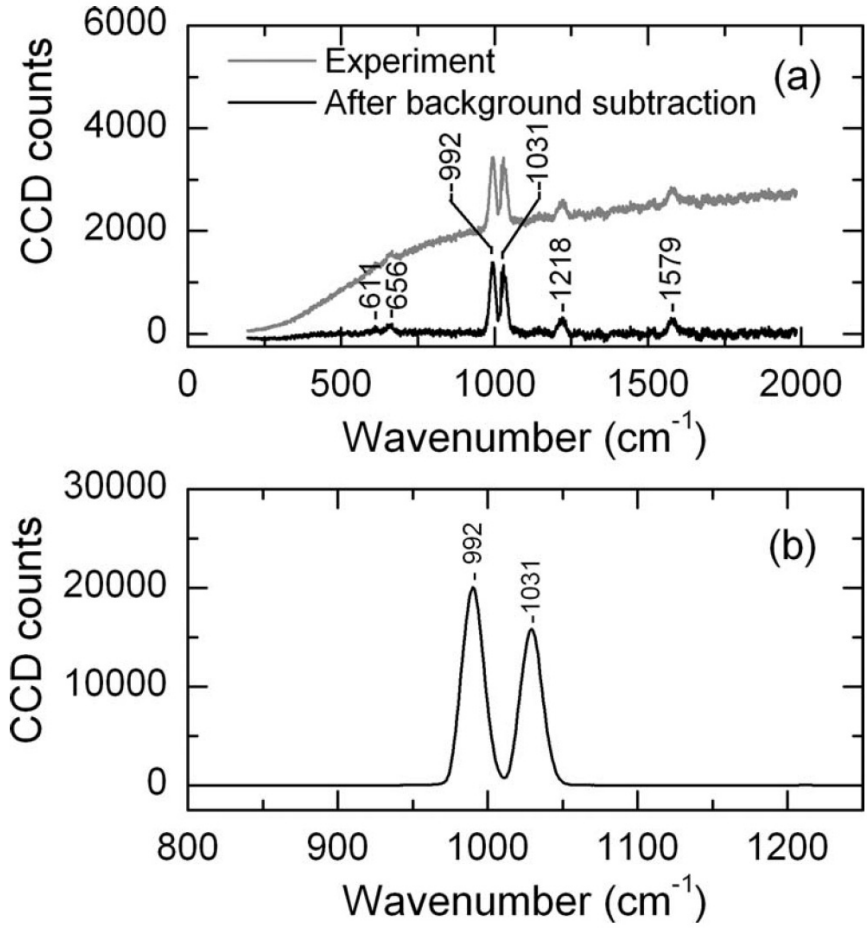

Fig. 59. Spontaneous Raman and CSRS measurements on pyridine: (a) spontaneous Raman spectrum. Probe pulse: λ_{pr}=577.9 nm, FWHM $\approx$ 19 cm^{-1}, the average power is 0.13mW (0.13μJ/pulse, 1 kHz rep rate). The integration time is 3 min. The estimated collection angle $\Omega_{eff} \approx 0.004 \times 4\pi$. The cuvette path length is 200μm. (b) CSRS spectrum. The probe delay relative to the preparation pulses is fixed and equal to 1.8 ps. At this delay, the nonresonant background is suppressed, since the preparation pulses are overlapped at the node of the probe pulse profile [see the spectrograms in Fig. 58(d). Pump: λ_p = 738 nm, FWHM $\approx$ 260 cm^{-1}, 0.72 μJ/pulse; Stokes: λ_s = 802 nm, FWHM $\approx$ 480 cm^{-1}, 1.36 μJ/pulse. Probe parameters and the sample are the same as in part (a). Integration time is 1 s after 10^4-fold attenuation by a set of neutral density filters.

cate that the efficiency of CSRS process is much higher than of spontaneous Raman scattering. However, their quantitative comparison requires some analysis of the light collection. Indeed, while virtually all CSRS photons contributed into the spatially filtered beam of the coherently scattered light, only a small fraction of spontaneous Raman photons was collected with the 2 in. lens. We estimate the effective collection angle, Ω_{eff}, to be $0.004\times4\pi$, and therefore, for the two excited Raman transitions (992 and 1031 cm^{-1}),

$$\frac{P_{CSRS}}{P_{SpRaman}} = \frac{P_{CSRS}}{P^{c}_{SpRaman} \times (4\pi/\Omega_{eff})} \approx 10^{5}. \tag{7.4}$$

Here, $P^{c}_{SpRaman}$ stands for the time-averaged flux of the spontaneously scattered photons collected in the experiment. From the parameters of the cell, it is reasonable to infer that $\Delta L \approx 200\mu m$. This assumption was confirmed by the proper scaling of the number of the acquired photons when the 200μm cuvette was substituted with a $100\mu m$ one. Namely, we observed a reduction by a factor of 2 and 4 for the spontaneous Raman and CSRS signal amplitude, respectively. Putting in $\Delta L = 200\mu m$, the density of pyridine molecules, and the probe wavelength, we have $(N/V)\lambda^{2}_{pr}\Delta L \approx 5 \times 10^{11}$. Since the thermal population of the excited Raman states is negligible, we take $\rho_{cc} \approx 1$ and using (Eqs. (7.3) ,(7.4)) get $\rho_{bc} \approx 0.5 \times 10^{-3}$ with a 30% uncertainty from one measurement to another due to alignment. A crude estimate of the expected magnitude of the coherence, $\rho_{bc} \approx |\Omega^{*}_{p}\Omega_{s}/\Delta|\tau$, from the solution of the density matrix equations gives $\rho_{bc} \sim 10^{-2}$, which is in reasonable agreement with the retrieved values. Here, $\Omega_{j} \equiv \wp_{j}E_{j}/(2\hbar)$ stands for Rabi frequencies of the pump and Stokes fields, Δ is the detuning from the electronic resonance, and τ is the pulse length. For the estimate, we take the dipole moments to be 1 D, $\tau \sim 50$ fs, and the detuning $\Delta L \approx 3 \times 10^{15} rad/s$, since the closest absorption band of pyridine is at $\lambda \sim 260$ nm. As one can see, the coherence is far from maximal ($\rho_{bc} \ll 0.5$).

The observed 10^5-fold gain in the efficiency of the coherent Raman scattering over the incoherent one comes entirely from the phase-locked accumulation of the signal over the active volume. For similar excitation strength but $\Delta L \sim 1\mu m$, typical for microscopy [146], one would have $P_{CSRS}/P_{SpRaman} \approx 500$.

3. Conclusion

We performed comparative spontaneous and coherent Raman measurements on pyridine. Background-free coherent Raman spectra were acquired by means of the hybrid CSRS technique. We quantified the increase in the efficiency of Raman scattering process due to the broadband pump Stokes excitation of molecular vibrations and retrieved the coherence amplitude for the corresponding Raman transitions. In particular, we demonstrated that for the 200 μm interaction length and reasonably high energies of the preparation pulses ($\sim$ 1 μJ/pulse, $\sim$ 50 fs; the estimated peak intensity is $\sim 4 \times 10^{11} W/\text{cm}^2$), the number of CSRS photons exceeds the number of spontaneous Raman photons by five orders of magnitude. The coherence amplitude for the excited molecular vibrations was determined experimentally, with no *ab initio* calculations involved. The procedure separates out the preparation and probing of the coherence, which can be useful for analyzing of complex molecular systems.

CHAPTER VIII

ACCOMPLISHMENTS TOWARDS PRACTICAL APPLICATIONS*

In this chapter, we first demonstrate SOS in dye solution and then detection of bacterial spores at a single laser-shot level.

Two aspects of the SOS Technique [99] were demonstrated using a femtosecond laser system and an organic dye. First, three cells of a solution of Rhodamine B dye in ethanol were pumped with a single wavelength. Amplification of the light generated by two-photon absorption occurred when the pulses were overlapped temporally, in a direction opposite to that of the pump laser beam. Second, the dispersion of the dye solution permitted two pulses of different wavelength to overlap at a specified location in the solution. The overlapped pulses generated light as the result of two-photon absorption in both the forward and backward directions, relative to that of the pump laser beam.

Recent advances in coherent Raman spectroscopy hold exciting promise for many potential applications. For example, a technique, mitigating the non-resonant four-wave-mixing noise while maximizing the Raman-resonant signal, has been developed and applied to the problem of real-time detection of bacterial spores. After a brief review of the technique essentials, we show how extensions of our earlier experimental

---

*Part of the data reported in this chapter is reprinted with permissions from "A model experiment for stand-off sensing" by G.O. Ariunbold, M.M. Kash, H. Li, V.A. Sautenkov, Yu.V. Rostovtsev, G.R. Welch, and M.O. Scully, 2008. *J. Mod. Opt.*, 55, 3273-3281, Copyright [2008] by Taylor & Francis, and "Single-shot Detection of Bacterial Endospores via Coherent Raman Spectroscopy" by D. Pestov, X. Wang, G. O. Ariunbold, R. K. Murawski, V. A. Sautenkov, A. Dogariu, A. V. Sokolov, and M. O. Scully, 2007. *PNAS*, 105, 422-427, Copyright [2008] by The National Academy of Sciences of the USA

work (Chapter VI) yield single-shot identification of a small sample of Bacillus subtilis spores ($\sim 10^4$ spores). The results convey the utility of the technique and its potential for on-the-fly detection of biohazards, such as Bacillus anthracis. The application of optimized coherent anti-Stokes Raman scattering scheme to problems requiring chemical specificity and short signal acquisition times is demonstrated.

A. A Model Experiment for Stand-Off Sensing

1. Introduction

Stand-Off Sensing (SOS) is a remote detection method for chemical species with the potential of high sensitivity and specificity. Applications might include monitoring atmospheric quality, observing environmental stress such as fire smoke, and detecting and identifying chemical warfare agents. These samples might be located at distances of 1 to 100 kilometers from the detection system. The theoretical details of this scheme have been discussed elsewhere [99], but a brief description of the ideas is in order here. These concepts are illustrated in Fig. 60.

A pair of laser pulses with different wavelengths is directed toward a region containing a suspect chemical. Because of the dispersion of the potentially contaminated atmosphere, the time between the pulses controls at what distance from the lasers the pulses will overlap; that is, when the faster, longer-wavelength pulse will catch up with the slower, shorter-wavelength pulse. The wavelengths are selected so that, for the chemical under consideration, neither pulse by itself causes much excitation of the sample. Together, however, the pulses produce a strong signal if, and only if, the suspected chemical is present. Because this is a coherent excitation process, the light resulting from this excitation travels primarily parallel (forward) and antiparallel (backward) to the laser beams. We wish to detect this signal light back

at our lasers. The first pair of pulses is followed by a second pair of pulses with a

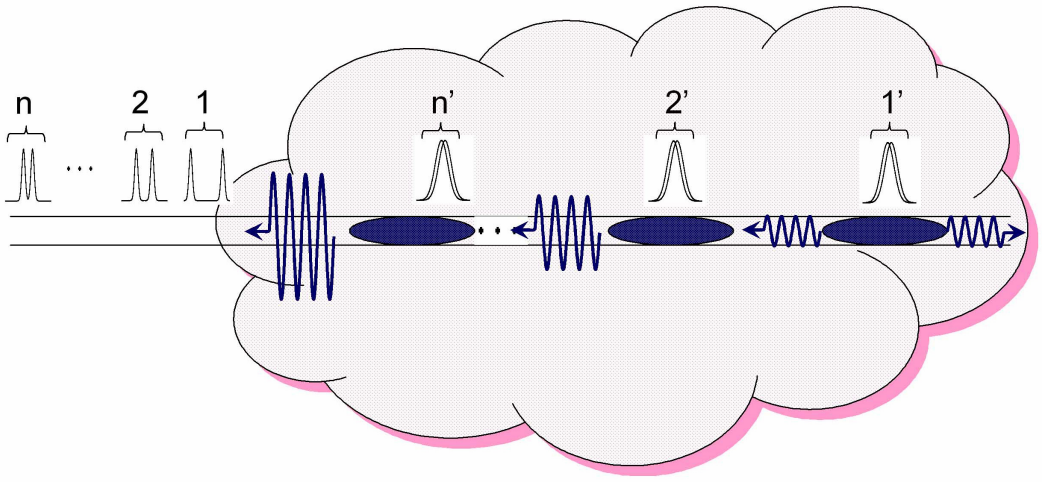

Fig. 60. SOS concepts. Several pairs of laser pulses would be directed toward a region containing a suspect chemical. In each pair, the second member would have a longer wavelength than the first. Because of the dispersion of the medium, the members of each pair would overlap at a position determined by the initial time interval between the members of the pair: separated pairs 1, 2, ..., n would later become overlapped pairs 1', 2', ..., n'. The chemical would emit light where the pulses overlap (1'), primarily parallel and antiparallel to the lasers. Subsequent pulse pairs (2', ..., n') would amplify the backward-traveling signal.

smaller time interval. This second pair overlaps at a position between the location of the overlap of the first pair and the location of the lasers. The second pair creates a region of gain, which can amplify the backward-traveling signal that reaches the gain region, as long as the timing is just right. More pairs of pulses with shorter time intervals, and sent out later from the lasers, can create additional volumes of excited molecules that can further amplify the backward-moving signal.

Though related to LIDAR and LIDAR's more revealing refinement, DIAL [148,

149], SOS offers several potential advantages. The large pulse energy available from modern lasers allows, in principle, the possibility of detection and identification of targets with only a single set of laser pulse pairs. This implies that the method may take less than a second to detect the specified chemical. Furthermore, the SOS method should be able to be used in daylight.

This part reveals the experimental progress toward implementing the SOS method. Two important aspects of the technique are shown here: amplifying the light signals at several regions, or distributed gain, and overlapping of the laser pulses at a predetermined location, or pulse catch-up. The experiment was scaled down to table-top size by using a dye solution, which has much greater dispersion and two-photon emission than the terrestrial atmosphere.

Although the energy-level structure of dye molecules in solution is complicated, many dyes have been well studied. We found the work of Xu and Webb [150] to have been particularly helpful in both the selection of the dye and in the choice of wavelengths. There were two main criteria in our project: First, the solution had to have little one-photon absorption at our laser wavelengths, so that the laser beams would not be completely attenuated upon entering the medium. Second, the solution had to emit light when absorbing two photons with the proper wavelengths from the laser pulses. The details of our study of distributed gain and pulse catch-up appear below.

2. Distributed Gain

Figure 2(j) in Xu and Webb [150] gives the two-photon absorption cross-section of Rhodamine B in methanol as a function of the wavelength of an excitation laser. The curve shows that the dye solution emits relatively large amounts of approximately 600 nm (orange) light when irradiated with laser pulses at about 800 nm. In our

work, the dye was dissolved in ethanol with a concentration of 1.0 g/L. A schematic

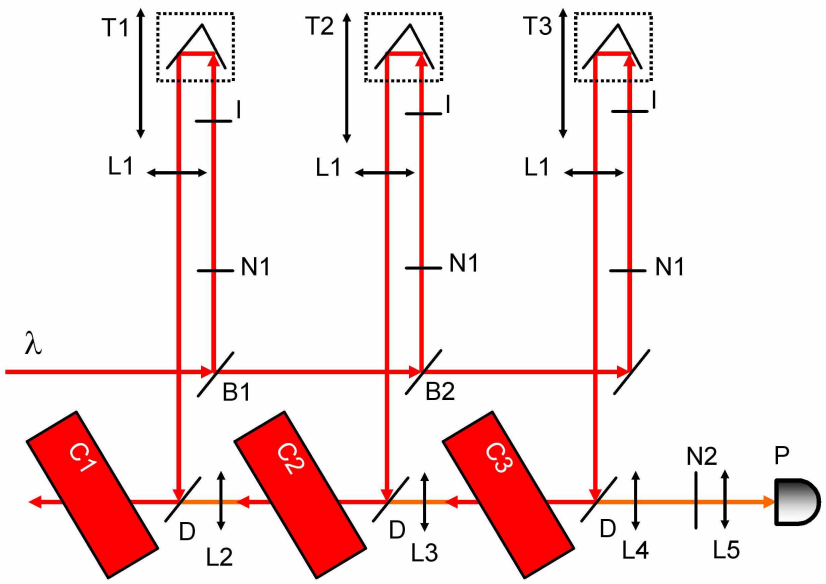

Fig. 61. Distributed gain schematic diagram. A laser beam (λ) was split into three branches, each of which possessed a variable path length to control the travel time of the laser pulses. Three dye cells were pumped by these laser beams, arranged so that the backward-traveling light generated in the dye solution was amplified. Components - B1, B2: beam splitters; C1, C2, C3: dye cells; D: dichroic mirrors; I: iris diaphragm; L1, L2, L3, L4, L5: lenses; N1, N2: neutral density filters; P: photodiode detector; T1, T2, T3: translation stages; λ: 804 nm laser beam.

diagram of the apparatus that we used to exhibit distributed gain is presented in Fig. 61. The goal of the optical system was to deliver laser pulses to three dye cells (C1, C2 and C3). The timing of these pulses was variable and could be selected to control the amplification of the generated orange light. Dichroic mirrors (D) were employed to make the laser beams and the generated orange light beams parallel. Importantly, the optics were arranged so that part of the generated light from cell C1

and the amplification from cells C2 and C3 were backward-traveling with respect to the pump laser.

Laser pulses at 804 nm were provided by the Legend amplifier. The pulses were approximately 50 fs in duration. The beam diameter was approximately 3 mm. The energy of the pulses was of order 1 mJ. This energy was greater than that needed for our experiment, and the laser was attenuated by a 3 mm thick glass filter, which transmitted about 50% of the average laser power.

Two beam splitters divided the laser beam into three branches. Each branch had approximately the same power as the result of using the following scheme: The first beam splitter (B1) reflected about 30% of the light, and transmitted about 70%, while the second (B2) transmitted and reflected about 50% of the light transmitted by the first beam splitter (B1). These were dielectric beam splitters on a 1.0 mm thick substrate of BK7 glass. Each branch contained a continuously variable metallic neutral density filter (N1), made of 2.0 mm thick UV grade fused silica, and an iris diaphragm (I).

The path length of each branch could be precisely varied, but the reflectors were carefully aligned so that changing the path length did not change the location of the beam. The beam in the first branch was reversed by two silver mirrors oriented at a right angle and mounted at on a translation stage (T1). The beams in the second and third branches were reflected by corner-cube retroreflectors (Newport UBBR2.5-2UV) mounted on translation stages (T2 and T3). These retroreflectors were designed for reflecting blue light, and reflected about 50% of the laser beam power. Mirrors attached to flip mounts (not shown) allowed the power in each branch to be measured upstream of the reflectors on the translation stages.

The dye solution was circulated through three flowing cells (C1, C2, C3; Starna 46-Q-10 quartz spectrophotometer flow cells), which were connected in series. Each

of the three branches of the laser was focused into the center of its corresponding dye cell by a lens (L1) with a focal length of 50 cm. The laser light in each of the branches was deflected into its corresponding cell by using custom-made dichroic mirror (D) from CVI, Model SWP-45-RP800-TP610-PW-0504-C, constructed on 1 mm thick BK7 glass. The dichroic mirror reflected the 800 nm laser light, but transmitted the orange light at 600 nm generated in the dye solution. This arrangement allowed the laser beam and the backward-directed orange light to be parallel. The orange light from the first cell (C1) was coupled to the second cell (C2) by a 2.5 cm focal length lens (L2), and the orange light from the second cell (C2) was coupled to the third cell (C3) by a 3.0 cm focal length lens (L3). The flow cells were slightly turned so as not to be normal to the laser beams, in order to avoid etalon effects. The internal geometric path length in each cell was approximately 1.1 cm.

The orange light from the third cell (C3) was our signal. The beam was collimated by using a 10 cm focal length lens (L4), attenuated as needed by Thorlabs Model NDXXB calibrated reflective metallic neutral density filters (N2) on 0.10 cm thick BK7 glass substrates, and lastly focused by a 15 cm focal length lens (L5) onto a Thorlabs Model DET210 fast photodiode detector (P). A digital storage oscilloscope displayed and recorded the signals.

Our results are displayed in Fig. 62, which shows the size of the amplified orange light pulse as measured by the photodiode P as a function of the timing of the laser pulses that enter cells C2 and C3; i.e., the positions of translation stages T2 and T3. The average laser powers into cells C1, C2 and C3 were 16.0 mW, 5.5 mW and 3.5 mW, respectively, uncorrected for the reflectance of the retroreflectors in the second and third branches. These powers remained constant during the collection of the entire data set. The amount of generated orange light remained constant throughout most of the data collection, but decreased somewhat at the end of the data run. We

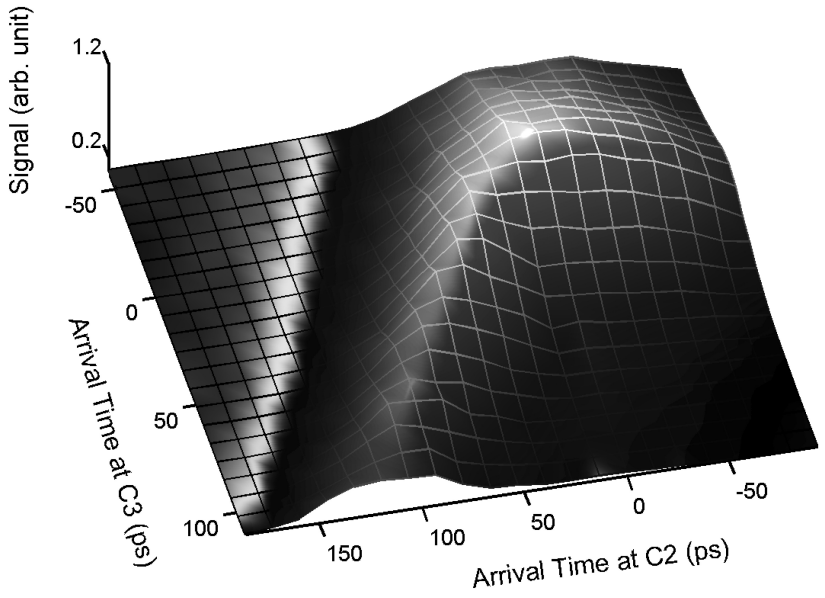

Fig. 62. Amplification by dye cells. The signal of the generated light from cell C3 (see Fig. 61) was plotted as function of the arrival time of the laser pulses at cell C2 and cell C3. These arrival times were controlled by the position of translation stages T2 and T3, respectively. The zeros of the time axes were taken to be at the settings of the translation stages that gave the maximum signal. Positive arrival times indicate that the pulses arrive later than the time for maximum signal.

averaged 5000 pulses to obtain each signal data point, in order to reduce the effect of fluctuations in the energy of the laser pulses. The positions of the translation stages in the second and third branches were varied and converted to the arrival time of the laser pulses. The zeros in the arrival time of the second and third branches were taken at the location of the absolute maximum signal. A positive delay time means that the path length of that branch was increased.

The data show both local and absolute maxima in the signal. The local maxima indicate the amplification of the signal from cell C1 by cell C2 or cell C3, and also the

amplification of some signal from cell C2 itself by cell C3. The absolute maximum marks the condition of timing for which the signal from cell C1 is amplified once by cell C2 and again by cell C3.

To estimate the magnitude of the amplification, we set the translation stages to produce the absolute maximum signal, and observed the effect of blocking the lasers into each cell. The laser powers were set to the values listed above. With only cell C1 pumped, the signal from cell C3 was 0.07 arb. unit; with cells C1 and C2 pumped, the signal from cell C3 was 0.88 arb. unit; with all three cells pumped, the signal from cell C3 was 13.0 arb. unit. With only cell C3 pumped, the signal from cell C3 was 0.38 arb. unit. The total gain of the second and third cells was about 190. By increasing the laser powers to the cells, we were able to obtain a total gain of about 1100.

It is useful to consider the scalability of our model experiment to a detector of trace contaminants in the atmosphere. For our experiment on distributed gain, the density of Rhodamine B was of order 10^{18} molecules/cm^3. An atmospheric contaminant at 10 ppm corresponds to a density of order 10^{14} molecules/cm^3. Clearly, our present setup would give a very small signal, and a practical atmospheric detector would require many more gain regions and more sensitive detectors.

3. Pulse Catch-up

Figure 3(j) in Xu and Webb also shows that Rhodamine B dye solution emits relatively small amounts of orange light when irradiated with laser pulses at 750 nm or 870 nm. Note, however, that the energy gained by the dye when absorbing one photon at 750 nm and one photon at 870 nm is nearly the same as the energy gained when absorbing two photons at 800 nm. This means that the dye will emit more orange light at locations where the two laser pulses are overlapped than at places where only

one laser pulse is present. For this project, the dye was dissolved in ethanol at a concentration of 4.0 g/L. A schematic diagram of the apparatus used to demonstrate

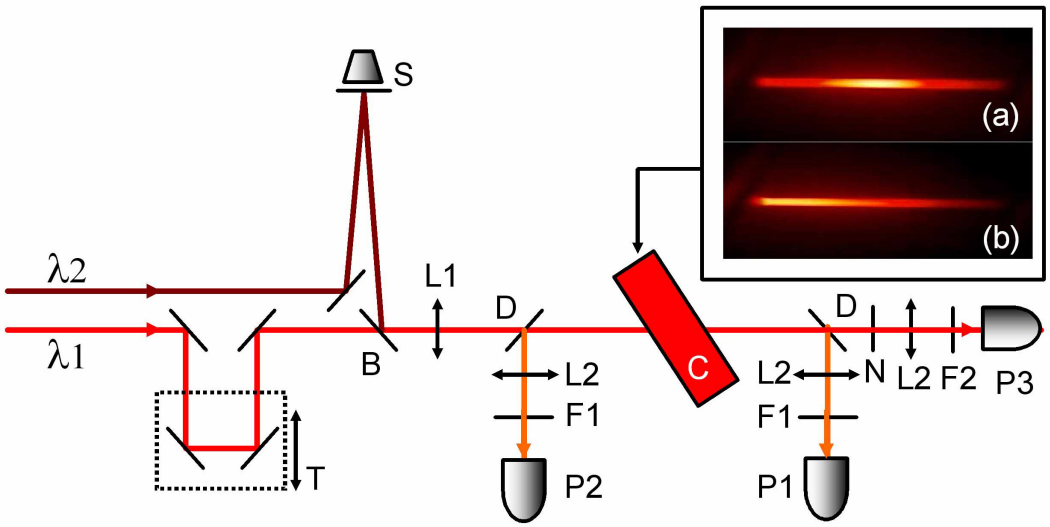

Fig. 63. Pulse catch-up schematic diagram. Components - B: beam splitter; C: dye cell; D: dichroic mirrors; F1, F2: filters; L1, L2: lenses; N: neutral density filter; P1, P2, P3: photodiode detectors; S: loudspeaker; T: translation stage; $\lambda 1$: 750 nm laser beam; $\lambda 2$: 870 nm laser beam.

pulse catch-up is shown in Fig. 63.

The system was designed to provide a pair of different-colored pulses to one dye cell (C). These components allowed us to control the delay between the pulses, make the two laser beams collinear, and measure the amounts of forward- and backward-traveling orange light generated by the dye, as well as the amount of laser light transmitted by the cell.

Laser pulses with wavelengths of 750 nm and 870 nm were furnished by the doubled signal and doubled idler outputs of a Coherent Opera optical parametric amplifier. This device was pumped by the output of the Coherent Legend amplifier described above. The linewidth of the 750 nm light was about 14 nm, and that

of the 870 nm light was about 23 nm, as measured by an Ocean Optics USB2000 spectrometer.

We made a preliminary measurement of the dispersion of the dye solution. Collimated and collinear beams of light from the two lasers were directed through an empty (air-filled) dye cell, and then were focused onto a thin glass slide. The time delay between the pulses was adjusted until four-wave mixing was observed from the slide. Then the cell was filled with dye, and the time delay of the 870 nm laser pulses was increased until four-wave mixing was again observed. The time delay was 0.24 ps for the 1.1 cm path length. This gives a difference in the effective refractive index of 0.0066 for the two lasers, with the smaller index for the 750 nm laser light. Therefore, the 870 nm pulses caught up to the 750 nm pulses in the cell filled with dye solution.

The 750 nm laser light traveled to two mirrors oriented at a right angle and mounted on a translation stage (T), and subsequently was transmitted through a beam splitter (B). The 870 nm laser light moved toward a mirror mounted on a loudspeaker (S), and then was reflected from the same beam splitter, aligned so that the two laser beams were collinear in the dye cell (C). We confirmed that the loudspeaker motion did not move the 870 nm laser beam. The beam splitter was a broadband dielectric component on BK7 glass substrate, nominally 50% transmitting and 50% reflecting. Consequently, the useful power from each laser beam was reduced by a factor of 2. A mirror attached to a flip mount (not shown) was located just after the beam splitter (B), which allowed us to measure the laser power going into the cell.

The lasers were focused by a 15 cm focal length lens (L1) to the center of a flowing dye cell (C), with specifications given above. Using the knife-edge technique, we measured the beam diameters in the cell to be 0.032 mm for the 750 nm beam and 0.035 mm for the 870 nm beam. After passing through the cell, the lasers were

attenuated by Thorlabs Model ND20B 1% transmission reflective metallic neutral density filter, focused by a 5 cm focal length lens (L2), and isolated by a CVI Model LPF-800-1.00 longpass interference filter, with a cut-on wavelength of 800 nm. The lens focused the light onto a Thorlabs Model DET 210 fast photodiode detector. This detector P3 produced a signal proportional to the amount of 870 nm laser light transmitted by the cell.

We separated the generated orange light from the 750 nm and 870 nm laser light by using a pair of dichroic mirrors (D) surrounding the cell (C). These mirrors (Thorlabs Model FM03 "cold mirror") transmitted more than 85% of the laser light and reflected more than 90% of the orange light. The orange light in each branch was focused by a 5 cm lens (F2) and passed through a blue glass filter that removed any remaining laser light from the beams. The lens focused the orange light onto a Thorlabs Model DET210 fast photodiode (P1 and P2). Therefore, detector P1 measured the forward-traveling orange light, and detector P2 measured the backward-traveling orange light.

The position of the translation stage and the loudspeaker controlled the delay time between the two laser pulses in the cell. The translation stage position was selected to place the overlap of the two pulses near the center of the dye cell. The loudspeaker moved approximately 0.054 mm/V and was driven by an SRS Model DS345 function generator. The generator triggered our digital storage oscilloscope, which allowed us to record the signals from the dye cell as a function of loudspeaker voltage, or equivalently, the delay between the pulses.

The position of the overlap of the pulses in the dye solution could be detected visually. A small region (about 3 mm long) of dye solution along the laser beam emitted orange fluorescence through the top of the dye cell. This region moved as the delay between the pulses was varied. The photographic insert in Fig. 63 shows this

phenomenon: picture (a) shows the overlap near the center of the cell, and picture (b) shows the overlap near the entrance of the cell, when the time delay of the 870 nm pulses relative to the 750 nm pulses was decreased. The path length shown in the photograph is approximately 1.1 cm. Fig. 64 shows our quantitative results for

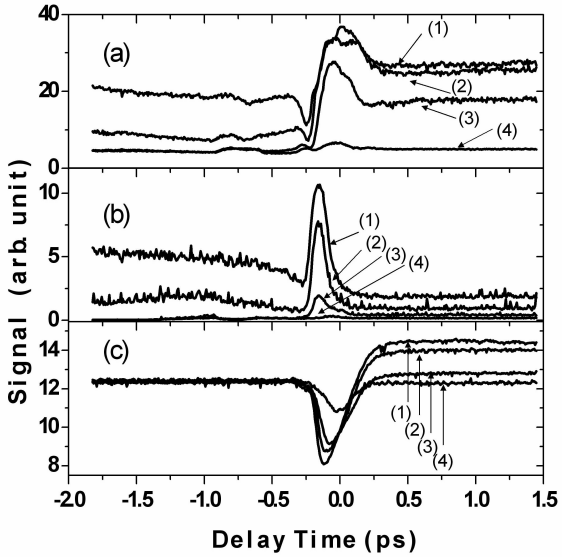

Fig. 64. Light signals versus delay time. Signals from P1, P2 and P3 (see Fig. 63) were plotted as a function of the time between the 870 nm and 750 nm laser pulses. The zero of the time axis was taken to be the time at which the forward-traveling signal was a maximum. Positive delay time means the 750 nm pulses go through the dye cell before the 870 nm pulses. (a) Forward-traveling generated light. (b) Backward traveling generated light. (c) Transmitted 870 nm laser light. Each graph shows curves for one power of the 870 nm laser, 1.4 mW, and four different powers of the 750 nm laser: (1) 5.4 mW, (2) 3.8 mW, (3) 2.2 mW and (4) 0.6 mW.

the forward- and backward-traveling orange light and the transmission of the 870 nm laser as a function of the delay time of the 870 nm pulses relative to the 750 nm pulses. The zero of the delay time was selected to be the time of the maximum

signal of the forward-traveling orange light. The three graphs each have four curves, showing the effect of different laser powers. In these data, the average power of the 870 nm laser was held constant at 1.4 mW, while the average power of the 750 nm laser was changed: 5.4 mW (curve 1), 3.8 mW (curve 2), 2.2 mW (curve 3) and 0.6 mW (curve 4). Significant amounts of orange light were generated that traveled in the backward as well as the forward directions, confirming the prediction of Kocharovsky, et al. [99] The greatest amount of forward-traveling orange light occurred when the pulse overlap was near the exit side of the cell, while the greatest amount of backward-traveling orange light occurred when the pulse overlap was near the entrance side of the cell. In both cases, the time scale for the maximum generation was of the order of the duration of a laser pulse. In magnitude, the maximum backward-traveling light was about one-third of the maximum forward traveling light. Also, when the 750 nm pulses go through the dye cell before the 870 nm pulses, the amount of 870 nm light transmitted by the dye solution increased with power of the 750 nm laser.

4. Conclusion

We experimentally demonstrated the distributed gain and pulse catch-up concepts using femtosecond optical pulses propagating through a dye solution. The timing of laser pulses directed toward two dye cells produced significant amplification of part of the light generated by two-photon absorption from a third cell, using one wavelength (804 nm) of laser light. The light generation in the first cell and the amplification by the second and third cells were backward-traveling relative to the direction of the pump laser beams. The gain ranged from 190 to 1100, depending on the laser powers. The dispersion of the dye solution for two different wavelengths (750 nm and 870 nm) displayed pulse catch-up at a point determined by the time interval between the pulses. A significant amount of backward-traveling light generated by

two-photon absorption was produced, about one-third of the amount of forward-traveling generated light. These results confirm two aspects of the SOS technique.

B. Single-Shot Detection of Bacterial Spores via Coherent Raman Spectroscopy

1. Introduction

The Raman spectra of spores have been characterized as their fingerprints. Detection schemes based on conventional spontaneous Raman spectroscopy [74, 75, 76, 77, 78, 79] and surface-enhanced Raman spectroscopy (SERS) (see, e.g., [151]) have been reported. For 1.4×10^3 spores, a data collection time as low as 10 s has been achieved [152].

In this part, we consider a complementary approach, coherent anti- Stokes Raman scattering (CARS) spectroscopy [153, 154], and demonstrate the acquisition of a CARS spectrum from $\approx 10^4$ Bacillus subtilis spores in a single laser shot.

The use of CARS for spore detection was suggested several years ago [95]. A set of femtosecond adaptive spectroscopic techniques for CARS (FAST CARS), including electronicresonance- enhanced coherent Raman scattering [96, 97], laser pulse shaping [98], and timing, was proposed and analyzed. We showed how to boost the CARS efficiency and discussed possible strategies for real-time bacterial spore detection in Chapter VI.

In Chapter VI, we introduced the hybrid CARS technique to obtain the spectrum from highly scattering samples of sodium dipicolinate powder and Bacillus subtilis spores. The same approach was applied by Stauffer et al. [155] to CARS on neat solutions of toluene and chloroform as well as rhodamine 6G with an emphasis on prospective monitoring of intramolecular vibrational energy redistribution; another but conceptually similar scheme was also implemented by Hamaguchi et al. [116].

By delaying a narrow-band pump pulse relative to dispersion-compensated supercontinuum (used as a Stokes pulse within a standard broadband CARS scheme), they observed NR background-free CARS signal from impulsively excited vibrational modes of indene. Finally, the time-resolved dynamics of the resonant and NR broadband picosecond CARS signals from gas-phase nitrogen was investigated in [156].

In this part, we improve on our hybrid CARS measurements on Bacillus subtilis spores (Chapter VI) and elaborate on the optimization of the initially proposed experimental setup. First, the wavelengths of the pump, Stokes, and probe beams are shifted into the near-IR domain, where the photo-damage threshold for the spores is higher as compared with the visible-range wavelengths. Second, the bandwidth and delay of the probe pulse are carefully optimized. These steps have led to a 10^2 to 10^3 increase in the sensitivity of our CARS setup and enabled us to acquire the spectrum from a small sample volume ($\approx 10^4$ spores) in a single laser shot.

Because CARS efficiency is expected to be proportional to the intensity of the excitation laser pulses, the generated signal can in principle be increased (and the required sample size decreased) by tighter focusing of the applied laser beams. However, there is obviously a limit imposed by the laser-induced damage to the sample. In our previous work, wherein signal collection was done over many laser shots, the applied laser intensities (and therefore the average signal strengths) were limited by cumulative damage to the sample. An obvious question that one may ask is whether higher peak intensities can be used when the signal is generated on a sub-picosecond time scale. In this part, we provide an experimental answer to this question by measuring the optimized CARS signal vs. the applied laser energy fluence on a single-shot basis.

2. Experimental Results and Discussions

We used the similar experimental setup as in Chapter VI. An essential improvement in performance was achieved by shifting of the pump, Stokes, and probe wavelengths from the visible into the IR domain. This allowed us to increase the energy of the pulses and their peak intensities by three to five times without destroying the spores. The signal beams at two different wavelengths, generated in the OPAs by the down-conversion of 805-nm photons, provided pump ($\lambda_1 \sim 1.25$ μm) and Stokes ($\lambda_2 \sim 1.55$ μm) pulses. The probe pulses came from the residual 805-nm beam spectrally filtered and shaped by a 4f pulse shaper with a mechanical slit in its Fourier plane. The resulting pulse shape had a sinc-squared intensity profile. The three beams were arranged in folded-BOXCAR geometry and focused on the sample, as shown schematically in Chapter VI. The FWHM diameters for the pump, Stokes, and probe beams on the sample were 36, 43, and 32 μm, respectively (from knife-edge measurements). The timing between the three input pulses was adjusted by computer-controlled delay stages. The generated CARS signal was collected in the backward direction, at an angle (30 degree) to the main axis, by a 2-inch-diameter lens (focal length of 10 cm) and directed into a spectrometer with the liquid nitrogen-cooled CCD.

The next step toward superior sensitivity was the optimization of the spectral bandwidth and the time delay of the probe pulse. Because the observed NR background in the recorded CARS spectra was dominated by the multiple scattering within the sample, this was done experimentally. A set of spectrograms, shown in Fig. 65 *Left*, was recorded for different spectral bandwidths of the probe pulse. For each probe delay in a spectrogram, the acquired spectrum was processed to remove the NR background and account for the pumpStokes excitation profile. Note that we have found it useful to obtain a smoothed replica of the acquired CARS spectrum by

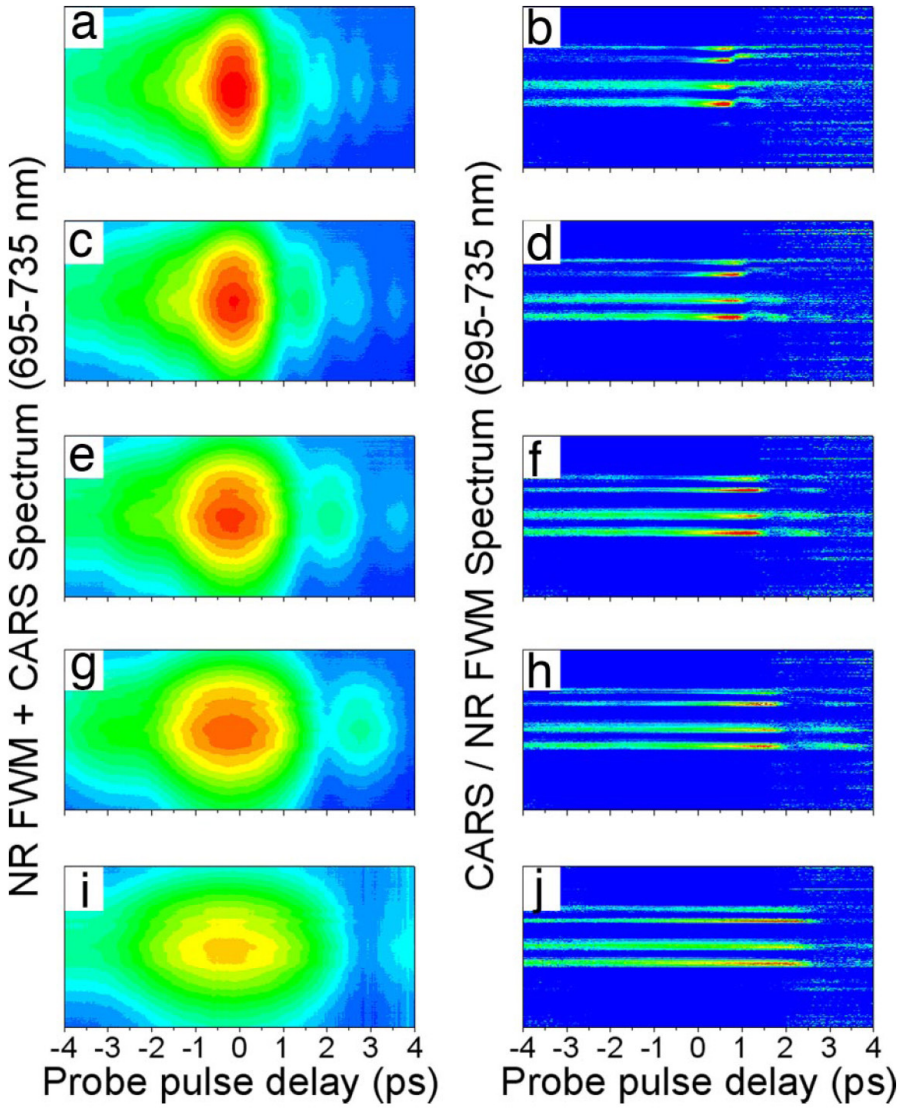

Fig. 65. The experimentally obtained CARS spectrograms (*Left*) and processed CARS-vs.-FWM profiles (*Right*) acquired with a pellet of Bacillus subtilis spores for different FWHM spectral bandwidths of the probe pulse $\Delta\omega_3$: 40 cm^{-1} (a and b), 30 cm^{-1} (c and d), 20 cm^{-1} (e and f), 15 cm^{-1} (g and h), and 10 cm^{-1} (i and j). The integration time is 1 s. The central wavelengths of the pump, Stokes, and probe pulses are 1.28 μm, 1.62 μm, and 805 nm, respectively. The energy of the probe pulse is kept constant while the spectral bandwidth is adjusted.

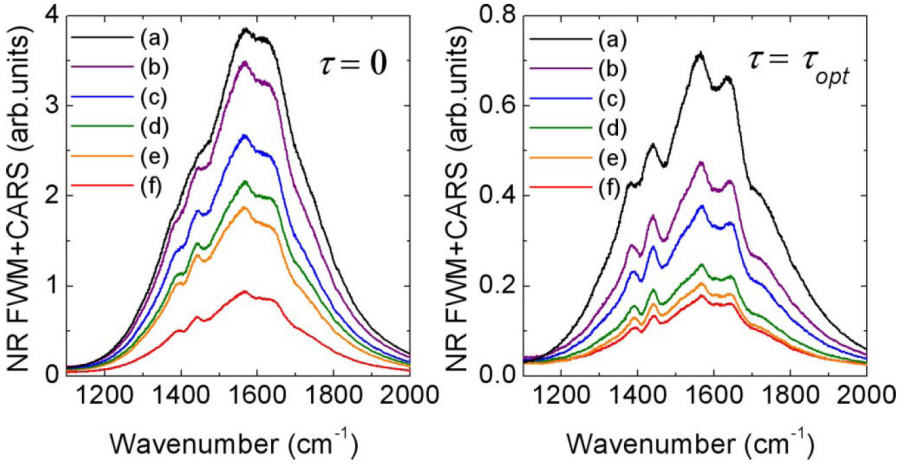

Fig. 66. Cross-sections of the recorded CARS spectrograms, similar to those in Fig. 65, for two different probe delays: zero delay (*Left*) and optimal delay (*Right*). The last one is adjusted for different values of $\Delta\omega_3$: 60 cm^{-1} (a), 40 cm^{-1} (b), 30 cm^{-1} (c), 20 cm^{-1} (d), 15 cm-1 (e), and 10 cm^{-1} (f).

averaging the recorded counts over 200 adjacent pixels and then dividing the original spectrum by the generated profile. It is analogous to forming the ratio of CARS plus NR FWM over NR FWM. The normalized spectrograms (see Fig. 65 *Right*) reveal sharp resonant features on top of the smooth NR background as well as the optimal probe delay τ_{opt}, corresponding to the maximal ratio between CARS and NR FWM, for every chosen value of $\Delta\omega_3$. Fig. 66 illustrates the recorded, flat-field corrected CARS spectra at $\tau = 0$ and $\tau = \tau_{opt}$. Note also that the etaloning effect, common for back-illuminated CCDs in the spectral range of interest, leads to inhomogeneous optical response of the CCD over its surface. It results in parasitic amplitude modulation of recorded spectra. To correct for ghost spectral peaks, we acquired a sample spectrum with the probe beam blocked (high harmonic generation due to the pump and Stokes fields contributed as a smooth background) and then divided all CARS spectra by the obtained profile. As expected, two tendencies can be observed. If the

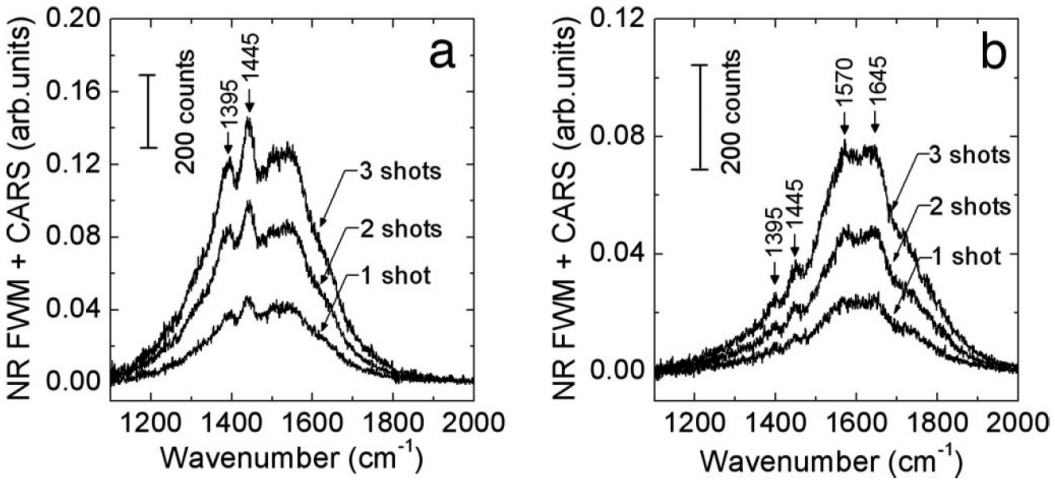

Fig. 67. Acquired CARS spectra for one, two, and three laser shots at the optimal probe delay. Parameters were as follows. (*a*) Pump wavelength $\lambda_1 = 1.25$ μm, 4 μJ per pulse; probe, λ_3=805.8 nm, $\Delta\omega_3 = 30$ cm^{-1}, 3 μJ per pulse; Stokes, $\lambda_2 = 1.54$ μm, (*b*) Stokes, $\lambda_2 = 1.56$ μm, 4 μJ per pulse.

probe bandwidth is small compared with the Raman line width, the visibility of the Raman peak depends only weakly on the probe delay, and the signal magnitude is low. If the probe bandwidth is large, the signal is stronger but the contrast degrades. For the observed Raman transitions, $\Delta\omega_3 \approx 30$ cm^{-1} and the time delay $\tau \approx 0.77$ ps were found to be optimal (see Figs. 65 d and 66 c). Once we had the parameters optimized, the setup performance was evaluated by decreasing the acquisition time. Fig. 67 shows CARS spectra of Bacillus subtilis spores taken in only one to three laser shots. The spore Raman transitions in the fingerprint region (from 1.300 to 1.700 cm^{-1}) are apparent even after a single shot. For these measurements, the laser system was switched from normal (continuous) operation at 1 kHz rep rate into the single-shot mode, and the laser pulses were fired manually. The integration time of the charge-coupled device (CCD) camera was set to 3 s to ensure a comfortable time

span for the manual firing of up to 10 shots. The variation of the CCD integration time from 0.5 to 10 s did not show any appreciable change in the noise level of the single-shot spectra because the dominant part of the noise came from the scattered laser radiation entering the spectrometer. At last, the reported pulse energies were deduced from the power measurements in the normal (continuous) operation mode. We found that they differed from the actual pulse energies when the laser system was operated in the single-shot mode. The ratio of the single-shot to the continuous-mode pulse energy was 0.75, 0.47, and 1.3 for the pump, Stokes, and probe pulses, respectively.

Note that the single-shot spectra were obtained from a fairly small number of spores. Taking the effective laser pulse penetration depth for the highly scattering sample (a clump of closely packed spores) to be 10 μm and the diameter of the probed region to be 32 μm, one gets a rough estimate for the probed volume of 10^4 μm^3. Allocating 1 μm^3 for a single spore gives $\approx 10^4$ contributing spores. The dependence of the resonant CARS signal on the energy of the pump and Stokes pulses is shown in Fig. 68. Here, the resonant contribution is defined as an integral over the two Raman peaks, 1.395 cm^{-1} and 1.445 cm^{-1}. The data reveal that at high enough pulse energies, the dependence strongly deviates from the expected linear increase. The CARS signal magnitude saturates and even drops down at higher pulse energies. The total acquired signal, which is dominated by the nonresonant contribution, exhibits similar dependence on the pulse energies but with a slightly weaker decay at the high-energy limit (data not shown). Within the available range (up to 3 μJ per pulse), we observed a linear dependence of the CARS signal on the energy of the probe pulse.

The saturation and decrease of the generated CARS signal as a function of the pump or Stokes pulse energies is probably due to the laser-induced damage of the

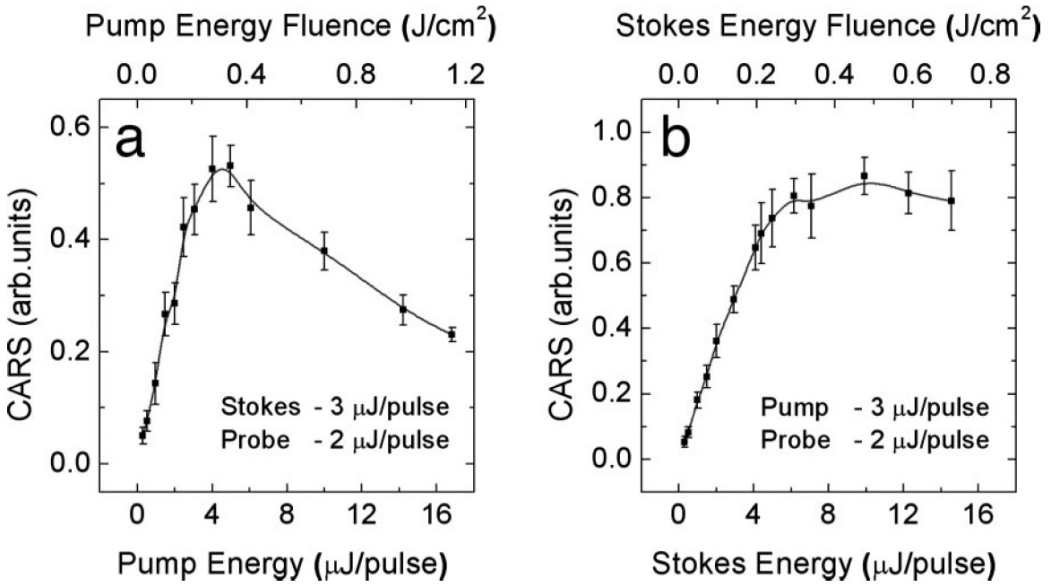

Fig. 68. Dependence of the CARS signal on the energy of the pump (*a*) and Stokes (*b*) pulses. Other parameters are $\lambda_1 = 1.24$ μm, $\lambda_2 = 1.54$ μm $\lambda_3 = 805.7$ nm, and $\Delta\omega_3 = 30$ cm^{-1}. The CARS signal was recorded in the single-shot regime, moving the sample after each laser shot to avoid the laser-induced damage.

exposed spores. Accounting for the beam focusing and the scaling factors, we estimate the damage threshold for our spore sample to be 0.2 J/cm^2 per ultrashort pump or Stokes pulse. For 50-fs pulses, this energy fluence corresponds to a peak intensity of $\approx 3 \times 10^{12} W/cm^2$. Note that this threshold is retrieved from the single-short measurements and corresponds to ultrafast (femtosecond- scale) photodamage. We have also observed a longer- scale cumulative effect of CARS signal degradation as a function of the shot number. To avoid the substantial damage of the sample over 100 laser shots, one needs to use a pulse energy fluence that is at least three times lower than the single-shot threshold value.

3. Conclusion

To conclude, we have optimized our earlier hybrid CARS experiment and demonstrated that the CARS spectrum from $\approx 10^4$ bacterial spores can be obtained in a single, femtosecond laser shot. This is to be compared with our initial acquisition time of many seconds. The dependence of the CARS signal on the energy of the ultrashort preparation pulses shows that it scales linearly, up to a peak energy fluence of $\approx 0.2 J/cm^2$ per pulse. Further signal increase is hampered by photodamage of the sample interacting with the strong electric field of the femtosecond pulses. Finally, it is important to note that spore detection, addressed in this part, is only one application of our technique. The technique can be adapted in a straightforward fashion for many other applications requiring chemical specificity and short acquisition times. A particularly interesting example is CARS microscopy ([125, 157, 158, 159]).

CHAPTER IX

SUMMARY

Ultrafast cooperative phenomena in coherently prepared media, and various applications of both superfluorescence and coherent Raman scattering have been explored in this dissertation. We summarize the major results and achievements in this chapter.

Motivated by a reasonable analogy between cooperative emission and coherent Raman scattering, parallel research on cooperative emission (superradiance, superfluorescence etc.) and coherent Raman scattering has been performed.

In particular, the superfluorescent pulse with a time duration of a few tens of picoseconds in rubidium vapor has been observed for the first time. The realization of the shortest superfluorescent pulse has been achieved due to a dense rubidium vapor pumped by ultrashort (100 fs) pulses. According a peer-reviewer (in the private communication) "one of the most clean and distinct measurements of superfluorescence" has been observed.

Macroscopic fluctuations of quantum initiation of superfluorescence development have been explored. The measurement of the fluctuations in delay time of the ultrashort superfluorescent pulse was carried on a picosecond time scale.

Possible applications of the superfluorescent pulse in a remote sensing technique, and ultraviolet upconversion of the input infrared laser pulse have been studied.

A new coherent Raman spectroscopic technique has been developed. A novel advantage of the reduction of the background noise has been achieved by shaping and delaying the probe pulse which scatters off from the coherently prepared medium. A robustness and superiority of signal-to-noise ratio of the developed technique have been confirmed by identifying as few as 10000 bacterial spores at a single laser shot level.

Finally, several comparative studies between cooperative and uncooperative processes have been presented. A picosecond cooperative phenomenon in a three-photon resonant medium induced by a single as well as two-color ultrashort pulses has been investigated. A time-resolved study has uncovered that a picosecond cooperative effect is crucial in a well-established field of resonant-enhanced multiphoton ionization. A quantitative analysis for photon fluxes for spontaneous and broadband coherent Raman scattering on pyridine molecules has been performed in the comparative experiment. The spontaneous Raman signal has been enhanced by more than 5 orders of magnitude as a result of cooperative process.

REFERENCES

[1] R. H. Dicke. Coherence in spontaneous radiation proceses. *Phys. Rev.*, 93:99–110, 1954.

[2] N. E. Rehler and J. H. Eberly. Superradiance. *Phys. Rev. A*, 3:1735–1751, 1971.

[3] R. Bonifacio and L. Lugiato. Cooperative radiation processes in two-level systems: Superfluorescence. *Phys. Rev. A*, 11:1507–1521, 1975.

[4] N. Skribanowitz, I. P. Herman, J. C. MacGillivray, and M. S. Feld. Observation of Dicke superradiance in optically pumped HF gas. *Phys. Rev. Lett.*, 30:309–312, 1973.

[5] J. Marek. Observation of superradiance in Rb vapour. *J. Phys. B: Atom. Molec. Phys.*, 12:L229–L234, 1979.

[6] F. T. Arecchi and E. Courtens. Cooperative phenomena in resonant electromagnetic propagation. *Phys. Rev. A*, 2:1730–1737, 1970.

[7] J. C. MacGillivray and M. S. Feld. Theory of superradiance in an extended, optically thick medium. *Phys. Rev. A*, 14:1169–1189, 1976.

[8] H.M. Gibbs. *In Cooperative Effects in Matter and Radiation*. Edited by C.M. Bowden, D.W. Howgate, and H.R. Robl. Plenum, pages 61–78, 1977.

[9] R. Florian, L. O. Schwan, and D. Schmid. Time-resolving experiments on Dicke superfluorescence of O_2- centers in KCl. Two-color superfluorescence. *Phys. Rev. A*, 29:2709–2715, 1984.

[10] R. Bausch, P. Borgs , R. Kree, and F. Haake. Forward-Backward Synchronization in Solid-State Superfluorescence. *Europhys. Lett.*, 10:445–449, 1989.

[11] D. Jansen and A. Stahl. Correlation between counterpropagating pulses in superfluorescence. *Europhys. Lett.*, 18:33–38, 1992.

[12] H. Steudel. Forward-backward coupling in superfluorescence. *Ann. Phys.*, 503:563–569, 1991.

[13] R. Friedberg and S. R. Hartmann. Superradiant lifetime: Its definitions and relation to absorption length. *Phys. Rev. A*, 13:495–496, 1976.

[14] D. Polder, M. F. H. Schuurmans, and Q. H. F. Vrehen. Superfluorescence: Quantum-mechanical derivation of Maxwell-Bloch description with fluctuating field source. *Phys. Rev. A*, 19:1192–1203, 1979.

[15] M. Gross and S. Haroche. Superradiance: an essay on the theory of collective spontaneous emission. *Phys. Report*, 93:301, 1982.

[16] R. Bonifacio, M. Gronchi, L. A. Lugiato, and A. M. Ricca. *In Cooperative Effects in Matter and Radiation*. Edited by C. M. Bowden, D. W. Howgate, and H. R. Robl. Plenum, pages 193–208, 1977.

[17] R. Bonifacio, M. Cronchi, L. A. Lugiato, and A. M. Ricca. *In Coherence and Quantum Optics IV*. Edited by L. Mandel and E. Wolf. Plenum, pages 939–951, 1978.

[18] D. C. Burnham, and R. Y. Chiao. Coherent resonance fluorescence excited by short light pulses. *Phys. Rev.*, 188:667–675, 1969.

[19] A. Kumarakrishnan, S. Chudasama, and X. Han. Collision-induced superfluorescence. *J. Opt. Soc. Am. B*, 22:1538–1546, 2005.

[20] A. Kumarakrishnan, and X. L. Han. Superfluorescence from optically trapped calcium atoms. *Phys. Rev. A*, 58:4153–4162, 1998.

[21] F. P. Mattar, H. L Gibbs, S. L McCall, and M. S. Feld. Transverse effects in superfluorescence. *Phys. Rev. Lett.*, 46:1123–1126, 1981.

[22] D. J. Heinzen, J. L. Thomas and M. S. Feld. Coherent ringing in superfluorescence. *Phys. Rev. Lett.*, 54:677–680, 1985.

[23] M. O. Scully and M. S. Zubairy. *Quantum Optics*, Cambridge University Press, 1997.

[24] V. DeGiorgia. Statistical properties of superradiant pulses. *Opt. Commun.*, 2:362–364, 1971.

[25] F. Haake, J. Haus, H. King, G. Schrder, and R. Glauber. Delay-time statistics and inhomogeneous line broadening in superfluorescence. *Phys. Rev. Lett.*, 45:558–561, 1980.

[26] F. Haake J. Haus, H. King, G. Schrder, and R. Glauber. Delay-time statistics of superfluorescence pulses. *Phys. Rev. A*, 23:1322–1333, 1981.

[27] F. Haake , M. I. Kolobov, C. Seeger, C. Fabre, E. Giacobino, et al.. Quantum noise reduction in stationary superradiance. *Phys. Rev. A*, 54:1625–1637, 1996.

[28] F. Haake, J. Haus, H. King, G. Schrder, R. Glauber, et al.. Macroscopic quantum fluctuations in superfluorescence. *Phys. Rev.Lett.*, 42:1740–1743, 1979.

[29] R. Bonifacio, P. Schwendimann, and F. Haake. Quantum statistical theory of superradiance. I. *Phys. Rev. A*, 4:302–313, 1971

[30] C. T Lee. Fluctuations in tipping angles and delay times of simple superfluorescence. *Appl. Phys.Lett.*, 41:821–823, 1982.

[31] C. T. Lee. Exact solution of the superraiant master equation. I. Complete initial excitation. *Phys. Rev. A*, 15:2019–2031, 1977.

[32] C. T. Lee. Exact solution of the superraiant master equation. II. Arbitrary initial excitation. *Phys. Rev. A*, 16:301–312 ,1977.

[33] C. T. Lee. Superfluorescene pumped by a short pulse of arbitrary shape. *Phys. Rev. A*, 29:217–224, 1984.

[34] Q. H. F Vrehen and J. J. der Weduwe. Quantum fluctuations in superfluorescence delay times. *Phys. Rev. A*, 24:2857–2860, 1981.

[35] A. V. Andreev, V. I. Emel'yanov, and Yu. A. Il'inskii. *Cooperative Effects in Optics*. Institute of Physics, 1993.

[36] M. G. Benedict, A. M. Ermolaev, V. A. Malyshev, I.V. Sokolov and E.D. Trifonov. *Super-Radiance Multiatomic Coherent Emission*. Institute of Physics, 1996.

[37] J. Okada , K. Ikeda, and M. Matsuoka. Cooperative cascade emission. *Opt. Commun.*, 26:189–192, 1978.

[38] J. Okada, K. Ikeda and M. Matsuoka. Streak Camera Investigation of Superradiance Development. *Opt. Commun.*, 27:321–324, 1978.

[39] J. H. Brownell, X. Lu, and S. R. Hartmann. Yoked Superfluorescence. *Phys. Rev. Lett.*, 75:3265–3268, 1995.

[40] A. I. Lvovsky, S. R. Hartmann, and F. Moshary. Omnidirectional superfluorescence. *Phys. Rev. Lett.*, 82:4420–4423, 1999.

[41] A. I. Lvovsky. *Omnidirectional Superfluorescence Transients*. PhD thesis, Columbia University, 1998.

[42] E. Paradis, B. Barrett, A. Kumarakrishnan, R. Zhang, and G. Raithel. Observation of superfluorescent emissions from laser-cooled atoms. *Phys. Rev.A*, 77:043419, 2008.

[43] D. Meshulach and Y. Silberberg. Coherent quantum control of two-photon transitions by a femtosecond laser pulse. *Nature*, 396:239–242, 1998.

[44] A. A. Senin, H. C. Tran, J. Gao, Z. H. Lu, C. J. Zhu, et al.. Molecular dissociation observed with an atomic wavepacket and parametric four-wave mixing. *Chem. Phys. Lett.*, 381:53–59, 2003.

[45] Z. H. Lu, C. J. Zhu, A. A. Senin, J. R. Allen, J. Gao, et al.. Production and probing of atomic wavepackets with ultrafast laser pulses: Apllications to atomic and molecular dynamics. *IEEE J. Selected Topics in Quantum Elect.*, 10:159–168, 2004.

[46] C. -J. Zhu, Y. Xiao, A. A. Senin, J. Gao, J. G. Eden, et al.. Quantum beating in Rb at 18.3 THz (608 cm^{-1}) detected by parametric six-wave mixing and sum-frequency generation in $LiIO_3$. *Phys. Rev. A*, 75:053405, 2007.

[47] V. Blanchet, C. Nicole, M. -A. Bouchene, and B. Gigard. Temporal coherent control in two-photon transitions: From optical interferences to quantum interferences. *Phys. Rev. Lett.*,78:2716–2719, 1997.

[48] D. Felinto, L. H. Acioli, and S. S. Vianna. Temporal coherent control of a sequential transition in rubidium atoms. *Opt. Lett.*, 25:917–919, 2000.

[49] H. G. Barros, W. B. Lozano, S. S. Vianna, and L. H. Acioli. Influence of propagation and external phase in sequential two-photon absorption of femtosecond pulses. *Opt. Lett.*, 30:3081–3083, 2005.

[50] H. G. Barros, J. Ferraz, W. B. Lozano, L. H. Acioli, and S. S. Vianna. Coherent control of quantum interference in two-photon absorption. *Phys. Rev. A*, 74:055402, 2006.

[51] A. H. Zewail. Laser femtochemistry. *Science*, 242:1645–1653, 1988.

[52] R. M. Bowman, M. Dantus and A.H. Zewail. Femtosecond transition-state spectroscopy of iodine: From strongly bound to repulsive surface dynamics. *Chem. Phys. Lett.*, 161:297–302, 1989.

[53] M. Gruebele, G. Roberts, M. Dantus, R.M. Bowman, and A.H. Zewail. Femtosecond temporal spectroscopy and direct inversion to the potential: Application to iodine. *Chem. Phys. Lett.*, 166:459–469, 1990.

[54] T. Baumert, B. Buhler, R. Thalweiser, and G. Gerber. Femtosecond spectroscopy of molecular autoionization and fragmentation. *Phys. Rev. Lett.*, 64:733–736, 1990.

[55] T. Baumert, M. Grosser, R. Thalweiser, and G. Gerber. Femtosecond time-resolved molecular multiphoton ionization: The Na_2 system. *Phys. Rev. Lett.*, 67:3753–3757, 1991.

[56] J. M. Papanikolas, R. M. Williams, P. D. Kleiber, J. L. Hart, C. Brink, et al.. Wave-packet dynamics in the Li_2 $E(^1\sum_g^+)$ shelf state: Simultaneous observation of vibrational and rotational recurrences with single rovibronic control of an intermediate state. *J. Chem. Phys.*, 103:7269–7277, 1995.

[57] R. M. Williams, J. M. Papanikolas, J. Rathje, and S. R. Leone. Compositional control of rovibrational wave packets in the $E(^1\sum_g^+)$ shelf state of Li_2 via quantum-state-resolved intermediate state selection. *J. Chem. Phys.*, 106:8310–8323, 1997.

[58] T. S. Rose, M. J. Rosker, and A. H. Zewail. Femtosecond real-time observation of wave packet oscillations (resonance) in dissociation reactions. *J. Chem. Phys.*, 88:6672–6681, 1988.

[59] M. H. M. Janssen, R. M. Bowman, and A. H. Zewail. Femtosecond temporal spectroscopy of ICI: inversion to the $A_3\prod^1$ state potential. *Chem. Phys. Lett.*, 172:99–108, 1990.

[60] G. Rodriguez and J.G. Eden. Dynamics of vibrational wave packets in the $C_1\prod^u$ state of Cs_2. *Chem. Phys. Lett.*, 205:371–379, 1993.

[61] G. Rodriguez, P.C. John, and J.G. Eden. Vibrational wave packets in the $C^1\prod_u$ state of Cs_2: Two color pumpprobe experiments. *J. Chem. Phys.*, 103:10473–10483, 1995.

[62] A. L. Oldenburg, P. C. John, and J. G. Eden. Vibrational wave packets in the $B^1\prod_u$ and $D^1\sum_u^+$ states of Cs_2: Determination of improved $Cs_2^+(X)$ and $Cs_2(B)$ spectroscopic constants. *J. Chem. Phys.*, 113:11009–11017, 2000.

[63] J. J. Gerdy, M. Dantus, R. M. Bowman, and A. H. Zewail. Femtosecond selective control of wave packet population. *Chem. Phys. Lett.*, 171:1–4, 1990.

[64] E. D. Potter, J. L. Herek, S. Pedersen, Q. Liu, and A. H. Zewail. Femtosecond laser control of a chemical reaction. *Nature*, 355:66–68, 1992.

[65] V. Blanchet, M. A. Bouchene, O. Cabrol, and B. Girard. One-color coherent control in CO_2. Observation of 2.7 fs beats in the ionization signal. *Chem. Phys. Lett.*, 233:491–499, 1995.

[66] V. Blanchet, M. A. Bouchene, and B. Girard. Temporal coherent control in the photoionization of CO_2: Theory and experiment. *J. Chem. Phys.*, 108:4862–4877, 1998.

[67] H. Katsuki, H. Chiba, B. Girard, C. Meier, and K. Ohmori. Visualizing picometric quantum ripples of ultrafast wave-packet interference. *Science*, 311:1589–1592, 2006.

[68] A. Peter, E. A. Shapiro, M. C. Stowe, M. Shapiro, and J. Ye. Precise control of molecular dynamics with a femtosecond frequency comb. *Phys. Rev. Lett.*, 98:113004, 2007.

[69] S. Mukamel. *Principles of Nonlinear Optical Spectroscopy*. Oxford University Press, 1995.

[70] S. Mukamel. Femtosecond optical spectroscopy: A direct look at elementary chemical events. *Ann. Rev. Phys. Chem.*, 41:647–652, 1990.

[71] S. H. Lin, R. Alden, R. Islampour, H. Ma and A. A. Villaeys. *Density Matrix Methods and Femtosecond Processes*. World Scientific, 1991.

[72] W. T. Pollard, H. L. Fragnito, J. Y. Bigot, C. V. Shank, and R. A. Mathies. Quantum-mechaninal theory for 6 fs dynamic absorption spectroscopy and its application to nile blue. *Chem. Phys. Lett.*, 168:239–245, 1990.

[73] R. K. Murawski, Y. V. Rostovtsev, Z.Sariyanni, V. A. Sautenkov, S. Backus, et al.. Resonant uv pump-probe spectroscopy of dipicolinic acid via impulsive

excitation. *Phys. Rev. A*, 77:023403, 2008.

[74] T. G. Spiro. *Biological Applications of Raman Spectroscopy*. Wiley, 1987.

[75] Z. Arp, D. Autrey, J. Laane, S. A. Overman, and G. J. Thomas. Structural studies of viruses by Raman spectroscopy part LXXITyrosine Raman signatures of the filamentous virus Ff are diagnostic of non-hydrogen-bonded phenoxyls: Demonstration by Raman and infrared spectroscopy of p-cresol vapor. *Biochemistry*, 40:2522–2529, 2001.

[76] A. P. Esposito, C. E. Talley, T. Huser, C. W. Hollars, C. M. Schaldach, et al.. Analysis of single bacterial spores by micro-Raman spectroscopy. *Appl. Spectrosc.*, 57:868-871, 2003.

[77] J. W. Chan, A. P. Esposito, C. E. Talley, C. W. Hollars, S. M. Lane, et al.. Reagentless identification of single bacterial spores in aqueous solution by confocal laser tweezers Raman spectroscopy. *Anal. Chem.*, 76:599-603, 2004.

[78] W. H. Nelson, R. Dasari, M. Feld, and J. F. Sperry. Intensities of calcium dipicolinate and bacillus subtilis spore Raman spectra excited with 244 nm Light. *Appl. Spectrosc.*, 58:4408–1412, 2004.

[79] S. Farquharson, L. Grigely, V. Khitrov, W. Smith, J. F. Sperry, et al.. Detecting Bacillus cereus spores on a mail sorting system using Raman spectroscopy. *J Raman Spectrosc.*, 35:82-86, 2004.

[80] R. Aroca. *Surface-Enhanced Vibrational Spectroscopy*. John Weliy & Son, 2006.

[81] P. R. Regnier and J. P.E. Taran. On the possibility of measuring gas concentrations by stimulated anti-Stokes scattering. *Appl. Phys. Lett.*, 23:240–242, 1973.

[82] J. W. Nibler and G. V. Knighten. *In Raman Spectroscopy of Gases and Liquids.* Edited by A. Weber, Springer-Verlag, pages 253–299, 1979.

[83] W. M. Tolles and R. D. Turner. A comparative analysis of the analytical capabilities of coherent anti-Stokes Raman spectroscopy (CARS) relative to Raman scattering and absorption spectroscopy. *Appl. Spectrosc.*, 31:96–103, 1977.

[84] J. L. Oudar, R. W. Smith, and Y. R. Shen. Polarization-sensitive coherent anti-Stokes Raman spectroscopy. *Appl. Phys. Lett.*, 34:758–760, 1979.

[85] Y. Yacoby, R. Fitzgibbon, and B. Lax. Coherent cancellation of background in four-wave mixing spectroscopy. *J. Appl. Phys.*, 51:3072–3075, 1980.

[86] E. O. Potma, C. L. Evans, and X. S. Xie. Heterodyne coherent anti-Stokes Raman scattering (CARS) imaging. *Opt. Lett.*, 31:241–243, 2006.

[87] D. Oron, N. Dudovich, D. Yelin, and Y. Silberberg. Quantum control of coherent anti-Stokes Raman processes. *Phys. Rev. A.*, 65:043408, 2002.

[88] D. Oron, N. Dudovich, D. Yelin, and Y. Silberberg. Narrow-band coherent anti-Stokes Raman signals from broad-band pulses. *Phys. Rev.Lett.*, 88:063004, 2002.

[89] S. H. Lim, A. G. Caster, and S. R. Leone. Single-pulse phase-control interferometric coherent anti-Stokes Raman scattering spectroscopy. *Phys. Rev. A.*, 72:041803, 2005.

[90] T. W. Kee, H. Zhao, and M. T. Cicerone. One-laser interferometric broadband coherent anti-Stokes Raman scattering. *Opt. Express*, 14:3631–3640, 2006.

[91] Wikipedia, The Free Encyclopedia, http://en.wikipedia.org/wiki/Anthrax.

[92] K. A. Edwards, H. A. Clancy, and A. J. Baeumner. Bacillus anthracis: toxicology, epidemiology and current rapid-detection methods. *Anal. Bioanal. Chem.*, 384:73-84, 2006.

[93] M. B. Pushkarsky, M. E. Webber, T. Macdonald, and C. K. N. Patel. High-sensitivity, highselectivity detection of chemical warfare agents. *Appl. Phys. Lett.*, 88:044103, 2006.

[94] M. B. Pushkarsky, I. G. Dunayevskiy, M. Prasanna, A. G. Tsekoun, R. Go, et al.. High-sensitivity detection of TNT. *Proc. Natl. Acad. Sci. USA*, 103:19630-19634, 2006

[95] M. O. Scully, G. W. Kattawar, R. P. Lucht, T. Opatrn, H. Pilloff, et al.. FAST CARS: Engineering a laser spectroscopic technique for rapid identification of bacterial spores. *Proc. Natl. Acad. Sci. USA*, 99:10994–11001, 2002.

[96] S. F. Hanna, W. D. Kulatilaka, Z. Arp, T. Opatrny, M.O. Scully, et al.. Electronic-resonance-enhanced coherent anti-Stokes Raman spectroscopy of nitric oxide. *Appl. Phys. Lett.*, 83:1887-1889, 2003.

[97] A. Rebane, M. Drobizhev, M. Kruk, A. Karotki, I. Tehver, et al.. Femtosecond resonance enhanced CARS for background-free detection of organic molecules. *J. Mod. Opt.*, 52:1243–1253, 2005.

[98] H. Rabitz, R. de Vivie-Riedle, M. Motzkus, and K. Kompa. ChemistryWhither the future of controlling quantum phenomena? *Science*, 288:824–828, 2000.

[99] V. Kocharovsky, S. Cameron, K. Lehman, R. Lucht, R. Miles, et al.. Gain-swept superradiance applied to the stand-off detection of trace impurities in the atmosphere. *Proc. Natl. Acad. Sci. U.S.A*, 102:7806–7811, 2005.

[100] L. Mandel and E. Wolf. *Optical Coherence and Quantum Optics*. Cambridge University Press, 1995.

[101] K. Ikeda, J. Okada and M. Matsuoka. Theory of cooperative cascade emission. I. Linear stochastic theory. *J. Phys. Soc. Japan*, 48:1636–1645, 1980.

[102] H. M. Gibbs, Q. H. F. Vrehen, and H. M. J. Hikspoors. Single-pulse superfluorescence in cesium. *Phys. Rev. Lett.*, 39:547–550, 1977.

[103] G. O. Ariunbold, M. M. Kash, V. A. Sautenkov, H. Li, Yu. V. Rostovtsev, et al.. Observation of picosecond superfluorescent pulses in rubidium vapor pumped by 100-femtosecond laser pulses. *Phys. Rev. A*, 82:043421, 2010.

[104] R. Netz, T. Feurer, G. Roberts, and R. Sauerbrey. Coherent popultation dynamics of a three-level atom in spacetime. *Phys. Rev. A*, 65:043406, 2002.

[105] G. O. Ariunbold, V. A. Sautenkov, and M. O. Scully. A rapid inspection of atomic interference using superfluorescent picosecond pulses. *CLEO Conference, OSA Technical Digest Series*, CMA4, 2010.

[106] D. Pestov, A. Gombojav, X. Wang, R. K. Murawski, V. A. Sautenkov, et al.. Monitoring vibrational wave packet dynamics via direct femtosecond pump-probe measurements. *CLEO, OSA Technical Digest*, JThD34, 2007.

[107] B. Xu, J. M. Gunn, J. M. Dela Cruz, V. V. Lozovoy, and M. Dantus. Quantitative investigation of the multiphoton intrapulse interference phase scan method for simultaneous phase measurement and compensation of femtosecond laser pulses. *J. Opt. Soc. Am. B*, 23:750–759, 2006.

[108] A. N. Nesmeyanov. *Vapor Pressure of the Chemical Elements*. Edited by G. Robert, Elsevier, 1963.

[109] D. Steele and E. R. Lippincott. Comparative study of empirical internuclear potential functions. *Rev. Mod. Phys.*, 34:239–251, 1962.

[110] P. Atkins and R. Friedman. *Molecular Quantum Mechanics*. Oxford University Press, 2005.

[111] G. Herzberg. *Molecular Spectra and Molecular Structure I. Spectra of Diatomic Molecules*. Edited by D. Van, Nostrand Company, 1950.

[112] P. M. Morse. Diatomic molecules according to the wave mechanics. II. Vibrational levels. *Phys. Rev.*, 34:57–64, 1929.

[113] S. Wallentowitz, I. A. Walmsley, L. J. Waxer, and T.Richter. Rotationally induced collapse and revivals of molecular vibrational wavepackets: model for environment-induced decoherence. *J. Phys. B: At. Mol. Opt. Phys.*, 35:1967–1984, 2002.

[114] D. Klick, K. A. Marko, and L. Rimai. Broadband single-pulse CARS spectra in a fired internal combustion engine. *Appl. Opt.*, 20:1178–1781, 1981.

[115] A. Voroshilov, C. Otto, and J. Greve. On the coherent vibrational phase in polarization sensitive resonance CARS spectroscopy of copper tetraphenylporphyrin. *J. Chem. Phys.*, 106:2589–2598, 1997.

[116] H. Kano and H. Hamaguchi. Femtosecond coherent anti-Stokes Raman scattering spectroscopy using supercontinuum generated from a photonic crystal fiber. *Appl. Phys. Lett.*, 85:4298–4300, 2004.

[117] G. I. Petrov and V. V. Yakovlev. Enhancing red-shifted white-light continuum generation in optical fibers for applications in nonlinear Raman microscopy. *Opt. Express*, 13:1299–1309, 2005.

[118] Y. R. Shen. *The Principles of Nonlinear Optics*. John Wiley & Sons, 1984

[119] H. A. Rinia, M. Bonn, and M. Muller. Quantitative multiplex CARS spectroscopy in congested spectral regions. *J. Phys. Chem. B*, 110:4472–4479, 2006.

[120] R. Leonhardt, W. Holzapfel, W. Zinth, and W. Kaiser. Terahertz quantum beats in molecular liquids. *Chem. Phys. Lett.*, 133:373–377, 1987.

[121] A. Materny, T. Chen, M. Schmitt, T. Siebert, A. Vierheilig, et al.. Wave packet dynamics in different electronic states investigated by femtosecond time-resolved four-wave-mixing spectroscopy. *Appl. Phys. B*, 71:299–317, 2000.

[122] P. Beaud, H. M. Frey, T. Lang, and M. Motzkus. Flame thermometry by femtosecond CARS. *Chem. Phys. Lett.*, 344:407–412, 2001.

[123] R. P. Lucht, S. Roy, T. R. Meyer, and J. R. Gord. Femtosecond coherent anti-Stokes Raman scattering measurement of gas temperatures from frequency-spread dephasing of the Raman coherence. *Appl. Phys. Lett.*, 89:251112, 2006.

[124] P. Carmona. Vibrational spectra and structure of crystalline dipicolinic acid and calcium dipicolinate trihydrate. *Spect. Acta A: Mol. Spectrosc.*, 36:705–712, 1980.

[125] M. D. Duncan, J. Reintjes, and T. J. Manuccia. Scanning coherent anti-Stokes Raman microscope. *Opt. Lett.*, 7:350–352, 1982.

[126] A. Zumbusch, G. R. Holton, and X. S. Xie. Three-dimensional vibrational imaging by coherent anti-Stokes Raman scattering. *Phys. Rev. Lett.*, 82:4142–4145, 1999.

[127] X. Wen, S. Chen, and D. D. Dlott. Time-resolved three-color coherent Raman scattering applied to polycrystalline and opaque solids. *J. Opt. Soc. Am. B*, 8:813–819, 1991.

[128] R.W. Boyd. *Nonlinear Optics*. Academic Press, 2003.

[129] V. A. Kiyashko, A. K. Popov, V. P. Timofeev, and G. V. Yurov. Resonant upconversion of $\lambda = 1.06$ μm radiation in rubidium vapors. *Appl. Phys. B*, 30:157–159, 1983.

[130] A. K. Popov. Upconversion of IR radiation into the visible and UV ranges. *Infrared Phys.*, 25:21–27, 1985.

[131] A. S. Zibrov, M. D. Lukin, L. Hollberg, and M. O. Scully. Efficient frequency up-conversion in resonant coherent media. *Phys. Rev. A*, 65:051801, 2002.

[132] T. Meijer, J. D. White, B. Smeets, M. Jeppesen, and R. E. Scholten. Blue five-level frequency-upconversion system in rubidium. *Opt. Lett.*, 31:1002–1004, 2006.

[133] A. M. Akulshin, R. J. McLean, A. I. Sidorov, and P. Hannaford. Collinear and collimated blue light generated by four-wave mixing in Rb vapour. *Opt. Express*, 17:22861–22870, 2009.

[134] A. Vernier, S. Franke-Arnold, E. Riis, and A. S. Arnold. Enhanced frequency up-conversion in Rb vapor. *Opt. Express.*, 18:17020–17026, 2010.

[135] M.O. Scully, Yu. Rostovtsev, A. Svidzinsky, and J.T. Chang. XUV coherent Raman superradiance. *J. Mod. Opt.*, 55:3219–3236, 2008.

[136] J. C. Miller, R. N. Compton, M. G. Payne, and W. W. Garrett. Resonantly enhanced multiphoton ionization and third-harmonic generation in xenon gas. *Phys. Rev. Lett.*, 45:114–117, 1980.

[137] R. N. Compton, J. C. Miller, A. E. Carter, and P. Kruit. Resonantly enhanced multiphoton ionization of xenon: Photoelectron energy analysis. *Chem. Phys. Lett.*, 71:87–90, 1980.

[138] M. G. Payne, W. R. Garret, and H. C. Baker. Effects of collective emission on multiphoton excitation and ionization near a three-photon resonance. *Chem. Phys. Lett.*, 75:468–472, 1980.

[139] M. G. Payne and W. R. Garrett. Cooperative effects on multiphoton ionization and third-harmonic generation in the near three-photon resonance. *Phys. Rev. A*, 26:356–371, 1982.

[140] M. Poirier. Competition between resonant multiphoton ionization and third-harmonic generation: A mean-field model. *Phys. Rev. A*, 27:934–943, 1983.

[141] V. Peet. Wave-mixing interference in three-photon resonant atomic excitation with cross-polarized angled beams. *Phys. Rev. A*, 74:033406, 2006.

[142] R. B. Miles and S. E. Harris. Optical third-harmonic generation in alkali metal vapors. *IEEE J. Quant. Elect.*, 9:470–484, 1973.

[143] W. M. Tolles and R. D. Turner. A comparative analysis of the analytical capabilities of coherent anti-Stokes Raman spectroscopy (CARS) relative to Raman scattering and absorption spectroscopy. *Appl. Spectrosc.*, 31:96–103, 1977.

[144] A. Volkmer, L. D. Book, and X. S. Xie. Time-resolved coherent anti-Stokes Raman scattering microscopy: Imaging based on Raman free induction decay.

Appl. Phys. Lett., 80:1505–1507, 2002.

[145] P. Kukura, D. W. McCamant, S. Yoon, D. B. Wandschneider, and R. A. Mathies. Structural observation of the primary isomerization in vision with femtosecond stimulated Raman. *Science*, 310:1006–1009, 2005.

[146] G. I. Petrov, R. Arora, V. V. Yakovlev, X. Wang, A. V. Sokolov, et al.. Comparison of coherent and spontaneous Raman microspectroscopies for noninvasive detection of single bacterial endospores. *Proc. Natl. Acad. Sci. USA*, 104:7776–7779, 2007.

[147] D. Pestov, R. K. Murawski, G. O. Ariunbold, X. Wang, M. Zhi, A. V. Sokolov, et al.. Optimizing the laser-pulse configuration for coherent Raman spectroscopy. *Science*, 316:265–268, 2007.

[148] W. Steinbrecht, K. W. Rothe, and H. Walther. Lidar setup for daytime and nighttime probing of stratospheric ozone and measurements in polar and equatorial regions. *Appl. Opt.*, 28:3616–3624, 1989.

[149] S. E. Bisson, E. M. Goldsmith, and M. G. Mitchell. Narrow-band, narrow-field-of-view Raman lidar with combined day and night capability for tropospheric water-vapor profile measurements. *Appl. Opt.*, 38:1841–1849, 1999.

[150] C. Xu and W. W. Webb. Measurement of two-photon excitation cross sections of molecular fluorophores with data from 690 to 1050 nm. *J. Opt. Soc. Am. B*, 13:481–491, 1996.

[151] X. Y. Zhang, M. A. Young, O. Lyandres, and R. P. Van Duyne. Rapid detection of an anthrax biomarker by surface-enhanced Raman spectroscopy. *J Am. Chem. Soc.*, 127:4484–4489, 2005.

[152] X. Y. Zhang, J. Zhao, A. V. Whitney, J. W. Elam, and R. P. Van Duyne. Ultrastable substrates for surface-enhanced Raman spectroscopy: Al_2O_3 overlayers fabricated by atomic layer deposition yield improved anthrax biomarker detection. *J Am. Chem. Soc.*, 128:10304–10309, 2006.

[153] P. D. Maker and R. W. Terhune. Study of optical effects due to an induced polarization third order in electric field strength. *Phys. Rev.*, 137:A801–A818, 1965.

[154] M. D. Levenson and N. Bloembergen. Dispersion of nonlinear optical susceptibility tensor in centrosymmetric media. *Phys. Rev. B*, 10:4447–4463, 1974.

[155] B. D. Prince, A. Chakraborty, B. M. Prince, and H. U. Stauffer. Development of simultaneous frequency- and time-resolved coherent anti-Stokes Raman scattering for ultrafast detection of molecular Raman spectra. *J. Chem. Phys.*, 125:044502, 2006.

[156] S. Roy, T. R. Meyer, and J. R. Gord. Time-resolved dynamics of resonant and nonresonant broadband picosecond coherent anti-Stokes Raman scattering signals. *Appl. Phys. Lett.*, 87:264103, 2005.

[157] M. D. Duncan, J. Reintjes, and T. J. Manuccia. Scanning coherent anti-Stokes Raman microscope. *Opt Lett.*, 7:350–352, 1982.

[158] C. L. Evans, E. O. Potma, M. Puoris'haag, D. Ct, C. P. Lin, et al.. Chemical imaging of tissue in vivo with video-rate coherent anti-Stokes Raman scattering microscopy. *Proc. Natl. Acad. Sci. USA*, 102:16807–16812, 2005.

[159] J. P. Ogilvie, E. Beaurepaire, A. Alexandrou, and M. Joffre. Fourier-transform coherent anti-Stokes Raman scattering microscopy. *Opt Lett.*, 31:480–482, 2006.

APPENDIX A

INTENSITY CORRELATION AND ANTICORRELATIONS IN COHERENTLY DRIVEN ATOMIC VAPOR*

Motivated by the recent experiment [V.A. Sautenkov, Yu.V. Rostovtsev, and M.O. Scully, Phys. Rev. A 72, 065801 (2005)], we study the field intensity fluctuations due to interaction between a laser with a finite bandwidth and a dense atomic medium. The intensity-intensity cross correlation of two orthogonal, circular polarized beams can be controlled by the applied external magnetic field. A smooth transition from perfect correlations to anti-correlations (at zero delay time) of the outgoing beams is observed.

1. Introduction

The fundamental limits of spectral resolution and sensitivity of spectroscopic techniques, the information transfer and computation rates, the spatial resolution of optical microscopy and imaging are determined by statistical properties of light. For last five decades, enormous theoretical and experimental research activities have been devoted to studying fluctuations in classical and quantum systems [1,2].

The first experimental demonstration of the correlation between the intensity fluctuations recorded at two different photo-detectors illuminated by the same thermal light source was performed by Hanbury-Brown and Twiss [3]. In their experiment, photon bunching, i.e. an enhancement in the intensity-intensity correlations, has been observed.

---

*Reprinted with permission from "Intensity correlation and anti-correlations in coherently driven atomic vapory", by Gombojav O. Ariunbold, Yuri V. Rostovtsev, Vladimir A. Sautenkov and Marlan O. Scully, 2010. *J. Mod. Opt.*, in print, Copyright [2010] by Taylor & Francis

Quantum approach to optical coherence was introduced in pioneering work [4]. Photon anti-bunching has been predicted in [5]. Later, it was first observed in the resonance fluorescence experiment [6]. The second order correlations in fluorescence has been calculated for two-level atomic systems [7,8].

Its generalization to Λ-type three-level atomic systems that also exhibits an anti-bunching effect has been done [9]. Particularly, under the condition of electromagnetically induced transparency (EIT) [10], the correlation between Stokes and anti-Stokes photons emitted from Rb atoms with a short time delay has been measured [11]. It has been shown that the correlations occur due to four-wave mixing in cold atoms [12].

Generation of pairs of photons with a controllable time delay has been shown in [13]. The storage and retrieval of weak probe pulses [14,15] in a macroscopical ensemble of atoms [16] have been achieved A transition from anti-bunching to bunching of light emitted from a few atoms in a very high finesse cavity has been experimentally demonstrated [17] by increasing a number of atoms interacting with light as was shown in [18].

The phase fluctuations of the input field after interacting with the atomic vapor can be transformed into amplitude fluctuations. As has been shown in [19], the intensity fluctuations of laser beam transmitted through an atomic medium can be used as a spectroscopic tool. For this reason, a great deal of interest has been devoted to the study of the conversion of the laser phase fluctuations into the intensity fluctuations of the transmitted light [20,21,22,23,24].

Noise spectroscopy of nonlinear magneto-optical resonances in Rb atomic vapor has been developed in [24] and the observed experimental data has been explained by a theoretical model based on the absorption induced intensity fluctuations [20]. Assuming an optically thin medium, the qualitative agreement with the experiment has been obtained.

Photon bunching in the intensity-intensity correlations between pump and probe fields for different probe detunings in Rb vapor [25] and in the temporal correlations between forward and backward anti-Stokes photons scattered from sodium vapor [26] has been demonstrated.

Recently, the observation of a smooth transition from EIT correlated to anti-correlated photons emitted from coherently prepared ^{87}Rb vapor has been reported in [27,28,29,30,31]. In the present work, we develop a theory to explain the results of the previous experiments [27], considering a laser source with a finite bandwidth. Furthermore, we suggest a method based on the numerical results to estimate the relaxation rate for coherence between the Zeeman sub-levels.

The work is organized as follows. In Part 2, the experimental setup is described, and the obtained results are reported. In Part 3, we study the absorption induced fluctuations of laser beam intensities and their correlations by considering a generic three-level Λ atomic system interacting with the orthogonal polarized fields. We obtain the approximate analytical solutions elucidating an origin of perfect correlations as well as anti-correlations between two modes. Then in Part 4, we solve equations of motion, numerically, to prove the results of the analytical predictions. The last part is conclusion.

2. Experimental setup and obtained results

An experimental setup is shown in Fig. 69 (more details can be found in [27]). An external-cavity diode laser [32] is tuned to D_1 line ($5S_{1/2}(F = 2) \leftrightarrow 5P_{1/2}(F' = 1)$) of ^{87}Rb. An output laser beam is divided by a beam-splitter into two beams. One of the beam passes through a $\lambda/2$-wave plate, then the polarizations of these two beams become orthogonal. The beams are combined together by a polarizing beam-splitter (PBS). After the $\lambda/4$ wave-plate each of orthogonally polarized beams converted in a beam with circular polarization. Thus the input beam can be considered as a

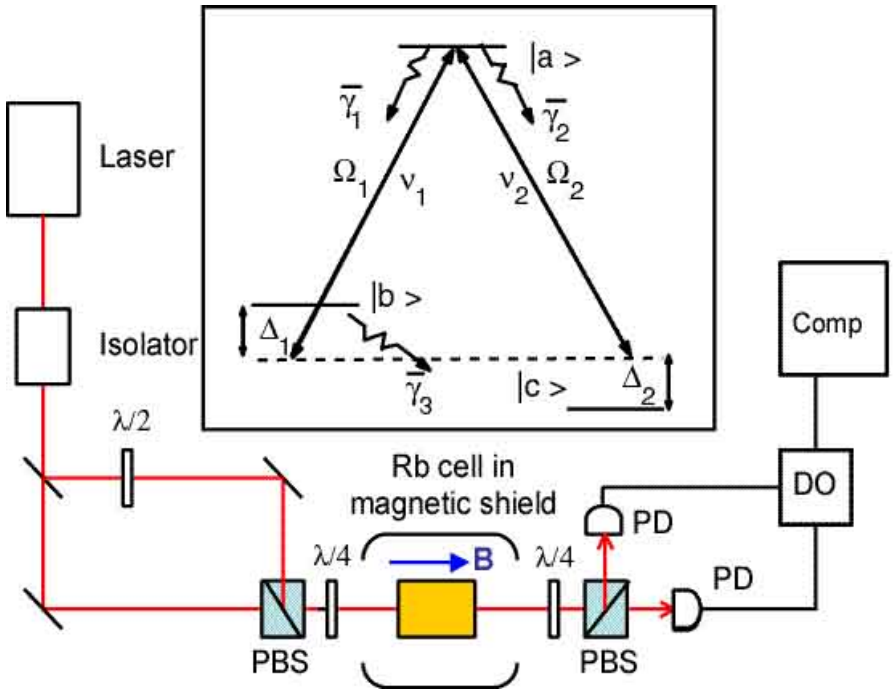

Fig. 69. Appendix A. Schematics of the experimental setup and the simplified level scheme of Rb atoms. PBS is the polarizing beam-splitter; $\lambda/2$, $\lambda/4$ are the half- and quarter-wave plates correspondingly; PD is the photo-detector; DO is the digital oscilloscope; Comp is the computer.

combination of two circular polarized optical fields.

A glass cell of length $L = 7.5$ cm with Rb vapor (natural abundance) at density approximately 10^{12} cm^{-3} is installed in a two-layer magnetic shield. A simplified level scheme is depicted in the inset of Fig. 69.

The transmitted through the cell laser beams pass the second $\lambda/4$ wave-plate, and then they are separated by another polarizing beam-splitter and focused on fast photodiodes (PD) with frequency bandwidth 75kHz$-$1.2 GHz. The optical path lengths for both beams are approximately the same.

The opposite circular polarized optical beams interact with the Rb vapor and

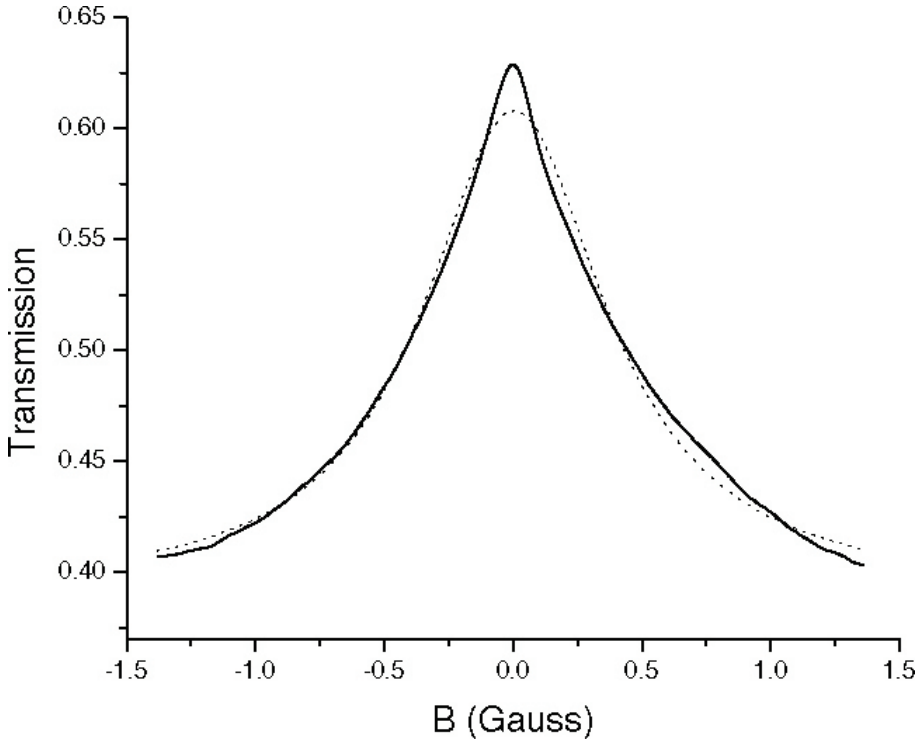

Fig. 70. Appendix A. A transmission of the optical field through the Rb cell as a function of magnetic field B (solid curve). Dots stand for the Lorentzian fit. The total optical power at the entrance window is 1 mW.

induce ground state Zeeman coherence. By changing the magnitude of a longitudinal magnetic field, we effectively introduce two-photon detuning (see the inset of Fig. 69 that induces quantum coherence. As a result, the optical transmission of the cell is also depends on the longitudinal magnetic field. The dependence of the transmission on the magnetic field is shown in Fig. 70. The effect of the EIT can be easily seen in Fig. 70. The data is obtained at the optical power of 0.5 mW (total power 1 mW) and beam diameter of 0.1 cm for each beam at the entrance window of the Rb cell. The waveforms from photo-detectors with total optical power of laser beams at front window of Rb cell is 1 mW are shown in Fig. 71(a,b); (a) the fluctuations of

intensities versus time when one of the laser beams is blocked and (b) the fluctuations of intensities versus time for two spatially separated beams.

The time dependent intensity fluctuations $\delta I_{1,2}(t)$ of both optical beams transmitted through Rb vapor, are registered by the photodetectors (see Fig. 69). Data presented here is part of the recorded data in 10 μsec. The signal is proportional to the laser intensity as

$$\text{Signal} = 500[V/W]I_{Laser}.$$

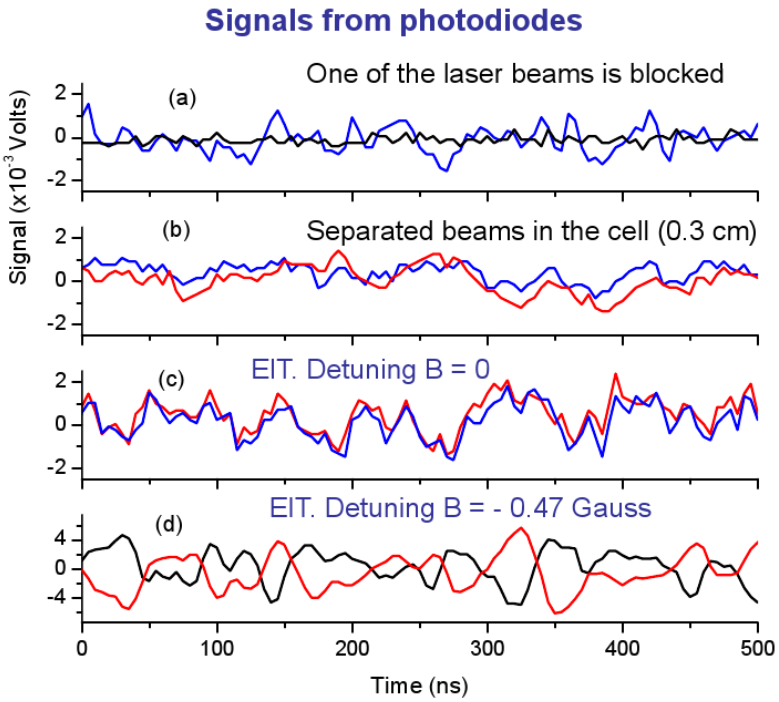

Fig. 71. Appendix A. Waveforms from photo-detectors with total optical power of laser beams at front window of Rb cell is 1 mW. (a) The fluctuations of intensities versus time when one of the laser beams is blocked. (b) The fluctuations of intensities versus time for two separated beams. The fluctuations of intensities versus time for two coinciding beams with (c) no magnetic field $B = 0$ and (d) applied magnetic field $B = -0.47$ Gauss.

Furthermore, the intensity-intensity correlations between two beams can be calculated using the recorded data.

The second order correlation function $G^{(2)}(\tau)$ [33] for intensity fluctuations of two optical beams with time delay τ is given by

$$G^{(2)}(\tau) = \frac{\langle \delta I_1(t) \delta I_2(t+\tau) \rangle}{\sqrt{\langle [\delta I_1(t)]^2 \rangle \langle [\delta I_2(t+\tau)]^2 \rangle}}, \tag{A.1}$$

where the time average of arbitrary variable $Q(t)$ is defined as $\langle Q(t) \rangle = \int_t^{t+T} Q(t)dt/T$. The integration time T is taken to be as large as 10 μs.

In the absence of the external magnetic field $B = 0$, the two-photon detuning equals to zero, and the EIT is observed. In this case, the induced fluctuations of the transmitted beams through Rb vapor are almost synchronized (see Fig. 71(c)). Thus the intensity-intensity correlation curve of Fig. 72(a) has a sharp spike, clearly showing strong correlations (bunching). The magnitude of the correlation peak at $\tau = 0$ is 0.9 and the average background is near 0.15. The width of the correlation peak is increased with reduced optical power, and is inversely proportional to the population decay rate of the excited state and the Rabi frequency.

On the other hand, the most intriguing feature is observed when the applied magnetic field is $B = -0.47$ Gauss. As shown in Fig. 71(d), the intensity fluctuations are anti-correlated. The magnetic field causes switching from correlation to anticorrelation (see Fig. 72(b)). The width of the peaks is related to the saturated width of resonance in Rb vapor absorption (a single photon resonance) [34]. Moreover, the second order correlation $G^{(2)}(\tau)$ obtained with spatially separated beams (see Fig. 72(b)) (distance between beams 0.3 cm is bigger than the beam diameter 0.1cm) has a correlation peak (at $\tau = 0$) of 0.7 and a larger background of 0.3. This reduced contrast indicates that the enhanced correlations are clearly due to interac-

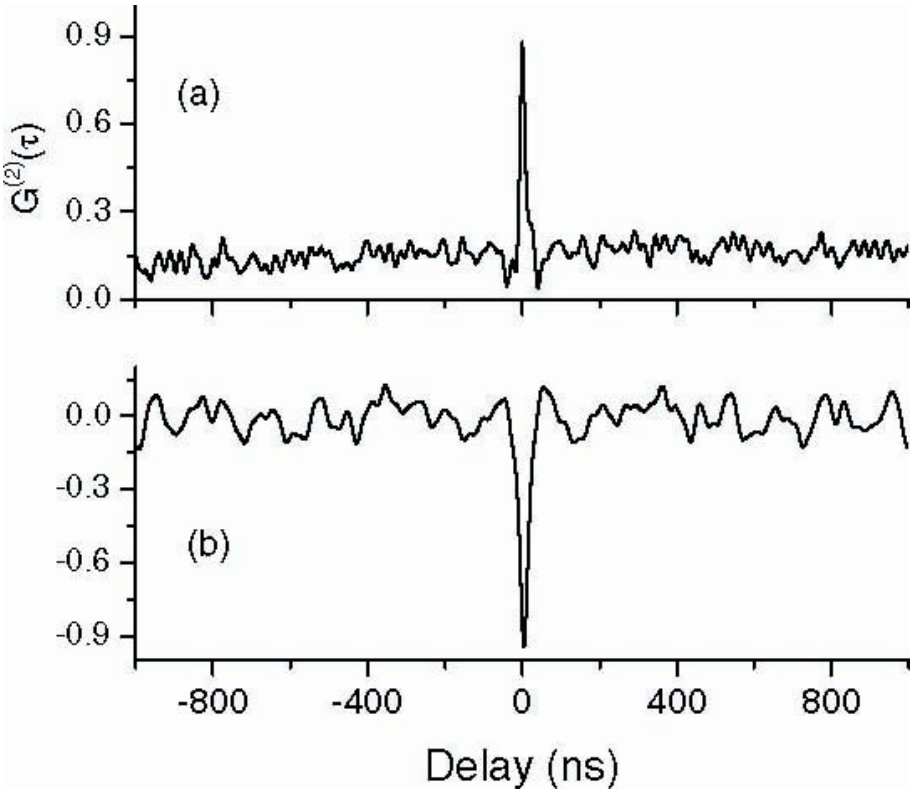

Fig. 72. Appendix A. Intensity-intensity correlation functions $G^{(2)}(\tau)$ as functions of time delay τ for magnetic fields $B = 0$ (above) and $B = -0.47$ (bottom).

tion of the two beams. The measurements show that a perfect switching from photon correlation to anticorrelation where the correlation peak with magnitude 0.9 for zero magnetic field $B = 0$ switches to the anticorrelation dip with magnitude -0.9 for $B = -0.47$ Gauss.

As we show below, this pronounced modification of waveforms is very important for determination of experimental parameters. The width related to intensity-intensity correlations $G^{(2)}(\tau = 0)$ are 0.24 Gauss, almost four times narrower than the corresponding EIT width, which is 0.85 Gauss for optical power 1 mW.

3. Theoretical results

Λ-type Three-level Atoms Driven by Laser with Finite Bandwidth

Let us consider Λ-type three-level atoms (a level scheme shown in Fig. 69 interacting with two radiation modes generated by the diode laser. The laser beams are in resonance with a three-level medium as depicted in Fig. 69. The Hamiltonian of the atom is given by

$$\hat{H} = \hbar\Omega_1|a\rangle\langle b| + \hbar\Omega_2|a\rangle\langle c| + h.c., \tag{A.2}$$

where $\Omega_{1,2} = \wp_{c,b}E_{1,2}/\hbar$ are the Rabi frequencies of left- and right-circularly polarized beams; $\wp_{c,b}$ and $E_{1,2}$ are the corresponding dipole moments of the atomic transitions and the electric fields. The density matrix equation is given by

$$\dot{\rho} = -\frac{i}{\hbar}[H,\rho] - \frac{1}{2}(\hat{\Gamma}\rho + \rho\hat{\Gamma}), \tag{A.3}$$

where $\hat{\Gamma}$ is the relaxation matrix, introduced to describe relaxation processes in the atomic medium [2,33].

The density matrix equations in the rotating wave approximation are given by (e.g., see [9])

$$\begin{aligned}
\dot{\rho}_{bc} &= -(\gamma_3 + i\Delta)\rho_{bc} + i\Omega_1\rho_{ac} - i\Omega_2\rho_{ba}, \\
\dot{\rho}_{ba} &= -(\gamma_1 + i\Delta_1)\rho_{ba} - i\Omega_1(\rho_{bb} - \rho_{aa}), \\
&\quad -i\Omega_2\rho_{bc} + i\dot{\phi}(t)\rho_{ba}, \\
\dot{\rho}_{ca} &= -(\gamma_2 - i\Delta_1)\rho_{ca} - i\Omega_2(\rho_{cc} - \rho_{aa}), \\
&\quad -i\Omega_1\rho_{cb} + i\dot{\phi}(t)\rho_{ca}, \\
\dot{\rho}_{bb} &= \tilde{\gamma}_3\rho_{cc} + \tilde{\gamma}_1\rho_{aa} + i\Omega_1\rho_{ab} - i\Omega_1\rho_{ba}, \\
\dot{\rho}_{cc} &= \tilde{\gamma}_2\rho_{aa} - \tilde{\gamma}_3\rho_{cc} - i\Omega_2\rho_{ca} + i\Omega_2\rho_{ac},
\end{aligned} \tag{A.4}$$

where $\rho_{aa} = 1 - \rho_{bb} - \rho_{cc}$; the one- and two-photon detunings are $\Delta_1 = \omega_a - \omega_c - \nu_2 =$

$\nu_1 - \omega_a + \omega_b$, $(\nu_1 = \nu_2)$ and $\Delta = \omega_b - \omega_c$; the effective decay rates [35] are $\gamma_3 = (\tilde{\gamma}_3 + \tilde{\gamma}_{21} + \tilde{\gamma}_{12})/2$, $\gamma_1 = (\tilde{\gamma}_1 + \tilde{\gamma}_2 + \tilde{\gamma}_{21} + \tilde{\gamma}_{31})/2$ and $\gamma_2 = (\tilde{\gamma}_1 + \tilde{\gamma}_2 + \tilde{\gamma}_3 + \tilde{\gamma}_{12} + \tilde{\gamma}_{32})/2$, $\tilde{\gamma}_1$ and $\tilde{\gamma}_2$ correspond to the spontaneous emission rates from level $|a\rangle$ to levels $|c\rangle$ and $|b\rangle$, respectively; $\tilde{\gamma}_{21}$, $\tilde{\gamma}_{12}$, $\tilde{\gamma}_{32}$ and $\tilde{\gamma}_{31}$ stand for the dephasing rates, and $\tilde{\gamma}_3$ is the population decay rate of the level $|b\rangle$.

We assume that diode laser radiation has phase noise. The $\phi(t)$ in Eq.(A.4) represents the fluctuating phase [8] of the driven field that is characterized by the Wiener-Levy diffusion process [1]. For such a process, the average and the two-time correlation of the stochastic variables are given by

$$\begin{aligned} \langle\overline{\dot{\phi}(t)}\rangle &= 0 \\ \langle\overline{\dot{\phi}(t)\dot{\phi}(t')}\rangle &= 2D\delta(t-t'), \end{aligned} \tag{A.5}$$

where D is the diffusion coefficient; the stochastic averaging is denoted by the upper bar. Thus, the input laser field has a Lorentzian spectrum with a full width at half maximum (FWHM) of D/π Hz. In a realistic situation, the phase correlation has a finite relaxation time. The Gaussian process in which the correlations are determined by the exponential function of time delay is often referred to as Ornstein-Uhlenbeck [36] or the colored noise.

Absorption Induced Intensity-Intensity Correlations

The propagation equations for the laser fields are given by

$$\frac{\partial\Omega_1}{\partial z} = i\eta_1\rho_{ab}, \quad \frac{\partial\Omega_2}{\partial z} = i\eta_2\rho_{ac}, \tag{A.6}$$

where $\eta_{1,2} = 3\lambda^2 N\gamma_{r1,2}/8\pi$, N is the density of Rb atoms, λ is the wavelength of radiation at the resonant D_1 transition, γ_{r1} and γ_{r2} are the radiation relaxation rates for transitions $a-b$ and $a-c$ correspondingly; ρ_{aq} is the atomic coherence between

levels a and q, $(q = b, c)$.

For the sake of simplicity. let us consider a thin absorbing medium and assume that the transmitted field is a superposition of the input and the created fields in the first order approximation for $\eta_{1,2}L/\gamma_{r1,2}$, if $\eta_{1,2}L \ll \gamma_{r1,2}$; here L is the length of the atomic cell. Furthermore, this should be still valid for a preferably long medium with weak absorption that satisfies the condition $\eta_{1,2}L \ll \gamma_{r1,2}$. In what follows, we show that this approximation reproduces the observed results qualitatively.

Following by the approach developed in [20,24], the transmitted fields are given by

$$\begin{aligned} \Omega_1^{out}(t) &\approx \Omega_1 + i(\eta_1 L)\rho_{ab}(t), \\ \Omega_2^{out}(t) &\approx \Omega_2 + i(\eta_2 L)\rho_{ac}(t). \end{aligned} \tag{A.7}$$

We do not include the Doppler effect (the density matrix elements in Eq.(A.7) should be averaged over the thermal velocity distribution), because the two-photon detuning is Doppler free (one can see the importance of Doppler averaging in [37] for details).

Then, the transmitted intensities $I_{1,2}(t) \Rightarrow |\Omega_{1,2}^{out}(t)|^2$ are written as

$$\begin{aligned} I_1(t) &\approx \Omega_1^2 + \Omega_1(\eta_1 L)\mathrm{Im}\{\rho_{ab}(t)\} \\ I_2(t) &\approx \Omega_2^2 + \Omega_2(\eta_2 L)\mathrm{Im}\{\rho_{ac}(t)\}. \end{aligned} \tag{A.8}$$

We assume that the input fields are real and much stronger than the generated ones. We define a fluctuation of an arbitrary variable $Q(t)$ as $\delta Q(t) = Q(t) - \overline{Q(t)}$. Then, the intensity fluctuation is read as

$$\begin{aligned} \delta I_1(t) &= \Omega_1(\eta_1 L)\mathrm{Im}\{\delta\rho_{ab}(t)\}, \\ \delta I_2(t) &= \Omega_2(\eta_2 L)\mathrm{Im}\{\delta\rho_{ac}(t)\}. \end{aligned} \tag{A.9}$$

From the above expression, it is easy to see that $\langle \delta I_{1,2}(t) \rangle = 0$, because $\langle \delta \rho_{aq}(t) \rangle = 0$, $q = c, b$. From Eq.(A.9), using Eq.(A.1), and taking into account that the process is stationary, the intensity-intensity correlation is given by

$$G^{(2)}(\tau) = \frac{\langle \mathrm{Im}\{\delta\rho_{ac}(t)\}\mathrm{Im}\{\delta\rho_{ab}(t+\tau)\}\rangle}{\sqrt{\langle [\mathrm{Im}\{\delta\rho_{ac}(t)\}]^2\rangle \langle [\mathrm{Im}\{\delta\rho_{ab}(t)\}]^2\rangle}}. \tag{A.10}$$

Approximate Theoretical Analysis: Two-photon Zero Detuning

Let us consider a resonant case where all detunings are set to be zero, and $\Omega_1 = \Omega_2$, $\tilde{\gamma}_3 = 0$, $\gamma_1 = \gamma_2$. It is easy to show analytically that $\langle \overline{\rho}_{bc} \rangle = \langle \overline{\rho}_{cb} \rangle$. According to the performed simulations of Eq.(A.4), the coherence term ρ_{bc} is real, i.e. $\rho_{bc} = \rho_{cb}$. Therefore, the equations for the coherence terms ρ_{ba} and ρ_{ca} have a symmetrical form as

$$\begin{aligned} \dot{\rho}_{ba} &= -\gamma_1 \rho_{ba} - i\Omega_1(\rho_{bb} - \rho_{aa}) + i\dot{\phi}(t)\rho_{ba} - i\Omega_1 \rho_{bc}, \\ \dot{\rho}_{ca} &= -\gamma_1 \rho_{ca} - i\Omega_1(\rho_{cc} - \rho_{aa}) + i\dot{\phi}(t)\rho_{ca} - i\Omega_1 \rho_{bc}. \end{aligned} \tag{A.11}$$

From Eq.(A.11), These two equations are identical if ρ_{bb} and ρ_{cc} are the same. Note that, because of the symmetrical atomic configuration, it is obvious that populations ρ_{bb}, and ρ_{cc} are the same, $\rho_{bb} \approx \rho_{cc}$. This is, of course, true only in the resonant case. From Eq.(A.11), it follows that

$$\rho_{ba}(t) \approx \rho_{ca}(t). \tag{A.12}$$

This correlated behavior could be understood as follows. The phase fluctuations of the incident beams are converted into the intensity fluctuations due to the atom-field interactions as is seen from Eq.(A.4). Roughly speaking, the three-level atoms would experience the driven fields with the effective laser frequencies fluctuating around the

resonant frequency of the transition between the upper level and degenerate lower levels. Because the noise fluctuations are the same in two laser modes, any instant deviations from the resonance are identical. Therefore, the induced absorption are the same for both modes. In this regard, the system could be related to what is called a correlated emission laser, firstly proposed in [2,38], in which pairs of stimulated photons of different modes can be generated simultaneously exhibiting a sharp bunching.

Approximate Theoretical Analysis: Non-zero Two-photon Detuning

In the situation of non-zero two-photon detuning, the equations for two modes are different. However, the effective Rabi frequencies would have again the same fluctuations, but, Ω_1 is no longer resonant (see, a level scheme in Fig. 69. The absorption should not be the same for both modes in this case. Any instant deviations of the effective laser frequencies tend to be resonant to one transition, but off-resonant to the other. As a consequence, the populations of the excited and the ground states would also fluctuate. By virtue of $\dot{\rho}_{bb} + \dot{\rho}_{cc} \approx 0$, since $\dot{\rho}_{aa} \approx 0$, it is possible to do the following assumption as

$$\begin{aligned} \rho_{bb}(t) &= c + f(t), \\ \rho_{cc}(t) &= c - f(t). \end{aligned} \tag{A.13}$$

where a fluctuation $f(t)$ is real and c is constant. Note that it is not necessary to know an explicit expression for $f(t)$. This coupling function $f(t)$ appears only because of non-zero detuning, otherwise it is zero. The equations for two polarizations, ρ_{ba} and ρ_{ca}, are given by

$$\dot{\rho}_{ba} = -(\gamma_1 + i\Delta_1)\rho_{ba} - i\Omega_1 f(t) + i\dot{\phi}(t)\rho_{ba} - i\Omega_1\rho_{bc} + c'$$

$$\dot{\rho}_{ca} \quad = \quad -(\gamma_1 - i\Delta_1)\rho_{ca} + i\Omega_1 f(t) + i\dot{\phi}(t)\rho_{ca} - i\Omega_1\rho^{\dagger}_{bc} + c'.$$

The formal solutions are to be read

$$\begin{aligned} \rho_{ba}(t) &\sim +\Phi(t) + \mathrm{c}_1, \\ \rho_{ca}(t) &\sim -\Phi(t) + \mathrm{c}_2, \end{aligned} \tag{A.14}$$

where $\Phi(t) = -i\Omega_1 \int_{t_0}^{t} dt'\, \mathrm{e}^{-\gamma_1(t-t')+i(\phi(t)-\phi(t'))} f(t')$, $c_{1,2} = -i\Omega_1 \int_{t_0}^{t} dt'\, \mathrm{e}^{-\gamma_1(t-t')+i(\phi(t)-\phi(t'))}$ $(\rho_{bc,cb}+c)$ which can be slowly varying for $t_0 \Rightarrow -\infty$, $t \Rightarrow \infty$. Note that, contributions of Δ_1 to solutions are neglected since, later on, only imaginary part of amplitudes will be of interest. Eq.(A.14) clearly indicates anti-correlation between two radiation modes.

4. Numerical results

In the Ornstein-Uhlenbeck process [36], the colored noise $\xi(t)$ yields the steady-state correlation function

$$\langle\overline{\xi(t)\xi(t')}\rangle = \Theta\lambda_L \mathrm{e}^{-\lambda_L|t-t'|} \tag{A.15}$$

with $\langle\xi(t)\rangle = 0$. The stochastic differential equation Eq.(A.4) can be solved using Monte-Carlo numerical simulations. A Box-Mueller algorithm and the Euler-Maruyama method are used to realize the colored noise. Namely, one can see that the generated noise by the fast, integral algorithm developed in [39] is in a perfect agreement with the analytical definition given by Eq.(A.15) due to averaging over as many as 1000 different realizations.

A relaxation time $1/\lambda_L$ is taken to be small, to ensure that the undertaking process should be approximately white noise, i.e., $\xi(t) \sim \dot{\phi}(t)$. As a matter of fact, various choices of parameters Θ and λ_L, do not affect the final results, drastically. The numerical solutions of Eq.(A.4) allows one to obtain the intensity fluctuations

defined by Eq.(A.9).

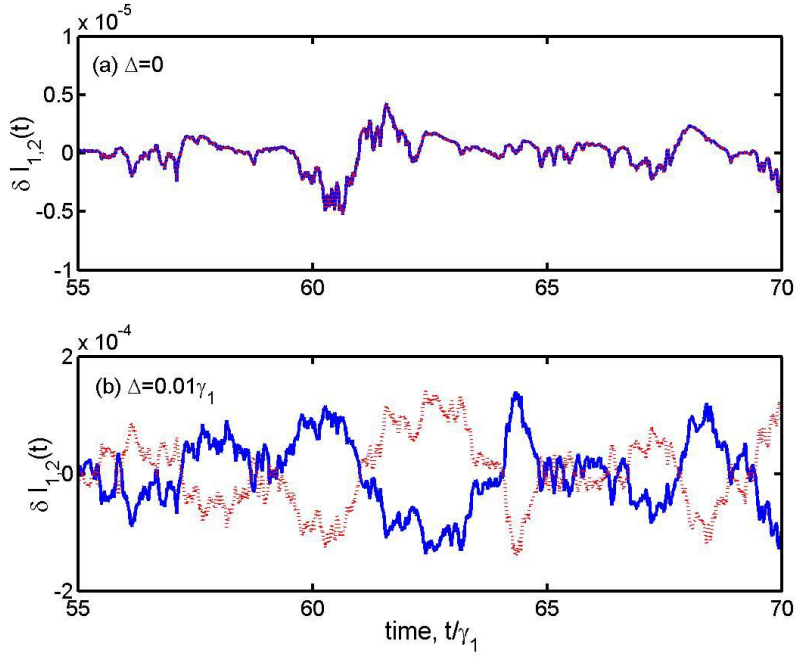

Fig. 73. Appendix A. Synchronized dynamics for intensity differences of two fields (dotted and solid curves) given by Eq.(A.9) are depicted for resonant (above figure, $\Delta = 0$) and non-resonant (bottom figure, $\Delta = 0.01\tilde{\gamma}_1$) cases. All rates and Rabi frequencies are taken to be $\tilde{\gamma}_{12,21} = 0.01\tilde{\gamma}_1$, $\tilde{\gamma}_{13,31} = \tilde{\gamma}_3 = 0$, $\tilde{\gamma}_1 = \tilde{\gamma}_2$ and $\Omega_1 = \Omega_2 = \tilde{\gamma}_1$

The numerical results of Eq.(A.9) are plotted by dotted and solid curves in Fig. 73. In resonant case, dynamics of two modes are in phase (i.e., well synchronized). The dephasing rate for both cases are much smaller than decay rates. Absolute values of two Rabi frequencies are the same as considered in the experiment. If two-photon detuning Δ becomes comparable to γ_3, then the dynamics is absolutely out of phase (see, Fig. 73). The dynamics, which is shown in Fig. 73, can be seen more clearly in terms of cross correlation functions. Figure 74 describes a switching between two completely different behaviors, namely, correlation and anti-correlation of two modes.

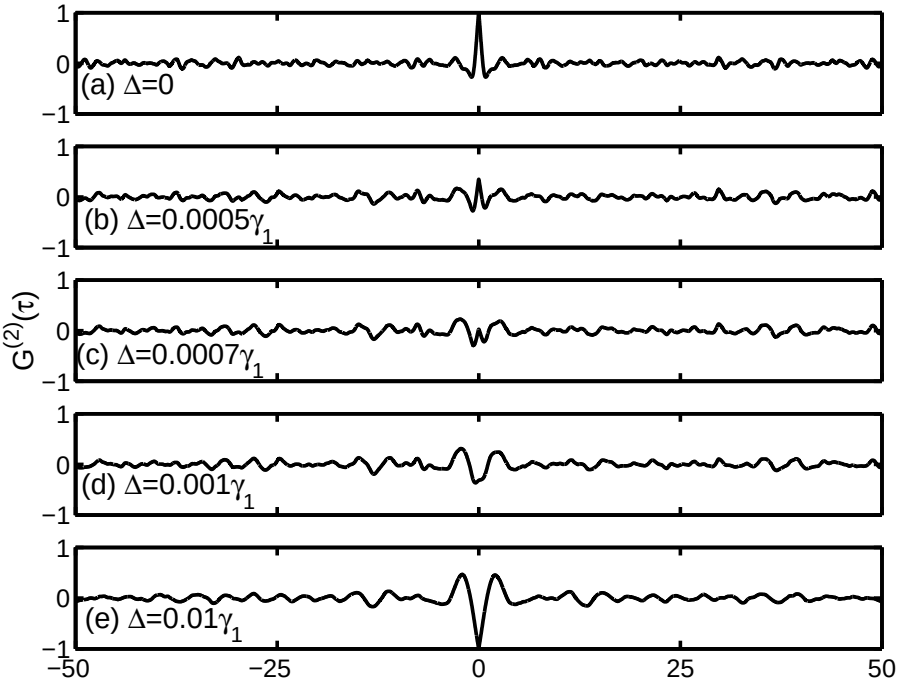

Fig. 74. Appendix A. A perfect photon correlation (a spike at $\tau = 0$, see, (a)) for $\Delta = 0$ and an anti-correlation of two modes (a dip at $\tau = 0$, see, (b)) between two modes for $\Delta = 0.01\tilde{\gamma}_1$ are obtained. The plots are calculated for the same parameters as in Fig. 73.

5. A Decoherence rate determined by switching in intensity-intensity correlations

In what follows, we analyze this switching in more detail. Similarly as in [27], we focus on correlation functions with zero time delay $G^{(2)}(\tau = 0)$. First of all, Eq.(A.10) is obtained for fixed Ω_1 but different γ_3 and shown in Fig. 75. Note that the transition from correlations to anti-correlations appears to be smooth and has certain width. The width is getting wider with the increase of dephasing rate. Surprisingly, as is shown in Fig. 76, the width is "invariant" in terms of re-scaled detuning Δ/γ_3 by the corresponding decoherence rates γ_3.

Next, let us test how a Rabi frequency affects correlations. In Fig. [77], we depict

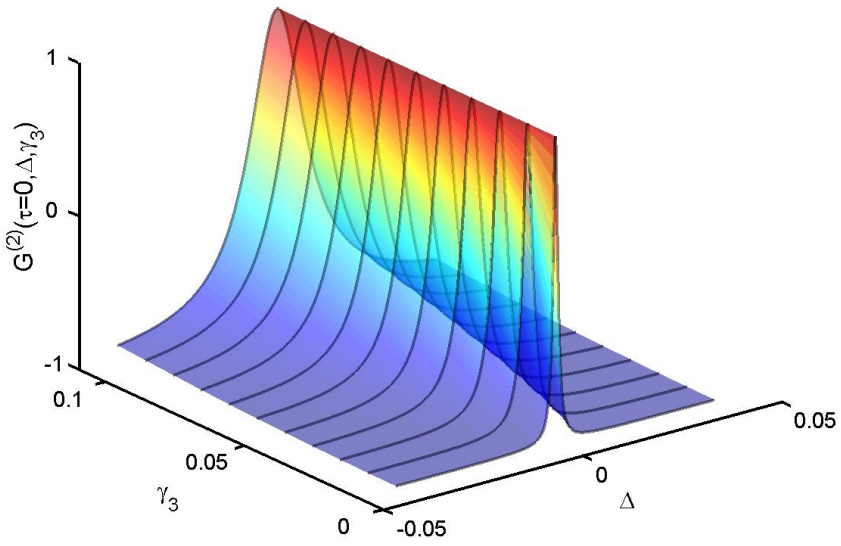

Fig. 75. Appendix A. 3D plot for correlation $G^{(2)}(\tau = 0, \Delta, \gamma_3)$ with zero time delay $(\tau = 0)$ as a function of detuning Δ and decoherence rate γ_3. Rabi frequencies are $\Omega_1 = \Omega_2 = \tilde{\gamma}_1$.

numerical results from Eq.(A.10) which depends not only on detuning, but also on the Rabi frequencies with fixed γ_3. As a matter of fact, the correlation curves are again "invariant" for all Rabi frequencies that satisfy $\Omega_1 \geq \tilde{\gamma}_1$.

These two key results for the correlation functional invariance do promise a relatively precise determination of the decoherence rate in a robust way from an experimental point of view. As is mentioned in the introduction, the atomic energy levels are perturbed, due to the interaction of the magnetic moments of atoms with the external magnetic field B. This leads to a non-degeneracy of atomic ground levels. This shift is given by

$$\Delta = aB. \tag{A.16}$$

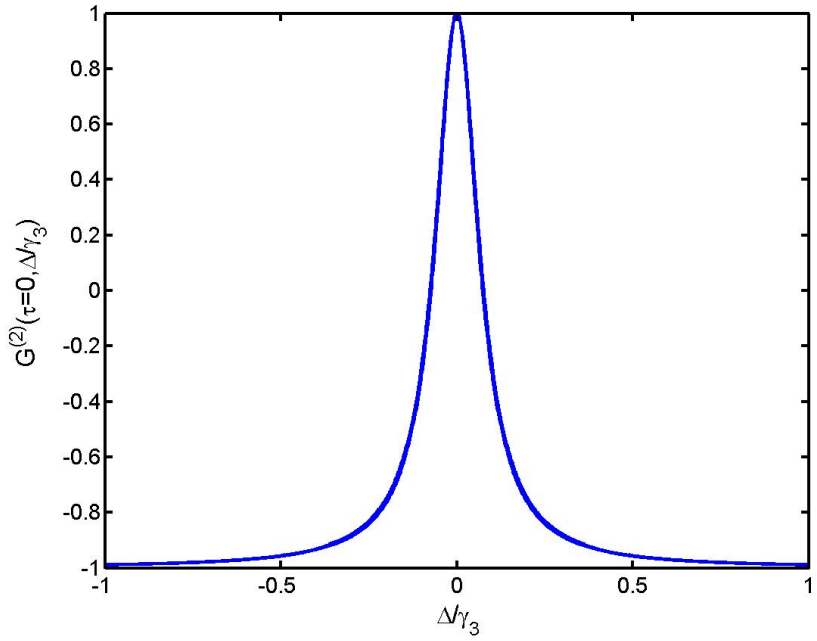

Fig. 76. Appendix A. A sample of correlation functions $G^{(2)}(\tau = 0, \Delta/\gamma_3)$ with scaled variable as Δ/γ_3 for different decoherence rates: $\gamma_3 = 0.01, 0.02, ..., 0.11\tilde{\gamma}_1$. All curves coincide. The plots are calculated for the parameters taken from Fig. 73.

The constant is defined by Bohr's magneton, the magnetic quantum numbers, and gyromagnetic factor as $a = (\mu_B/\hbar)g(m_2 - m_1)$. To be more explicit, let us concentrate on ^{87}Rb vapor in connection to our experiment [27]. An external-cavity diode laser is tuned to $5S_{1/2}(F = 2) \leftrightarrow 5P_{1/2}(F' = 1)$. Applied magnetic field leads approximately to three level Λ atomic configuration with a common upper level $5P_{1/2}(F' = 1, m_3 = 0)$ and two lower levels $5S_{1/2}(F = 2, m_1 = -1)$ and $5S_{1/2}(F = 2, m_2 = +1)$. Using the facts that $g = 0.5$ for $S_{1/2}(F = 2)$ and $\mu_B/\hbar = 1.4$MHz, the constant to be estimated as $a = 1.4$MHz/G. Moreover, from Eq.(A.16), the relation for B can be rewritten as

$$B = \alpha \frac{\Delta}{\gamma_3}, \tag{A.17}$$

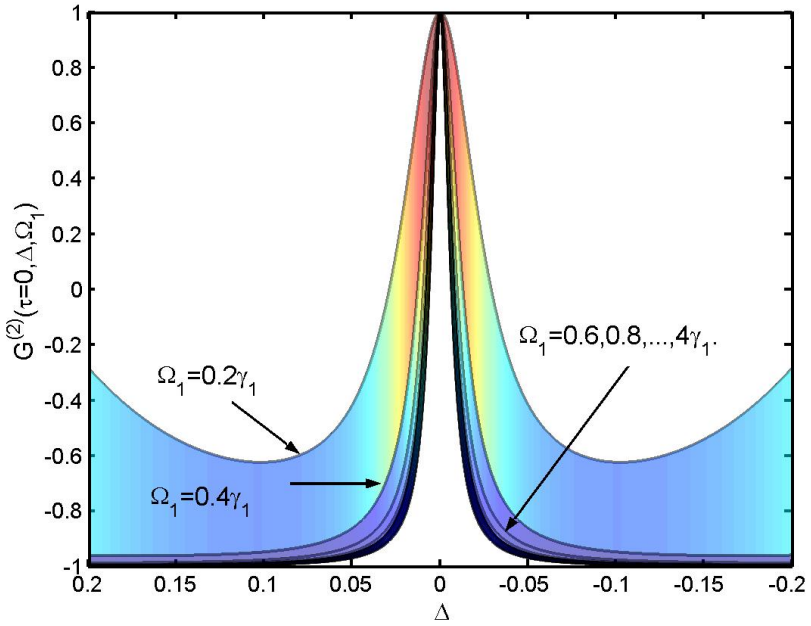

Fig. 77. Appendix A. 2D view of 3D plot for correlation $G^{(2)}(\tau = 0, \Delta, \Omega_1)$ depending on different values of both detuning and Rabi frequency for fixed dephasing rate $\gamma_3 = 0.1\tilde{\gamma}_1$.

where α is a scaling factor. For fixed α, all correlations with no time delay are supposed to be invariant. The experimental data are plotted in Fig. 78.

An asymmetry with respect to the zero detuning may be due to Stark shift which is not of interest in the present situation. Because of two conditions of invariance, there is a very good reason to believe that a form of theoretical correlation functions for all $\Omega_1 \gg \tilde{\gamma}_1$ and any of γ_3, should be equivalent to the experimental data measured for particular Ω_1 and γ_3. In this spirit, theoretical curves by changing scale α, can be compared with the measurements. Remember that $\alpha = \gamma_3/a$, a new formula for dephasing rate, can be given as

$$\gamma_3 = \alpha a. \tag{A.18}$$

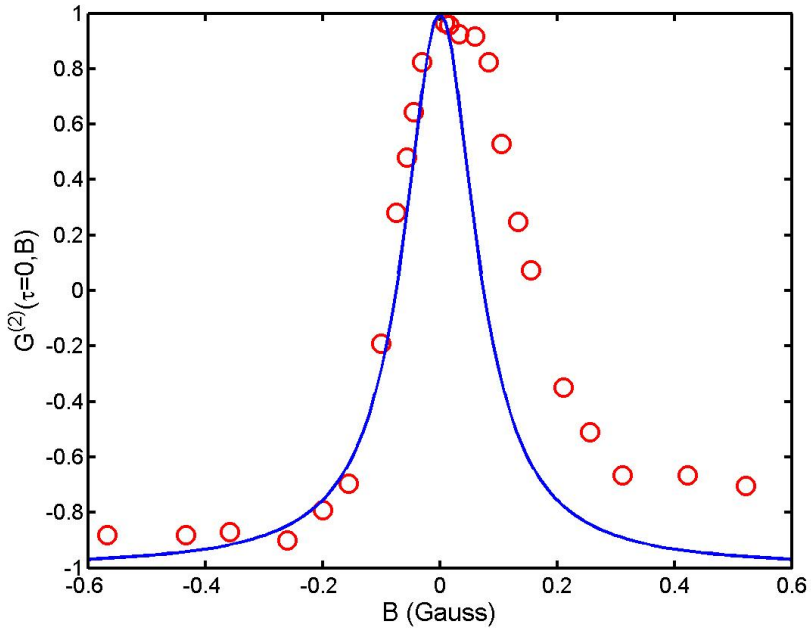

Fig. 78. Appendix A. A finding dephasing rate in Rb vapor. Correlation $G^{(2)}(\tau = 0, B)$ varying with magnetic field strength B is compared to the experimental data which allows us to get scaling factor being $\alpha \sim 1[G]$. Dephasing rate is, thus, found to be $\gamma_3 \sim 1$MHz independently from $\tilde{\gamma}_1$. No free parameters are used here. Experimental data is presented by circles for optical power 1 mW

Once α is found from experimental data, the dephasing rate for that atomic vapor is determined by Eq.(A.18). As we expected this is also independent from population decay rates. For Rb vapor, we have found from Fig. 78, that scaling factor $\alpha \sim$ 1Gauss. Therefore, the decoherence rate is estimated to be $\gamma_3 \sim 1$ MHz.

6. Conclusion

An experimental demonstration of intensity correlations and anti-correlations of coupled fields in a dense Rb vapor is reported. A ground state coherence is created between Zeeman sub-levels by two laser beams with orthogonal circular polarizations. Intensity fluctuations induced by resonant medium are correlated under resonance

EIT condition and anti-correlated in the presence of non-zero two photon detuning. A narrow correlation peak and anti-correlation dip, in time domain are associated with frequencies wider than the EIT width and the natural optical width, and it is related to the Rabi frequency.

A dependence of correlations on the magnetic field (two-photon detuning) shows resonance behavior. The resonances are nearly four times narrower than the width of the observed EIT resonances. A smooth transition from perfect correlations to anti-correlations (at zero delay time) between the outgoing beams as functions of the magnetic field strength is robust with respect to a variety of different choices of physical parameters involved and, thus, can provide us with the desired information about decoherence in a three-level atomic vapor.

Moreover, correlation properties of coupled fields in Λ scheme can be used to reduce noise and improve performance of EIT based atomic clocks and magnetometers. The phase noise to intensity noise conversion is an important physical process limiting the accuracy. In EIT atomic clock and magnetometers [40,41,42], it is possible to avoid the contribution of the atomic medium induced excess intensity noise.

REFERENCES

[1] C. W. Gardiner and P. Zoller, "Quantum noise," Springer-Verlag, Berlin, 2000.

[2] M. O. Scully and S. Zubairy, "Quantum optics," Cambridge University Press, Cambridge, 1997.

[3] R. Hanbury-Brown and R. Q. Twiss, "Correlation between photons in two coherent beams of light," Nature, vol. 177, pp. 27-29, 1956.

[4] R. J. Glauber, "The quantum theory of optical coherence," Phys. Rev. Lett., vol. 130, pp. 2529-2539, 1963.

[5] H. J. Carmichael and D. F. Walls, "A quantum-mechanical master equation

treatment of the dynamical Stark effect," J. Phys. B, vol. 9, pp. 1199-1219, 1976.

[6] H. J. Kimble, M. Dagenais, and L. Mandel, "Photon antibunching in resonance fluorescence," Phys. Rev. Lett., vol. 39, pp. 691-695, 1977.

[7] H. J. Kimble and L. Mandel, "Theory of resonance fluorescence," Phys. Rev. A, vol. 13, pp. 2123-2144, 1976.

[8] G. S. Agarwal, "Exact solution for the influence of laser temporal fluctuations on resonance fluorescence," Phys. Rev. Lett., vol. 37, pp. 1383-1386, 1976.

[9] G. S. Agarwal and S.S. Jha, "Antibunching effects in resonant raman scattering involving laser fields of arbitrary strengths," Z. Physik B, vol. 35, pp. 391-397, 1979.

[10] S. E. Harris, "Electromagnetically induced transparency," Phys. Today, vol. 50, pp. 36-42, 1997.

[11] V. Balić, D. A. Braje, P. Kolchin, G. Y. Yin, and S. E. Harris, "Generation of paired photons with controllable waveforms," Phys. Rev. Lett. vol. 94, 183601, 2005.

[12] D. A. Braje, V. Balić, S. Goda, G. Y. Yin, and S. E. Harris, "Frequency mixing using electromagnetically induced transparency in cold atoms," Phys. Rev. Lett., vol. 93, 183601, 2004.

[13] A. Kuzmich, W. P. Bowen, A. D. Boozer, A. Boca, C. W. Chou, et al., "Generation of nonclassical photon pairs for scalable quantum communication with atomic ensembles," Nature, vol. 423, pp. 731-734, 2003.

[14] C. H. van der Wal, M. D. Eisaman, A. Andre, R. L. Walsworth, D. F. Phyllips, et al., "Atomic memory for correlated photon states," Science, vol. 301, pp. 196-200, 2003.

[15] I.L. Chuang and M.A. Nielsen, "Quantum computation and quantum information," Cambridge University Press, Cambridge, 2000.

[16] L. -M. Duan, M. D. Lukin, J. I. Cirac, and P. Zoller, "Long-distance quantum communication with atomic ensembles and linear optics," Nature, vol. 414, pp. 413-418, 2001.

[17] M. Hennrich, A. Kuhn, and G. Rempe, "Transition from antibunching to bunching in cavity QED," Phys. Rev. Lett., vol. 94, 053604, 2005.

[18] H. J. Carmichael, P. Drummond, P. Meystre, and D.F. Walls, "Intensity correlations in resonance fluorescence with atomic number fluctuations," J. Phys. A, vol. 11, pp. L121-L126, 1978.

[19] T. Yabuzaki, T. Mitsui, and U. Tanaka, "New type of high-resolution spectroscopy with a diode laser," Phys. Rev. Lett., vol. 67, pp. 2453-2456, 1991.

[20] R. Walser and P. Zoller, "Laser-noise-induced polarization fluctuations as a spectroscopic tool," Phys. Rev. A, vol. 49, pp. 5067-5077, 1994.

[21] D. H. McIntyre, C. E. Fairchild, J. Cooper, and R. Walser, "Diode-laser noise spectroscopy of rubidium," Opt. Lett., vol. 18, pp. 1816-1818, 1993.

[22] J. C. Camparo, "Conversion of laser phase noise to amplitude noise in an optically thick vapor," J. Opt. Soc. Am. B, vol. 15, pp. 1177-1186, 1998.

[23] M. Bahoura and A. Clairon, "Diode-laser noise conversion in an optically dense atomic sample," Opt. Lett., vol. 26, pp. 926, 2001.

[24] M. Martinelli, P. Valente, H. Failache, D. Felinto, L.S. Cruz, et al., "Noise spectroscopy of nonlinear magneto-optical resonances in Rb vapor," Phys. Rev. A, vol. 69, 043809, 2004.

[25] C. G. Alzar, L. Cruz, J. A. Gomez, M. F. Santos, and P. Nussenzveig, "Super-Poissonian intensity fluctuations and correlations between pump and probe fields in Electromagnetically Induced Transparency ," Europhys. Lett., vol. 61, pp. 485-491, 2003.

[26] K. Motomura, M. Tsukamoto, A. Wakiyama, K. Harada, and M. Mitsunaga,

"Observation of correlated anti-Stokes emissions by multiwave mixing in sodium vapor," Phys. Rev. A, vol. 71, 043817, 2005.

[27] V. A. Sautenkov, Yu. V. Rostovtsev, and M.O. Scully, "Switching between photon-photon correlations and Raman anticorrelations in a coherently prepared Rb vapor," Phys. Rev. A, vol. 72, 065801, 2005.

[28] V. Sautenkov, H. Li, Y. Rostovtsev, and M.O. Scully, "Power spectra and correlations of intensity fluctuations in electromagnetically induced transparency," J. Mod. Opt., vol. 54, pp. 2451-2457, 2007.

[29] H. Li, V. A. Sautenkov, T. S. Varzhaperyan, Yu. V. Rostovtsev, and M.O. Scully, "Atomic noise spectra in nonlinear magneto-optical rotation in a rubidium vapor,", J. Opt. Soc. Am. B, vol. 25, pp. 1702-1707, 2008.

[30] T. S. Varzhapetyan, H. Li, G. O. Ariunbold, V. A. Sautenkov, Yu. V. Rostovtsev, and M.O. Scully "Intensity correlations in a coherently prepared Rb vapor in a magnetic field," Opt. Commun. vol. 282, pp. 39-44, 2009.

[31] Y. Xiao, T. Wang, M. Baryakhtar, M. Van Camp, M. Crescimanno, et al., "Electromagnetically induced transparency with noisy lasers," Phys. Rev. A, vol. 80, 041805(R), 2009.

[32] V. V. Vassiliev, S. A. Zibrov, and V. L. Velichansky, "Compact extended-cavity diode laser for atomic spectroscopy and metrology ," Rev. Sci. Instrum., vol. 77, 013102, 2006.

[33] M. Orzag, "Optics," Springer, Berlin, 2000.

[34] A. M. Akulshin, V. A. Sautenkov, V. L. Velichansky, A. S. Zibrov, and M. V. Zverkov, "Power broadening of saturation absorption resonance on the D2 line of rubidium," Opt. Commun., vol. 77, pp. 295-298, 1990.

[35] P. A. Roos, S. K. Murphy, L. S. Meng, J. L. Carlsten, T. C. Ralph, et al., "Quantum theory of the far-off-resonance continuous-wave Raman laser: Heisenberg-

Langevin approach," Phys. Rev. A, vol. 68, 013802, 2003.

[36] G. E. Uhlenbeck and L. S. Ornstein, in Selected papers on noise and stochastic processes, edited by N. Wax, Dover Publications, New York, 1954.

[37] A. B. Matsko, D. V. Strekalov, and L. Maleki, "On the dynamic range of optical delay lines based on coherent atomic media," Opt. Express, vol. 13, pp. 2210-2223, 2005.

[38] H. Xiong, M.O. Scully, and M.S. Zubairy, "Correlated spontaneous emission laser as an entanglement amplifier," Phys. Rev. Lett., vol. 94, 023601, 2005.

[39] R. F. Fox, I. R. Gatland, and G. Vemuri, "Fast, accurate algorithm for numerical simulation of exponentially correlated colored noise," Phys. Rev. A, vol. 38, pp. 5938-5940, 1988.

[40] M. Fleishhauer and M.O. Scully, "Quantum sensitivity limits of an optical magnetometer based on atomic phase coherence," Phys. Rev. A, vol. 49, pp. 1973-1986, 1994.

[41] J. Kitching, S. Knappe, and L. Hollberg, "Miniature vapor-cell atomic-frequency references," Appl. Phys. Lett., vol. 81, pp. 553-555, 2002.

[42] D. Budker, W. Gawlik, D. F. Kimball, S.M. Rochester, V.V. Yashchuk, et al., "Resonant nonlinear magneto-optical effects in atoms," Rev. Mod. Phys., vol. 74, pp. 1153-1201, 2002.

[43] K. Wódkiewicz, "Exact solutions of some multiplicative stochastic processes," J. Math. Phys., vol. 20, pp. 45-49, 1979.

APPENDIX B

A RAPID INSPECTION OF ATOMIC INTERFERENCE USING SUPERFLUORESCENT PICOSECOND PULSES*

The conventional method to measure atomic interference is usually based on incoherent processes on a nano- or microsecond time scale. However, atomic interference may be studied in association with coherent process such as superfluorescence. Producing the superfluorescent picosecond pulses in a Rb vapor pumped by the 100 fs laser pulses, we report an observation of a quantum beating due to Rb D-lines. The relative delay of the superfluorescent pulses is recorded by the streak camera with a 2 ps time resolution, as a function of time interval between the input pulses as it enables us to study the atomic interference.

In this work, we study atomic interference with the superfluorescent light emitted from a Rb vapor. Rb atomic density is 3.6×10^{15} cm^{-3}. The experimental setup is sketched in Fig. 79(A), where the input beam at 785 nm (with an average power of 8 mW measured after the optical parametric amplifier) is furnished by a commercial femtosecond laser system with a repetition rate of 1 kHz. The Rb energy level scheme is depicted in Fig. 79(B). A two-photon excitation from $5S$ to $5D$ leads to the yoked-superfluorescence associated with the upper ($5D$ - $6P$) and the lower ($6P$ - $5S$) transitions. An interference of the input pulses (see, Fig. 79(C)) is measured by the slow photo-detector. Since the laser bandwidth is broad enough to cover the $5P$

*Reprinted with permission from "A Rapid Inspection of Atomic Interference using Superfluorescent Picosecond Pulses", 2010. G. O. Ariunbold, V. A. Sautenkov, and M. O. Scully *Cleo Conference OSA Technical Digest Series* paper CMA4. Copyright [2010] Optical Society of America

level splitting (7.12 THz or 140 fs). The atomic coherence is induced by completion of two possible two-photon excitations through the intermediate states $5P_{1/2}$ and $5P_{3/2}$. The constructive or destructive interference is controlled by the delay of the input pair pulses. The atomic interference is recorded by the second photo-detector which is identical to the first one (see, Fig. 79(D)). On the other hand, one can use a streak camera to measure the 421 nm pulses while the generated pulse characteristics can be recorded at each time interval between the input pulses. In Fig. 80, (A) the normalized temporal profile of the superfluorescent pulses, (B) the relative delay of the superfluorescent pulse, (C) the inverse of the delay, (D) the sum over time of the unnormalized pulse profile, are plotted as functions of time interval between the input pulses. The averaged (smoothed) results are plotted by solid curves in Figs. 80(B - D). As is seen from Fig. 80(E) that the results of the Fourier transforms of the data in Fig. 79(D) (circles) and the smoothed solid curve in Fig. 80(C) (squares) are consistent.

We conclude that the coherent emissions from the collective atoms result in much faster decay than that for incoherent processes. The present idea can be used in, e.g., a rapid inspection of the quantum interference.

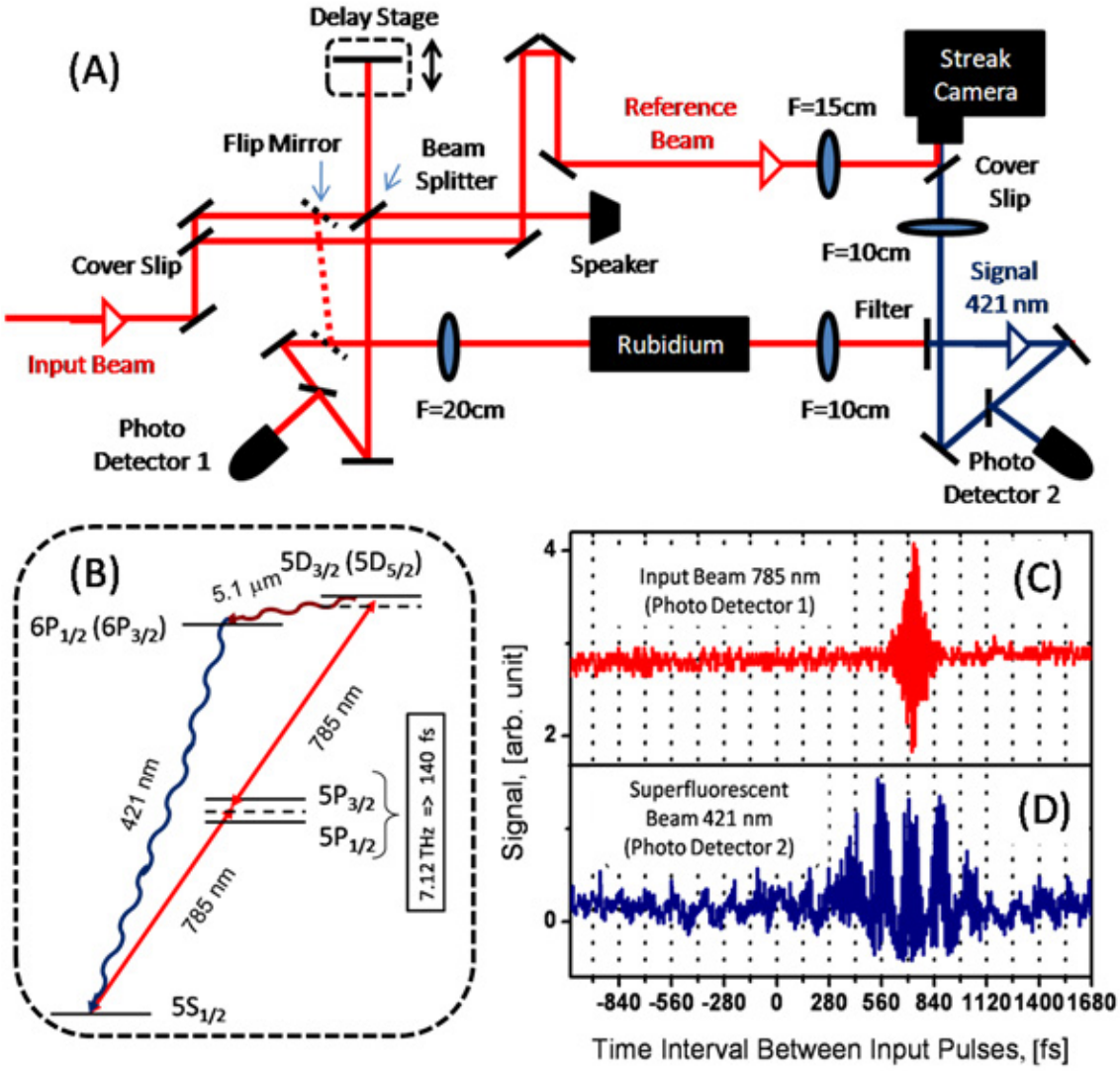

Fig. 79. Appendix B. (A) Experimental setup. (B) Rb energy level diagram. (C) and (D) The recorded data.

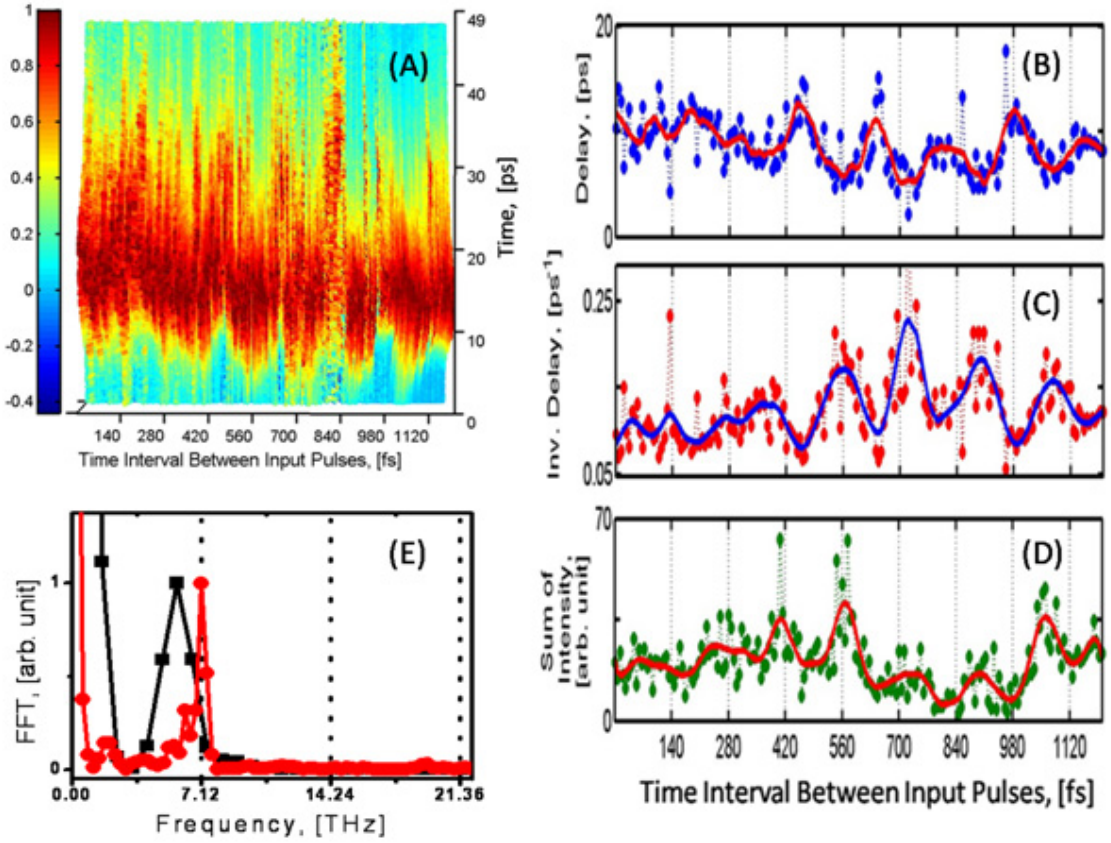

Fig. 80. Appendix B. An inspection of atomic interference by the superfluorescent pulse characteristics, see the text for detail.

VITA

Ariunbold Gombojav was born in Ulaanbaatar, Mongolia. He received his B.S. and M.S. degrees from the National University of Mongolia, Ulaanbaatar, Mongolia and a Ph.D. degree in (theoretical) optics and optoelectronic from Palacky University, Olomouc, Czech Republic. He entered the doctoral program in the Department of Physics at the Texas A&M University in May 2006 and graduated with his Ph.D. in May 2011. From May 2006 to November 2010 he, mostly under the name Gombojav O. Ariunbold, has published 10 articles in peer-reviewed journals including Science magazine, Proceedings of the National Academy of Sciences, and Physical Review A; 5 summaries in the Proceedings of the Optical Society of America; and submitted 4 papers for the publication. His current address is Department of Physics, Texas A&M University, College Station, TX 77843-4242, e-mail: g.o.ariunbold at gmail.com.

The typist for this dissertation was Ariunbold Gombojav.